System behaviour in prestressed concrete T-beam bridges

Ensink, S.W.H.

DOI
10.4233/uuid:15f5628b-9175-4ef3-8f39-41a97cb7749a

Publication date
2024

Document Version
Final published version

Citation (APA)
Ensink, S. W. H. (2024). *System behaviour in prestressed concrete T-beam bridges*. [Dissertation (TU Delft), Delft University of Technology]. https://doi.org/10.4233/uuid:15f5628b-9175-4ef3-8f39-41a97cb7749a

SYSTEM BEHAVIOUR IN PRESTRESSED CONCRETE T-BEAM BRIDGES

Sebastiaan Ensink

SYSTEM BEHAVIOUR IN PRESTRESSED CONCRETE T-BEAM BRIDGES

SYSTEM BEHAVIOUR IN PRESTRESSED CONCRETE T-BEAM BRIDGES

Dissertation

for the purpose of obtaining the degree of doctor
at Delft University of Technology,
by the authority of the Rector Magnificus prof. dr. ir. T.H.J.J. van der Hagen,
chair of the board for Doctorates,
to be defended publicly on Monday 12 February 2024 at 15:00 o'clock

by

Sebastiaan Willem Hendrik ENSINK

Master of Science in Civil Engineering,
Delft University of Technology, The Netherlands,
born in Nijmegen, The Netherlands.

This dissertation has been approved by the promotors.

Composition of the doctoral committee:

Rector Magnificus	chairperson
Prof. dr. ir. M.A.N. Hendriks	Delft University of Technology and Norwegian University of Science and Technology, Norway, promotor
Prof. dr. ir. E.O.L. Lantsoght	Delft University of Technology and Universidad San Francisco de Quito, Ecuador, promotor

Independent members:

Prof. dr. dipl.-ing. J. Kollegger	TU Wien, Austria
Ir. D.G. Schaafsma	Rijkswaterstaat, The Netherlands
Prof. dr. S.E. Taylor	Queen's University, Belfast, UK
Prof. dr. ir. J.G. Rots	Delft University of Technology
Dr. ir. C. van der Veen	Delft University of Technology
Prof. dr. M. Veljkovic	Delft University of Technology, reserve member

Prof. dr. ir. D.A. Hordijk has contributed greatly to the preparation of this dissertation.

Keywords: compressive membrane action, arching action, T-beam bridge, collapse test, assessment, nonlinear finite element analysis

Printed by: Ipskamp Printing

Cover design: Ilse Modder

An electronic version of this dissertation is available at
`http://repository.tudelft.nl/`.

CONTENTS

SUMMARY

ABOUT 70 prestressed concrete T-beam bridges, constructed in the Netherlands between 1953–1977, are still in use today with many located in the main highway network. This type of bridge consists of prefabricated and prestressed T-shaped beams, with an integrated deck slab, cross-beams and transverse prestressing. Even if these bridges are well maintained, two important factors demand the current need for assessment: (1) increased traffic loading and (2) potential lack of shear resistance. Using traditional assessment methods it was concluded that about 50% of these bridges do not fulfil the current design code requirements. However, this does not automatically imply that these bridges are structurally unsafe, since some potentially significant additional load-transfer mechanisms are not taken into account in a traditional assessment. This is strengthened by the observation that, in general, these bridges do not show any signs of distress.

In previous research the integrated deck slab with transverse prestressing was investigated and a substantially higher load capacity was found due to the presence of compressive membrane action (CMA). For the current research, the focus is on the load capacity of the main T-beams. The main characteristics and shear-related deficiencies for the Dutch T-beam bridge stock are therefore investigated. The presence of 2–4 cross-beams in each span, as well as transverse prestressing, in both the cross-beams and the integrated deck slab, led to the concept of 'system behaviour', in which the capacity of a structure is increased due to the restraint provided by the connected members. This concept is investigated using the theory of compressive arching, for both the integrated deck slab (CMA) as well as the T-beams, with the latter designated as compressive arch action (CAA).

The main part of this research is related to a case study of a typical Dutch T-beam bridge called the Vecht bridge. The Vecht bridge is a multispan T-beam bridge, constructed in 1962, located near the town of Muiden crossing the Vecht river. Using a single concentrated load at the centre of the T-beam at two different a/d positions, seven full-scale collapse tests are conducted on this bridge prior to its scheduled demolition. Three tests are conducted with the original structural system unchanged. On a separate span, four tests are conducted on individual T-beams, with the deck in-between the beams sawn in the longitudinal direction. The two types of tests allow for a direct comparison between the load capacity of an individual T-beam versus a connected T-beam. The individual beam tests resulted in a flexural shear failure, whereas the connected beam tests resulted in an explosive failure for both the bridge deck (punching failure) and the T-beam (shear failure).

The case study is extensively analysed with conventional cross-sectional evaluations for shear and bending and using nonlinear finite element analysis. In addition, a generic analytical model for arch action is derived, to investigate the effects of CMA and CAA. Following the conventional assessment, using a linear model for the load effect and a

cross-sectional analysis for the verification, the governing failure mode for connected T-beams is shear tension. On the contrary, analysing an individual simply supported T-beam, the governing failure mode is either the ultimate bending moment at midpoint or flexural shear close to the support. Using a full 3D nonlinear finite element model of the complete span with 15 beams, the experimentally observed failure mode(s) are confirmed. In addition, the model allowed insight in the development of the mechanisms of CMA and CAA. With the exception of the stiffness of the elastomeric bearings, no other parameters needed to be calibrated. From the numerical parameter study, an optimal incremental-iterative solution method combined with an automatic adaptive step size method has been found resulting in nonlinear analyses in which all steps are converged, regardless of the size of the finite element model.

Using the experimental, numerical and analytical methods, it is demonstrated that for T-beam bridges a combination of compressive membrane action (CMA) and compressive arch action (CAA) contributes to the 'system behaviour', which differs significantly from the behaviour of an individual T-beam. Compressive membrane action (CMA), and the corresponding increased (punching) capacity, is found in the deck in case of a (concentrated) load at the centre of a T-beam. Compressive arch action (CAA), and the corresponding increased shear capacity, is found in the T-beam in case of a (concentrated) load positioned in-between the cross-beams. This research has explained and quantified the contribution of the aforementioned mechanisms resulting in an increased capacity for these types of bridges. These effects are not considered in a traditional assessment.

SAMENVATTING

VANDAAG de dag zijn nog circa 70 voorgespannen betonnen T-ligger bruggen in Nederland in gebruik uit de bouwperiode tussen 1953 en 1977. Vele van deze bruggen bevinden zich in het hoofdwegennet. Dit type brug bestaat uit geprefabriceerde voorgespannen T-liggers, een tussenstort, dwarsbalken en dwarsvoorspanning. Zelfs als deze bruggen goed worden onderhouden zijn er twee belangrijke redenen voor een herbeoordeling: (1) toename van de verkeersbelasting en (2) potentieel gebrek aan dwarskrachtcapaciteit. Uit een eerdere beoordeling kwam naar voren dat circa 50% van deze bruggen niet voldoen aan de eisen van de huidige ontwerpnormen. Dit betekent echter niet automatisch dat deze bruggen constructief onveilig zijn, aangezien bij een traditionele beoordeling een aantal potentieel zeer gunstige aanvullende draagmechanismen niet in rekening worden gebracht. Deze conclusie wordt verder versterkt door het feit dat over het algemeen deze bruggen bij een nadere inspectie in een goede conditie blijken te verkeren.

Uit voorgaand onderzoek is gebleken dat de tussenstort, voorzien van dwarsvoorspanning, een aanzienlijk hogere last kan dragen ten gevolge van drukmembraamwerking. Met het huidige onderzoek wordt aansluitend de belastbaarheid van de T-liggers zelf onderzocht. Voor de Nederlandse T-ligger bruggen worden daarom de algemene eigenschappen en de eventuele tekortkomingen, met name in relatie tot dwarskracht, onderzocht. De aanwezigheid van 2 tot 4 dwarsdragers in iedere overspanning en van dwarsvoorspanning, in zowel de dwarsbalken als in het dek hebben hierbij geleid tot het concept van 'systeemgedrag'. Hierbij wordt aangenomen dat de draagcapaciteit van een constructie toeneemt als gevolg van verhindering van vervorming (opsluiting) die wordt veroorzaakt door de aansluitende constructie-onderdelen. Dit concept wordt onderzocht met behulp van de theorie van drukmembraamwerking, voor zowel het dek als de T-liggers, waarbij het laatste fenomeen zal worden aangeduid als drukboogwerking.

Het voornaamste deel van dit onderzoek is gerelateerd aan de casestudy van de Vechtbrug. Dit betreft een representatieve Nederlandse T-ligger brug uit 1962 met meerdere overspanningen die nabij de stad Muiden de rivier de Vecht kruist. Voordat deze brug definitief gesloopt zou worden zijn er door middel van het aanbrengen van een enkele geconcentreerde last in het hart van een T-ligger, op twee verschillende afstanden vanaf de oplegging, in totaal zeven bezwijkproeven op deze brug uitgevoerd. Bij drie van de zeven bezwijkproeven is het originele brugdek intact gelaten. Vervolgens zijn op een ander veld nog eens vier bezwijkproeven uitgevoerd op losse T-liggers waarbij de tussenstort in langsrichting is doorgezaagd. Doordat er twee verschillende soorten testen zijn uitgevoerd, kan de draagcapaciteit van een losse ligger direct worden vergeleken met die van een verbonden ligger. Bij de bezwijkproeven van de losse liggers is sprake van afschuifbuigbreuk, terwijl bij de verbonden liggers sprake is van een explosief bezwijken van zowel het brugdek (pons) als de T-ligger (dwarskrachtbreuk).

De casestudy wordt uitgebreid geanalyseerd door middel van traditionele doorsnede

controles voor buiging en dwarskracht en met behulp van niet-lineaire analyse. Tevens wordt er een analytisch model afgeleid voor het onderzoeken van de effecten van zowel drukmembraamwerking als drukboogwerking. Uit de traditionele controles, met een lineair elastisch model voor de krachtsverdeling en een verificatie op basis van doorsnede controles, volgt voor de verbonden liggers afschuiftrekbreuk als maatgevende faalmechanisme. Voor de losse vrij opgelegde ligger volgt op basis van eenzelfde analyse ofwel het breukmoment halverwege de overspanning ofwel afschuifbuigbreuk nabij de eindoplegging als maatgevende faalmechanisme. Met behulp van een volledig 3D niet-lineair eindige-elementenmodel van een enkele overspanning, bestaande uit totaal 15 liggers, worden de experimenteel waargenomen bezwijkmechanismen bevestigd. Tevens geeft dit model inzicht in de ontwikkeling van de zowel drukmembraamwerking als drukboogwerking. Met uitzondering van de veerstijfheid van de rubber oplegblokken is geen andere kalibratie van parameters toegepast. Door middel van een numerieke parameterstudie is een optimale incrementele iteratieve oplosmethode gevonden. Hierbij is tevens gebruik gemaakt van een automatische adaptieve stapgrootte. Deze aanpak heeft geresulteerd in niet-lineaire analyses waarbij alle last stappen zijn geconvergeerd ongeacht de grootte van het eindige-elementenmodel.

Door middel van zowel experimentele, numerieke als analytische methoden is aangetoond dat bij T-ligger bruggen, door een combinatie van drukmembraamwerking en drukboogwerking, sprake is van 'systeemgedrag' en dat dit gedrag significant afwijkt van die van een losse ligger. Drukmembraamwerking, met de bijbehorende toegenomen (pons) capaciteit, is waargenomen in het brugdek in het geval van een geconcentreerde last in het hart van een T-ligger. Drukboogwerking, met de bijbehorende toegenomen dwarskrachtcapaciteit is waargenomen in de T-ligger in het geval van een geconcentreerde last met een positie tussen de dwarsdragers. Dit onderzoek heeft de bijdrage van de hiervoor genoemde draagmechanismen verklaard en gekwantificeerd hetgeen resulteert in een toename van de draagkracht van dit type brug. Deze effecten worden bij een traditionele herberekening niet in rekening gebracht.

NOTATIONS

GREEK LOWER CASE

α_1, α_2	multiplication factors related to the color segments used in the principal strain plots
β	factor related to the height of the compression zone
β	load-reduction factor for shear according to Eurocode
β_{rel}	reliability index
γ_{c}	partial factor for concrete
δ	deflection, deformation
δ_{2a}	deflection up until phase 2a in nonlinear analysis
δ_{jack}	total jack extension at failure
$\delta_{\text{sb,end}}$	linear elastic deformation steel bridge (end value)
$\delta_{\text{sb,start}}$	linear elastic deformation steel bridge (start value)
δ_{u}	ultimate deflection or deformation
$\delta_{\text{u,CAA}}$	ultimate deflection or deformation related to compressive arch action
$\delta_{\text{u,CMA}}$	ultimate deflection or deformation related to compressive membrane action
δ_z	vertical deflection
ϵ	strain
ϵ_{c}	strain at maximum concrete compressive strength
ϵ_{e}	maximum elastic strain
ϵ_{u}	strain of reinforcement or prestressing steel at maximum load
ϵ_{u}	ultimate strain of concrete in compression
ϵ_{uk}	characteristic strain of reinforcement or prestressing steel at maximum load
ϵ_{ult}	ultimate strain of concrete in tension

ζ_{span}	influence factor of the bending moment in the span on the compression zone resultant
ζ_{supp}	influence factor of the bending moment at the support on the compression zone resultant
η	degree of edge restraint
η	reduction factor for concrete compressive strength used in stress-strain model
θ	compressive strut angle
θ'	additional compressive strut rotation as a result of elastic deformation
θ^{∞}	rigid compressive strut angle
κ	curvature
λ	member slenderness
λ	reduction factor for compression zone depth used in stress-strain model
ν	Poisson's ratio
ν_{min}	coefficient related to flexural shear according to Eurocode
ρ	density of concrete
ρ	maximum shear stress according to GBV (NNI 1962)
ρ_{l}	reinforcement ratio of longitudinal reinforcement in the tensile zone
ρ_{w}	reinforcement ratio for shear reinforcement
$\rho_{\text{w,min}}$	minimum shear reinforcement ratio
σ	stress
σ_1	principal tensile stress in uncracked concrete
σ_{cp}	axial stress in concrete caused by loading or prestressing
σ_{pi}	initial stress in prestressing steel
σ_{pw}	working stress in prestressing steel
σ_x	stress in x-direction (axial)
σ_y	stress in y-direction (vertical)
τ, τ_{xy}	shear stress
τ_{max}	maximum shear stress
$\tau_{\text{S,d}}$	average design shear stress according to VB (NNI 1977)
ϕ	change in angle of the system line

GREEK UPPER CASE

$\Delta\sigma_p$	additional stress in prestressing reinforcement(s) due to bending
Δl	elastic deformation of the compressive strut
Δl_v	additional vertical deformation as a result of the elastic deformation of the compressive strut
Δu	horizontal displacement
ΔF	additional normal force due to displacement Δu
ΔN_p	additional axial force in prestressing reinforcement(s) due to bending

ROMAN LOWER CASE

a	distance between the center of the concentrated load and the center of the support
a_v	shear span
a_v	vertical displacement
b	width
b_{flange}	T-beam top flange width
b_{min}	minimal width of the cross-section
b_{slab}	integrated deck slab width
b_w	width of the cross-section for shear according to Eurocode
d	effective depth of the cross-section
d_p	effective depth of the prestressing reinforcement
d_s	effective depth of the ordinary reinforcement
f	drape of a curved prestressing tendon
f_b	tensile strength of concrete according to VB (NNI 1977)
f_c	compressive strength of concrete
f_{cd}	design value of concrete compressive strength
$f_{cd,pl}$	design value of unreinforced concrete compressive strength
f_{ck}	characteristic compressive cylinder strength of concrete
f_{cm}	mean concrete cylinder compressive strength

$f_{cm,cube}$	mean concrete cube compressive strength
$f_{cm,slab}$	mean concrete cylinder compressive strength, integrated deck slab
$f_{cm,T\text{-}beam}$	mean concrete cylinder compressive strength, T-beam
f_{ctm}	mean axial tensile strength of concrete
$f_{p0.1k}$	characteristic 0.1% proof-stress of prestressing steel
f_{pd}	design yield strength of prestressing steel
f_{pk}	characteristic yield strength of prestressing steel
f_u	tensile strength of reinforcement or prestressing steel
f_y	yield strength of reinforcement or prestressing steel
f_{yd}	design yield strength of reinforcement
f_{yk}	characteristic yield strength of reinforcement
f_{ym}	mean yield strength of reinforcement or prestressing steel
h	height
h_{avg}	average thickness concrete slab
h_{eq}	equivalent length or crack-band width
$h_{eq,max}$	maximum equivalent length or crack-band width to avoid a snap-back in the softening curve
k	coefficient related to flexural shear (size effect) according to Eurocode
k_1	coefficient related to flexural shear (axial stress) according to Eurocode
k_{hor}	linear horizontal stiffness
l	length
p	distance between top side concrete slab and bottom side pile anchorage plate or ribs
q	distributed line load
q_{pw}	equivalent distributed line load caused by working prestressing load
q_u	ultimate distributed line load
q_{u0}	initial distributed line load
s	spacing of the shear reinforcement
tol_1	bottom side tolerance underwater concrete

tol_2	top side tolerance underwater concrete
x	distance of a control section to the center of the support
x_{span}	height of compression zone in the span
x_{supp}	height of compression zone at the support
z	inner lever arm of internal forces
z_{cb}	distance from the centre of gravity of a concrete section to the bottom edge
z_{ct}	distance from the centre of gravity of a concrete section to the top edge
z_{u}	inner lever arm of internal forces at failure
$z_{x_{\text{span}}}$	distance between the top edge and the stress resultant in the span compression zone
$z_{x_{\text{supp}}}$	distance between the bottom edge and the stress resultant at the support compression zone

ROMAN UPPER CASE

A	cross-sectional area
A	length of concrete compressive strut
A'	reduced length of concrete compressive strut as a result of elastic deformation
A_1	length of concrete compressive strut ($a_{\text{v}} = 0$)
A_2	length of concrete compressive strut ($a_{\text{v}} > 0$)
A_{c}	cross-sectional area of concrete
$A_{\text{c,1}}$	phase 1 cross-sectional area, T-beam
$A_{\text{c,2}}$	phase 2 cross-sectional area, T-beam with integrated deck slab
A_{p}	cross-sectional area of prestressing reinforcement
A_{s}	cross-sectional area of ordinary reinforcement
A_{sl}	cross-sectional area of longitudinal reinforcement in the tensile zone
A_{sw}	cross-sectional area of shear reinforcement within length s
B	width
C	volumetric compressive modulus

$C_{\mathrm{Rd,c}}$	design value of coefficient related to flexural shear according to Eurocode
$C_{\mathrm{Rm,c}}$	mean value of coefficient related to flexural shear according to Eurocode
$D_{\max}$	maximum aggregate size
E	modulus of elasticity
E_1	maximum principal strain
E_3	minimum principal strain
E_{cm}	secant modulus of elasticity of concrete
E_{p}	Young's modulus of prestressing steel
E_{s}	Young's modulus of reinforcement
E_{slab}	modulus of elasticity, integrated deck slab
$E_{\mathrm{T\text{-}beam}}$	modulus of elasticity, T-beam
F	force or unit load
F_0	initial normal force due to soil and water pressure against retaining walls ($a_{\mathrm{v}} = 0$)
$F_{2\mathrm{a}}$	load up until phase 2a in nonlinear analysis
$F_{\max}$	maximum concentrated (live) load
$F_{\max,\mathrm{M_{cr}}}$	maximum concentrated (live) load related to cracking moment
$F_{\max,\mathrm{M_u}}$	maximum concentrated (live) load related to ultimate bending moment
$F_{\max,V_{\mathrm{FS}}}$	maximum concentrated (live) load related to flexural shear resistance
$F_{\max,V_{\mathrm{ST}}}$	maximum concentrated (live) load related to shear tension resistance
$F_{\mathrm{pw,kink}}$	working prestressing force at a kink in the system line
F_{tot}	total normal force
$F_{\mathrm{tot,span}}$	total normal force in the span
$F_{\mathrm{tot,supp}}$	total normal force at the support
F_{u}	ultimate load
$F_{\mathrm{u,CAA}}$	ultimate load related to compressive arch action
$F_{\mathrm{u,CMA}}$	ultimate load related to compressive membrane action
$F_{\mathrm{u,max}}$	maximum ultimate load

$F_{u,NL}$	ultimate load determined by nonlinear analysis
$F_{u,test}$	ultimate load determined by collapse test
G	shear modulus
G_c	compressive fracture energy
G_f	tensile fracture energy
I_c	second order moment of area of concrete section
K	vertical stiffness of a single rubber layer
$K_{x,y}$	lateral support stiffness
K_z	vertical support stiffness
L	length, span
LF	load factor
$LF_{M_{cr}}$	load factor for cracking moment
LF_{M_u}	load factor for ultimate bending moment
LF_{shear}	load factor for shear
$LF_{V_{FS}}$	load factor for flexural shear
$LF_{V_{ST}}$	load factor for shear tension
M	bending moment
M_1	phase 1 bending moment ($M_{dw} + M_{pw}$)
M_2	phase 2 bending moment (M_F)
M_{cr}	cracking moment
M_F	bending moment caused by unit load F
M_{dw}	bending moment caused by dead weight
M_{pw}	bending moment caused by working prestressing force
M_u	ultimate bending moment
$M_{u,span}$	ultimate bending moment in the span
$M_{u,supp}$	ultimate bending moment at the support
M_y	vertical bending moment in nonlinear analysis (DIANA)
N	axial force

N_1	phase 1 axial force (N_{pw})
N_2	phase 2 axial force ($N_F = 0$)
N_{Ed}	axial force caused by loading or prestressing
N_F	axial force caused by unit load F
$N_{M_{u,span}}$	compression zone resultant as a result of the ultimate bending moment in the span
$N_{M_{u,supp}}$	compression zone resultant as a result of the ultimate bending moment at the support
N_p	axial prestressing force
$N_{p,span}$	axial prestressing force in the span
$N_{p,supp}$	axial prestressing force at the support
N_{pi}	initial axial prestressing force
N_{pw}	working axial prestressing force
$N_{pw,hor}$	working prestressing force, horizontal component
$N_{pw,vert}$	working prestressing force, vertical component
N_x	axial force in x-direction in nonlinear analysis (DIANA)
N_{xx}	in-plane distributed line force in x-direction in nonlinear analysis (DIANA)
Q_z	shear force in z-direction in nonlinear analysis (DIANA)
R	radius
R_A	support reaction force (loaded side)
R_B	support reaction force (non-loaded side)
S_{xx}	embedded reinforcement stress in nonlinear analysis (DIANA)
S_{XX}	concrete stress in x-direction in nonlinear analysis (DIANA)
S_y	first moment of area around the y-axis
S_{YY}	concrete stress in y-direction in nonlinear analysis (DIANA)
T	ratio coefficient
$TDtZ$	vertical deformation in nonlinear analysis (DIANA)
V	shear force
V_{dw}	shear force caused by dead weight

V_{F}	shear force caused by unit load F
V_{FS}	shear force related to flexural shear
V_{pw}	shear force caused by working prestressing force
V_{Rd}	design value of the shear resistance
$V_{\mathrm{Rd,c}}$	design value of the flexural shear resistance, contribution of concrete
$V_{\mathrm{Rd,s}}$	design value of the flexural shear resistance, contribution of shear reinforcement
$V_{\mathrm{Rm,c}}$	mean value of the flexural shear resistance, contribution of concrete
$V_{\mathrm{S,d}}$	design value of the shear force according to VB (NNI 1977)
V_{ST}	shear force related to shear tension
V_{tot}	sum of shear force caused by dead weight and working prestressing force ($V_{\mathrm{dw}} + V_{\mathrm{pw}}$)
V_{u}	ultimate shear force
W_{cb}	section modulus of the bottom part of the concrete section
$W_{\mathrm{cb,1}}$	phase 1 section modulus of the bottom part of the concrete section, T-beam
$W_{\mathrm{cb,2}}$	phase 2 section modulus of the bottom part of the concrete section, T-beam with integrated deck slab
W_{ct}	section modulus of the top part of the concrete section

ABBREVIATIONS

AA	arch action
CAA	compressive arch action
CMA	compressive membrane action
FS	flexural shear
NLFEA	nonlinear finite element analysis
RBK	Dutch guideline for the assessment of existing bridges (Rijkswaterstaat 2013)
SLS	serviceability limit state
ST	shear tension
TPL	transverse prestressing level
ULS	ultimate limit state

1

INTRODUCTION

In this chapter the research topic of 'system behaviour in prestressed concrete T-beam bridges' is introduced and the scope and objectives of this research are given. In addition, the research methodology and the structure of this dissertation are explained.

1

1.1. BACKGROUND

PREFABRICATED prestressed concrete beam bridges have been built since the invention of prestressed concrete and the availability of high strength steel, starting shortly before and after WWII. One of the earliest examples in bridge construction of this type is the Adam Viaduct (1946) in the UK (McIlmoyle 1947). This multispan railway bridge consists of prefabricated prestressed concrete I-shaped beams transversely connected by post-tensioned steel rods in the top flange, see Figure 1.1.

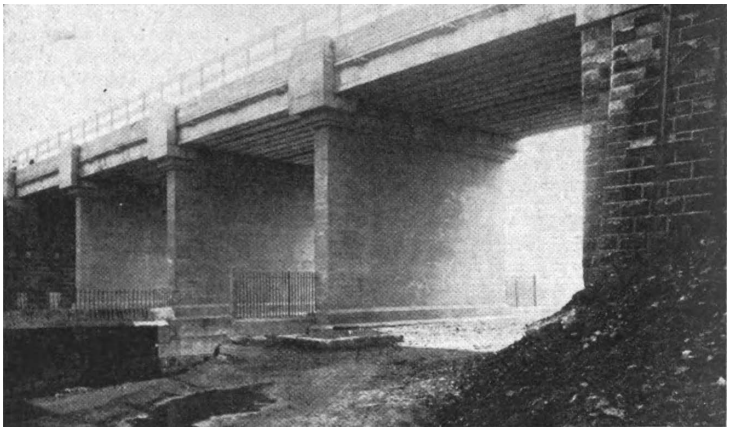

Figure 1.1: Adam Viaduct in the UK (1946) (taken from (McIlmoyle 1947))

After WWII there was an obvious high demand in Europe to construct new bridges. Consequently, many concrete bridges are built in the decades following WWII. The number of bridges built was at its peak in the 1960s and 1970s. The need for new bridges together with the increased knowledge of prestressed concrete fuelled the development of prefabricated concrete beams. With the advantages of rapid on-site construction and controlled prefabrication many such bridges have been built and are still being built today. Now, after more than 60 years many of these early bridges are reaching the end of their expected lifespan and the question arises whether these bridges are still structurally safe. Even if these bridges are well maintained and do not show any signs of distress, two important factors demand the current need for assessment: (1) increased traffic loading and (2) potential lack of shear resistance.

The road traffic has dramatically increased since these bridges were built both in numbers and in axle loads. This is also reflected in the changes in the design codes in the Netherlands over the last 80 years (NNI 2020). In the current design code, NEN-EN 1991-2 (NNI 2015), the axle loads are significantly higher and the axles more closely together as compared to the codes used in the past. In the period from 1933 to 2007, the code provisions in the Netherlands remained largely the same with only minor adjustments. Specifically, for the highest load class 60, used for highway bridges, the live load model consists of three axles with an equal load of 200 kN per axle. In this period, only the axle spacing changed from 1.5 m and 6.0 m (distance between the first and the second and between the second and third axle) (<1963) to 1.0 m and 4.0 m (1963-2007).

From 2007 onwards, the current live load model 1 from NEN-EN 1991-2 (NNI 2015), is adopted with just two axles at a distance of only 1.2 m and an equal load of 300 kN per axle. Consequently, compared to the original design, with the current code, the design sectional shear forces have increased significantly.

The other important factor for assessment is the increased knowledge in concrete shear resistance. In the Netherlands, before 1974, the code provisions used for shear generally resulted in very low shear reinforcement and the shear resistance was substantially over-estimated[1]. In current design of concrete members, according to NEN-EN 1992-1-1 (NNI 2011a), the shear resistance is significantly reduced as compared to previous codes and, contrary to slabs, for (prestressed) beams a minimum amount of shear reinforcement is now required. In many cases the existing beam bridges do not satisfy this minimum requirement. Additionally, the current detailing rules for stirrups are different from the engineering practices in the past[1]. Consequently, even if a sufficient amount of stirrups is present in existing prestressed concrete beam members, it is unclear if they can be taken fully into account for assessment. Furthermore, because of the relatively low steel classes used in the past, their capacity is also limited.

On the more positive side, continued hardening of concrete often results in a higher strength compared to the 28 days strength used in the original design. The increase in concrete strength can be significant and the corresponding increased shear resistance can sometimes mitigate (some of) the above mentioned factors.

In the Netherlands in the early 2000s, the need for assessment of existing structures was recognised and the Dutch Ministry of Infrastructure and Water Management (Rijkswaterstaat) started with the evaluation of the structural safety and the remaining life span of their existing concrete bridge stock (Rijkswaterstaat 2007). This evaluation was executed starting with the (expected) structurally most critical and heavily loaded highway bridges to the less critical and less heavily loaded viaducts in secondary roads.

One subset under investigation are the prestressed concrete T-beam bridges (Roosen 2015, Roosen and Sliedrecht 2018). About 70 of these bridges, constructed in the Netherlands between 1953–1977, are still in use today, with many located in the main highway network. This type of bridge consists of prefabricated and prestressed T-shaped beams, with an integrated deck slab, cross-beams and transverse prestressing, see Figure 1.2. A more detailed description of this bridge type is given in Chapter 2.

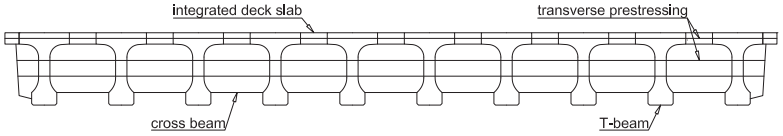

Figure 1.2: Typical cross-section prestressed concrete T-beam bridge

From the initial assessment, it was concluded that about half of these bridges do not fulfil the current design code requirements for existing structures, i.e. NEN 8700 and RTD 1006 (NNI 2011b, Rijkswaterstaat 2013), in the ultimate limit state (ULS), warranting further investigation. It should be noted that this does not automatically imply that

[1]This is treated in Chapter 2 Section 2.8.

these bridges are structurally unsafe since some potentially significant additional load-transfer mechanisms are not taken into account in a traditional assessment. This is strengthened by the observation that, in general, these bridges do not show any signs of distress.

In previous research (Amir 2014), the integrated deck slab with transverse prestressing was investigated. Compared to conventional bending theory, the slab proved to have a substantially higher load capacity due to the presence of compressive membrane action (CMA). Compressive membrane action is activated after initial cracking has occurred and the slab starts bending under load. When the lateral (horizontal) movement of the slab is restrained by stiff boundaries, compressive membrane forces are induced. Since the integrated deck slab is no longer the governing, or weakest, structural element in T-beam bridges, the focus is shifted to the main T-beams.

With assessment of existing bridges, and in general also for new structures, secondary nonlinear effects like arching action are often not taken into account. However, for this type of bridge these secondary nonlinear effects could be substantial. Compressive membrane action (CMA) in the deck slab is possibly also activated with a load placed directly on the T-beam. Additionally, in longitudinal direction, the T-beams are locked between the cross-beams and compressive arching action (CAA) could potentially significantly increase their load capacity. This leads to the concept of 'system behaviour', in which the capacity of a structure is increased due to the restraint provided by the connected members.

1.2. SCOPE AND OBJECTIVES

NOT much research has been done on the structural or 'system behaviour' of concrete beam bridges as is defined in the previous section. In most concrete research, the emphasis is on separate or individual components, like beams and slabs. However, a better understanding of the workings of a complete structure, in the ultimate limit state, can be beneficial when assessing existing concrete structures to reveal 'hidden' capacity. In this research the scope is limited to the existing prestressed concrete T-beam bridges still in use in the Netherlands. Some of these bridges contain atypical aspects which are excluded for this research; these atypical features are listed in Chapter 2 Section 2.3. Furthermore, the focus of this research is on the load capacity of the main T-beams and not on other bridge deck components such as the cross-beams or the integrated deck slab.

The objectives of this research are a better understanding of the restraining effects in T-beam bridges, in relation to the ultimate load capacity of the T-beams, and to identify the requisites needed for the development of additional load-transfer mechanisms such as compressive membrane action in the deck slab and compressive arching action in the T-beam. In addition, the ultimate load capacity of individual T-beams will be directly compared to connected T-beams, to understand the differences in behaviour and load-transfer mechanisms. Ultimately, the goal of this research is to investigate whether the existing T-beam bridges in the Netherlands still have sufficient load capacity or if they require strengthening measures.

1.3. RESEARCH QUESTIONS

FOLLOWING the scope and objectives as stated in the previous section, the main research question that is addressed in this dissertation is as follows:

In concrete T-beam bridges, how does the structural or 'system behaviour', benefit the ultimate load capacity of the main T-beams?

In this context structural or 'system behaviour' refers to the restraint provided by the connected members. In concrete T-beam bridges the main T-beams are connected by prestressed cross-beams and by the transverse prestressing in the integrated deck slab. To answer the main question, the following sub questions are stated:

- To which extent does compressive membrane action (CMA) in the integrated deck slab increase the ultimate load capacity of the main T-beams?
- To which extent is the ultimate load capacity of the main T-beams, locked between the cross-beams, increased by arching action?
- How does the resistance of an individual (isolated) T-beam translate to the resistance of connected T-beams and what are the benefits of large-scale testing and nonlinear finite element analysis?

For the first two sub questions the necessary boundary conditions needed for compressive membrane action and arching action are also investigated. These mechanisms will be introduced in Chapter 3.

1.4. RESEARCH METHODOLOGY

TO investigate the 'system behaviour' of existing T-beam bridges, the main part of this research is related to a case study of a typical Dutch multispan T-beam bridge from 1962 called the Vecht bridge. Prior to its demolition, seven full-scale collapse tests are executed on this bridge as part of this research. The case study of the Vecht bridge is split into three parts, starting with an assessment based on linear elastic analysis, following up with the full-scale collapse tests and finalizing with the nonlinear analysis which includes a numerical parameter study. The case study is preceded by an overview of the existing prestressed concrete T-beam bridges in the Netherlands, to investigate the dimensions, geometry and materials used, and to compare these aspects to the Vecht bridge. In addition, the theories related to compressive membrane action in thin slabs as well as arching action in beams, and the current state-of-the-art theories and assessment approaches used for existing structures, are researched for their application to T-beam bridges. In this context, for compressive arching action in beams, an analytical model is proposed. The results of the case study, together with the theoretical parts, are combined in order to investigate the additional load capacity of T-beam bridges by 'system behaviour'. The different parts of the research, and how they connect, are visualised in Figure 1.3.

1

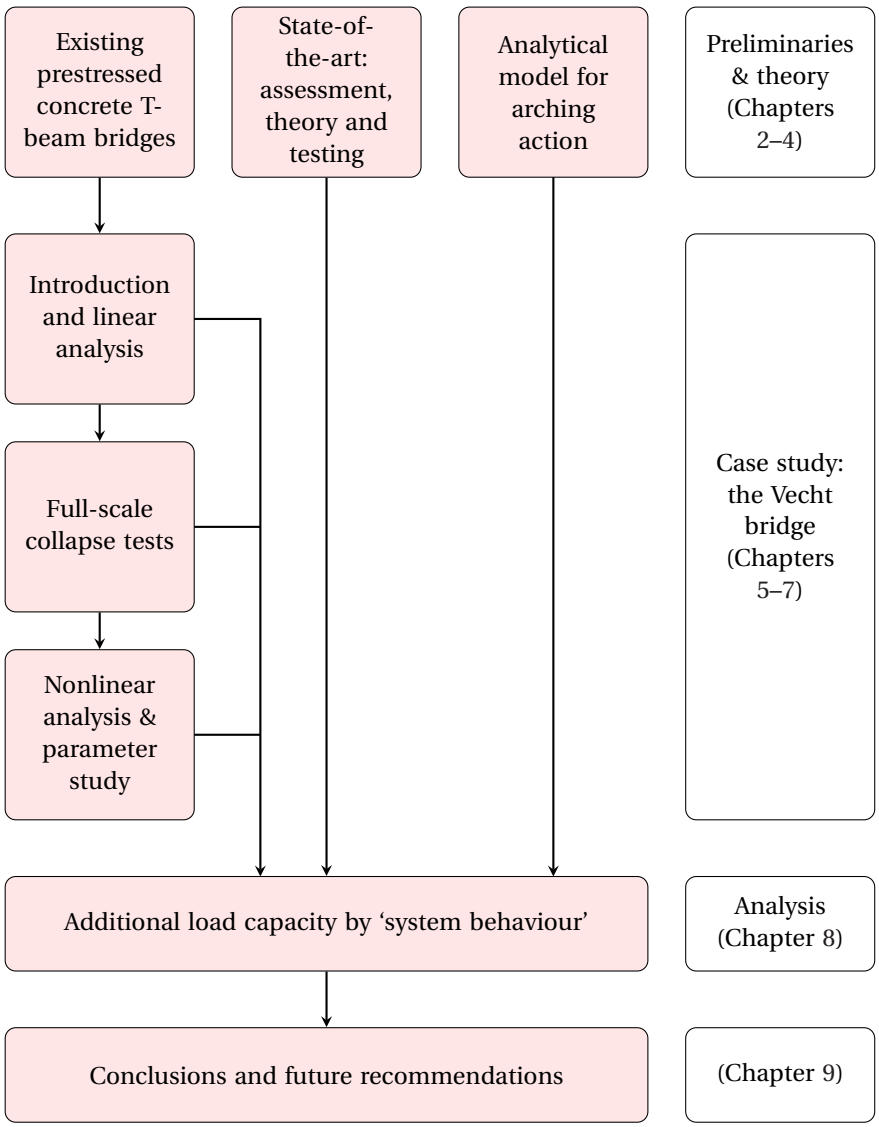

Figure 1.3: Research overview

1.5. OUTLINE

To guide the reader, a brief description of each chapter is given. In total this dissertation is comprised of nine chapters. The relation between Chapters 2–9 is also outlined in Figure 1.3. In Chapter 2 the existing Dutch T-beam bridges are introduced with their construction and execution methods, typical geometry and dimensions as well as the material properties and the reinforcement and prestressing layout. In addition, the deficiencies specifically related to shear are detailed. Chapter 3 outlines the current state-of-the-art assessment approaches used for existing structures. In addition, the theories related to compressive membrane action in thin slabs as well as compressive arching action in beams are treated. This chapter also includes an overview of other bridge collapse tests found in the literature. In Chapter 4 an analytical model for arching action in restrained beams is proposed. This model will be used to analyse the load capacity of the T-beams in the full-scale collapse tests.

Chapters 5–7 are related to a case study of a typical Dutch T-beam bridge called the Vecht bridge (1962). In Chapter 5 the Vecht bridge is introduced with a short history of the bridge and a detailed description of its geometry, reinforcement and prestressing. The results of the material investigation are also treated in this chapter. In addition, a linear elastic FEM model is used to analyse the (concentrated) live load location in relation to the sectional forces. In combination with the prestressing forces, an assessment based on linear analysis is carried out to determine the critical load and associated position(s) based on sectional calculations. In Chapter 6 the details of the experimental setups and the results of the full-scale collapse tests are given. For this research seven full-scale collapse tests are executed on the Vecht bridge. Three experiments are carried out with the original structural system unchanged. In four experiments, the integrated deck slab is sawn in the longitudinal direction, so that the individual behaviour of the T-beams can be tested. In Chapter 7 the details and the results of the nonlinear analysis of the full-scale collapse tests are given. In addition, a numerical parameter study is carried out.

In Chapter 8 the results of the case study together with the theoretical parts (Chapters 3–4), are combined in order to analyse the 'system behaviour' of T-beam bridges. The analysis focusses on compressive membrane action in the integrated deck slab and compressive arch action in the T-beams and the boundary conditions necessary to activate these mechanisms. In addition, the differences in behaviour, ultimate load capacity and load-transfer mechanism between individual T-beams and connected T-beams are examined. Finally, Chapter 9 contains the overall conclusions and the recommendations for future research.

2

EXISTING PRESTRESSED CONCRETE T-BEAM BRIDGES

In this chapter prestressed concrete T-beam bridges are introduced. The construction and execution methods, their typical geometry and main components are described. In addition, their material properties, reinforcement and prestressing layout as well as their most common shear-related deficiencies are described.

2.1. INTRODUCTION

T-BEAM bridges consist of prefabricated and prestressed T-shaped beams, with an integrated deck slab, cross-beams and transverse prestressing. In Figure 2.1 a typical example of a bridge deck cross-section for this type of bridge is shown. In the Netherlands about 70 of these bridges were constructed between 1953–1977 and many are still in use today. For 33 Dutch T-beam bridges the year of construction versus number of bridges is shown in Figure 2.2. At present, this type of bridge has fallen out of fashion due to the labour-intensive construction method, mainly due to the casting of the cross-beams and the integrated deck slab. In France this type of bridge is referred to as 'viaduc à travées indépendantes à poutres précontraintes' or 'VIPP' for short, which translates to simply supported and post-tensioned prestressed beam viaduct.

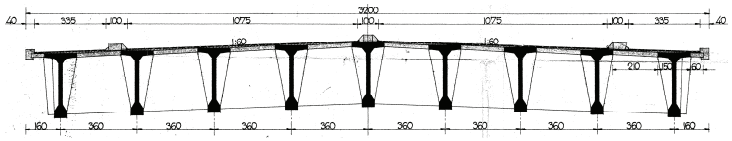

Figure 2.1: Typical cross-section of a T-beam bridge (Van Brienenoord bridge Rotterdam 1963) (Kamp 2017, Roosen and Sliedrecht 2018)

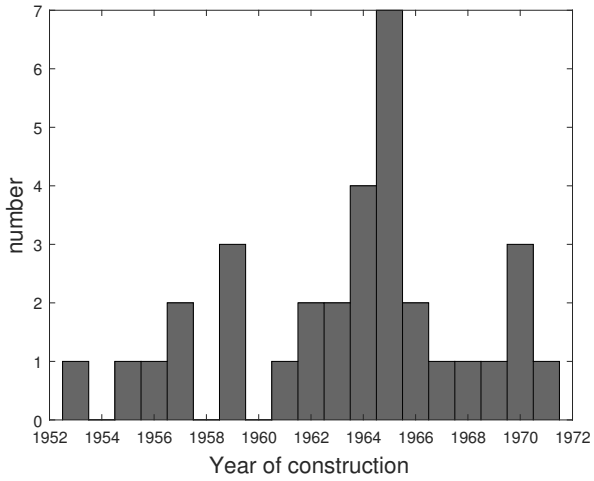

Figure 2.2: Number of bridges built versus year of construction based upon 33 Dutch bridges (Kamp 2017, Roosen and Sliedrecht 2018)

Although no comprehensive overview has been made, this type of bridge appears to have been constructed worldwide as references are found related to T-beam bridges in France (Godart 2015, Tonnoir et al. 2018), Belgium, the US, China and Japan. Typically, in the Netherlands this type of bridge is used as an approach bridge as part of a river crossing where the main span over the river itself is constructed in a different manner, for

instance as an arch bridge or a movable bridge. As these approach bridges generally require multiple spans, the benefits of prefabrication can be fully exploited. An example of such a river crossing is shown in Figure 2.3.

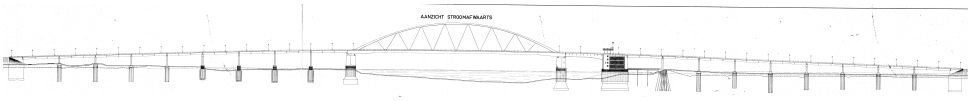

Figure 2.3: Typical river crossing with approach bridges constructed with T-beams (Van Brienenoord bridge Rotterdam 1963) (Kamp 2017, Roosen and Sliedrecht 2018)

Usually, these bridges are located in the main highway network and are therefore of significant regional and national importance in terms of traffic flow. For the present research most information comes from the Dutch Ministry of Infrastructure and Water Management (Rijkswaterstaat), therefore in this chapter the emphasis will be on the Dutch bridge stock. The results of this chapter are based upon various Rijkswaterstaat reports (Kamp 2017, Roosen 2015, Roosen and Sliedrecht 2018), available technical drawings of more than 30 Dutch T-beam bridges, an online photo archive (Rijkswaterstaat 2020) as well as other available sources (Freyssinet 1972, Goedhart 1956).

2.2. CONSTRUCTION AND EXECUTION

THE superstructure of T-beam bridges is usually constructed in a similar fashion, the basic approaches for construction are:

- Preferably, the T-beams all have the same size and length, and are prefabricated on-site or in a factory. In some cases two different lengths of spans are used for each side of the river crossing. In addition, the edge T-beams can be slightly different from the other T-beams due to the one-sided connection with the cross-beams and the anchorage of the transverse prestressing.
- At the ends of the T-beams, prefabricated concrete end blocks are placed in the form. These hold the anchorage zones of the, in most cases curved, prestressing tendons, see Figures 2.4a and 2.7. Since the end blocks are already completely cured, early stressing of the tendons is possible to avoid shrinkage cracks (Freyssinet 1972).
- After prefabrication, the T-beams are transported to the span under construction. In some cases this is done by utilizing a temporary railway track on the already completed spans, and then using an assembly truss to lift the T-beams into position, see Figure 2.4b. In other cases the T-beams are simply lifted in place by using a crane, see Figure 2.5.

2.3. MAIN DIMENSIONS

IN this section the main dimensions of the T-beam bridges are described based upon the Dutch bridge stock using the available data of 33 bridges (Kamp 2017, Roosen and Sliedrecht 2018), see also Tables 2.1–2.2. In most cases, the T-beam bridges have multiple

(a) Prefabrication of T-beam on-site

(b) On-site transportation of prefabricated T-beam using railway track

Figure 2.4: Construction of the Van Brienenoord bridge Rotterdam (1963) (Rijkswaterstaat 2020)

Figure 2.5: Construction of a T-beam bridge deck (Vechtbrug 1962) (Rijkswaterstaat 2020)

spans of equal length and are simply supported with expansion joints at the piers and at the abutments, see Figure 2.3. In some cases, a separate bridge is used for each driving direction. River crossings are typically straight bridges or bridges with a negligible skew. Most bridges show similarities in their general layout, dimensions and geometry. However, some bridges contain atypical properties and can therefore not be readily compared to the other bridges within this group. To distinguish these bridges, the following aspects are considered to be atypical:

1. Acute angle between the superstructure and substructure.
2. Continuous system, i.e. statically indeterminate.
3. The use of half-joints.
4. T-beams with a varying height.
5. An additional concrete overlay on top of the deck slab.

The atypical bridges are listed in Table 2.1 where the atypical properties relate to the numbering listed above. The beam spacing given in Table 2.1 refers to the centre-to-centre distance between the T-beams. An example of the use of half-joints and a varying height is shown in Figure 2.6.

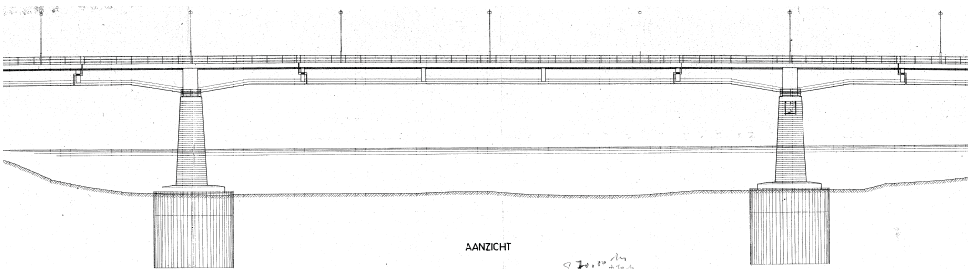

Figure 2.6: Maasbrug Roermond with half-joints and variable height (1959) (Kamp 2017, Roosen and Sliedrecht 2018)

The more common bridges that do not contain atypical properties are listed in Table 2.2. As can be seen in Table 2.2, the span lengths range between 17–50 m, with an average slenderness of 19.0. Naturally, the slenderness is also related to the beam spacing. In general a larger beam spacing with equal span length will result in a lower slenderness. However, larger beam spacing is also directly related to the beam dimensions. With increasing width of the top flange, the beam spacing naturally increases as well, see also Table 2.4. Finally, the beam height increases from 900 to 3000 mm as the span lengths increase.

Table 2.1: Main dimensions of 9 atypical Dutch T-beam bridges (in order of span length)

Name of bridge	Atypical property[a]	Span length [m]	Beam height [mm]	Slenderness [-]	Beam spacing [mm]
Uitgeest[b,c]	1,2,5	15.9	1100	14.5	1500
aansluiting Schiphol	2,5	18.0	650	27.7	800
Brug o/d Rijn[b,c]	1	21.9	1100	19.9	1200
Hollandsche IJssel[c]	2,4	21.9	1320	16.6	1400
Spoorweg Harderwijk[c]	3,4	24.2	1250	19.3	2118
Terbregseplein[b,c]	3	24.4	1150	21.3	1600
Schellingwouderbrug	2	28.9	1500	19.3	1500
Amsterdamse brug	2	28.9	1500	19.3	1500
Maasbrug Roermond[b,c]	3,4	50.0	2550	19.6	2560

[a] see Section 2.3, [b] used in material investigation see Section 2.5

[c] used in transverse prestressing investigation see Sections 2.5.3 and 2.7.2

Table 2.2: Main dimensions of 24 typical Dutch T-beam bridges (in order of span length)

Name of bridge	Span length [m]	Beam height [mm]	Slenderness [-]	Beam spacing [mm]
Brasserskade	17.4	900	19.3	*1000*
Maastrichterlaan[c]	18.0	1050	17.1	1150
Ringvaart noord	19.1	1100	17.4	2240
Steenenhoek[c]	20.4	1200	17.0	1250
Helperzoom[a,b,c]	22.9	1100	20.8	1610
Hereweg[a]	22.9	1100	20.8	1610
Paterswoldseweg[a]	22.9	1100	20.8	1610
Vechtbrug[a]	24.0	1150	20.9	1225
Schieplein	24.5	1150	21.3	1600
Kruithuisweg[b,c]	24.7	1100	*22.5*	1600
Brug o/d Rotte[b,c]	25.1	1150	21.8	1500
Brug o/h Amsterdam-Rijnkanaal[c]	26.1	1500	17.4	1770
Hamersbrug[b,c]	26.2	1400	18.7	2450
Koningsbrug	26.5	1500	17.7	1440
Meeuwerderbaan[a,b,c]	26.7	1250	21.4	1560
Thoolsebrug[b,c]	34.4	1800	19.1	2144
Volkeraksluizen	36.8	2240	*16.4*	2390
Schinkelbrug	39.0	2100	18.6	3234
Draaibrug Sas van Gent[b,c]	40.0	2100	19.1	4080
Draaibrug Sluiskil[c]	40.0	2100	19.1	3340
Brug o/d Beneden Merwede[c]	44.1	2500	17.6	3625
Brug o/d Boven Merwede[c]	44.1	2450	18.0	2056
Hollandse brug	49.6	3000	16.5	*4110*
Van Brienenoord[b,c]	50.2	3000	16.7	3600
average	30.2	1627	19.0	2175

[a] no longer in use (demolished), [b] used in material investigation see Section 2.5

[c] used in transverse prestressing investigation see Sections 2.5.3 and 2.7.2

2.4. BRIDGE COMPONENTS

IN this section the individual components of the superstructure of a T-beam bridge are described in more detail. This section is based on the bridges listed in Table 2.2.

2.4.1. T-BEAM

THE general design of a prefabricated prestressed T-beam is shown in Figure 2.7. In case of post-tensioned tendons (see also Section 2.7.1), a prefabricated end block is used at the ends of the beam, which also holds the anchorage zones of the prestressing tendons, see also Figure 2.4a. The thickness of this part is normally equal to the thickness of the bottom flange. The prefabricated end block is continued in the non-prefabricated part, see Figure 2.7, section A, and a transition piece is used between the end block and

the T-beam. The transition between the web and the flanges can either be curved (see Figure 2.7, section B) or bevelled. In the top view of Figure 2.7, the partly absent top flange near the ends of the T-beam is shown, presumably for easier casting of the end cross-beams. In section C it is shown that the onset of the intermediate cross-beams is usually cast as part of the prefabricated T-beam. In top view it is shown that these are usually slightly wedge-shaped, presumably for easier formwork removal.

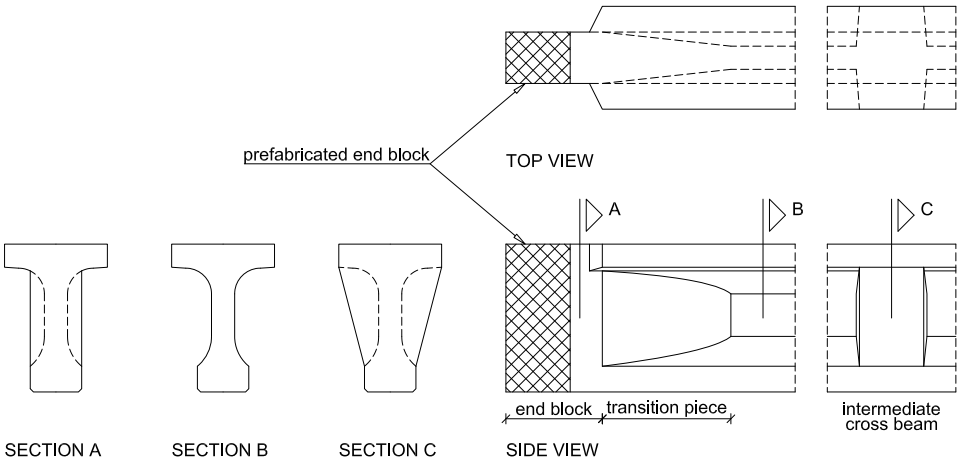

Figure 2.7: Typical design of T-beam

The width of the top flange is usually 1000 mm for T-beams with a span length up to 28 m and increases with increasing span length until a width of 1520 mm for the Van Brienenoord and Hollandse brug, see also Table 2.4. The web thickness is usually 180 or 200 mm. Most T-beams have an end block with a length of 1000 mm. However, no end block or transition piece is used in the bridges Steenenhoek and Koningsbrug. The transition piece usually has a length of 1000 mm. However, for larger span length bridges (> 30 m), longer transition pieces are used with lengths up to 2500 mm. The reinforcement and prestressing layout are described in sections 2.6 and 2.7.

2.4.2. CROSS-BEAMS

THE number of cross-beams per span, the spacing between the cross-beams as well as their thickness is given in Table 2.3. The spacing refers to the centre-to-centre distance between the cross-beams. Most bridges have four cross-beams per span: two end cross-beams and two intermediate cross-beams. In some cases the thickness of the end cross-beam differs from the intermediate cross-beam(s), but in general they have an equal thickness. The reinforcement and prestressing layout are described in sections 2.6 and 2.7.

2.4.3. INTEGRATED DECK SLAB

THE beam spacing, the width of the top flange of the T-beam, the width of the integrated deck slab and its thickness are given in Table 2.4. As can be seen in Table 2.4

Table 2.3: Cross-beams of 24 typical Dutch T-beam bridges (in order of span length)

Name of bridge	Number of cross-beams [-]	Spacing ECB–ICB [mm]	Spacing ICB–ICB [mm]	Thickness ECB / ICB [mm]
Brasserskade	0	-	-	-
Maastrichterlaan	0	-	-	-
Ringvaart noord	2	-	-	400 / -
Steenenhoek	4	6966	7168	450 / 450
Helperzoom	4	7550	7550	450 / 420
Hereweg	4	7550	7550	450 / 420
Paterswoldseweg	4	7550	7550	450 / 420
Vechtbrug	4	8000	8000	400 / 500
Schieplein	2	-	-	500 / -
Kruithuisweg	4	8251	8100	500 / 500
Brug o/d Rotte	2	-	-	500 / -
Brug o/h Amsterdam-Rijnkanaal	4	8710	8680	600 / 400
Hamersbrug	4	8750	8700	400 / 400
Koningsbrug	5	6631	6631	250 / 250
Meeuwerderbaan	2	-	-	500 / -
Thoolsebrug	4	11450	11500	580 / 500
Volkeraksluizen	4	11925	12950	500 / 500
Schinkelbrug	4	13000	13000	600 / 600
Draaibrug Sas van Gent	4	12900	14200	600 / 600
Draaibrug Sluiskil	4	12900	14200	600 / 600
Brug o/d Beneden Merwede	4	14680	14740	500 / 500
Brug o/d Boven Merwede	4	14700	14700	500 / 500
Hollandse brug	4	16525	16500	500 / 500
Van Brienenoord	4	16825	16500	500 / 500

ECB: end cross-beam, ICB: intermediate cross-beam

the thickness of the integrated deck slab does not vary much and is usually 180 or 200 mm. However, as the beam spacing varies significantly so does the width, and therefore its span length in the transverse direction, of the integrated deck slab. The smallest width is 150 mm, whereas the largest width is 2780 mm. The reinforcement and prestressing layout are described in sections 2.6 and 2.7.

2.5. MATERIAL PROPERTIES

IN this section the material properties of the T-beam bridges are described based upon a material investigation of 12 Dutch T-beam bridges (Roosen 2015); these are also indicated in Tables 2.1–2.2.

Table 2.4: Integrated deck slab dimensions of 24 typical Dutch T-beam bridges (in order of span length)

Name of bridge	Beam spacing [mm]	Flange width [mm]	Slab width [mm]	Slab thickness [mm]
Brasserskade	1000	750	250	200
Maastrichterlaan	1150	1000	*150*	250
Ringvaart noord	2240	1000	1240	210
Steenenhoek	1250	1000	250	200
Helperzoom	1610	1000	610	180
Hereweg	1610	1000	610	180
Paterswoldseweg	1610	1000	610	180
Vechtbrug	1225	800	425	180
Schieplein	1600	1000	600	210
Kruithuisweg	1600	1000	600	200
Brug o/d Rotte	1500	1000	500	210
Brug o/h Amsterdam-Rijnkanaal	1770	1000	770	180
Hamersbrug	2450	1100	1350	180
Koningsbrug	1440	1000	440	180
Meeuwerderbaan	1560	1000	560	200
Thoolsebrug	2144	1250	894	200
Volkeraksluizen	2390	1400	990	180
Schinkelbrug	3234	1300	1934	200
Draaibrug Sas van Gent	4080	1300	*2780*	200
Draaibrug Sluiskil	3340	1300	2040	200
Brug o/d Beneden Merwede	3625	1520	2105	200
Brug o/d Boven Merwede	2056	1400	656	180
Hollandse brug	4110	1520	2590	200
Van Brienenoord	3600	1520	2080	200
average	2175	1132	1043	196

2.5.1. CONCRETE

FOR the T-beams the characteristic cylinder concrete compressive strength f_{ck} was found to be between 40–70 N/mm^2 with an average of 53 N/mm^2. For the integrated deck slab the characteristic cylinder concrete compressive strength f_{ck} was found to be between 28–55 N/mm^2 with an average of 47 N/mm^2. Note that for prestressed concrete T-beams, as well as for the integrated deck slab, when constructed before 1976 and not showing any defects, the Dutch guideline for assessing existing bridges, RTD 1006 (Rijkswaterstaat 2013), allows the use of a minimal value of f_{ck} = 35 N/mm^2, without performing a material investigation.

2.5.2. REINFORCEMENT

IN most cases, the steel grade is either QR22 or QR24[1]. In three cases a steel grade of QR40 was found. Sometimes different steel grades are used for the stirrups and the longitudinal reinforcement. Also a lower strength is sometimes used for reinforcement that needed to be welded. Welding is sometimes applied to the stirrups when they are connected by cross-bars. Steel grades QR22 and QR24 are generally smooth bars, whereas steel grade QR40 are ribbed bars. The material properties of the mentioned steel grades are given in Table 2.5.

Table 2.5: Material properties of old reinforcement steel grades (Rijkswaterstaat 2013)

Steel grade	f_{yk} N/mm^2	f_{yd} N/mm^2
QR22	220	191
QR24	240	209
QR40	400	330

2.5.3. PRESTRESSING

THE prestressing steel grade is often not written on the original technical drawings, but rather the cross-section and the used prestressing system (brand name) are indicated. However, from this information the steel grade can normally be deduced. For the longitudinal prestressing tendons used in the T-beams, the grades varies between QP150 and QP190, but in most cases QP170 was used. Some bridges apply two different prestressing steel grades, QP170 for smaller diameter tendons and QP190 for larger diameter tendons.

The steel strength for the transverse prestressing steel was of special interest and was investigated for 20 bridges (Roosen 2015); these are also indicated in Tables 2.1–2.2. Transverse prestressing is applied in all bridges except one: 'aansluiting Schiphol' see also Table 2.1. The steel grade of the transverse prestressing in the cross-beams and in the slab-flange system, varies much more compared to the longitudinal prestressing. In a few cases (5 times), prestressing steel grades of QP90 and QP150 are used. However, in all other cases prestressing steel grades of QP105 or QP170 are used. The material properties of the mentioned steel grades are given in Table 2.6.

Table 2.6: Material properties old prestressing steel grades (Rijkswaterstaat 2013)

Steel grade	f_{pk} N/mm^2	f_{pd} N/mm^2
QP90	883	580
QP105	1030	713
QP150	1470	1115
QP170	1670	1293
QP190	1864	1742

[1] Steel grades formerly used in the Netherlands.

2.6. REINFORCEMENT LAYOUT

In Figure 2.8 some examples are given for the T-beam reinforcement. As shown in Figure 2.8a the shear reinforcement is anchored in the top flange but follows the contour of the bottom flange. In Figure 2.8b the shear reinforcement is anchored in the bottom flange but here it follows the contour of the top flange. Obviously, both shapes do not comply with current detailing rules as the stirrups should be completely straight to avoid spalling of the concrete cover when the stress in the stirrups is high. From the investigation, the bar diameters of the stirrups were found to be either ø8, ø10 or ø12. The stirrup spacing varied between 350 and 710 mm, although the most common distance was found to be 400 mm.

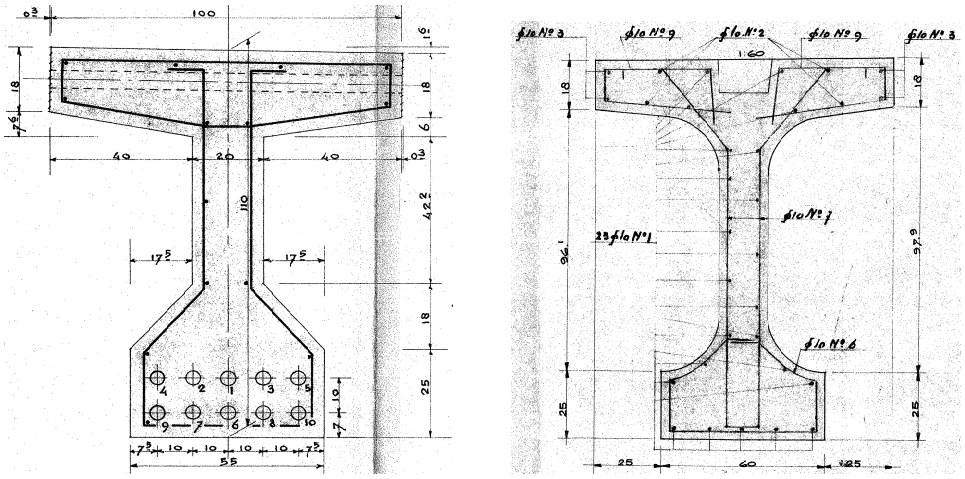

(a) Helperzoom (b) Hamersbrug

Figure 2.8: Examples of T-beam reinforcement (Kamp 2017, Roosen and Sliedrecht 2018)

The (prefabricated) end blocks normally contain more closely spaced stirrups as well as the splitting reinforcement in the anchorage zone of the prestressing tendons. The integrated deck slab is generally very lightly reinforced. Also, other than the transverse prestressing, there is no reinforcement connection between the T-beam and the deck slab. To improve this connection, it was common practice to have an indented concrete interface between the T-beam and the slab. Previous research has shown that this interface is not critical or governing (Amir 2014). An example of the reinforcement in the integrated deck slab is shown in Figure 2.9. Note that for smaller width slabs, intermediate stirrups are often not necessary.

2.7. PRESTRESSING LAYOUT AND SYSTEMS

In this section the common prestressing layout and systems of the longitudinal and transverse prestressing of T-beam bridges are described. This overview is based upon the Dutch bridge stock using the available data of 33 bridges (Kamp 2017, Roosen and Sliedrecht 2018), see also Tables 2.1–2.2.

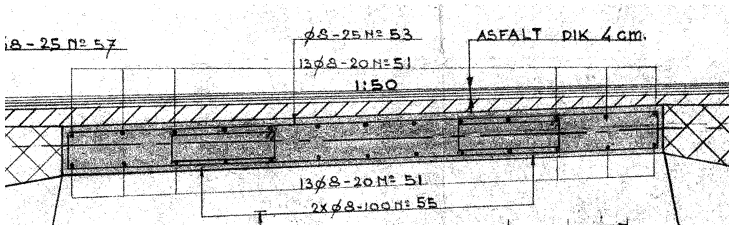

Figure 2.9: Reinforcement integrated deck slab (Draaibrug Sluiskil) (Kamp 2017, Roosen and Sliedrecht 2018)

2.7.1. LONGITUDINAL PRESTRESSING

THE longitudinal prestressing tendon layout can be rather complicated and has many variations between the different T-beam bridges. Most commonly, multiple post-tensioned draped tendons are used that fan out near the anchorages. In addition, most tendons are anchored at the end of the T-beam, at the end block, but typically one or more tendons are anchored in the top flange. The most commonly used system in the Netherlands is that of Freyssinet (Freyssinet 1972). The number of tendons can vary between six and sixteen for larger span length bridges. If two types of tendons are used, the ones with a smaller cross-section are anchored in the top flange. Figure 2.10 shows an example of the longitudinal prestressing tendon layout. In addition to the vertical, the tendons also have a horizontal layout towards the centre of the span.

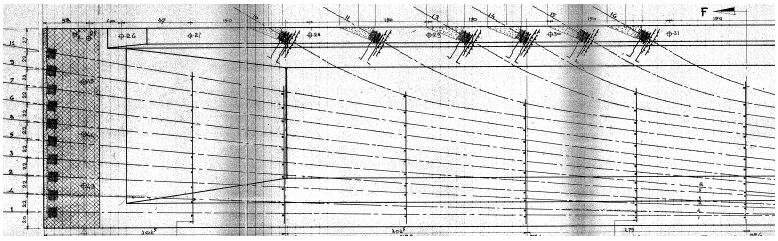

Figure 2.10: T-beam with 16 post-tensioned prestressing tendons (Brug o/d Boven Merwede) (Kamp 2017, Roosen and Sliedrecht 2018)

Instead of draped tendons, in some T-beam bridges straight and/or kinked individual wires or strands are used (aansluiting Schiphol (1965), Brasserskade (1964), Hollandsche IJssel (1955), Steenenhoek (1959), Uitgeest (1957)). Presumably, these are manufactured using a pre-tensioning system. Note that these T-beams do not have a prefabricated end block; an example of this is shown in Figure 2.11. As these bridges are constructed between 1955–1965, there does not appear to be a specific time period in favour of this method.

Not much information is available about the prestressing procedure of the tendons. Presumably, all tendons are prestressed using two-sided prestressing. Sometimes the numbering on the technical drawing reveals the order of prestressing (Rijkswaterstaat 1962). On the technical drawing of the Schellingwouderbrug, it is mentioned that the tendons anchored in the top flange use one-sided prestressing.

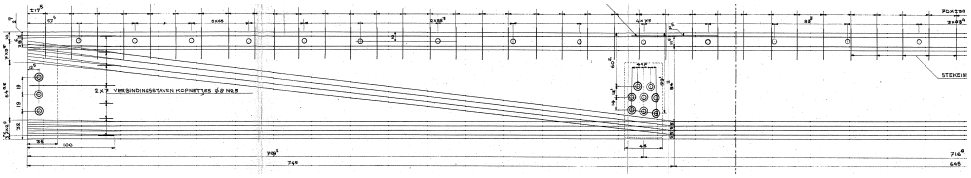

Figure 2.11: T-beam manufactured with a pre-tensioned prestressing system (Steenenhoek) (Kamp 2017, Roosen and Sliedrecht 2018)

2.7.2. TRANSVERSE PRESTRESSING

TRANSVERSE prestressing is commonly applied to the deck slab and the cross-beams using post-tensioned tendons. Generally, the tendons are more or less evenly spaced to realise a constant transverse compressive stress (see also Figure 2.11). However, it is equally common to have more concentrated transverse prestressing at the location of the cross-beams. The prestressing tendons are either of the same type as the longitudinal prestressing used in the T-beams, or can have a smaller cross-section. The intermediate cross-beams often contain more prestressing tendons as compared to the end cross-beams (see also Figure 2.11). Transverse prestressing was of special interest and was investigated for 20 bridges; these are also indicated in Tables 2.1–2.2. From this investigation it was concluded that the average transverse compressive stress was between 0.8–3.4 N/mm^2 with an average of 2.3 N/mm^2 (Roosen 2015).

2.8. SHEAR-RELATED DEFICIENCIES

BEFORE 1974 the Dutch code for reinforced concrete was called the 'GBV', of which the last version was the 'GBV 1962' (NNI 1962). After 1974 a new code was adopted, called the 'VB 1974' (NNI 1977), which included revised, i.e. stricter, rules for shear. Generally speaking, the T-beam bridges constructed using the newer code will be less shear-critical than those that were constructed using the older code. Consequently, the amount of shear reinforcement in the T-beams often does not comply with today's codes. Until 1974, the following rules applied for shear reinforcement using the Dutch code 'GBV 1962' (NNI 1962):

- The stresses are calculated in the serviceability limit state (SLS).
- An uncracked cross-section is assumed with a parabolic shear stress distribution.
- The maximum shear stress is calculated using: $\rho = \tau_{\max} = 1.5\frac{V}{bh}$.
- No shear reinforcement is required if:
  concrete class K160 (f_{ck} = 9 N/mm^2): $\rho \leq 0.6$ N/mm^2
  concrete class K225 (f_{ck} = 13 N/mm^2): $\rho \leq 0.7$ N/mm^2
  concrete class K300 (f_{ck} = 19 N/mm^2): $\rho \leq 0.8$ N/mm^2

After 1974 the following rules applied for shear reinforcement using the Dutch code 'VB 1974' (NNI 1977):

- The stresses are calculated in the ultimate limit state (ULS), using a global resistance factor of 1.7.

- A cracked cross-section is assumed with a constant shear stress distribution.
- The shear stress is calculated using: $\tau_{S;d} = \frac{V_{S;d}}{bd}$.
- No shear reinforcement required if: $\tau_{S;d} \leq 0.5 f_b + 0.15 \frac{N}{bd}$.

Low levels of shear reinforcement make the T-beams vulnerable for shear failure. In addition, in terms of detailing of the stirrups the following observations can be made:

- The stirrups partially follow the contour of the T-beam, see also Figure 2.8. Current detailing rules state that they should be straight to prevent outward forces at the kinks under loading, which may cause spalling, rupture or failure of the concrete cover.
- In addition to the previous point, at the top side, the stirrups are often bent outward. In this way, the compression zone is not sufficiently confined.
- Often the stirrups are welded, see also Section 2.5.2. For high strength steel, this can reduce the tensile strength.
- Longitudinal reinforcement bars are not always present in the corners of the stirrups.

Considering that the steel grade used for the stirrups in older bridges is generally also relatively low it is a conservative approach to determine the shear capacity without the contribution of the stirrups that are not code-compliant (Kamp 2017, Roosen and Sliedrecht 2018).

3

STATE-OF-THE-ART: ASSESSMENT, THEORY AND TESTING

In this chapter the current methods for assessment of existing concrete beam bridges are treated. In addition, the theory and methods of several mechanisms, related to structural or 'system behaviour', such as compressive membrane action (CMA) and compressive arch action (CAA), that can potentially increase the load-carrying capacity of prestressed T-beam bridges are treated. Finally, full-scale collapse tests found in literature, related to 'system behaviour' of prestressed concrete beam bridges are summarised.

3.1. INTRODUCTION

UNDERSTANDING of the structural behaviour is important for the design of new bridges as well as for the assessment of existing concrete bridges. For existing bridges, the 'real' structural behaviour is important to be able to fully exploit all possible relevant load bearing mechanisms for the evaluation. In many cases the current assessment is based on the checking of the sectional forces to assess the individual parts of a structure. In addition, the design codes are also mostly based on the testing of individual members, such as beams and slabs, and generally do not consider structural behaviour. This is an obvious choice, since testing of a complete structure is both expensive and the results can not always be generalised to all structures. However, some mechanisms, such as compressive membrane action (CMA) and compressive arch action (CAA), are dependent on the structural behaviour and can potentially significantly increase the load bearing capacity in concrete beam bridges. These mechanisms depend on a (horizontal) restraint that can be provided by the connected members. In this dissertation these phenomena are referred to as 'system behaviour'. In Section 3.2 first the current assessment approaches for existing bridges are treated. Section 3.3 will then give some examples related to 'system behaviour' found in the literature. Next, in Section 3.4 the theories, methods and applications for compressive membrane action are treated. In addition, the use of full-scale testing is treated in Section 3.5. Finally, the main conclusions of the chapter are summarised in Section 3.6.

3.2. ASSESSMENT APPROACHES EXISTING BRIDGES

IN the Netherlands, the starting point for a structural assessment of an existing concrete bridge is based on the level of safety that applies to new structures. In addition, standard code formulations and modelling approaches are adopted. If deficits remain, several options for structural assessment refinements are possible. For existing concrete road bridges, the different options, according to RBK (Rijkswaterstaat 2013) and NEN 8700 (NNI 2011b), are summarised in Figure 3.1. The design load can be reduced by reducing the level of safety combined with a reduced remaining lifespan of 30 years[1]. In addition, the use of fixed (actual) traffic lane positions, as opposed to free positions, can be adopted to reduce the sectional forces in critical sections. If deficits still remain, an on-site material investigation can be used to, potentially, increase the concrete (compressive) strength used in the assessment, which is especially beneficial for shear. In addition, for their existing bridges, the Dutch Ministry of Infrastructure and Water Management (Rijkswaterstaat) allows for code modifications of the Eurocode equations related to flexural shear. For prestressed beams with sufficient stirrups Equation 3.1 is allowed[2] using a prescribed fixed strut angle of $\theta = 30°$.

$$V_{Rd} = V_{Rd,s} + V_{Rd,c} \tag{3.1}$$

Equation 3.1 allows for the concrete contribution ($V_{Rd,c}$) to be added to the resistance of the stirups ($V_{Rd,s}$), using a fixed angle θ. As is described in Chapter 2 Section 2.8, for the

[1] This corresponds to a minimum reliability index of $\beta_{rel} = 3.3$.

[2] Note that the full equation includes additional terms for variable height box girders which are not relevant here.

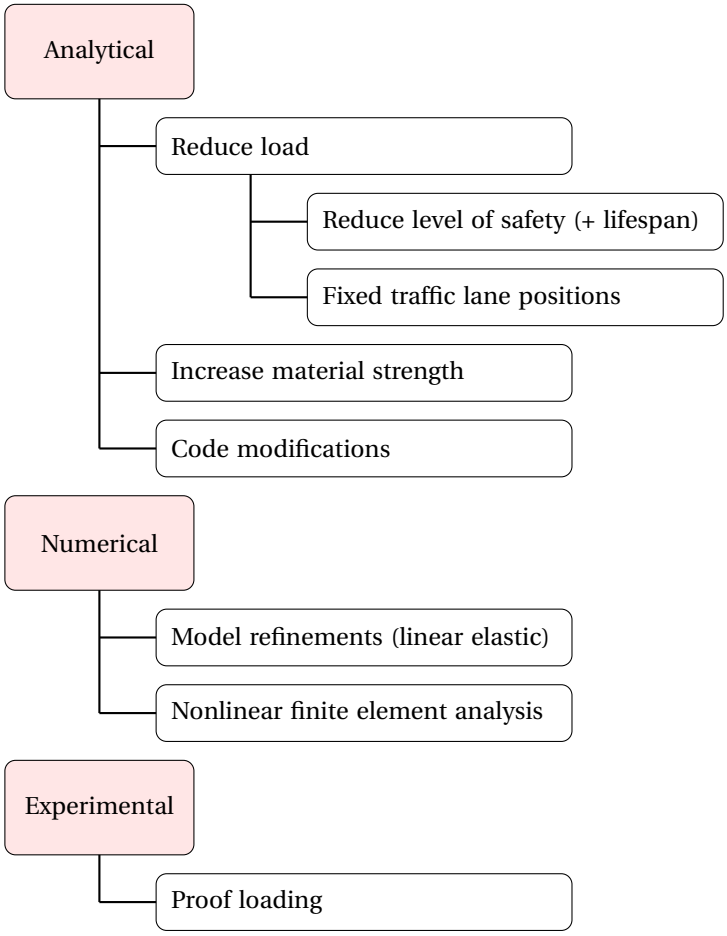

Figure 3.1: Methods of structural assessment refinements for existing concrete bridges (according to RBK (Rijkswaterstaat 2013) and NEN 8700 (NNI 2011b))

T-beam bridges in the present research, generally, the amount of stirrups is below the minimum requirement ($\rho_w < \rho_{w,min}$) or the stirrups are not correctly detailed. Thus, in these cases Equation 3.1 does not apply and only $V_{Rd,c}$ is used for the capacity. In addition to the analytical options (see Figure 3.1), efforts can be made to improve, i.e. refine, the initially adopted linear elastic finite element model. For example, the use of more sophisticated elements, such as shells or solids, can be considered. Another example is to model the exact positions, dimensions and the linear stiffness of the supports.

When all of the analytical and linear elastic modelling options have been exhausted, the use of a nonlinear finite element analysis (NLFEA) can be considered. For prestressed concrete beam bridges, this is generally a two step procedure. The first step is to determine the most unfavourable load positions and corresponding maximum acting shear using a linear elastic model of the full bridge deck as before. The second step is to anal-

yse the shear resistance using a nonlinear model of, in most cases, an individual beam member. The use of a nonlinear model of the full bridge deck (Chapter 7) is not standard practice. These nonlinear analyses generally also include a sensitivity study (load positions (a/d), prestressing level etc.).

If uncertainties still remain (for instance due to insufficient or missing records), structural damages are present (corrosion, cracking) or the analytical and/or numerical investigations still yield an insufficient load capacity, a proof loading of the bridge deck can be considered (Alampalli et al. 2021).

Although the author did not perform an extensive literature review on this particular topic, the assessment methods used in other countries for existing concrete bridges show similarities and generally fall within one of the categories as shown in Figure 3.1. For example in Germany, with regard to flexural shear it is permissible, under certain conditions, to extend the limit values for θ (Bundesministerium für Verkehr 2011). However, some countries additionally make use of what can be described as 'advanced analytical methods'. Some examples of the methods used in Germany are: 'The simplified arch action model' (SAAM), 'The arch action model' (AAM) and the 'Extended technical bending theory' (ETB) (Kolodziejczyk and Maurer 2017). For the present research, the (simplified) arch action model used in Germany is of particular interest and will be shortly treated in Section 3.4.3.

3.3. SYSTEM BEHAVIOUR OF BEAM BRIDGES

IN the context of this research, system behaviour of beam bridges refers to the behaviour in the ultimate limit state (ULS) of a bridge deck. Specifically, the aim is to investigate additional load-carrying mechanisms, such as compressive membrane action (CMA) and compressive arch action (CAA), that only occur after initial cracking. These mechanisms rely on a restraint provided by the connected members (adjacent beams, cross-beams, transverse prestressing). In most concrete research the emphasis is more on the separate or individual components such as beams and slabs. However, the author has found a few relevant examples of research related to system behaviour of beam bridges that are treated in this section.

One example is the research done by Sato et al. (2019) in which a single experiment is conducted on a narrow simply supported T-beam bridge, consisting of four prestressed T-beams and cross-beams. The edge beam is loaded at midspan to failure and the research includes a 3D nonlinear finite element analysis of the full bridge deck. Interestingly, during the experiment the 20 mm gap at the joint near the end support, between the loaded span and the adjacent span, is closed, due to the deflection of the loaded span, causing an unexpected contact between the T-beams of the consecutive spans. From the analysis it becomes clear that this restraint is causing a significantly higher failure load demonstrating that additional compressive normal forces can have a positive effect.

Another interesting example is the research done by Floyd et al. (2016), Murray and Floyd (2018) and Murray et al. (2019) in which half scaled I-beams are tested individually and compared to a bridge deck test consisting of four similar prestressed I-beams connected by a cast in-situ deck slab and cross-beams. The results of this research indicate that the cross-beams (diaphragms) play an important role in the load distribution and

the two-way bending behaviour. In addition, it was found that the cross-beams can arrest (i.e. reduce or prevent) cracking of the I-beams and that the deck and cross-beams can also provide additional redundancy at post-beam failure by transferring the load to the adjacent beams. Finally, from this research there are indications that slip of the prestressing tendons at the anchorages is postponed in case of the bridge deck test as compared to the individual beam tests. This could possibly indicate that shear anchorage failure is postponed or prevented by system behaviour.

In the aforementioned examples the bridge deck behaviour will naturally be greatly influenced by the bridge deck layout (beam spacing, position and number of cross-beams, amount of (transverse) prestressing). In addition, the type of loading, i.e. concentrated load(s) or distributed load(s), is of importance. For the current research the focus is on the load capacity of the main T-beams by applying a concentrated (live) load directly on the T-beam[3].

3.4. THEORY, METHODS AND APPLICATIONS OF COMPRESSIVE MEMBRANE ACTION

IN this section the theory, methods and applications of compressive membrane action (CMA) will be treated. The general mechanism of compressive membrane action will be briefly explained in Section 3.4.1. Next, in Sections 3.4.2–3.4.3 the established methods and applications of compressive membrane action, respectively for slabs and beams, are treated. Finally, in Section 3.4.4 the theoretical application of compressive membrane action in a T-beam bridge, for the current research, is treated.

3.4.1. INTRODUCTION TO COMPRESSIVE MEMBRANE ACTION

COMPRESSIVE membrane action occurs in structural members where the edges are restrained against lateral displacement, see Figure 3.2. With the lateral movement restrained, an internal arching mechanism is induced as the slab deflects, resulting in compressive membrane forces. These forces increase the flexural resistance as typical moment-axial force interaction diagrams show. In addition, the punching shear resistance is also increased. CMA increases the load capacity of a slab with failure loads much higher than those predicted with standard yield line theory, see Figure 3.3. The arching phenomenon occurs in concrete members due to the large difference between the tensile and compressive strengths. The weak strength in tension causes cracking due to the application of the load. This shifts the neutral axis towards the compressive face.

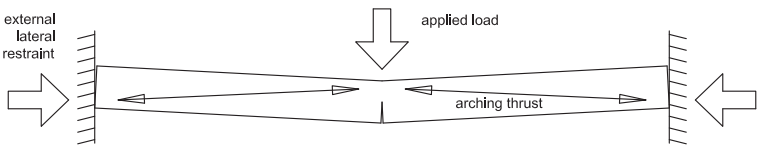

Figure 3.2: Compressive membrane action in laterally restrained reinforced concrete slab

[3]Note that research on system behaviour of beam bridges related to arching action while loading a main beam could not be found by the author.

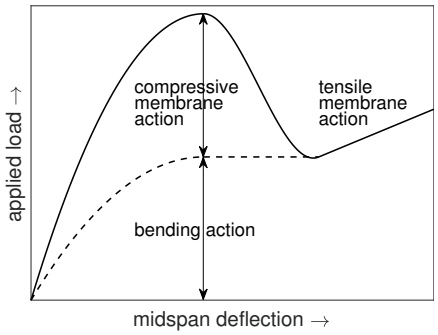

Figure 3.3: Typical load versus deflection for restrained reinforced concrete slab

The main parameters influencing the extent in which compressive membrane action can occur in structural members are:

- degree of edge restraint ($\eta \leq 1.0$);
- member slenderness ($\lambda = L/h$);
- concrete compressive strength (f_c).

Note that the value for η can vary between 0 (zero restraint, i.e. simply supported) and 1 (fully restrained) (Batchelor 1987).

3.4.2. COMPRESSIVE MEMBRANE ACTION IN SLABS

IN concrete slabs, compressive membrane action enhances both the flexural resistance, see Figure 3.3, as well as the punching shear resistance. However, when considering a concentrated load, since the flexural resistance is increased the most, generally a punching shear failure will be the governing failure mode. For both reinforced and unreinforced concrete slabs, CMA has been extensively researched most notably in Canada, New Zealand and the UK, for instance by Batchelor (1987) (Canada) and Taylor et al. (2002) (UK). In addition, more recently, the use of CMA in prestressed concrete deck slabs has also been researched by Amir (2014). Most of this research is aimed specifically at concrete bridge deck slabs.

Provided that sufficient restraint is present, from this research it can be concluded that CMA enhances the load-bearing capacity also in cases with very low or no reinforcements. In addition, the position of the reinforcements in the cross-section, i.e. top and bottom or centrically, can effect the load-bearing capacity but to a lesser degree than the main parameters listed in the previous section.

In the case of a prestressed concrete slab, a linear relation between the (transverse) prestressing level and the punching failure load was found (Amir 2014). In addition, the presence of prestressing increases the cracking loads, thereby also improving the serviceability limit state (SLS).

To calculate the effect of compressive membrane action several analytical methods have been developed over the years, some of which are also listed in Batchelor (1987) and Taylor et al. (2002). Among all proposed models, the model by Park and Gamble

(2000) is one of the most widely accepted.

For reinforced concrete, the aforementioned research led to several design codes in which CMA is taken into account. The Canadian (CSA 2006) and New Zealand (TNZ 2003) code both adopt a similar approach and take into account an edge restraint. The UK (UK HA 2002) code uses a simplified method, and assumes a fully restrained slab in which the reinforcement is neglected. In addition, in the Netherlands, CMA can also be taken into account in the design of unreinforced underwater concrete slabs (SBR CUR 2014). The latter method will be extended and modified so it can be applied to pre-stressed concrete T-beams in the next chapter. For a general description of this method, the reader is referred to Chapter 4 Section 4.1.

3.4.3. COMPRESSIVE MEMBRANE ACTION IN BEAMS

ALTHOUGH the mechanism of compressive membrane action is identical for beams and slabs, in the literature, compressive membrane action in beams is most commonly referred to as compressive arch action (CAA) or simply as arch action (AA). In the present research, to distinguish between arch action in beams and slabs, the designation CMA is adopted for slabs and the designation CAA is adopted for beams.

Over the last decade, CAA is of particular interest in the analysis of beam-column assemblies, or frame structures, in preventing a progressive collapse after a column removal. Based upon experimental findings, numerical models have been validated and several analytical models have been proposed.

In one study, the model by Park and Gamble (2000) is improved upon for reinforced concrete beams (Lu et al. 2018). This research is validated by 50 reinforced concrete progressive collapse tests. Of particular interest in this study, is the influence of cross-section, specifically a rectangular versus a T-shaped cross-section, i.e. a beam or a beam-slab configuration respectively. From this study it is concluded that the model by Park and Gamble (2000) is not sufficiently accurate in case of a beam-slab configuration. This is due to the fact that this model assumes full plasticity at the position of the maximum bending moments. However, in case of a beam-slab configuration, contrary to a rectangular cross-section, this assumption is no longer valid as some of the reinforcements, at the position of the maximum bending moments, will remain linear elastic. After an extensive parametric study and using appropriate modifications to the model by Park and Gamble (2000) and assuming fixed boundaries, the authors (Lu et al. 2018) are able to predict the maximum CAA capacity, including the peak displacement (δ), with sufficient accuracy.

Another arch action related phenomenon in beams is the so-called tied-arch action. This type of arch action does not require an external restraint, as shown in Figure 3.2, but is instead caused by an internal restraint.

For reinforced concrete beam members, an example of this type of arch action is described by Jeong and Kim (2014). In this research, for a simply supported beam, an analytical behavioural model is derived in which the shear resisted by arch action is quantified. The arch is formed by the fact that the value of the resultant normal force in the compression zone, and its vertical position in the cross-section, decreases towards the end support, due to the decreasing bending moment, creating an arch-shaped line of

thrust, between the resultant points, towards the end support, see Figure 3.4. The researchers found that, for the investigated beams, 29-46% of the shear is resisted by arch action (the remaining part is resisted by aggregate interlocking and the stirrups). It was also found that the amount of shear resisted by this type of arch action highly depends on the load position (a/d) and, albeit to a lesser degree, on the shape of the cross-section. A higher contribution of arch action is observed with load positions closer to the end support and for T-shaped beams with a more slender web.

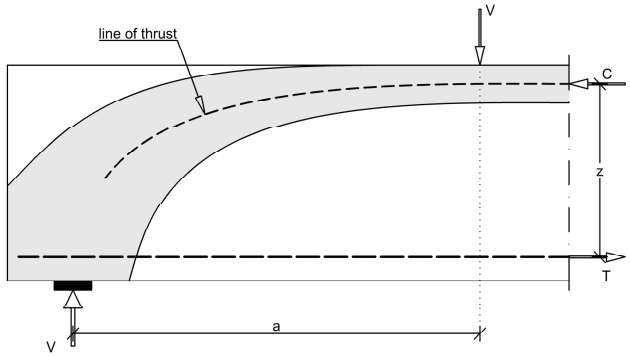

Figure 3.4: Tied-arch action in areas close to end support

Likewise, for prestressed concrete, similar models are adopted by Kiziltan (2012) and Gleich (2020) called the 'The simplified arch action model' (SAAM) and 'The arch action model' (AAM) (Gleich and Maurer 2017, 2018). The main difference between the two analytical models is the inclusion of an additional compressive normal force, due to shear, in the 'The arch action model', whereas in 'The simplified arch action model' this force is neglected. These models are especially beneficial for taken into account the local arching effect in the areas close to the (inner) supports. When utilizing these models for the assessment of several existing prestressed beam bridges in Germany, a significant increase in shear resistance was found when taking the arching effect into account (Kolodziejczyk and Maurer 2017). This conclusion is also confirmed by other researchers (Huber et al. 2018).

3.4.4. COMPRESSIVE MEMBRANE ACTION IN PRESTRESSED T-BEAM BRIDGES

THE established methods and applications for CMA and CAA, as treated in the previous sections, cannot be readily applied to the system behaviour of prestressed concrete T-beam bridges in case of a concentrated load at the centre of a T-beam.

Figure 3.5 displays the situation with a concentrated load placed at the centre of a T-beam. In transverse direction, a possible arching effect (CMA) can take place in the top flange of the loaded beam, and the integrated deck slab on either side, spanning the two adjacent T-beams as highlighted in Figure 3.5. This situation is very different from previous applications with the load situated on the slab. Firstly, CMA relies on cracking of the concrete slab at the position of the load as well as at either end of the arch. In this case, cracking at the load position is largely prevented by the prestressed T-beam. Secondly,

a relative deflection is needed between the loading point and the ends of the arch, to achieve the maximum arching effect. In this case, the deformation at the loading point is prevented by the relatively high stiffness of the prestressed T-beam. In addition, it can also be limited for loading positions in closer proximity to a cross-beam. Finally, as the two-way bending behaviour of the slab differs, the width of the activated part of the slab will be influenced by the presence of the prestressed T-beam. On the other hand, very high horizontal restraint is likely present created by the surrounding structural elements, such as the adjacent parts of the slab, the transverse prestressing and the cross-beams.

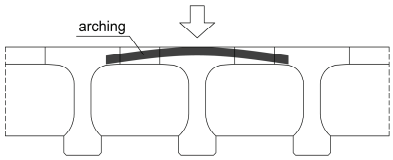

Figure 3.5: Possible slab arching effect (CMA) in T-beam bridge while loading T-beam

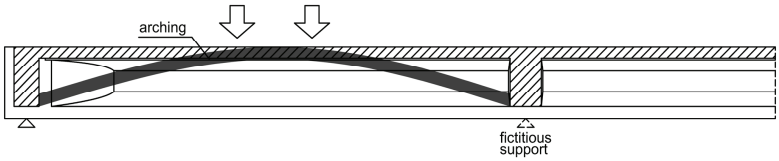

Figure 3.6: Possible beam arching effect (CAA) in T-beam bridge while loading T-beam

Figure 3.6 displays the situation with a concentrated load, or loads, placed at the centre of a T-beam between the cross-beams. In longitudinal direction, a possible arching effect (CAA) can take place in the loaded prestressed T-beam, spanning between the end cross-beam and the intermediate cross-beam, as highlighted in Figure 3.6. At the intermediate cross-beam, a fictitious vertical support is possibly provided by the stiffness of the intermediate cross-beam. A similar situation is possible in the longitudinal section between two intermediate cross-beams. This situation is very different from previous research related to CAA dealing mostly with individual, isolated beams. In this case, cracking at either end of the arch is possibly prevented by the lack of hogging bending moments. In addition, because of the connections with the integrated deck slab, along its longitudinal axis, the sectional forces will dissipate away from the loading point, including the possible axial membrane force, thereby preventing or limiting the formation of a complete arch.

3.5. FULL-SCALE TESTING OF EXISTING BRIDGES

FULL scale testing for the assessment of existing bridges can be classified in three distinct categories in order of increased loading:

- diagnostic load test;
- proof loading;

- collapse test.

With a diagnostic load test, the aim is to gain insight into the bridge behaviour by applying a known (non-destructive) load and measuring the bridge responses. This type of test can provide insights into the load distribution and can for instance be used to calibrate a finite element model of the bridge. With a proof loading, a code-prescribed live load is applied to directly demonstrate the bridge load-carrying capacity (see also Section 3.2). Depending on the load level, the amount of cracking and the crack widths, a proof loading might already reveal hidden capacities such as CMA (see also Section 3.4.1). Note that with a diagnostic load test or a proof load test the bridge deck is not irreversibly damaged as these tests are applied to in-service bridges.

In literature, many examples can be found of full-scale testing of the first two types, for instance by Lantsoght et al. (2017a,b) and Alampalli et al. (2021). However, in order to analyse the full load-carrying capacity and failure mechanism, a full-scale collapse test is required. In this section, examples of full-scale collapse tests of prestressed concrete (PC) beam bridges, are summarised. In light of the present research, only tests which resulted in a beam failure are treated.

An overview of tests on PC beam bridges, which resulted in a beam failure, is listed in Table 3.1. The listed bridge tests have been carried out by Anonymous (1951, 1952), South Bank bridge, Burdette and Goodpasture (1973), Boiling Fork Creek bridge, McClure and West (1984), Pennsylvania State University bridge, Plos et al. (1991), Stora Höga bridge 2, Oh et al. (2002), Seoul-Pusan highway bridge, Jiaquan et al. (2006), Xin Xing Tang bridge, Bagge (2017), Kiruna bridge and by Sato et al. (2019), Chikubetsu bridge.

The cited tests (except for the Chikubetsu bridge) are based on a literature review by Bagge et al. (2018) in which a total of 30 concrete bridges tested to failure are identified. A summary of these tests, can be found in Bagge et al. (2018). Of the 30 bridges, reinforced concrete (RC) slab or beam bridges are most commonly tested, with only 3 PC slab and 7 PC beam bridges.

All bridges listed in Table 3.1 are road bridges, except for the South Bank (pedestrian bridge). For different reasons, some of the listed bridges are less relevant for the present research. For instance, continuous span bridges consisting of a single beam and tested in flexure are less relevant, which rules out the South Bank (solid beam with RC cantilever slabs) and the Xin Xing Tang bridge (one-cell box beam with cantilever flanges and inclined webs). In addition, the Pennsylvania State University and the Stora Höga bridge 2 both have an unusual configuration and are therefore excluded, with the former a curved segmental box beam bridge and the latter a portal frame bridge, both consisting of just two beams.

Except for the Kiruna bridge, three of the remaining four bridges are all simply supported and constructed with prefabricated beams, i.e. the Boiling Fork Creek, the Seoul-Pusan highway and the Chikubetsu bridge[4]. All three bridges are relatively narrow and constructed with either four I-beams (Boiling Fork Creek, the Seoul-Pusan highway), or with four T-beams (Chikubetsu). The I-beam bridges have a deck slab on top, whereas the T-beam bridge has an integrated deck slab. In addition, the Seoul-Pusan bridge has six equally spaced RC cross-beams between the webs of the I-beams (not connected to

[4] Chikubetsu bridge also treated in Section 3.3.

Table 3.1: Prestressed concrete beam bridges tested to failure (in chronological order of test year), extract of list by Bagge et al. (2018) (except for Chikubetsu)

Bridge	Country[a]	Construction year	Test year	Length [m]	No. spans	Failure mode[c,d]	Loading system[e]
South Bank	GBR	1948	1952	86.56	4	F^1	W
Boiling Fork Creek	USA	1963	1970	80.47	4	P^1+S^2	HJ
Pennsylvania State Univ.	USA	1977	1981	36.88	1	F^1	HJ
Stora Höga 2	SWE	1980	1989	31.00[b]	1	S^1	HJ
Seoul-Pusan	KOR	1971	2000	360.00	12	F^1	HJ
Xin Xing Tang	CHN	1995	2005	114.00	3	F^2	W
Kiruna	SWE	1959	2014	121.50	5	S^2+P-S^2	HJ
Chikubetsu	JPN	1960	2019	180.00	5	F^2	HJ

[a] China (CHN), Great Britain (GBR), Japan (JPN), South Korea (KOR), Sweden (SWE) or United States of America (USA)
[b] frame structure, [c] flexural failure (F), punching failure (P) or shear failure (S)
[d] failure tested span specified by superscript, [e] hydraulic jacks (HJ) or weights (W)

the deck slab), whereas the Chikubetsu bridge has a number of PC cross-beams. Note that the Chikubetsu is the only bridge within the scope of the present research (see Section 1.2). Finally, the Kiruna bridge is a continuous five-span bridge and consists of three rectangular PC beams, a RC deck slab and four equally spaced RC cross-beams in each span.

Of the remaining four bridges, only two tests resulted in a PC beam shear failure, i.e. the Boiling Fork Creek and the Kiruna bridge, see Table 3.1.

In case of the Boiling Fork Creek bridge the load is applied at 8 points, located between the beams, representing two trucks. On the first span, this resulted in a local punching failure of the deck slab. On the second span, additional efforts are made to avoid a punching failure. In the second test, at higher loads, considerable curvature of the bridge occurred with the two interior beams deflecting much more than the two exterior beams. Due to this effect, the composite action between the interior beams and the deck slab was lost and the stirrups at the interface sheared. The loss of composite action resulted in a redistribution of the forces to the exterior beams, and ultimately resulted in a shear failure of the interior beams. Note that in this bridge no cross-beams are present.

In case of the Kiruna bridge the load is applied to 3 points, transversely aligned, in the middle of the shortest interior span, at the centre of the beams. The two tested beams are strengthened utilising two different systems, i.e. CFRP rods (in the concrete cover) and prestressed CFRP laminates (applied to the concrete surface). First the load is applied equally to the 3 points across all beams followed by an asymmetric loading to obtain failures in both an exterior and an interior beam. Both tests resulted in a shear failure of the loaded beam in addition to a punching failure of the deck slab. Although the loading points are situated in close proximity and in-between two cross-beams, in the analysis there is hardly any mentioning of the influence of the cross-beams. In addition, from the original drawings of the bridge it is not clear if the cross-beams are always present over the full height of the PC beams and therefore connected to the deck slab (Bagge 2017).

Note that none of the tests listed in Table 3.1 include a test (and resistance evaluation) of an individual beam as well as the bridge deck.

3.6. SUMMARY AND CONCLUSION

THE results of the current methods for assessment of existing concrete beam bridges as well as the theory and methods of the mechanisms related to 'system behaviour' together with the main conclusions of this chapter are summarised in this section.

Assessment approaches existing bridges:

- The three main categories for the assessment of existing bridges are: analytical, numerical and experimental. In addition, some countries make use of so called 'advanced analytical methods'.
- In the Netherlands, the extensions for flexural shear, according to RBK (Rijkswaterstaat 2013), can generally not be applied to prestressed T-beam bridges due to their lack of shear reinforcement ($\rho_w < \rho_{w,min}$).
- Generally, when NLFEA is used for assessment, the analysis is limited to an individual beam. Such an analysis will therefore not reveal any 'system behaviour'.

System behaviour of beam bridges:

- Most concrete research found in the literature is related to individual members, such as beams and slabs. Very few examples of research are found related to system behaviour.
- No research related to arching action (CAA) in beams, due to the effects of system behaviour, is found.

Theory, methods and applications of compressive membrane action:

- CMA occurs in concrete slabs where the edges are restrained against lateral displacement.
- The main parameters are: level of restraint, the slab slenderness and the concrete compressive strength.
- In the case of a concentrated load, the failure mode for slabs is punching.
- For prestressed slabs, a linear relation, between the level of prestressing and the punching failure load, is found.
- Several analytical methods for CMA have been developed over the years of which the model by Park and Gamble is one of the most widely accepted.
- CMA is used in several design codes, mainly in Canada, New Zealand and the UK. In the Netherlands, a CMA model is adopted in the design code for underwater concrete slabs.

Compressive membrane action in beams:

- The mechanism of compressive membrane action is identical for beams and slabs. For beams this is most commonly referred to as compressive arch action (CAA).

- CAA has been researched for the analysis of beam-column assemblies in preventing a progressive collapse after a column removal. With regard to a T-shaped cross-section, the model by Park and Gamble needed to be modified as this model assumes full plasticity at the position of the maximum bending moments. However, in this case some of the reinforcements remain linear elastic.
- Another arch action-related phenomenon is tied-arch arch action caused by an internal restraint. For reinforced concrete beam members, a significant amount of shear resistance can be contributed to this type of arch action. Higher contributions are found for loads closer to an end support and for T-shaped cross-sections.
- Two types of arch action models are used in Germany as 'advanced analytical methods' for the assessment of prestressed concrete beams in existing bridges. These models are especially beneficial in the areas close to the (inner) supports.

Compressive membrane action in prestressed T-beam bridges:

- The established methods and applications for CMA and CAA cannot be readily applied for the case of a concentrated load at the centre of a T-beam as part of a bridge deck.
- A possible arching effect (CMA) can occur in the transverse direction in the deck slab, with the load at the centre of the T-beam, despite the fact that the T-beam limits the cracking and the deformation of the deck slab at midspan.
- A possible arching effect (CAA) can occur in the longitudinal direction in the prestressed T-beam, with the load at the centre of the T-beam and the T-beam locked between the cross-beams, despite the fact that the sectional forces dissipate away from the loading point including the membrane force.

Full-scale testing of existing bridges:

- Full-scale testing of prestressed concrete beam bridges are extremely rare with only eight examples found in literature tested between 1952 and 2019.
- Only four examples have a configuration relevant for the current research, all of them narrow bridges with 3 or 4 prestressed concrete beams, of which only two tests resulted in a beam shear failure.

From the literature review it can be concluded that the arching effect in thin slabs is the same phenomenon as the arching effect in (prestressed) beams, with the former designated as CMA and the latter as CAA. Both arching effects are investigated as part of the current research (Chapter 1 Section 1.3). In order to investigate CMA for the deck slab and CAA for the T-beam, an established analytical model, normally applied to unreinforced underwater concrete slabs, is adopted. For the analysis of CAA the current model is extended and modified in the next Chapter.

4

ANALYTICAL MODEL FOR ARCH ACTION

In this chapter the basic analytical arch action model for unreinforced underwater concrete slabs (SBR CUR 2014) is extended and modified so it can be applied to connected prestressed concrete T-beams. The adopted model will be used to analyse the system behaviour of the Vecht bridge in Chapter 8.

4.1. DESCRIPTION OF THE BASIC ARCH ACTION MODEL

THE basic beam arch action model, utilized for unreinforced underwater concrete slabs with tension piles in the ultimate limit state, is shown in Figure 4.1 (SBR CUR 2014). The load is applied as a distributed (water) pressure against the bottom side of the slab in the upward direction. At both edges, the concrete slab is horizontally and vertically restrained by the retaining walls. In vertical direction all supports are assumed to be rigid. In addition, at the location of the retaining walls, a linear horizontal spring stiffness is assumed. At the position(s) of the maximum sagging and hogging bending moment, i.e. in the span and at the (pile) support(s), plastic hinges are assumed as a result of cracking. Between the plastic hinges, the concrete compressive struts are assumed to be infinitely stiff and the distance A is assumed to remain constant, see Figure 4.1. In the initial undeformed shape (top figure) the normal force F_0 results from the soil and water pressure against the retaining walls after casting and dewatering of the building pit. With increased loading, due to the additional vertical displacement a_v, the model stretches horizontally by Δu (bottom figure) causing an additional horizontal normal force ΔF. Due to the additional normal force ΔF the compression zones increase in height and at the same time the internal lever arm z is reduced. Conservatively, linear compression zones are assumed in this model. In addition, the concrete compressive strength $f_{cd,pl}$ includes an additional reduction factor of 0.8 to take into account the reduced ductility properties of unreinforced concrete.

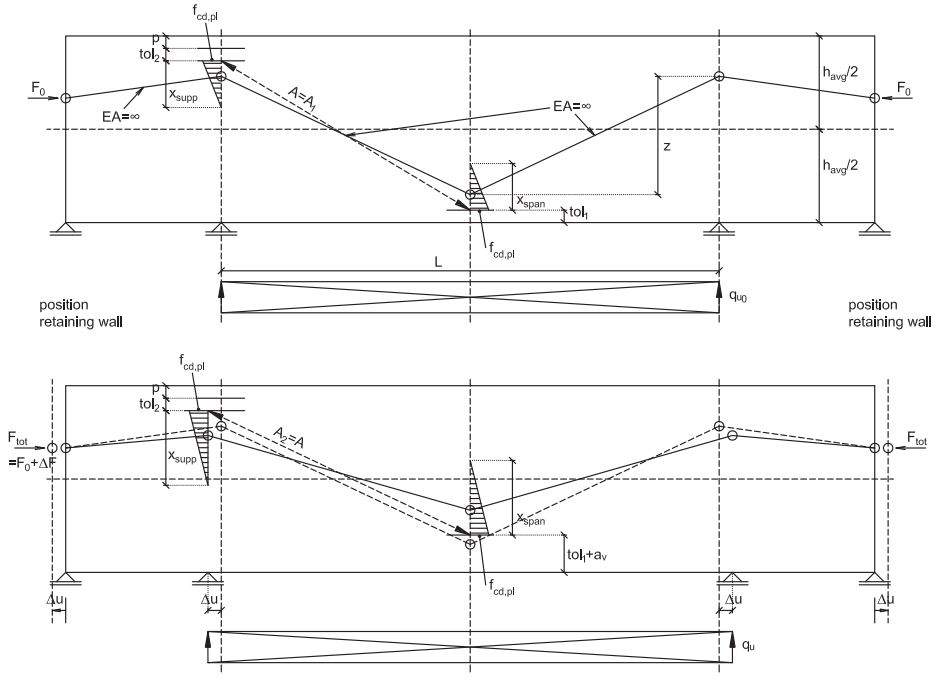

Figure 4.1: Basic arch action model for unreinforced underwater concrete slab

The parameters used in the basic arch action model are (see Figure 4.1):

A length of concrete compressive strut

A_1 length of concrete compressive strut ($a_v = 0$)

A_2 length of concrete compressive strut ($a_v > 0$)

EA axial stiffness concrete slab

ΔF additional normal force due to displacement Δu

F_0 initial normal force due to soil and water pressure against retaining walls ($a_v = 0$)

F_{tot} total normal force, see Equation 4.2

L span length between the tension piles

a_v vertical displacement

$f_{cd,pl}$ unreinforced concrete compressive strength

h_{avg} average thickness concrete slab

p distance between top side concrete slab and bottom side pile anchorage plate or ribs

q_u ultimate distributed line load

q_{u0} initial distributed line load

tol_1 bottom side tolerance underwater concrete

tol_2 top side tolerance underwater concrete

Δu horizontal displacement

x_{span} height of compression zone in span

x_{supp} height of compression zone at support

z inner lever arm, see Equation 4.7

By gradually increasing the value of Δu a full relationship between the displacement Δu and the load (water pressure) q can be determined until the maximum value of q_u is reached (maximum capacity arch action). In this research the following parameters are set equal to zero and will not be included in the equations: tol_1, tol_2 and p. In addition, h_{avg} is replaced by the concrete slab thickness h. The following steps are needed to calculate q for each value of Δu, see Equations 4.1–4.8.

$$\Delta F = f(\Delta u) \tag{4.1}$$

$$F_{\text{tot}} = F_0 + \Delta F \tag{4.2}$$

$$x_{\text{span}} = 2 \times F_{\text{tot}} / f_{\text{cd,pl}} \tag{4.3}$$

$$x_{\text{supp}} = 2 \times F_{\text{tot}} / (\beta \times f_{\text{cd,pl}}) = x_{\text{span}} / 0.6 \tag{4.4}$$

$$A^2 = h^2 + (L/2)^2 \rightarrow A \tag{4.5}$$

$$A^2 = (h - a_{\text{v}})^2 + (L/2 + \Delta u)^2 \rightarrow a_{\text{v}} \tag{4.6}$$

$$z = h - x_{\text{span}}/3 - x_{\text{supp}}/3 - a_{\text{v}} \tag{4.7}$$

$$q_{\text{u}} = 8 \times F_{\text{tot}} \times z / (L + 2 \times \Delta u)^2 \tag{4.8}$$

Note that the factor $\beta = 0.6$ in Equation 4.4 is related to the more concentrated acting width of the compression zone at the location of the (pile) support relative to the acting width of the compression zone in the span. In case of a point load F at midspan, Equation 4.8 can be replaced by Equation 4.9 to determine F_{u}.

$$F_{\text{u}} = 4 \times F_{\text{tot}} \times z / (L + 2 \times \Delta u) \tag{4.9}$$

In the following sections the basic arch action model will be extended and modified so it can be applied to connected prestressed concrete T-beams.

4.2. INCLUSION OF PRESTRESSING FORCE

In case of a prestressed T-beam the initial normal force F_0, see Section 4.1 and Equation 4.2, can be replaced by the normal force due to prestressing N_{p}. Additionally, a possible difference in prestressing force, between the span and the support(s), can be taken into account. Both effects are taken into account by replacing Equation 4.2 with Equations 4.10–4.11. The corresponding changes to Equations 4.3–4.9 will be treated in the following sections.

$$F_{\text{tot,span}} = N_{\text{p,span}} + \Delta F \tag{4.10}$$

$$F_{\text{tot,supp}} = N_{\text{p,supp}} + \Delta F \tag{4.11}$$

4.3. INCLUSION OF VARYING SECTIONAL FORCES

In the basic arch action model $\beta = 0.6$ is used to take into account the more concentrated acting width of the compression zone, at the location of the (pile) support, relative to the acting width of the compression zone in the span, see Equations 4.3–4.4. With $\beta < 1.0$, the height of the compression zone at the support is increased and consequently the height of the internal lever arm z is reduced. Note that, with the assumption of perfect hinges, the basic arch action model does not consider the effect of bending moments. However, for the application of connected prestressed T-beams, a similar approach can be used to include the effect of the bending moment in the span and at the support(s). The compression zone resultants, as a result of the bending moments, can be derived using Equations 4.12–4.13. For ease of use, fixed values for $M_{\mathrm{u,span}}$ and $M_{\mathrm{u,supp}}$ are utilized using the sectional forces at failure, i.e. the sectional forces corresponding to q_{u} or F_{u}, as well as the inner lever arm at failure z_{u}. Note that, for $q < q_{\mathrm{u}}$ or $F < F_{\mathrm{u}}$, this is a conservative approach.

$$N_{M_{\mathrm{u,span}}} = M_{\mathrm{u,span}} / z_{\mathrm{u}} \tag{4.12}$$

$$N_{M_{\mathrm{u,supp}}} = M_{\mathrm{u,supp}} / z_{\mathrm{u}} \tag{4.13}$$

The total normal force, in the span and at the support(s), including the effect of bending moments, can be derived by replacing Equations 4.10–4.11 with Equations 4.14–4.15[1].

$$F_{\mathrm{tot,span}} = N_{\mathrm{p,span}} + \Delta F + N_{M_{\mathrm{u,span}}} \tag{4.14}$$

$$F_{\mathrm{tot,supp}} = N_{\mathrm{p,supp}} + \Delta F + N_{M_{\mathrm{u,supp}}} \tag{4.15}$$

To isolate the effect of the bending moment(s), parameters ζ_{span} and ζ_{supp} are introduced, see Equations 4.16-4.17.

$$\zeta_{\mathrm{span}} = \frac{N_{M_{\mathrm{u,span}}}}{N_{\mathrm{p,span}} + \Delta F} \tag{4.16}$$

$$\zeta_{\mathrm{supp}} = \frac{N_{M_{\mathrm{u,supp}}}}{N_{\mathrm{p,supp}} + \Delta F} \tag{4.17}$$

Finally, Equations 4.14–4.15 can be rewritten to Equations 4.18-4.19.

$$F_{\mathrm{tot,span}} = (N_{\mathrm{p,span}} + \Delta F) \times (1 + \zeta_{\mathrm{span}}) \tag{4.18}$$

$$F_{\mathrm{tot,supp}} = (N_{\mathrm{p,supp}} + \Delta F) \times (1 + \zeta_{\mathrm{supp}}) \tag{4.19}$$

The corresponding changes to Equations 4.3–4.9 will be treated in the following sections.

[1] Note that in the context of the arch action model, the (total) normal force is defined as the stress resultant in the compression zone.

4.4. INCLUSION OF VARIABLE WIDTH CROSS-SECTION

THE basic arch action model considers a slab with a constant width. To take into account a variable cross-section width, the basic Equations 4.3–4.4 are no longer valid. Additionally, for ease of use, the linear compression zone is replaced by a rectangular stress block according to Eurocode. The rectangular stress block is defined by the parameter λ, to reduce the height of the compression zone, and by the parameter η, to reduce the concrete compressive strength, see Equations 4.20–4.21.

$$\lambda = 0.8 \qquad \text{for } f_{ck} \leq 50 \text{ MPa} \tag{4.20a}$$

$$\lambda = 0.8 - (f_{ck} - 50)/400 \qquad \text{for } 50 < f_{ck} \leq 90 \text{ MPa} \tag{4.20b}$$

$$\eta = 1.0 \qquad \text{for } f_{ck} \leq 50 \text{ MPa} \tag{4.21a}$$

$$\eta = 1.0 - (f_{ck} - 50)/200 \qquad \text{for } 50 < f_{ck} \leq 90 \text{ MPa} \tag{4.21b}$$

Finally, the concrete compressive strength for unreinforced concrete ($f_{cd,pl}$) is replaced by the concrete compressive strength for reinforced concrete (f_{cd}). The resulting formulas for the compression zones are given by Equations 4.22–4.23.

$$F_{tot,span} = \lambda \times x_{span} \times \eta \times f_{cd} \Leftrightarrow x_{span} = \frac{F_{tot,span}}{\lambda \times \eta \times f_{cd}} \tag{4.22}$$

$$F_{tot,supp} = \lambda \times x_{supp} \times \eta \times f_{cd} \Leftrightarrow x_{supp} = \frac{F_{tot,supp}}{\lambda \times \eta \times f_{cd}} \tag{4.23}$$

Due to the variable cross-section width, the height of the compression zones, using Equations 4.22–4.23, are determined iteratively until equilibrium is obtained between the normal force F_{tot} and the corresponding stress resultant. In addition, the closed form vertical position of the stress resultant in Equation 4.7 is replaced by the more general Equation 4.24.

$$z = h - z_{x_{span}} - z_{x_{supp}} - a_v \tag{4.24}$$

The new parameters used in Equation 4.24 are:

$z_{x_{span}}$ distance between the top edge and the stress resultant in the span compression zone

$z_{x_{supp}}$ distance between the bottom edge and the stress resultant at the support compression zone

Compared to the basic arch action model, using a linear compression zone (see Figure 4.1), the vertical distances of the stress resultants, $z_{x_{span}}$ and $z_{x_{supp}}$, using the modified model with a rectangular compression zone (see Figure 4.3), are reduced by a factor of $0.75/\eta$.

4.5. INCLUSION OF ELASTIC DEFORMATION

THE basic arch action model does not include the effect of elastic deformation of the compressive struts, see Figure 4.1 ($EA = \infty$). However, neglecting the elastic compressive strut deformation is a non-conservative approach. The fixed length of the compressive strut A is reflected in the kinematic Equations 4.5–4.6. When taking into account the elastic deformation Δl of the compressive strut, an additional strut rotation θ' will take place and the strut length is reduced from A to A'. In addition, the strut deformation Δl results in an additional vertical deformation Δl_v, see Figure 4.2.

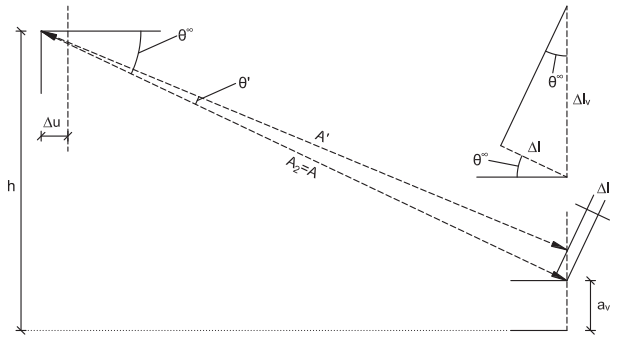

Figure 4.2: Additional strut rotation θ' and vertical deformation Δl_v resulting from the elastic deformation Δl of the compressive strut

The rigid strut angle θ^{∞} can be derived from rewriting Equation 4.6 into Equation 4.25.

$$\tan(\theta^{\infty}) = \frac{(h - a_v)}{(L/2 + \Delta u)} \rightarrow \theta^{\infty} \tag{4.25}$$

The elastic compressive strut deformation Δl can be approximated by Equation 4.26.

$$\Delta l = \frac{\Delta F \times (L/2)}{EA} \tag{4.26}$$

Finally, the additional vertical deformation Δl_v can be derived from the rigid strut angle θ^{∞} and the elastic compressive strut deformation Δl, see Equation 4.27.

$$\Delta l_v = \frac{\Delta l}{\sin(\theta^{\infty})} \tag{4.27}$$

As ΔF gradually increases with increasing Δu, the elastic compressive strut deformation Δl is also increasing. At the same time, as the member stretches horizontally, the rigid strut angle decreases. Both effects will amplify the deformation Δl_v, see Equation 4.27. To take into account the increased vertical deformation, Equation 4.24 is replaced by Equation 4.28.

$$z = h - z_{x_{span}} - z_{x_{supp}} - a_v - \Delta l_v \tag{4.28}$$

4.6. RESULTING MODIFIED MODEL FOR ARCH ACTION

IN the previous sections, the basic arch action model, introduced in Section 4.1, is extended and modified so it can be applied to connected prestressed concrete T-beams. The resulting modified model for arch action, with a distributed downward vertical load, is shown in Figure 4.3. At both edges, the prestressed concrete T-beam is horizontally and vertically restrained by the cross-beams and the end support. At the position of an intermediate cross-beam, a fictitious (intermediate) support is assumed, see Chapter 3 Section 3.4.4 Figure 3.6. At the interface, between the T-beam and the cross-beam(s), a linear horizontal stiffness is assumed, caused by the horizontal stiffness of the (connected) cross-beam. In the span, and at the edge of the cross-beam(s), plastic hinges are assumed. Between the plastic hinges, linear elastic concrete compressive struts are assumed with an initial length A. In the initial undeformed shape (top figure) the normal force is equal to the initial prestressing force N_p. With increased loading, due to the additional vertical displacement a_v, the model stretches horizontally by Δu (bottom figure) causing an additional horizontal force ΔF. Due to the additional normal force ΔF the compression zones increase in height and at the same time the internal lever arm z is reduced. In addition, the internal lever arm is reduced by the additional vertical deformation Δl_v caused by the linear deformation of the compressive strut resulting in a length A' (see Section 4.5). For ease of use, a rectangular stress block according to Eurocode is adopted in the compression zones. Finally, due to the variable width cross-section, the position of the stress resultant as well as the height of the compression zone are determined iteratively. Note that, for the application of connected prestressed T-beams, the modified arch action model is a significant simplification of the actual (variable) sectional forces in the area between the cross-beams. For instance, the sagging bending moments, at the location of the cross-beams, are likely insufficient to cause significant bending cracks and result in plastic hinges. In addition, because of the connection with the adjacent T-beams, the additional normal force ΔF will not be constant. Despite these deficiencies, the modified arch action model can still be utilized to determine an upper bound limit of the ultimate load q_u or F_u.

The following steps are needed to calculate q or F for each value of Δu, see (revisited) Equations below. When using a variable width cross-section, Equations 4.22–4.23 require iterations. In Equation 4.29, the maximum normal force due to prestressing, between the span and the support(s), is taken into account. For λ and η see Equations 4.20–4.21.

$$\Delta F = f(\Delta u)^2 \qquad \text{(4.1 revisited)}$$

$$F_{\text{tot}} = \max(N_{\text{p,span}}, N_{\text{p,supp}}) + \Delta F \qquad (4.29)$$

$$N_{M_{\text{u,span}}} = M_{\text{u,span}} / z_{\text{u}} \qquad \text{(4.12 revisited)}$$

$$N_{M_{\text{u,supp}}} = M_{\text{u,supp}} / z_{\text{u}} \qquad \text{(4.13 revisited)}$$

[2] With a linear horizontal stiffness, this equation simplifies to $\Delta F = k_{\text{hor}} \times \Delta u$.

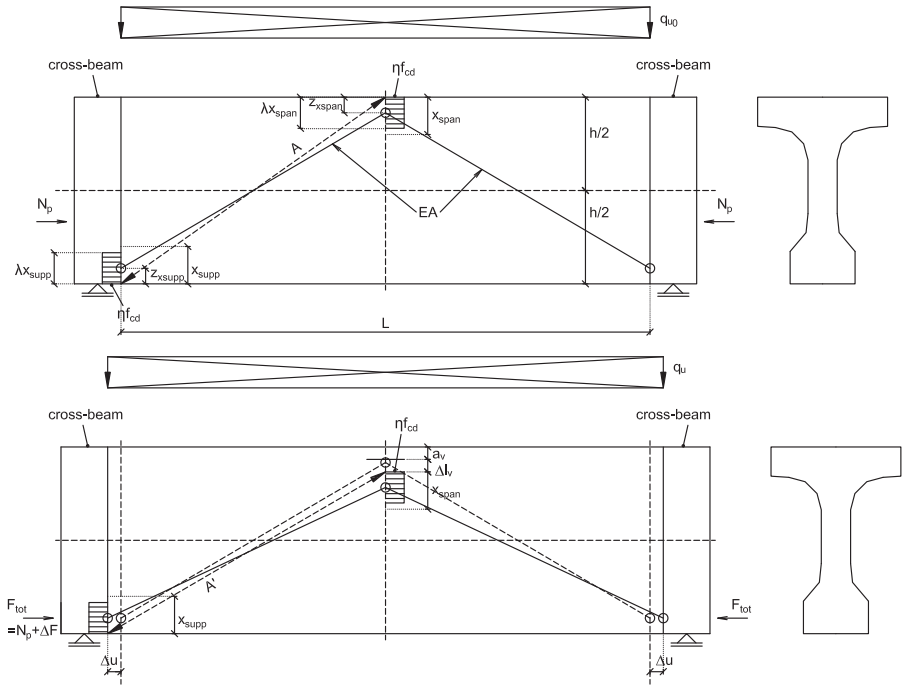

Figure 4.3: Modified arch action model for connected prestressed concrete T-beams

$$\zeta_{\text{span}} = \frac{N_{M_{\text{u,span}}}}{N_{\text{p,span}} + \Delta F} \tag{4.16 revisited}$$

$$\zeta_{\text{supp}} = \frac{N_{M_{\text{u,supp}}}}{N_{\text{p,supp}} + \Delta F} \tag{4.17 revisited}$$

$$F_{\text{tot,span}} = (N_{\text{p,span}} + \Delta F) \times (1 + \zeta_{\text{span}}) \tag{4.18 revisited}$$

$$F_{\text{tot,supp}} = (N_{\text{p,supp}} + \Delta F) \times (1 + \zeta_{\text{supp}}) \tag{4.19 revisited}$$

$$x_{\text{span}} = \frac{F_{\text{tot,span}}}{\lambda \times \eta \times f_{\text{cd}}} \tag{4.22 revisited}$$

$$x_{\text{supp}} = \frac{F_{\text{tot,supp}}}{\lambda \times \eta \times f_{\text{cd}}} \tag{4.23 revisited}$$

$$A^2 = h^2 + (L/2)^2 \rightarrow A \tag{4.5 revisited}$$

$$A^2 = (h - a_{\text{v}})^2 + (L/2 + \Delta u)^2 \rightarrow a_{\text{v}} \tag{4.6 revisited}$$

$$\tan(\theta^{\infty}) = \frac{(h - a_{\mathrm{v}})}{(L/2 + \Delta u)} \rightarrow \theta^{\infty} \qquad \text{(4.25 revisited)}$$

$$\Delta l = \frac{\Delta F \times (L/2)}{EA} \qquad \text{(4.26 revisited)}$$

$$\Delta l_{\mathrm{v}} = \frac{\Delta l}{\sin(\theta^{\infty})} \qquad \text{(4.27 revisited)}$$

$$z = h - z_{x_{\mathrm{span}}} - z_{x_{\mathrm{supp}}} - a_{\mathrm{v}} - \Delta l_{\mathrm{v}} \qquad \text{(4.28 revisited)}$$

$$q_{\mathrm{u}} = 8 \times F_{\mathrm{tot}} \times z/(L + 2 \times \Delta u)^2 \qquad \text{(4.8 revisited)}$$

$$F_{\mathrm{u}} = 4 \times F_{\mathrm{tot}} \times z/(L + 2 \times \Delta u) \qquad \text{(4.9 revisited)}$$

5

CASE STUDY: THE VECHT BRIDGE INTRODUCTION AND LINEAR ANALYSIS

In this chapter a case study of a typical Dutch T-beam bridge called the Vecht bridge is introduced. The different parts of the research related to the Vecht bridge are treated in chapters 5–7. In this chapter, a short history of the bridge, a description of its main geometry and structural components, as well as its prestressing and reinforcement layout are given. In addition, a linear elastic FEM model is used to analyse the (concentrated) live load location versus the sectional forces. Finally, cross-sectional verifications are carried out to investigate the critical load positions, gain insight into the governing failure mode(s) as well as provide analytical estimates for the ultimate load capacity of the bridge deck.

Parts of this chapter have been published in (Ensink et al. 2018).

5.1. INTRODUCTION TO CASE STUDY

IN 2016, a multispan T-beam highway bridge from 1962, called the Vecht bridge, was destined for demolition and became available for this research. The dimensions of this bridge are such that it is still possible to perform full-scale collapse tests on-site. In addition, compared to other Dutch T-beam bridges, with the exception of the low beam spacing (see Chapter 2 Table 2.4), the Vecht bridge has relatively average dimensions (see Chapter 2 Table 2.2) and has none of the atypical properties as defined in Chapter 2 Section 2.3.

The research related to the Vecht bridge is split into three parts, with each treated in a separate chapter:

- Introduction and linear analysis (Chapter 5)
- Full-scale collapse test (Chapter 6)
- Nonlinear analysis (Chapter 7)

In the first chapter (Chapter 5) the Vecht bridge is introduced with a short history and a detailed description is given of its structural components. In addition, the results of the material investigation are presented. Using a linear elastic FEM model, the (live) load distribution is analysed and analytical cross-sectional verifications are performed. The experimental setup as well as the results of the seven on-site collapse tests are then described in Chapter 6. Finally, Chapter 7 contains the detailed nonlinear analysis of the full-scale collapse tests.

5.2. THE VECHT BRIDGE

5.2.1. A SHORT HISTORY

THE Vecht bridge is a multispan T-beam bridge located near the town of Muiden crossing the Vecht river (the Netherlands), see Figure 5.2. For each driving direction, a parallel bridge is built. It is constructed in 1962 as a replacement of the existing bridge to allow for a dual carriageway in the highway A1 (Cement 1966). Photos of the construction are shown in Chapter 2 Figure 2.5 as well as in Figure 5.1. One span consists of a steel bascule bridge over the Vecht river, whereas all other spans are constructed using prestressed concrete T-beams. In 2010 the northern approach bridge was widened by placing two additional prefabricated inverted T-beams in the gap between the two parallel bridges. In addition, the piers and abutments were extended to support the new concrete beams. After more than 50 years, in 2014, it was decided to widen the highway A1 once again and construction started on a new aqueduct to replace the Vecht bridge, at the same time shifting the highway A1 more to the south, see Figure 5.2. Finally, collapse tests were executed for this research in October 2016 shortly after which the Vecht bridge was completely demolished.

5.2.2. MAIN GEOMETRY AND STRUCTURAL SYSTEM

A complete overview of the Vecht bridge, including the span numbering and the test locations, is shown in Figure 5.3. The approach bridges, on either side of the river,

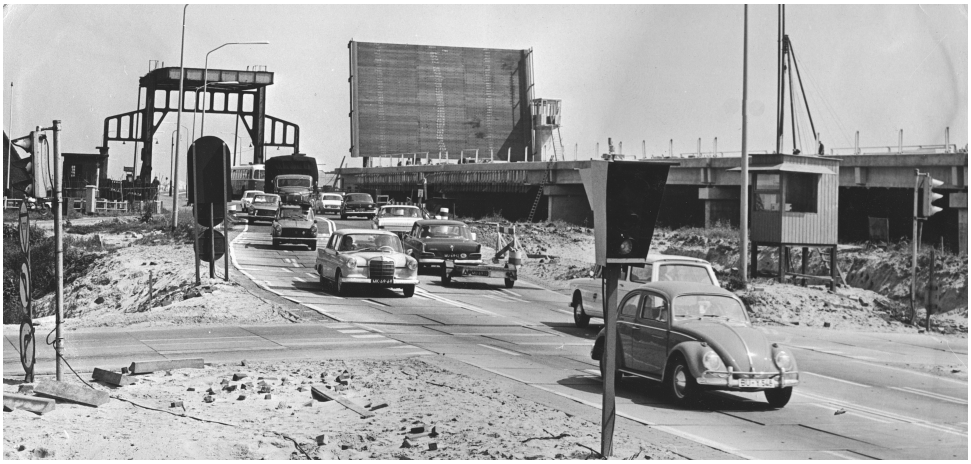

Figure 5.1: Construction of the new Vecht bridge in 1962 (right), existing bridge (left) (Rijkswaterstaat 2020)

Figure 5.2: Completed new aqueduct (right), decommissioned Vecht bridge with opened bascule bridge prior to its demolition (left) (Rijkswaterstaat 2020)

respectively have six and two spans on the west and on the east side. All spans are simply supported and 24 m long (centre-to-centre distance between the bearings). The bridge deck consists of 15 identical prestressed concrete T-beams with cross-beams at 8 m intervals, see Figures 5.4 and 5.5. At the piers and abutments expansion joints are used. The piers have a centre-to-centre distance of 24.9 m, whereas the T-beams have a length of 24.7 m. In transverse direction, the centre-to-centre distance between the T-beams is 1.225 m and the total width of the bridge deck, including the kerbs, is 18.40 m, see Figure 5.4. Since all tests are executed on the southern bridge, in its original 1962 form, the widening of the northern bridge is of no consequence and will not be described in detail. The piers consist of a continuous slender tapered wall with a wider rectangular beam at

the top to accommodate the bearings and support the bridge deck. The foundation of the piers consists of a slab on closely spaced square concrete piles.

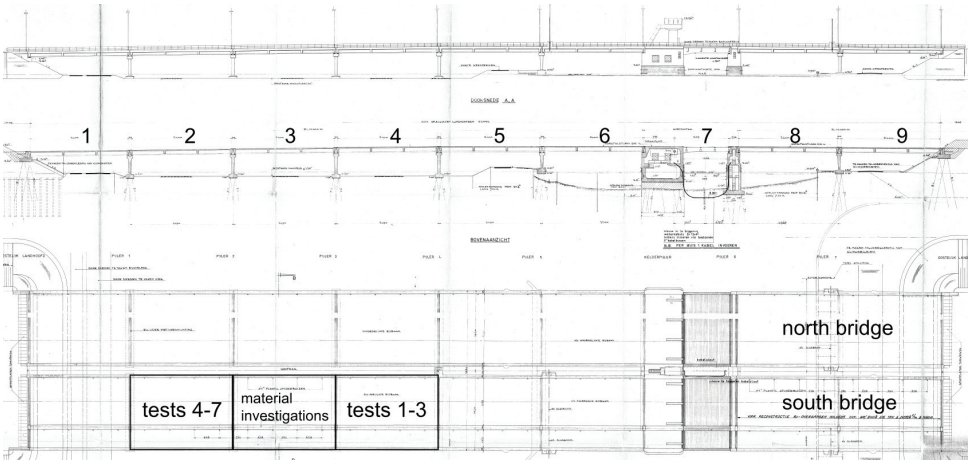

Figure 5.3: Overview of Vecht bridge, span numbering and test locations, side view (top), longitudinal cross-section (middle) and top view (bottom)

5.2.3. T-BEAM: GEOMETRY, REINFORCEMENT AND PRESTRESSING

THE dimensions, reinforcements and the draped prestressing tendons of the T-beam are shown in Figures 5.6 and 5.7. The T-beam has an end block with a thickness of 400 mm and a length of 750 mm followed by a transition piece with a length of 1000 mm. Part of the end block is prefabricated and this type of prefabrication is also shown in Chapter 2 Figure 2.7. The total length of the T-beams is 24700 mm. The onset of the intermediate cross-beams is cast as part of the T-beam, see Figure 5.7 section C. The height of the T-beam is 1150 mm and the web has a minimal thickness of 180 mm. As can be seen in Figure 5.7, very light shear reinforcement is present, with stirrups of just ø8-500 mm. In addition, the stirrups follow the contour of the T-beam and therefore do not comply with current detailing rules[1]. In Figure 5.6 the draped prestressing tendons are shown and numbered 1–7, this presumably being the original order of the post-tensioning. Note that, to improve legibility, parts of the T-beam have been left out in Figure 5.6. Six of the seven prestressing tendons are anchored at the end block, whereas one is anchored in the top flange at a distance of 1902 mm from the support. The complete tendon layout is also shown in Figure 5.10. At the end cross-beams, the intermediate cross-beams and the top flange, ducts ø50 mm are present to accommodate the transverse prestressing. The prestressing system is that of Freyssinet with each tendon 12ø7 mm (A_p = 462 mm^2) and ducts ø42 mm (Cement 1956, Freyssinet 1972, Rijkswaterstaat 2013).

[1] see Chapter 2 Section 2.8

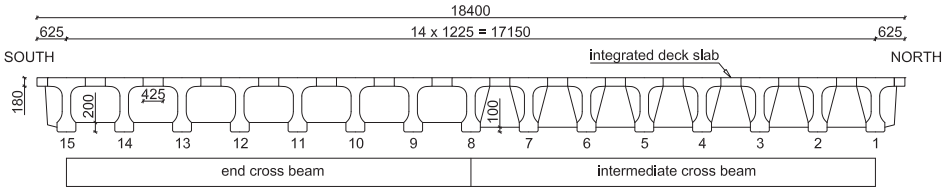

Figure 5.4: Vecht bridge, cross-section deck, T-beam numbering (measurements in mm)

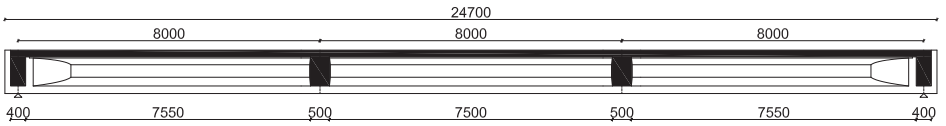

Figure 5.5: Vecht bridge, longitudinal section deck (measurements in mm)

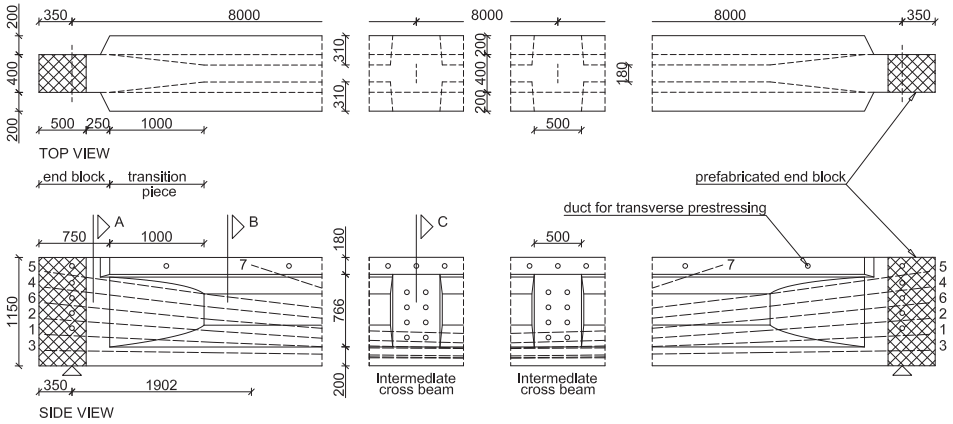

Figure 5.6: Vecht bridge, T-beam dimensions and draped prestressing tendons 1–7 (measurements in mm)

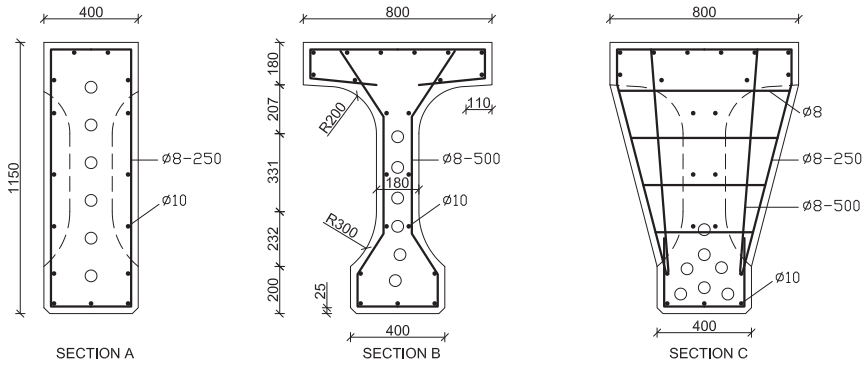

Figure 5.7: Vecht bridge, T-beam dimensions and reinforcement layout (location of cross-sections see Figure 5.6) (measurements in mm)

5.2.4. CROSS-BEAMS: GEOMETRY, REINFORCEMENT AND PRESTRESSING

THE end cross-beams have a thickness of 400 mm and are centred above the bearings, see Figure 5.5. The bottom is offset by 200 mm compared to the bottom of the T-beams, see left side of Figure 5.4. The reinforcement consists of stirrups ø8-200 mm and a longitudinal reinforcement of 5ø8 mm on either side. The end cross-beams also contain five transverse prestressing tendons of which one is located in the top flange, see Figure 5.6. The two intermediate cross-beams have a thickness of 500 mm and are located at 8 m intervals, see Figure 5.5. The bottom is offset by 100 mm compared to the bottom of the T-beams, see right side of Figure 5.4. The reinforcement in the wedge-shaped part, cast between the main T-beams, consists of three stirrups ø8 mm and a longitudinal reinforcement of 5ø8 mm on either side. The intermediate cross-beams contain eight transverse prestressing tendons, see Figure 5.6. The prestressing system is the same as for the T-beam, see Section 5.2.3.

5.2.5. INTEGRATED DECK SLAB: GEOMETRY, REINFORCEMENT AND PRESTRESSING

THE integrated deck slab is located between the top flanges of the T-beams and has a width of 425 mm and a thickness of 180 mm, see Figure 5.4. The integrated deck slab is only connected via the side of the top flange of the T-beam by transverse prestressing. To improve this connection, an indented concrete surface is used at the interface of the T-beam. The reinforcement consists of stirrups ø6-400 mm and a longitudinal reinforcement of 4ø6 mm. The slab is connected to the T-beams by 35 unevenly spaced transverse prestressing tendons, see Figures 5.6 and 5.10. Note that especially at the location of the intermediate cross-beams, the transverse prestressing is much more concentrated. The prestressing system is the same as for the T-beam, see Section 5.2.3.

5.2.6. SUPPORTS

THE T-beams are all individually supported by reinforced elastomeric bearings. The dimensions given on the original drawings are l×b×h = 206 × 306 × 46 mm. The reinforcement consists of three embedded 3 mm thick steel plates. The outer layer material is synthetic rubber, whereas the two 15.5 mm thick inner layers are made of natural rubber. The bearings have never been replaced and therefore have an age of 54 years.

5.3. MATERIAL INVESTIGATION

THIS section summarises the results of the material investigation of the Vecht bridge, which is performed for this research. More details about the material investigation are given in the reports (den Boef 2016, Koekkoek 2017). The investigation is carried out on the south-western approach bridge on the third span, see Figure 5.3. The following material properties are investigated:

- The concrete compressive strength and density.
- The strength of the reinforcing steel.
- The strength of the prestressing steel.

For the determination of the concrete compressive strength and the density, cores are drilled from the prestressed T-beams, the integrated deck slab and the kerb. For the T-beams three locations are used, designated with 'B' (top cores), 'L' (web cores) and 'O' (bottom cores), see Figure 5.8. The integrated deck slab cores are designated as 'T' and are taken from different locations along the span length, between T-beams 6 and 13. The kerb cores are designated as 'SK' and are also taken from different locations along the span length from the north side kerb.

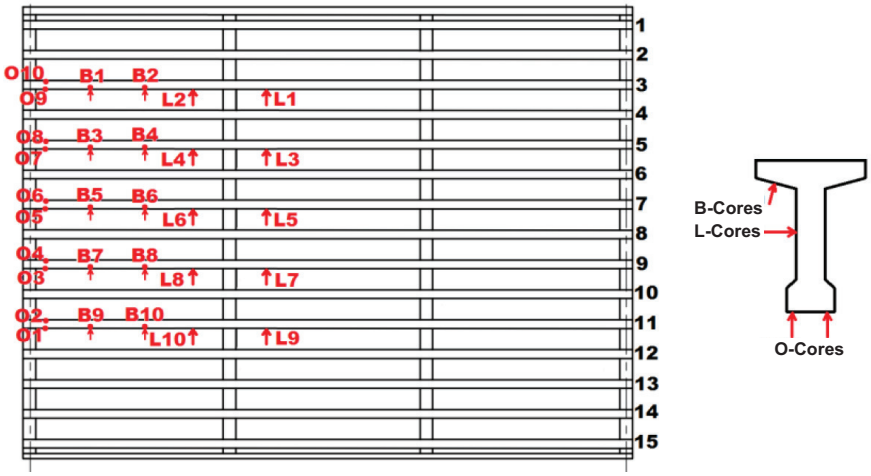

Figure 5.8: Location of concrete cores drilled from T-beams (taken from (den Boef 2016))

In total 61 cores are drilled, 30 in the T-beams, 23 in the integrated deck slab and 8 in the kerb. The results for the concrete compressive strength and the density are given in Table 5.1. A correction factor is included for samples that have a ratio between the height and the diameter of the cores unequal to 1.0, in accordance with RTD 1006 (Rijkswaterstaat 2013). The mean cylinder concrete compressive strength (f_{cm}) is determined by multiplying the mean cube concrete compressive strength ($f_{cm,cube}$) with a conversion factor of 0.82 (Gijsbers et al. 2011). The cores are also visually inspected and in general, the concrete is well compacted and does not show any signs of deterioration, cracking or corrosion of the reinforcement. In some cases (7 cores), a localised bad compaction is observed. In a large number of cases (27 cores), flint aggregates are found, which could make the concrete sensitive to alkali-silica reaction but no evidence of this is found. Finally, large maximum aggregate sizes are found in the range of D_{max} = 26–59 mm, see also Figure 5.9. Compared to the 28 days strength of $f_{cm,cube}$ = 51 N/mm^2 (based on 279 samples see (Rijkswaterstaat 1962)), after 54 years, the current strength for the T-beams has more than doubled over time.

The strength of the reinforcing steel and prestressing steel is determined by testing three ordinary reinforcement bars and four prestressing wires in the laboratory at TU Delft; the results are given in Table 5.2. More detailed information can be found in the measurement report (Koekkoek 2017). From the results it is concluded that the steel grade for the reinforcement steel is QR24 and the steel grade for the prestressing steel

Figure 5.9: Saw cut of T-beam (web) showing large aggregates (measurements in cm)

Table 5.1: Vecht bridge: concrete compressive strength and density

ID	Number of cores	Location	$f_{cm,cube}$ N/mm^2	f_{cm} [a] N/mm^2	ρ kg/m^3
B	10	T-beam top	111.1	91.1	2449
L	10	T-beam web	107.6	88.2	2435
O	10	T-beam bottom	101.5[b]	83.2	2449
	30	T-beam average	106.9	87.7	2444
T	23	Integrated deck slab	73.5[c]	60.3	2367
SK	8	Kerb	67.6	55.4	2383

[a] $f_{cm} = 0.82 \times f_{cm,cube}$, [b] based on 9 samples (1 outlier removed)
[c] based on 21 samples (2 outliers removed)

Table 5.2: Vecht bridge: strength of reinforcement and prestressing steel

ID	Type	Cal. ø[a] mm	f_y N/mm^2	f_u N/mm^2	ϵ_u %
VECHT7p_17	prestressing wire	7.006	1487.8	1746.6	7.7
VECHT7p_18	prestressing wire	7.006	1509.4	1797.1	10.0
VECHT7p_19	prestressing wire	7.025	1477.9	1753.7	9.6
VECHT7p_20	prestressing wire	7.017	1546.6	1780.7	8.7
prestressing wire average			1505.4	1769.5	9.0
VECHT10_21	reinforcement bar	9.626	287.9	340.9	>10
VECHT10_22	reinforcement bar	9.646	281.1	339.8	>10
VECHT10_23	reinforcement bar	9.778	294.0	374.6	6.2[b]
reinforcement bar average			287.7	351.8	10.0

[a] average thickness determined by weight of specimen
[b] measurement frame slipped of specimen

is QP170. The standard material properties of these steel grades are given in Chapter 2 Tables 2.5–2.6.

5.4. PRESTRESSING FORCES

THE tendon layout and prestressing system are described in Section 5.2.3. In this section the sectional forces as a result from the prestressing of the T-beams are determined that will be used in the linear analysis and the cross-sectional verification. For the Vecht bridge the prestressing steel grade for all tendons is QP170. Assuming 20% time-dependent losses, the working prestressing force for each tendon can be calculated from the allowable initial stress σ_{pi} in accordance with RTD 1006 (Rijkswaterstaat 2013):

$$N_{\text{pw}} = 0.8\,\sigma_{\text{pi}} A_{\text{p}} = 0.8 \times 1084 \times 462 \times 10^{-3} = 400.6 \text{ kN} \tag{5.1}$$

To calculate the internal, i.e. sectional, forces arising from the prestressing the 'equivalent prestressing load method' is adopted (Walraven and Braam 2018). The following forces are exerted on the concrete T-beam by the prestressing tendons:

- N_{pw} subdivided in a horizontal and a vertical component at the anchorages.
- Bending moment M_{pw} at the anchorages as a result of the eccentricities.
- Forces $F_{\text{pw,kink}}$ as a result of kinks in the system line from the end block, through the transition piece, to the regular T-shaped cross-section (see also Figure 5.6). Assuming a straight system line through the transition piece, this results in two kinks: one at the start and one at the end of the transition piece.
- Equivalent load q_{pw} as a result from the curvature of the prestressing tendons.

The original calculation of the Vecht bridge is not available. However, from the technical drawings the tendon layout can be derived. The vertical and horizontal layout, is given in 9 cross-sections at 1.5 m interval from the centre of the support until half the span length. An additional cross-section is also given at the position of the intermediate cross-beam. For the numbering of the tendons, see Figures 5.6 and 5.10. To approximate the vertical curvature of the prestressing tendons, third degree polynomials are derived using Equation 5.2. The horizontal curvature, of tendons 1, 3, 4 and 6, is limited and will not be taken into account.

$$y = ax^3 + bx^2 + cx + d \tag{5.2}$$

The following boundary conditions are used to solve the four polynomial coefficients (a–d) of Equation 5.2:

- The coordinates at the anchorage and at half the span length.
- The angle with the horizontal at the anchorage taken from the technical drawings, rounded to 0.5 of a degree.
- A zero slope at half the span length due to symmetry.

For tendon 7 two connecting third degree polynomials are used, with equal first and second derivative at the transition point chosen at x = 4.5 m (distance from the centre of the support). To verify the results, the polynomials are plotted on scale on top of the original technical drawing as shown in Figure 5.10.

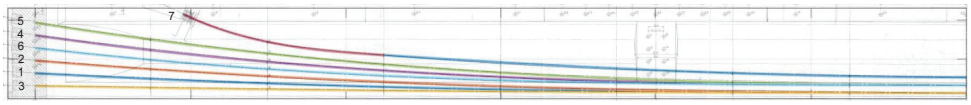

Figure 5.10: Third degree polynomial approximation of prestressing tendons 1–7 (half of span length), plotted on scale on top of the original drawing

The forces exerted on the concrete T-beam for each tendon are summarised in Table 5.3. The forces $F_{\text{pw,kink}}$ are calculated using Equation 5.3 where ϕ relates to the change in angle of the system line at the kink. To calculate the equivalent load q_{pw} at first a constant radius R and curvature κ are assumed, see Equations 5.4, 5.5 (Walraven and Braam 2018). The radius R can be derived from the length l and drape f of the prestressing tendon by using Equation 5.6 (Walraven and Braam 2018).

$$F_{\text{pw,kink}} = 2N_{\text{pw}} \sin(1/2\phi) \tag{5.3}$$

$$q_{\text{pw}} = \frac{N_{\text{pw}}}{R} \tag{5.4}$$

$$\kappa = \frac{1}{R} \tag{5.5}$$

$$R = \frac{l^2}{8f} \tag{5.6}$$

Assuming a constant radius results in a total error, for tendons 1–7, of 5% in the vertical equilibrium ($N_{\text{pw,vert}}$ versus $\int_0^{l/2} q_{\text{pw}}\,\mathrm{d}x$), with the extreme curvature of tendon 7 resulting in a 10% error. The accuracy of the equivalent load q_{pw} can be improved by using the full expression for curvature, see Equation 5.7. As a result of using Equation 5.7, the equivalent loads q_{pw} are no longer constant but vary over the length of the tendon, see Table 5.3.

$$\kappa = \frac{\ddot{f}(x)}{\left(1+\dot{f}(x)^2\right)^{3/2}} \tag{5.7}$$

The equivalent load q_{pw} for tendon 7, using Equation 5.7, is plotted in Figure 5.11a. The sectional forces as a result of the prestressing of tendons 1–7 as well as the self-weight are plotted in Figures 5.11b–d. The self-weight includes the parts of the intermediate cross-beams and the integrated deck slab dependent on the centre-to-centre spacing (acting width) of the T-beams. No additional dead load, such as asphalt, is taken into account (see Chapter 6 Section 6.3.1). As can be seen in Figure 5.11a, the equivalent load q_{pw} shows an extreme value near the anchorage where the curvature is also the most

Table 5.3: Forces exerting on T-beam from prestressing tendons 1–7

tendon	angle at anchorage	$N_{pw,hor}$	$N_{pw,vert}$	M_{pw}	$F_{pw,kink}$	q_{pw} anchorage/midspan
	°	kN	kN	kNm	kN	kN/m
1	3.0	400	21	-123	8.7	2.8 / 0.7
2	4.5	399	31	-56	8.7	3.7 / 1.6
3	1.0	400	7	-191	8.8	0.8 / 0.3
4	8.0	397	56	79	8.7	8.2 / 1.1
5	9.0	396	63	144	8.7	7.9 / 2.6
6	6.5	398	45	12	8.7	7.4 / 0.2
7(1)[a]	25.0	363	169	147	-	91.0 / 1.7
7(2)[a]	-	-	-	-	-	1.7 / 5.1

[a] for tendon 7 two connecting third degree polynomials are used, i.e. 7(1) and 7(2)

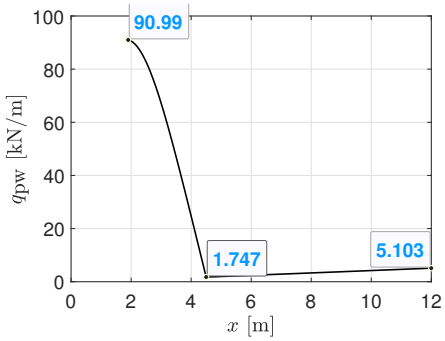

(a) Equivalent load q_{pw} tendon 7

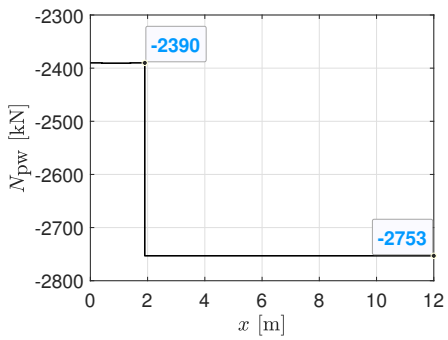

(b) Normal force N_{pw} tendons 1–7

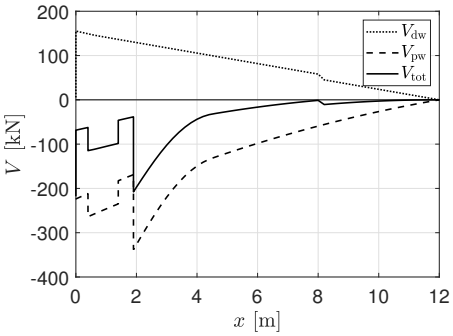

(c) Shear force tendons 1–7 and self-weight

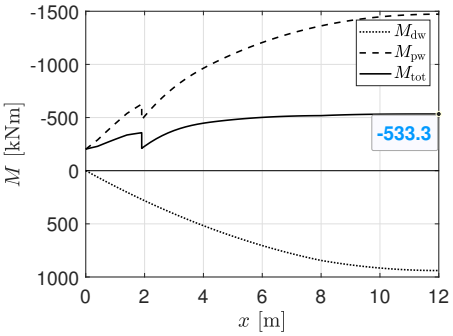

(d) Bending moment tendons 1–7 and self-weight

Figure 5.11: Equivalent load q_{pw} tendon 7 (a) and combined sectional forces as a result of prestressing tendons 1–7 and self-weight (b)–(d)

prominent. Tendon 7 is anchored in the top flange at a coordinate of x = 1.902 m, which causes jumps in the bending moment, shear and normal forces. In Figure 5.11c the effect of the forces $F_{\text{pw,kink}}$ at the start and end of the transition piece, at x = 0.4 m and x = 1.4 m, of tendons 1–6 can also be seen.

5.5. LIVE LOAD LOCATION VERSUS SECTIONAL FORCES

5.5.1. FEM MODEL FOR LIVE LOAD CALCULATION

To investigate the live load location versus sectional forces of a single span consisting of 15 T-beams, a linear elastic FEM model is created using the software of SCIA Engineer (Nemetschek 2020). The FEM model consists of a slab, representing the integrated deck slab and the top flange of the T-beams, strengthened by ribs, representing the remaining parts of the T-beams and the cross-beams, see Figures 5.12 and 5.13. Since this is a 2D model, 3D effects are not included and all elements, including the supports, are located in the centre plane of the slab. Due to the presence of prestressing, uncracked concrete is assumed for all components with a mean modulus of elasticity E_{cm} according to Table 5.4. Note that the concrete kerbs are not included in this model (see Chapter 6 Figure 6.1). The cross-beams are assumed to have a strength equal to the integrated deck slab. The equivalent modulus of elasticity of the slab in the FEM model is a combination of the concrete classes of the top flange of the T-beam and the integrated deck slab and is therefore calculated as:

$$E_{\text{slab + flange}} = \frac{b_{\text{flange}} E_{\text{T-beam}} + b_{\text{slab}} E_{\text{slab}}}{(b_{\text{flange}} + b_{\text{slab}})} = \frac{800 \times 42244 + 425 \times 38214}{(800 + 425)} = 40846 \text{ N/mm}^2 \tag{5.8}$$

Table 5.4: Concrete class and modulus of elasticity used in FEM model

	concrete class	E_{cm} N/mm^2
T-beam	C80/95	42244
Cross-beam & integrated deck slab	C55/67	38214

Using the results from the collapse tests, the support stiffness is determined to be 475 MN/m; this will be treated in Chapter 7 Section 7.3.1. The transition piece is not modelled, instead the length of the end block is slightly extended by 400 mm to 1150 mm. The loading is applied as a local surface load of 400 × 400 mm representing a single wheel load according to NEN-EN 1991-2 (NNI 2015). This loading is applied at the centre of the T-beam at every 200 mm interval, starting from the centre of the support to halfway the span length, on T-beam number 1–8 see Figures 5.14 and 5.15. In this way, due to double symmetry, a grid of load locations at 200 mm interval is realised for the complete span. In addition, a meshsize of 200 mm is specifically chosen to generate nodes that coincide with the load locations. Because of the cantilever of 350 mm, the transition point of the (extended) end block to the regular T-beam is now at a distance of 1150 - 350 = 800 mm from the support, which is exactly on the desired grid of 200 mm. This

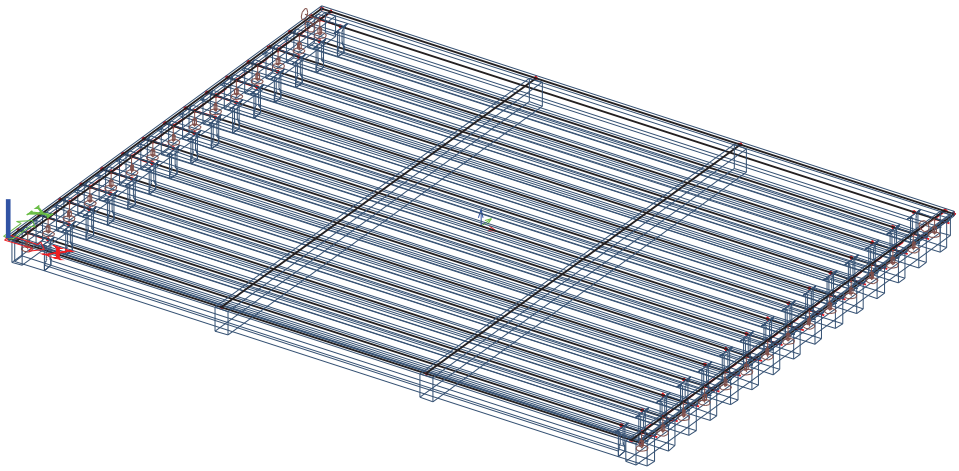

Figure 5.12: Single span linear elastic FEM model, 2D slab strengthened by ribs

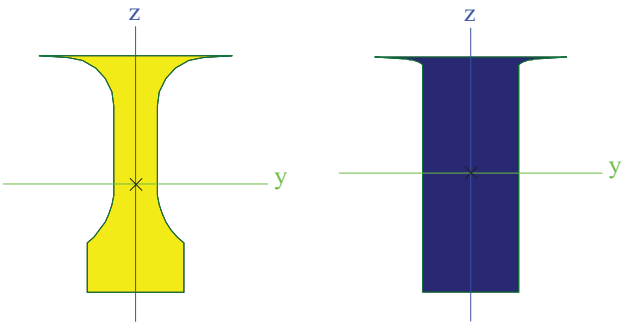

(a) Regular T-beam (b) T-beam end block

Figure 5.13: Cross-sections of T-beam without top flange (ribs in FEM model)

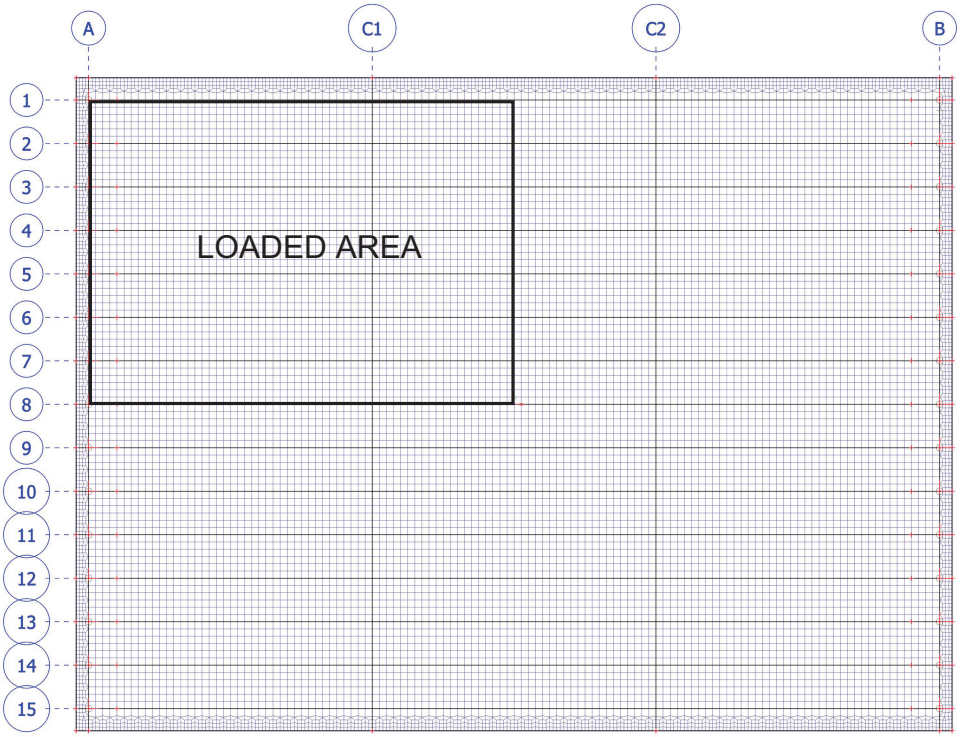

Figure 5.14: Top view of mesh, numbering of T-beams and loaded area

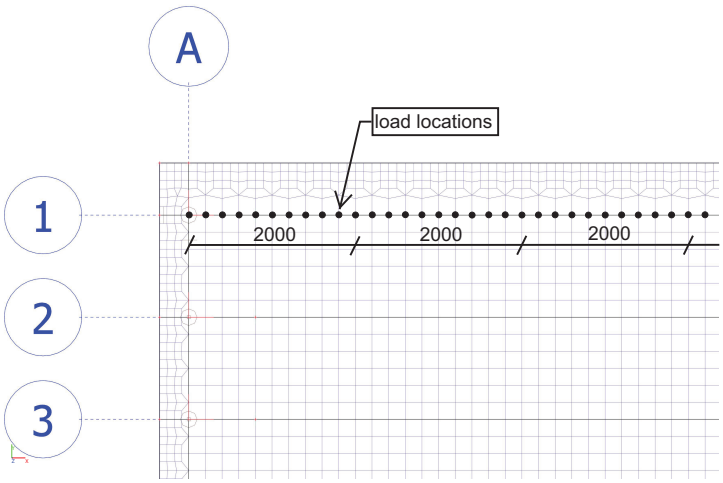

Figure 5.15: Detail of mesh and grid of load locations (grid only shown on T-beam 1) (measurements in mm)

modelling approach will enforce the FEM program to calculate the sectional forces at the desired grid locations. The Mindlin-Reissner plate theory (Nemetschek 2020) is used in combination with an edge mesh refinement of 100 mm, see Figures 5.14 and 5.15. Note that in Figures 5.14 and 5.15 axes A and B relate to the location of the supports and the end cross-beams, whereas axes C1 and C2 relate to the location of the intermediate cross-beams. The detailed geometry of the bridge deck is given in Figures 5.4–5.7.

5.5.2. ANALYSIS OF LIVE LOAD LOCATION

In order to analyse the influence of live load location, using the FEM model described in the previous section, a unit load of F = 1000 kN will be placed on T-beams 1, 5 and 8 (for T-beam numbering see Figure 5.14). In addition, the results will be compared to an individual, simply supported T-beam. In the longitudinal direction, the load locations are chosen at a = 2, 4, 6, 8, 10 and 12 m (distance from the centre of the support). The results of this analysis are given in Figures 5.16 and 5.17, showing half the span length. The results of T-beam 5 are similar to those of T-beam 8 and are therefore not included in Figure 5.17. Due to symmetry, T-beam number 1 equals 15 and T-beam number 5 equals 11.

As can be seen in Figure 5.17, the intermediate cross-beam, at a distance of x = 8 m from the support, has a significant influence on the load distribution. This is especially true for T-beams 5 and 8, where the shear force is generally close to zero after passing the intermediate cross-beam. In addition, with the load placed between the end cross-beam and the intermediate cross-beam, a behaviour of a simply supported beam with a span length equal to the distance between the cross-beams can be observed. This also holds true when the load is placed between the first and second intermediate cross-beam, see for instance Figures 5.17c, d with the load at a = 12 m. Comparing a simply supported individual T-beam to the connected T-beams (Figure 5.16 versus Figure 5.17), the main difference is the decrease of the shear force from the loading point to the supports or the intermediate cross-beam(s). This is due to the load transfer from the loaded beam to the adjacent beams, through the integrated deck slab.

For the edge beam, T-beam 1, this behaviour is somewhat less pronounced due to the one-sided connection with the intermediate cross-beam. For the edge beam, the most significant observation is the higher shear force of 696 kN (Figure 5.17a) close to the support, for a = 2 m, compared to T-beams 5 and 8 of 573 and 571 kN (Figure 5.17c).

Likewise, the bending moments show an equally significant influence of the intermediate cross-beam. In Figure 5.17, the bending moment is generally close to zero or has a low value at the location of the intermediate cross-beam, except when a load is placed directly on it. Again, for the edge beam this behaviour is somewhat less pronounced. For the edge beam, the highest bending moment of 2182 kNm (Figure 5.17b) is observed with the load at a = 12 m and is much higher compared to T-beams 5 and 8 with 1245 and 1164 kNm (Figure 5.17d).

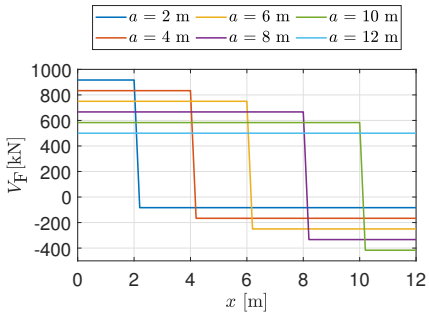

(a) Shear force V_F, individual T-beam

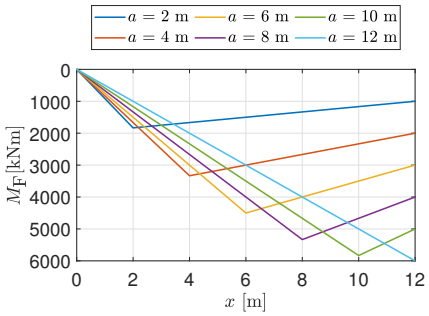

(b) Bending moment M_F, individual T-beam

Figure 5.16: Sectional forces for an individual, simply supported, T-beam with a unit load F = 1000 kN at different load locations (half of span length)

5

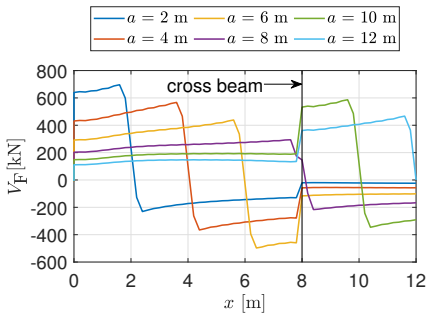

(a) Shear force V_F, T-beam 1 (15)

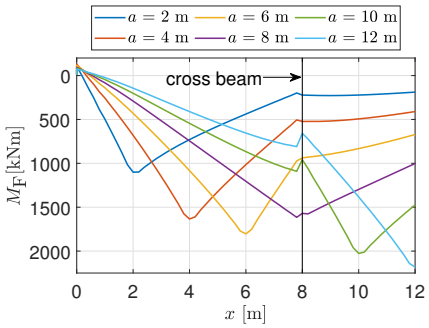

(b) Bending moment M_F, T-beam 1 (15)

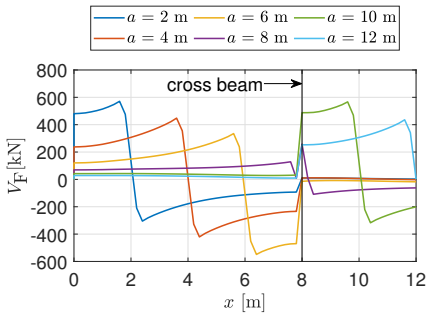

(c) Shear force V_F, T-beam 8

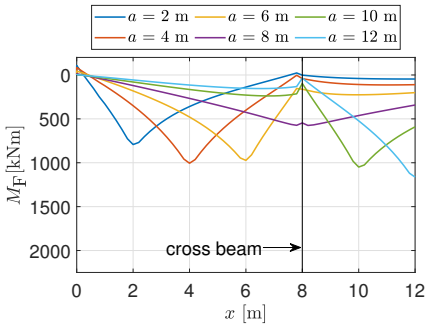

(d) Bending moment M_F, T-beam 8

Figure 5.17: Sectional forces for connected T-beams with a unit load F = 1000 kN at different load locations (half of span length)

5.6. ASSESSMENT BASED ON LINEAR ANALYSIS

5.6.1. INTRODUCTION TO CROSS-SECTIONAL VERIFICATION

FOR the Vecht bridge, considering the varying cross-sectional properties, the layout of the draped prestressing tendons and the load distribution, it is not straightforward to identify the most critical cross-section(s) and corresponding load position(s). Therefore this process is automated by combining the previously determined sectional forces from the self-weight, the prestressing and the concentrated (live) load, and performing a cross-sectional automated verification using Matlab (Matlab 2019). At all points on the 200 mm grid, as described in Section 5.5, a concentrated (live) load is placed and a cross-sectional verification is carried out. Additional control sections are added at locations where there is a sudden jump in normal force, shear force or bending moment arising from the prestressing forces giving two different numerical values at the same location (see Figure 5.11). The additional control sections are located at:

- x = 1400 mm (end of the transition piece (= 1750 - 350 mm), see Figure 5.6);
- x = 1902 mm (anchorage of tendon 7, see Figure 5.6).

Due to the presence of the transversely prestressed intermediate cross-beams, the control sections between x = 7.75–8.25 m (see Figure 5.5), in the case of connected T-beams, are excluded from the analysis. In addition, control sections close to the end support, at a distance of $x \leq 0.6$ m ($\approx 0.7 \times d$), are also excluded. Note that due to the draped prestressing tendons, the effective depth varies, see also Section 5.6.2.

It should be noted that the cross-sectional verification is not only performed at the same location as the position of the concentrated (live) load but also at surrounding location(s). Therefore, the concentrated (live) load can be considered as a movable load over the bridge. However in general, the governing control section 'x' is usually close or equal to the load position 'a'.

The cross-sectional verifications that will be analysed are:

- Flexural shear, denoted as 'V_{FS}' (Section 5.6.2).
- Shear tension, denoted as 'V_{ST}' (Section 5.6.3).
- Cracking moment, denoted as 'M_{cr}' (Section 5.6.3).
- Ultimate bending moment, denoted as 'M_u' (Section 5.6.4).

The goal of the analysis is to investigate the critical load positions, gain insight into the governing failure mode as well as provide analytical estimates for the ultimate load capacity of the bridge deck. In the chapter 8 these results will be compared to the experimental results and the detailed nonlinear analysis. It should be noted that in this research the emphasis is on the load capacity of the main T-beams and not on other bridge deck components such as the cross-beams or the integrated deck slab. Subsequently, the loading will be placed exclusively at the centre of the T-beams. The sectional forces as a result of the concentrated (live) load are based upon a unit load of F = 1000 kN, see Section 5.5.2. The maximum concentrated (live) load F_{max} for each control section is determined by multiplication of the unit load with a load factor 'LF' such that the resultant

sectional forces equal the resistance at the control section. The resistance is calculated using average material properties (see Section 5.3), the formulations of NEN-EN 1992-1-1 (NNI 2011a), adapted for average values, and with material and load factors set equal to 1.0. The sectional properties used in the calculations are given in Appendix E Figures E.1–E.2 showing the regular T-beam and the T-beam end block. Figure E.2 includes the acting width of the integrated deck slab equal to the centre-to-centre distance of the T-beams. In Matlab the variable width of the T-beam is approximated by using a number of layers with constant width. The same distribution of layers is used for all cross-sections, see Figures E.1–E.2.

5.6.2. FLEXURAL SHEAR

THE minimum required amount of stirrups according to NEN-EN 1992-1-1 (NNI 2011a), using lower bound material properties for the T-beam (concrete C55/67 and reinforcement QR24), is given by Equation 5.9.

$$\rho_{w,min} = (0.08\sqrt{f_{ck}})/f_{yk} = (0.08\sqrt{55})/240 = 0.00247 = 0.247\% \tag{5.9}$$

5

The shear reinforcement present in the T-beam consists of stirrups ø8-500 mm with a minimum web thickness of b_w = 180 mm, see also Figure 5.7. The resulting shear reinforcement ratio is given by Equation 5.10.

$$\rho_w = A_{sw}/(s b_w) = 2 \times {}^1\!/_4 \pi 8^2/(500 \times 180) = 0.00112 = 0.112\% \tag{5.10}$$

Thus, due to the lack of sufficient stirrups, the flexural shear resistance is based upon the concrete resistance only. The flexural shear resistance is calculated according to NEN-EN 1992-1-1 (NNI 2011a), see Equations 5.11 through 5.16.

$$V_{Rm,c} = [C_{Rm,c} k (100 \rho_l f_{ck})^{1/3} + k_1 \sigma_{cp}] b_w d \tag{5.11}$$

With a minimum of:

$$V_{Rm,c} = (\nu_{min} + k_1 \sigma_{cp}) b_w d \tag{5.12}$$

Where:

$$k = 1 + \sqrt{\frac{200}{d}} \leq 2.0 \text{ with } d \text{ in mm} \tag{5.13}$$

$$\rho_l = \frac{A_{sl}}{b_w d} \leq 0.02 \tag{5.14}$$

$$\sigma_{cp} = N_{Ed}/A_c < 0.2 f_{cd} \tag{5.15}$$

$$\nu_{min} = 0.035 k^{3/2} f_{ck}^{1/2} \tag{5.16}$$

For average values $C_{Rm,c}$ = 0.163 (König and Fischer 1995) and k_1 = 0.225 (default design values are $C_{Rd,c} = 0.18/\gamma_c$ and k_1 = 0.15) and f_{ck}, $f_{cd} = f_{cm}$ = 87.7 N/mm^2 (see Table

Table 5.5: Load-reduction factor β

x	d	a = 0.8 m	a = 1.0 m	a = 1.2 m	a = 1.4 m	a = 1.6 m
mm	mm			β		
800	820	0.49	0.61	0.73	0.85	0.98
1000	829	-	0.60	0.72	0.84	0.97
1200	786	-	-	0.76	0.89	-
1400	796	-	-	-	0.88	-
1600	806	-	-	-	-	0.99

5.1). For the longitudinal reinforcement, A_{sl} in Equation 5.14, only the prestressing tendons and the regular reinforcement below the centre of gravity of the cross-section are included. For the regular reinforcement this amount is the same for all cross-sections (9ø10 see Figure 5.7). However, for the draped prestressing tendons, this amount varies and depends on the location of the cross-section. For positive (sagging) moments, the effective depth is determined by using Equation 5.17. Negative (hogging) moments only occur at the position of the intermediate cross-beam in case of connected T-beams, see Figure 5.17d. However, these control sections have been excluded from the analysis, see Section 5.6.1. For each cross-section, the effective depth of the prestressing tendons d_p is defined using the third degree polynomials, as determined in Section 5.4, see Figure 5.10.

$$d = \frac{A_s d_s + A_p d_p}{A_s + A_p} = \frac{A_s d_s + A_p d_p}{A_{sl}} \tag{5.17}$$

The effect of direct load transfer is included by means of the reduction factor β on the concentrated (live) load. This holds for loads that are applied near the end support within a distance of $0.5d \le a_v \le 2d$. The contribution of the concentrated load to the shear force is then reduced by $\beta = a_v/2d$. Since the effective depth d is variable, the reduction factor β depends on both the control section 'x' as well as the load position 'a' of the concentrated (live) load, see Table 5.5. For the width b_w, the formulations for variable width cross-sections in accordance with RTD 1006 (Rijkswaterstaat 2013) are applied, with $b_w = 1.25 \times b_{min}$, where b_{min} is the minimal thickness of the cross-section. Referring to Figure 5.20, for the rectangular end block b_w = 400 mm and for the T-beam cross-section $b_w = 1.25 \times 180 = 225$ mm. For cross-sections close to or at the transition piece, inclined cross-sections are taken into account with a strut angle of $\theta \ge 30°$, thereby increasing the minimal thickness of the cross-section. In Equation 5.15 the compressive force N_{Ed} consists of the prestressing force only. In the analysis the load factor for flexural shear $LF_{V_{FS}}$ is determined by solving Equation 5.18 (for V_{dw} and V_{pw} see Figure 5.11c). The maximum concentrated (live) load related to flexural shear $F_{max,V_{FS}}$ is then calculated by Equation 5.19, with a unit load of F = 1000 kN.

$$V_{Rm,c} = V_{dw} + V_{pw} + LF_{V_{FS}} \beta V_F \tag{5.18}$$

$$F_{max,V_{FS}} = LF_{V_{FS}} \times F = LF_{V_{FS}} \times 1000 \text{ [kN]} \tag{5.19}$$

Table 5.6: Maximum concentrated (live) load for flexural shear

	x	a	$F_{\max,V_{FS}}$	Relative load capacity
	m	m	kN	%
Individual T-beam	1.9	2.0	609	100
Individual T-beam	3.4	3.4	703	115
Connected T-beam 1 (15)	1.9	2.4	840	138
Connected T-beam 1 (15)	8.4	8.8	935	154
Connected T-beam 5 (11)	1.8	2.2	1040	171
Connected T-beam 5 (11)	8.4	8.8	884	145
Connected T-beam 8	1.8	2.2	1045	172
Connected T-beam 8	7.6	7.2	879	144

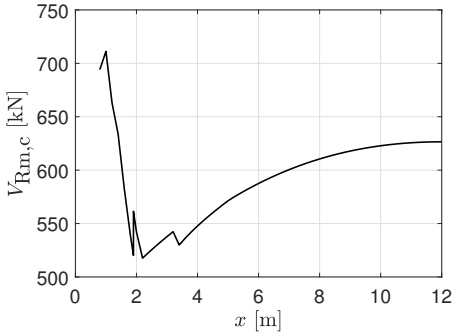

(a) Flexural shear resistance T-beam

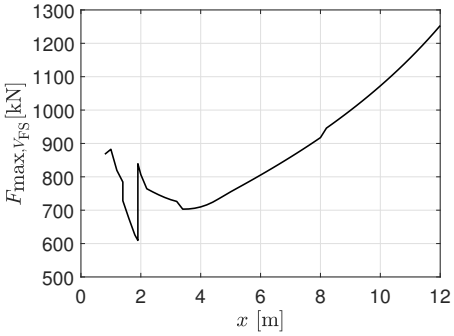

(b) Maximum concentrated (live) load for flexural shear, individual T-beam

Figure 5.18: Flexural shear resistance (a) and maximum concentrated (live) load for individual, simply supported T-beam (b)

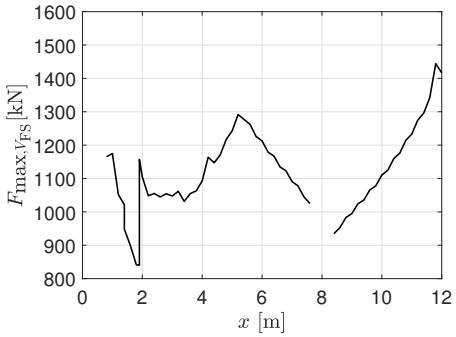

(a) Maximum concentrated (live) load for flexural shear, T-beam 1 (15)

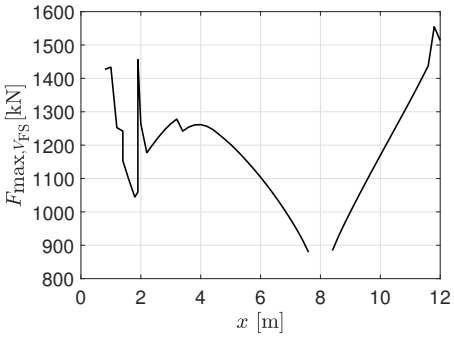

(b) Maximum concentrated (live) load for flexural shear, T-beam 8

Figure 5.19: Maximum concentrated (live) load for connected T-beams

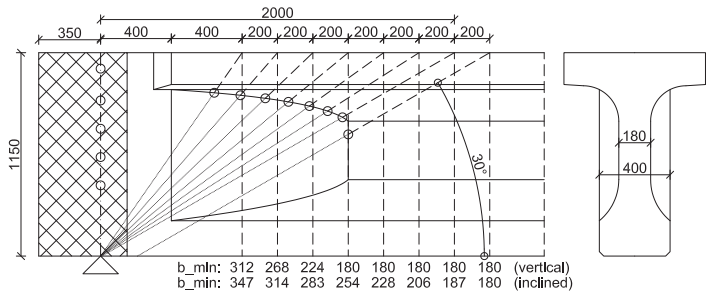

Figure 5.20: Width $b_{\min}$ near end support, vertical versus inclined cross-sections (measurements in mm)

The results of the analysis are shown in Figures 5.18–5.19, showing half the span length, and are summarised in Table 5.6. The results of T-beam 5 are similar to those of T-beam 8 and are therefore not included in Figure 5.19. Due to symmetry, T-beam number 1 equals 15 and T-beam number 5 equals 11, see Table 5.6. In Figures 5.18b and 5.19 the x-axis is the control section and the y-axis gives the maximum concentrated (live) load irrespective of load location (procedure described in Section 5.6.1). The calculated mean resistance $V_{\mathrm{Rm,c}}$ is plotted in Figure 5.18a showing an absolute minimum value of 518 kN at $x = 2.2$ m with $b_{\min} = 180$ mm, see Figure 5.20. Between the end support and $x = 2.2$ m the increased resistance is due to the increasing width $b_{\min}$. For $x > 2.2$ m the flexural shear resistance increases with increasing effective depth, due to the draped prestressing tendons, to a maximum value of 627 kN. The jump at $x = 1.902$ m is due to the change in the compressive force N_{Ed}. The calculated parameters are also given in Table 5.7. For an individual T-beam, see Figure 5.18b, the governing control section is at $x = 1.9$ m, at the anchorage of tendon 7, and an additional local minimum is found at $x = 3.4$, see Table 5.6. The jump of $F_{\max,V_{\mathrm{FS}}}$ at $x = 1.902$ m is caused by the change of the counter-balancing shear force V_{tot}, see Figure 5.11c. For connected T-beams, see Figure 5.19, the governing control section is either at $x = 1.902$ m (T-beam 1) or close to the intermediate cross-beam (T-beam 5 and 8). For an individual, simply supported T-beam, the minimum value for $F_{\max,V_{\mathrm{FS}}}$ is obviously lower compared to the connected T-beams, by at least a factor of 1.4, see Table 5.6.

Table 5.7: Mean flexural shear resistance $V_{\mathrm{Rm,c}}$ prestressed concrete T-beam

	control section			
Parameter	$x = 2.2$ m	$x = 12$ m	Units	Reference
d	788	984	mm	Equation 5.17
k	1.50	1.45	-	Equation 5.13
A_{sl}	3479	3941	mm^2	
ρ_{l}	0.020	0.018	-	Equation 5.14
f_{cm}	87.7	87.7	N/mm^2	Table 5.1
N_{Ed}	2753×10^3	2753×10^3	N	Figure 5.11d
σ_{cp}	6.91	6.91	N/mm^2	
$V_{\mathrm{Rm,c}}$	518×10^3	627×10^3	N	Figure 5.18a

5.6.3. SHEAR TENSION

PARTS uncracked by bending can be evaluated for shear tension according to NEN-EN 1992-1-1 (NNI 2011a). The basis for shear tension is assuming a fully uncracked cross-section. The principal stresses as a function of the internal sectional forces are determined and a maximum allowable tensile stress equal to the uniaxial tensile strength is assumed. For 2D the maximum principal stress is calculated by Equation 5.20. In this equation, the vertical stress, σ_y is assumed to be zero. For further details and discussions on shear tension failure the reader is referred to the thesis by Roosen (2020).

$$\sigma_1 = \frac{\sigma_x}{2} + \sqrt{\left(\frac{\sigma_x}{2}\right)^2 + \tau_{xy}^2} \tag{5.20}$$

The principal stresses σ_1 are evaluated over the full height of the cross-section, see Figure 5.21b, c. This method implies that if the maximum principal stress is at the bottom fibre (Figure 5.21c), which corresponds to the cracking moment, this can also be considered as a lower bound for shear tension resistance. To distinguish between a maximum principal stress occurring in the thin web or at the bottom fibre, these two situations are treated separately, with the former denoted as 'V_{ST}' (i.e. shear tension) and the latter as 'M_{cr}' (i.e. cracking moment).

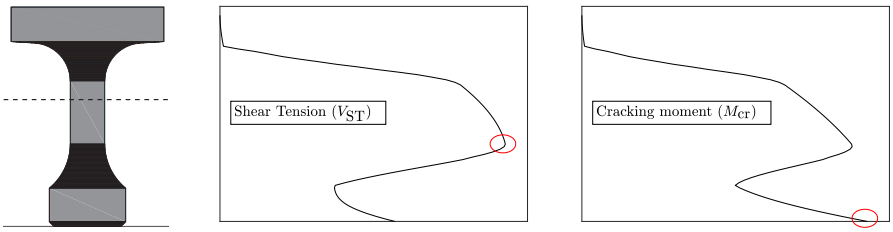

(a) T-beam (b) Shear tension (c) Cracking moment

Figure 5.21: Principal tensile stress σ_1, T-beam cross-section (a), shear tension (b) and cracking moment (c)

The presence of the prestressing tendons with grouted ducts is taken into account by using a reduction of the width of the cross-section to calculate the shear stresses. This reduction is set equal to half of the diameter of a single duct, i.e. ø42/2 = 21 mm (NNI 2011a). In the Matlab routine the stresses are evaluated at 20 (equally spaced) points distributed across the height. Based on the material investigation, see Table 5.1, the mean tensile strength is determined by Equation 5.21 (NNI 2011a).

$$f_{ctm} = 2.12 \times \ln(1 + f_{cm}/10) = 2.12 \times \ln(1 + 87.7/10) = 4.83 \text{ N/mm}^2 \tag{5.21}$$

Due to the construction stages, the following internal sectional forces (see also Figure 5.11) act on the T-beam cross-section without the integrated deck slab (Appendix E Figure E.1), i.e. construction stage 1:

- Normal force (prestressing): N_{pw}.
- Shear forces (self-weight and prestressing): V_{dw} and V_{pw}.

- Bending moments (self-weight and prestressing): M_{dw} and M_{pw}.

Note that the self-weight includes the acting width of the integrated deck slab as well as the cross-beams. The underlying assumption is that before hardening of the concrete this weight is carried by the main T-beam(s). For construction stage 2, the external load acts on the T-beam cross-section with the integrated deck slab, taking into account its acting width (Appendix E Figure E.2). The external load causes a shear force V_{F} and a bending moment M_{F} in each cross-section. The stresses calculated in both stages are then added to calculate the total principal stresses. Note that in this approach the effect of creep, related to construction stage 1, is ignored. Since a closed formulation is not available, an iterative solver is used to determine the load factor for shear tension $LF_{V_{\mathrm{ST}}}$, and the maximum concentrated (live) load related to shear tension resistance $F_{\mathrm{max},V_{\mathrm{ST}}}$ is then calculated by Equation 5.22, with a unit load of F =1000 kN. To prevent ambiguity and improve iteration speed, a restraint is set on the solution interval for $LF_{V_{\mathrm{ST}}}$, between zero (no external force) and the external force related to the cracking moment at the bottom fibre using Equation 5.23. The relationship of Equation 5.23 is also used to determine the load factor for the cracking moment, and the maximum concentrated (live) load related to the cracking moment, $F_{\mathrm{max},M_{\mathrm{cr}}}$, is determined by multiplication with the unit load similar to Equation 5.22.

$$F_{\mathrm{max},V_{\mathrm{ST}}} = LF_{V_{\mathrm{ST}}} \times F = LF_{V_{\mathrm{ST}}} \times 1000 \text{ [kN]} \tag{5.22}$$

$$\frac{N_1}{A_{\mathrm{c},1}} + \frac{M_1}{W_{\mathrm{cb},1}} + LF_{V_{\mathrm{ST}}} \left(\frac{N_2}{A_{\mathrm{c},2}} + \frac{M_2}{W_{\mathrm{cb},2}} \right) = f_{\mathrm{ctm}} \tag{5.23}$$

Where:

N_1 phase 1 axial force (N_{pw})

M_1 phase 1 bending moment ($M_{\mathrm{dw}} + M_{\mathrm{pw}}$)

$A_{\mathbf{c,1}}$ phase 1 cross-sectional area, T-beam (Appendix E Figure E.1)

$W_{\mathbf{cb,1}}$ phase 1 section modulus of the bottom part of the concrete section, T-beam (Appendix E Figure E.1)

N_2 phase 2 axial force ($N_{\mathrm{F}} = 0$)

M_2 phase 2 bending moment (M_{F})

$A_{\mathbf{c,2}}$ phase 2 cross-sectional area, T-beam with integrated deck slab (Appendix E Figure E.2)

$W_{\mathbf{cb,2}}$ phase 2 section modulus of the bottom part of the concrete section, T-beam with integrated deck slab (Appendix E Figure E.2)

The results of the analysis are shown in Figures 5.22–5.23, showing half the span length, and summarised in Table 5.8. The results of T-beam 5 are similar to those of T-beam 8 and are therefore not included in Figure 5.23. Due to symmetry, T-beam number 1

Table 5.8: Maximum concentrated (live) load for shear tension and cracking moment

	x	a	$F_{\max,V_{ST}}$	$F_{\max,M_{cr}}$	Relative load capacity
	m	m	kN	kN	%
Individual T-beam	1.6	1.6	939	-	-
Individual T-beam	12.0	12.0	-	284	100
Connected T-beam 1 (15)	1.8	2.2	1323	-	-
Connected T-beam 1 (15)	5.8	5.8	-	922	325
Connected T-beam 1 (15)	11.8	11.8	-	780	275
Connected T-beam 5 (11)	1.4	1.8	1652	-	-
Connected T-beam 5 (11)	4.6	4.6	-	1557	548
Connected T-beam 5 (11)	8.4	8.8	1416	-	-
Connected T-beam 5 (11)	12.0	12.0	-	1369	482
Connected T-beam 8	1.4	1.8	1659	-	-
Connected T-beam 8	4.4	4.4	-	1599	563
Connected T-beam 8	8.4	8.8	1424	-	-
Connected T-beam 8	12.0	12.0	-	1464	515

equals 15 and T-beam number 5 equals 11, see Table 5.8. In Figures 5.22b and 5.23 the x-axis is the control section and the y-axis gives the maximum concentrated (live) load irrespective of load location (procedure described in Section 5.6.1).

For an individual T-beam, the minimum value for the concentrated (live) load related to the cracking moment is obviously much lower compared to the connected T-beams, by at least a factor of 2.7, see Table 5.8. This can also be concluded from the live load location analysis in Section 5.5.2 by comparing Figure 5.16b to Figure 5.17b. For shear tension, the reduction of the width of the cross-section, due to the presence of the pre-stressing tendons, has a significant effect on the results. This increases the likelihood of a maximum principal stress in the thin web (see Figure 5.21b), and stretches the parts of the T-beam where shear tension can occur. For the connected T-beams, in addition to the area close to the supports, shear tension can also occur in the areas surrounding the intermediate cross-beams, see Figure 5.23b.

It may seem peculiar that for some control sections, the maximum concentrated (live) load related to shear tension appears to exceed the one for the cracking moment, i.e. $F_{\max,V_{ST}} > F_{\max,M_{cr}}$, see for instance $x = 5$ m in Figure 5.23b. However, this is a result of the different load positions taken into account. With the same combination of 'a' and 'x', this will not be the case. But here, only one combination of 'a' and 'x' results in shear tension, whereas multiple combinations result in a cracking moment with one or more combinations resulting in a lower value for $F_{\max,M_{cr}}$ compared to $F_{\max,V_{ST}}$. It is therefore important to realise, that shear tension resistance is dependent on both the control section as well as the load location.

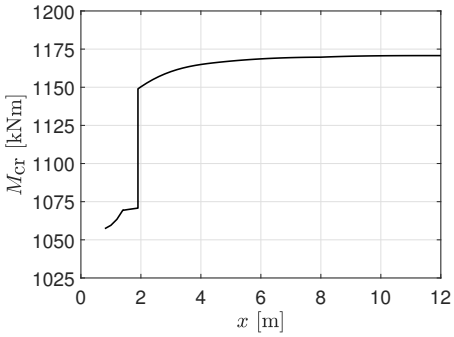

(a) Cracking moment

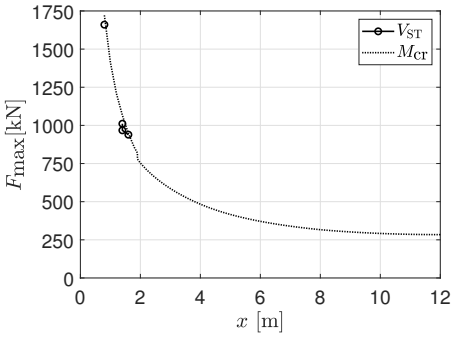

(b) Maximum concentrated (live) load for shear tension and cracking moment, individual T-beam

Figure 5.22: Cracking moment (a) and maximum concentrated (live) load for individual, simply supported T-beam

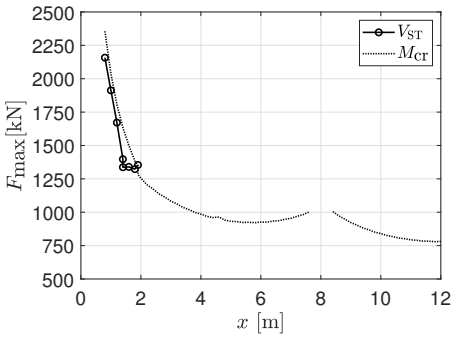

(a) Maximum concentrated (live) load for shear tension and cracking moment, T-beam 1 (15)

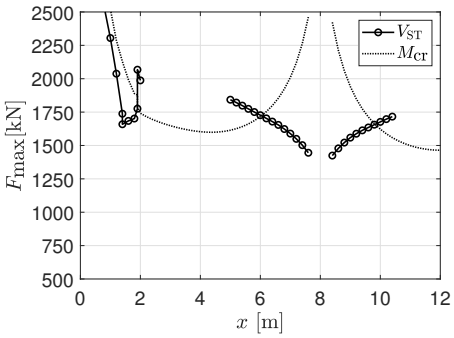

(b) Maximum concentrated (live) load for shear tension and cracking moment, T-beam 8

Figure 5.23: Maximum concentrated (live) load for connected T-beams

5.6.4. ULTIMATE BENDING MOMENT

FOR the calculation of the ultimate bending moment the T-beam cross-section includes the acting width of the integrated deck slab, see Appendix E Figure E.2. The difference in concrete compressive strength in the compression zone, between the T-beam and the integrated deck slab, is taken into account by reducing the acting width of the integrated deck slab by the ratio between the respective strengths (see Section 5.3 Table 5.1): $f_{\text{cm,slab}} / f_{\text{cm,T-beam}} = 60.3/87.7 = 0.688$. The integrated deck slab therefore has a fictitious acting width of: $0.688 \times 425 = 292$ mm. For both the prestressing tendons and the regular reinforcement, hardening is not taken into account and elasto-plastic stress-strain relationships are used with the average yielding strengths f_y given in Section 5.3 Table 5.2. In the analysis the load factor for the ultimate bending moment LF_{M_u} is determined by solving Equation 5.24 (for M_1 and M_2 see also Equation 5.23 Section 5.6.3). The maximum concentrated (live) load related to the ultimate bending moment $F_{\max,M_u}$ is then calculated by Equation 5.25, with a unit load of $F = 1000$ kN.

$$M_u = M_1 + LF_{M_u} M_2 \tag{5.24}$$

$$F_{\max,M_u} = LF_{M_u} \times F = LF_{M_u} \times 1000 \text{ [kN]} \tag{5.25}$$

The result of the analysis are shown in Figures 5.24–5.25, showing half the span length, and summarised in Table 5.9. The results of T-beam 5 are similar to those of T-beam 8 and are therefore not included in Figure 5.25. Due to symmetry, T-beam number 1 equals 15 and T-beam number 5 equals 11, see Table 5.9. In Figures 5.24b and 5.25 the x-axis is the control section and the y-axis gives the maximum concentrated (live) load irrespective of load location (procedure described in Section 5.6.1).

Table 5.9: Maximum concentrated (live) load for ultimate bending moment

	x	a	$F_{\max,M_u}$	Relative load capacity
	m	m	kN	%
Individual T-beam	12.0	12.0	662	100
Connected T-beam 1 (15)	5.4	5.4	2054	310
Connected T-beam 1 (15)	11.8	11.8	1818	275
Connected T-beam 5 (11)	4.2	4.2	3414	516
Connected T-beam 5 (11)	12.0	12.0	3193	482
Connected T-beam 8	4.0	4.0	3493	528
Connected T-beam 8	12.0	12.0	3415	516

For an individual, simply supported T-beam, the minimum value for the concentrated (live) load related to the ultimate bending moment is obviously much lower compared to the connected T-beams, by at least a factor of 2.8, see Table 5.9. The ratios are comparable to those found for the cracking moment (see Section 5.6.3 Table 5.8).

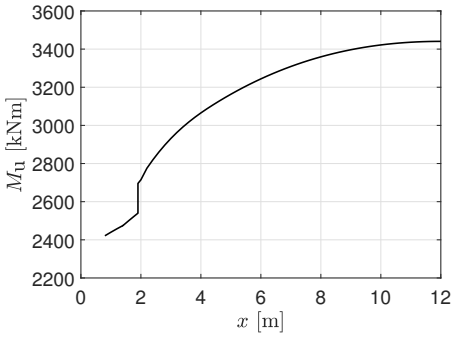

(a) Ultimate bending moment

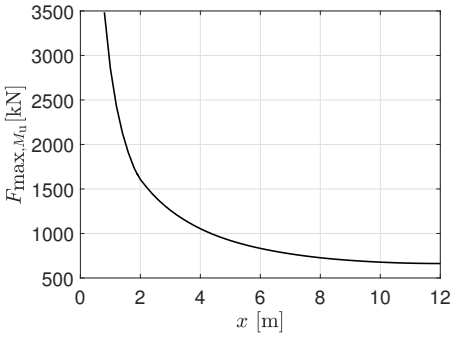

(b) Maximum concentrated (live) load for ultimate bending moment, individual T-beam

5

Figure 5.24: Ultimate bending moment (a) and maximum concentrated (live) load for individual, simply supported T-beam

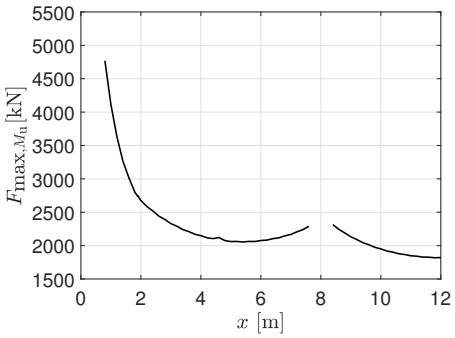

(a) Maximum concentrated (live) load for ultimate bending moment, T-beam 1 (15)

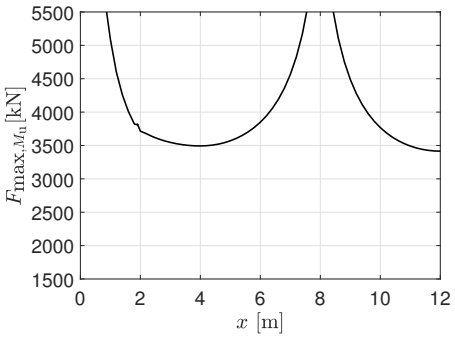

(b) Maximum concentrated (live) load for ultimate bending moment, T-beam 8

Figure 5.25: Maximum concentrated (live) load for connected T-beams

5.6.5. OVERALL VERIFICATION, SHEAR AND BENDING

THE overall verification of each control section consists of an evaluation of the flexural shear resistance, the shear tension resistance and the ultimate bending moment as treated in the previous sections. The shear tension resistance for the overall verification now includes a maximum principal stress at the bottom fibre in accordance with NEN-EN 1992-1-1 (NNI 2011a), see Section 5.6.3. To determine the overall governing load factor LF, for each combination of control section 'x' and load position 'a', the following rules are applied:

- The load factor for shear resistance, LF_{shear}, is determined by the maximum load factor for flexural shear ($LF_{V_{\text{FS}}}$) or shear tension ($LF_{V_{\text{ST}}}$).
- The overall governing load factor for shear and bending, LF, is determined as the minimum value for shear resistance (LF_{shear}) and the ultimate bending moment ($LF_{M_{\text{u}}}$).

The above described procedure is visualised in Figure 5.26. The maximum concentrated (live) load $F_{\max}$ for each control section 'x', is calculated by Equation 5.26, with a unit load of F =1000 kN.

$$F_{\max} = LF \times F = LF \times 1000 \text{ [kN]} \tag{5.26}$$

The results of the overall verification for an individual, simply supported T-beam as well as for the connected T-beams 1, 5 & 8 , are shown in Figures 5.27–5.30 and summarised in Table 5.10. Due to symmetry, T-beam number 1 equals 15 and T-beam number 5 equals 11, see Table 5.10. As stated in previous sections, combining the different cross-sectional verifications, especially for shear, is not straightforward. The governing control section(s) depend on the following factors:

- (Live) load distribution (individual versus connected T-beams);
- Varying sectional properties (regular T-beam versus end block and transition piece);
- Varying vertical positions of the draped prestressing tendons;
- Varying sectional forces as a result of the self-weight and prestressing;
- Combination of sectional forces, V, M and N for shear tension;
- Direct load transfer to the supports.

To demonstrate the effect of the procedure outlined in Figure 5.26, the control section at x = 8.4 m of the connected T-beam 1 is taken as an example, with the results of the cross-sectional verification given in Table 5.11. Considering all load positions, between a = 7.8–9.0 m, results in an overall governing, i.e. minimum, load factor of 1.085 (shear tension) with a position of the concentrated (live) load at 8.8 m. Note that with the concentrated (live) load at 8.6 m, the overall governing load factor is only marginally higher, at 1.088, and a different failure mode is found (flexural shear).

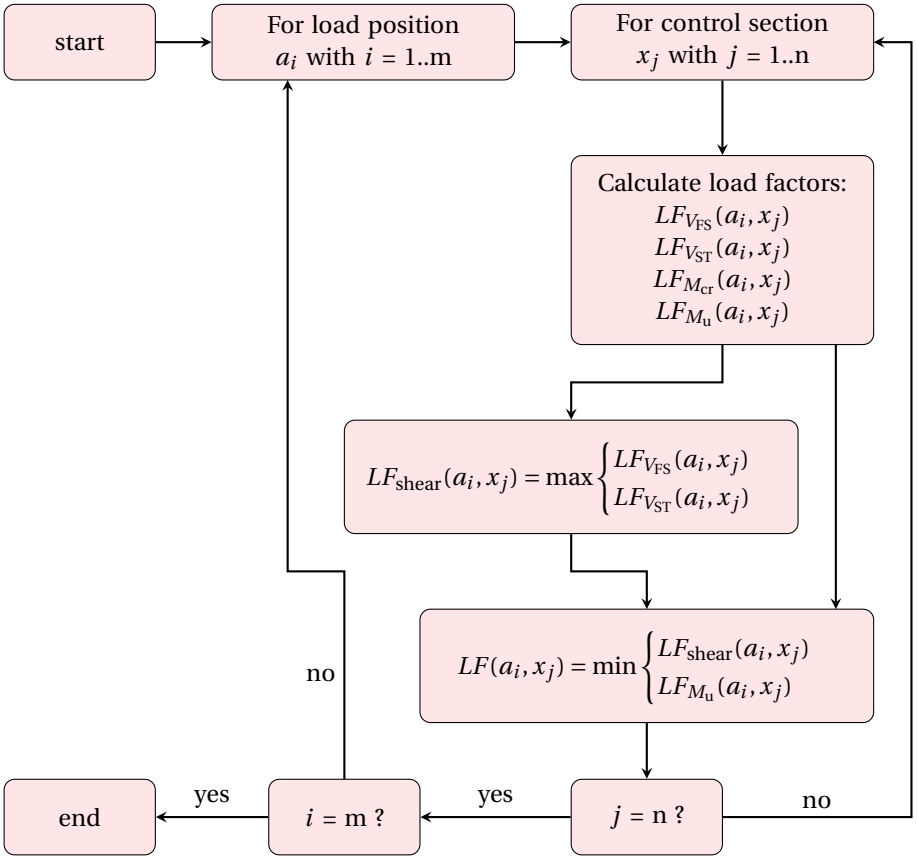

Figure 5.26: Flow chart for determining the overall governing load factor $LF(a_i, x_j)$

Table 5.10: Maximum concentrated (live) load overall verification

	x	a	Failure mode	F_{max}	Relative load capacity
	m	m		kN	%
Individual T-beam	3.4	3.4	V_{FS}	703	106
Individual T-beam	12.0	12.0	M_u	662	100
Connected T-beam 1 (15)	3.8	4.2	V_{ST}	1067	161
Connected T-beam 1 (15)	9.0	9.4	V_{FS}	995	150
Connected T-beam 5 (11)	1.4	1.8	V_{ST}	1652	250
Connected T-beam 5 (11)	8.4	8.8	V_{ST}	1416	214
Connected T-beam 8	1.4	1.8	V_{ST}	1659	251
Connected T-beam 8	8.4	8.8	V_{ST}	1424	215

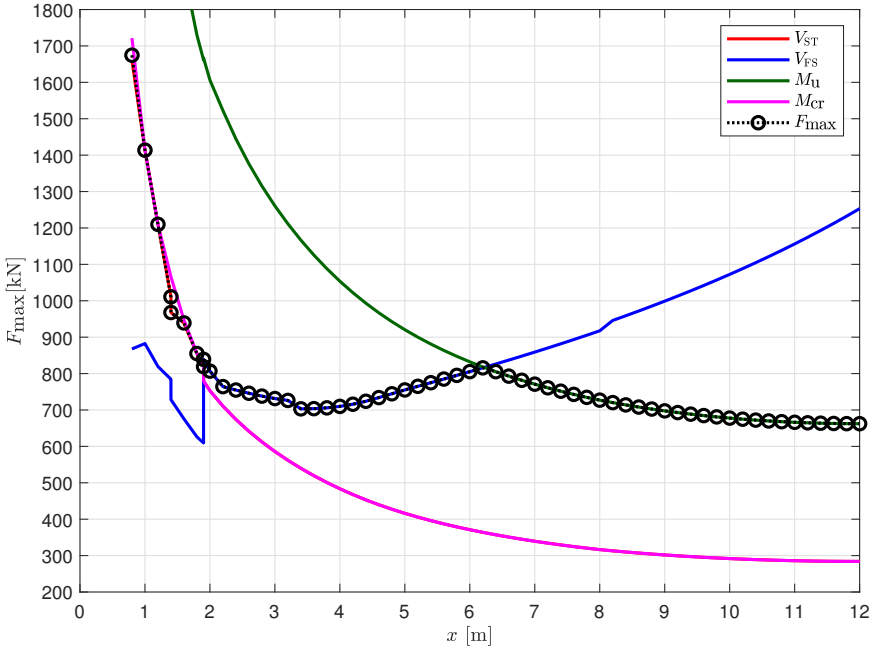

Figure 5.27: Overall verification individual, simply supported T-beam

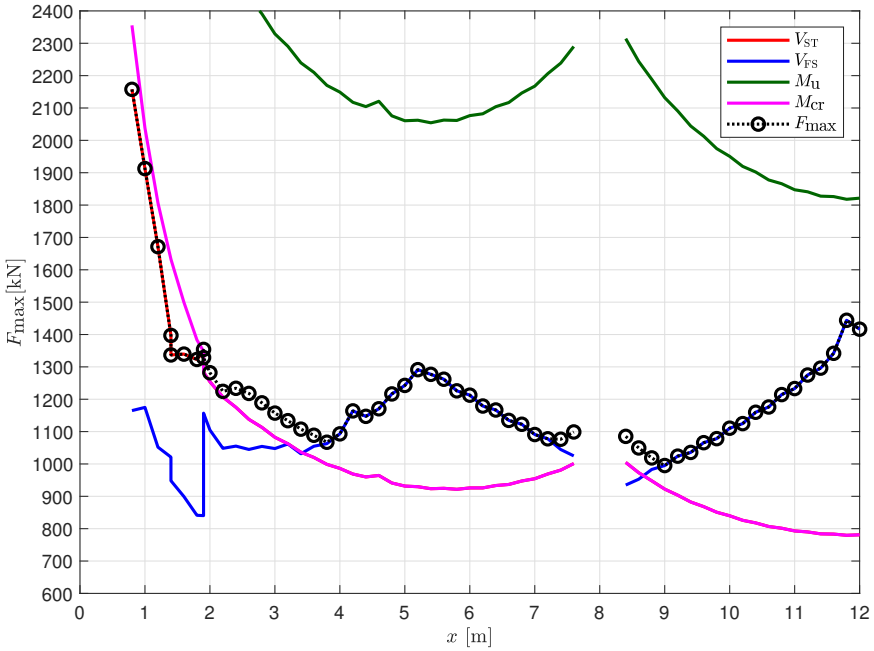

Figure 5.28: Overall verification T-beam 1 (15)

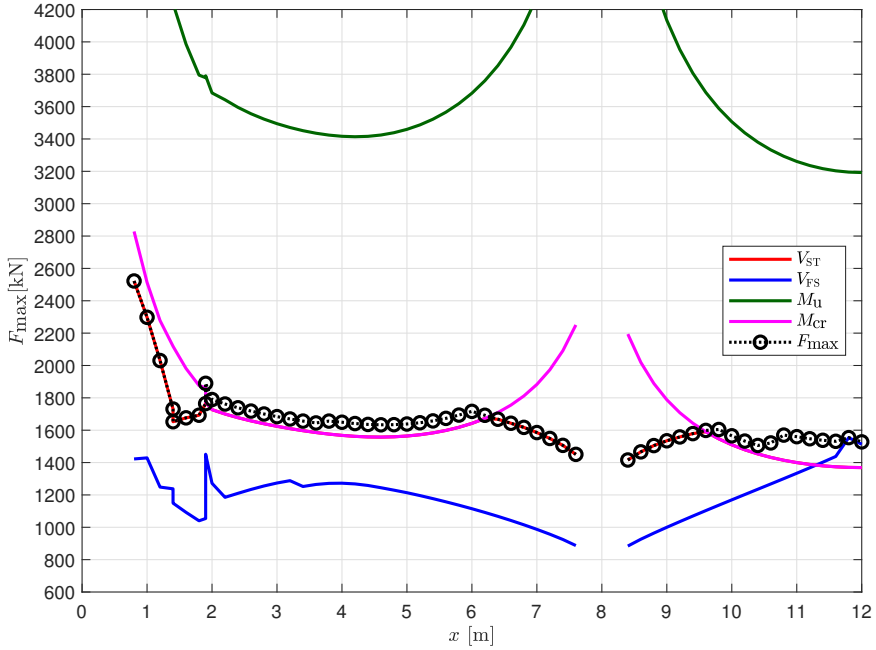

Figure 5.29: Overall verification T-beam 5 (11)

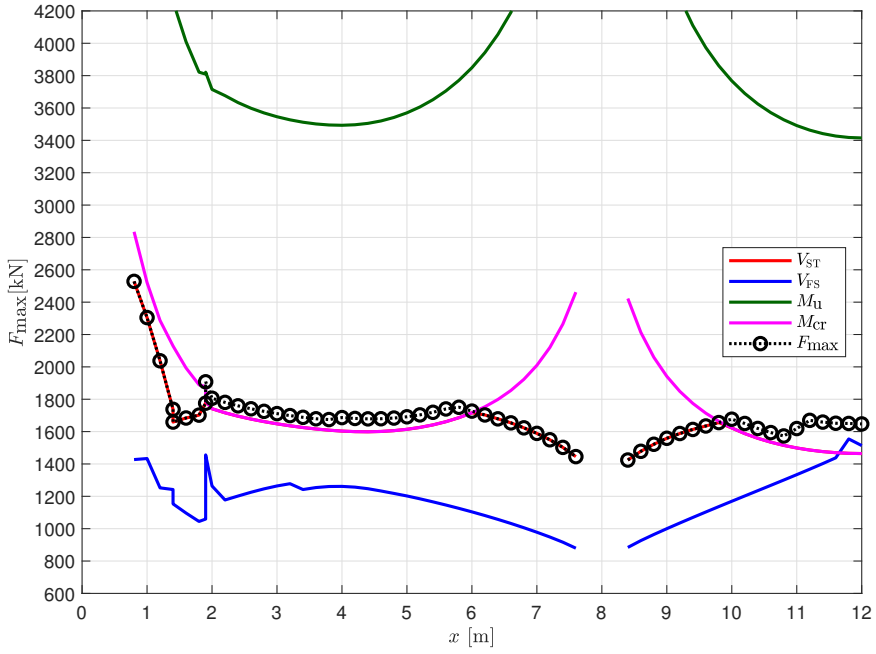

Figure 5.30: Overall verification T-beam 8

Table 5.11: Overall verification shear and bending at x = 8.4 m connected T-beam 1, F_{max} = 1085 kN (failure mode V_{ST} with a = 8.8 m) see also Figure 5.28

				a			
Load factor	7.8 m	8.0 m	8.2 m	8.4 m	8.6 m	8.8 m	9.0 m
$LF_{V_{FS}}$	3.025	2.791	5.113	2.740	1.088	0.935	0.972
$LF_{V_{ST}}$	1.157	1.096	1.035	1.005	1.029	**1.085**	1.142
$LF_{M_{cr}}$	1.157	1.096	1.035	1.005	1.029	1.085	1.142
LF_{M_u}	2.665	2.524	2.384	2.314	2.371	2.500	2.631
LF_{shear}	3.025	2.791	5.113	2.740	1.088	1.085	1.142
LF	2.665	2.524	2.384	2.314	1.088	1.085	1.142
Failure mode	M_u	M_u	M_u	M_u	V_{FS}	$\boldsymbol{V_{ST}}$	V_{ST}

5.6.6. SUMMARY AND CONCLUSION

THE results of the assessment based on linear analysis together with the main conclusions are summarised in this section.

Conclusions flexural shear:

- For an individual T-beam and connected T-beam 1, the governing control sections are close to the support starting from the end of the transition piece up until prestressing tendon 7, i.e. between x = 1.4–1.902 m.
- For connected T-beams 5 & 8, the governing control section(s) are close to the intermediate cross-beam.
- Close to the support, the increased width b_w ($x \leq 2.0$ m) as well as the effect of direct load transfer to the support ($x \leq 1.6$ m) result in a higher load capacity.
- Prestressing tendon 7, anchored in the top flange, in addition to increasing the compressive normal force, causes a high local counter-balancing shear force which results in a jump in load capacity at x = 1.902 m.
- For $F_{max,V_{FS}}$, the ratio between the connected T-beams and an individual, simply supported T-beam is between 1.4–1.5.
- For connected T-beams, in addition to control sections close to the support, governing control sections are also found close to the intermediate cross-beam. This becomes more apparent for T-beams closer to the centre of the bridge deck.
- Especially for beams with draped tendons, it is possible to maximise the flexural shear resistance $V_{Rm,c}$ by omitting (some) of the tendons to determine the effective depth d and other related parameters.

Conclusions shear tension:

- A maximum principal stress in the thin web is found more frequently in connected T-beams compared to an individual, simply supported, T-beam.
- For connected T-beams, in addition to control sections close to the support, governing control sections are also found close to the intermediate cross-beam. This becomes more apparent for T-beams closer to the centre of the bridge deck.

- For connected T-beams, theoretically, a maximum principal stress in the thin web can occur at a control section close to the end support with the load placed at relative large distance close to the intermediate cross-beam and vice versa. However, considering a movable load, for other load positions the control section will be cracked as a result of a much lower load in such cases, i.e. $F_{\max,M_{\mathrm{cr}}} << F_{\max,V_{\mathrm{ST}}}$.
- In the thin web the grouted ducts reduce the width of the cross-section, in this case from 180 mm to 159 mm, and therefore increase the shear stresses by 12%. Ignoring the influence of bending stresses in the thin web, the shear tension resistance is reduced by the same percentage.

Conclusions ultimate bending moment

- For connected T-beams, the governing control sections are at midpoint between the cross-beams.
- For $F_{\max,M_{\mathrm{u}}}$, the ratio between the connected T-beams and an individual, simply supported, T-beam is between 2.8–5.2.

Conclusions overall verification

- With the exception of connected T-beam 1, the governing failure mode for all connected T-beams is shear tension.
- For connected T-beams, the governing control section is not close to the support but close to the intermediate cross-beam at x = 8.4 m (T-beam 5 and 8) and x = 9.0 m (T-beam 1).
- The edge beam, i.e. T-beam 1, is much more sensitive to flexural shear compared to the other connected T-beams 5 and 8.
- For connected T-beams the ultimate bending moment is not governing at any location.
- For connected T-beams, the ratio between $F_{\max,M_{\mathrm{u}}}$ and $F_{\max}$, at governing control sections, is ≥ 2.
- For an individual, simply supported, T-beam, the governing failure mode is the ultimate bending moment at midpoint. However, $F_{\max,V_{\mathrm{FS}}}$ is within 6% of this value, with the corresponding control section and critical load position at $x = a$ = 3.4 m.
- For an individual T-beam, starting from the support, there is a rather smooth transition of the failure modes from shear tension, flexural shear to the ultimate bending moment.
- For $F_{\max}$, the ratio between the connected T-beams and an individual, simply supported, T-beam is between 1.5–2.2.

6

CASE STUDY: THE VECHT BRIDGE FULL-SCALE COLLAPSE TESTS

In this chapter the seven full-scale on-site collapse tests of the Vecht bridge are treated: three connected beam tests and four disconnected beam tests. The test preparations, the comprehensive loading system, the execution and used instrumentation are explained. The test results include a description of the failure mode, the measurement results and photos. A summary of the results and considerations for full-scale collapse tests are given in the final section.

Parts of this chapter have been published in (Ensink et al. 2018).

6.1. INTRODUCTION

THE case study of the Vecht bridge is split into three parts, and is treated in Chapters 5–7. For a detailed description of the Vecht bridge and its structural components the reader is referred to Chapter 5. In this Chapter the details and the results of the full-scale collapse tests are presented.

6.2. OVERVIEW OF THE EXPERIMENTS

IN total seven consecutive experiments are carried out on the Vecht bridge on two different spans of the southern bridge (see Chapter 5 Figure 5.3), see Table 6.1. Three of the experiments are carried out with the original structural system unchanged (tests 1–3), see Figure 6.1. These are referred to as the connected beam tests. In tests 1 and 2 at least four T-beams are present between the tested T-beam and the edge of the bridge. Therefore, in these tests a significant load distribution to the adjacent T-beams will take place. In four experiments (tests 4–7), the integrated deck slab is sawn in the longitudinal direction so that the individual T-beams can be tested, see Figure 6.2. These are referred to as the disconnected beam tests. As indicated in Figures 6.1–6.2, the loading consist of a single concentrated load at the centre of the T-beam, with dimensions 400 × 400 mm equal to a wheel load according to NEN-EN 1991-2 (NNI 2015). In order to compare the results of the disconnected beam tests to the connected beam tests, the same load positions are chosen. In both cases, two loading positions are selected, one at a = 2.25 m and the other at a = 4.00 m (distance from the centre of the support to the centre of the load). Prior to testing, the load position at 2.25 m is assumed to be governing for a (flexural) shear failure of the T-beam, as it is located beyond the transition piece and just beyond the anchorage of tendon 7 (see Chapter 5 Figure 5.6). However, according to the later executed and more detailed assessment (see Chapter 5 Section 5.6), the governing load position for flexural shear, in case of an individual T-beam, is at 3.40 m with negligible increase (≤ 1%) between 3.40–4.00 m (see Chapter 5 Figure 5.27). The second load position, at a = 4.00 m, is selected for studying arching effects, in case of connected T-beams, as it is centred exactly between the cross-beams.

Table 6.1: Overview of tests

test	span	a mm	a/d[a]	beam number	structural system	beam type
1	4	4000	4.8	11	unchanged	intermediate beam
2	4	2250	2.8	6	unchanged	intermediate beam
3	4	2250	2.8	1	unchanged	edge beam
4	2	2250	2.8	12	sawn	disconnected beam
5	2	2250	2.8	11	sawn	disconnected beam
6	2	2250	2.8	10	sawn	disconnected beam
7	2	4000	4.8	9	sawn	disconnected beam

[a] due to the draped prestressing tendons, the effective depth d is variable: at a = 2250 mm, d = 791 mm and at a = 4000 mm, d = 835 mm, see Chapter 5 Section 5.6.2

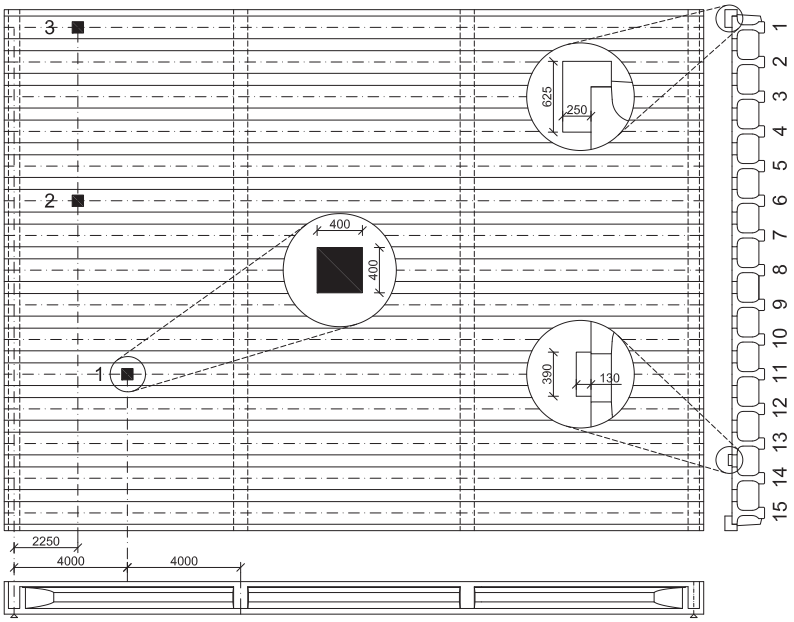

Figure 6.1: Connected beam tests 1–3, span 4, southern Vecht bridge showing details of loading plate, edge beam and barrier (measurements in mm)

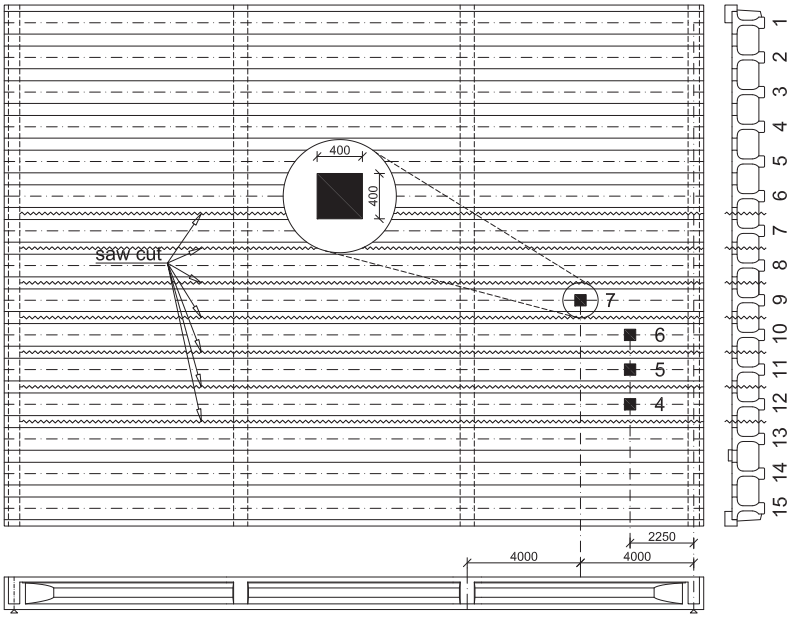

Figure 6.2: Disconnected beam tests 4–7 and locations of saw-cuts, span 2, southern Vecht bridge (measurements in mm)

6.3. TEST SETUP AND EXECUTION

6.3.1. ON-SITE PREPARATIONS

THE on-site test preparations started shortly after the highway A1 was rerouted to the south (see Chapter 5 Figure 5.2) and the Vecht bridge was decommissioned. First the asphalt on spans 2 and 4, between the expansion joints, is carefully removed by an asphalt ripper in such a way as to minimise damage to the concrete deck, see Figure 6.3. The concrete kerbs along the bridge edges, including the parapet on the south side, and the small kerb for the bicycle lane (between T-beams 13–14) are left in place; for the dimensions see Figure 6.1.

(a) Asphalt removed by asphalt ripper (span 4 is shown in the foreground, southern side is on the right)

(b) Expansion joint

Figure 6.3: Asphalt removed between the expansion joints

For the connected edge beam test (test 3, see Figure 6.1), the existing concrete kerb needed to be locally widened to have sufficient space for the loading plate, which is to be located at the centre of the T-beam. In addition, to prevent contact between the northern and southern bridge during testing, a part of the northern bridge kerb is sawn off to enlarge the gap between the two bridges (the covering of this gap by steel fences is visible in Figure 6.11b). The formwork and filling for the concrete widening of the edge beam kerb are shown in Figure 6.4. To limit the amount of fresh concrete needed on-site, the formwork is partially filled with concrete tiles. In preparation, a stack of concrete tiles is tested in compression in the laboratory at TU Delft, to ensure they have sufficient strength. The concrete mixture used on-site is a rapid hardening casting mortar.

For the disconnected beam tests on span 2, the integrated deck slab and three out of four cross-beams are sawn, see Figure 6.5. The saw cut is located at the centre of the integrated deck slab and is continued along the complete span length, with the exception of the end cross-beam opposite to the load location, see Figure 6.2. This is done for safety reasons, with the intention to keep the disconnected T-beams stable during testing, and to prevent unwanted friction forces. Otherwise, if all cross-beams are sawn, it is possible that the T-beam could tilt during testing and come into contact with the adjacent T-beam(s), as they are only separated by a narrow saw cut. Note that the bridge deck also has a slight transverse slope for dewatering (1:50), and therefore the T-beams

are already slightly tilted. The integrated deck slab is sawn from the topside using a concrete saw with a large blade that also penetrates part of the cross-beam (see Figure 6.5a). The remaining part of the cross-beam is then disconnected from underneath the bridge, using a combination of sawing and concrete cylinder drilling (see Figure 6.5b).

(a) Formwork

(b) Partially filling with concrete tiles

Figure 6.4: Local widening of the existing concrete kerb for the edge beam test (test 3, see Figure 6.1)

(a) Sawing through the integrated deck slab

(b) Sawing and cylinder drilling through the cross-beams

Figure 6.5: Sawing the integrated deck slab and the cross-beam(s) on span 4 for the disconnected beam tests

6.3.2. LOADING SYSTEM

THE complete loading system is shown in Figure 6.6 and consists of a 25 m long steel bridge with ballast placed on top. The load is applied by using a hydraulic jack positioned between the concrete deck and the steel bridge. Additionally, a sliding track is used to move the steel bridge transversely from one test location to the next. In this way, the time needed to change loading position is significantly reduced and, by utilizing two steel bridges (one for span 2, the other for span 4), the seven tests can be executed within one week. With the exception of the sliding track, the loading system is similar to those used in previous proof loading tests on existing bridges in the Netherlands; for more information see (Lantsoght et al. 2017a,b, Waarts et al. 2015). The steel bridge consists of two identical 'spreader beams', positioned side by side, composed of steel sections

(HEB600) creating a total width of 3 m, see Figure 6.7. For the ballast, standard crane ballast blocks are used, with each one weighing either 75 kN, 100 kN or 125 kN.

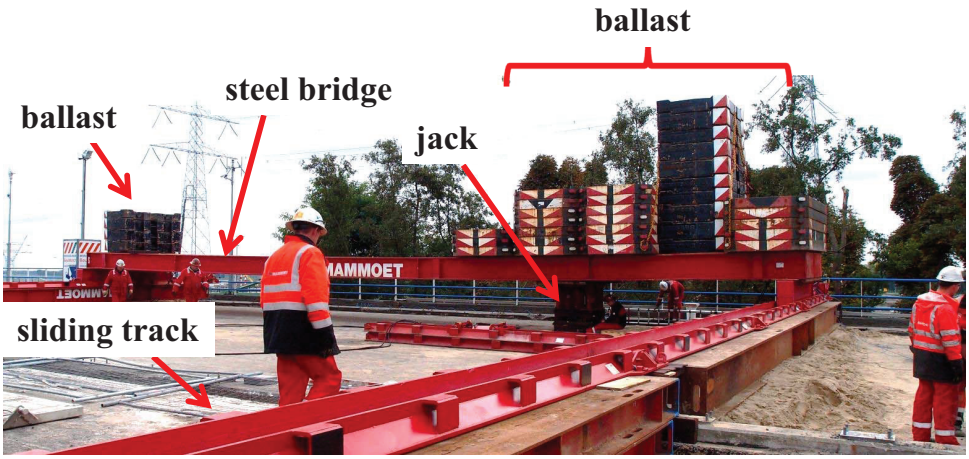

Figure 6.6: Loading system (test 1)

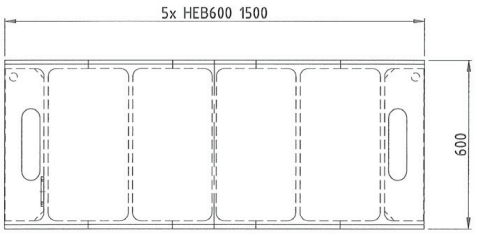

Figure 6.7: Single steel spreader beam cross-section (measurements in mm)

The supports of the steel bridge are positioned on a sliding track. This track consists of interconnected steel segments lined with teflon blocks, see Figure 6.8a. To move the steel bridge, a hydraulic jack is used, located inside each track, to push or pull it forward, see Figure 6.8b. The jack is directly connected to a support beam underneath the steel spreader beam(s). When moving the steel bridge, additional teflon spray is used to assist the sliding. For the connected beam tests, some of the ballast needs to be temporarily removed between the tests, to reduce the otherwise too high load on the sliding track and jack. In the single beam tests all ballast can remain while sliding.

The sliding track is supported by large rectangular steel beams ('loadspreader') placed on a sand filling, see Figures 6.6 and 6.9. The sand filling is needed to place the support beams exactly level, and to smooth out the irregular concrete deck surface, the slight transverse slope of the bridge deck (1:50), the remaining expansion joints (see Figure 6.3b), and the concrete kerbs (see Figure 6.1).

For the edge beam test, the sliding track needs to cross the gap between the northern and the southern bridge, see Figure 6.10. This gap is filled with smaller steel work and

(a) Sliding track lined with teflon blocks

(b) Detail of jack inside sliding track

Figure 6.8: Sliding track of steel bridge

Figure 6.9: Steel bridge support beam placed on sand filling

timber, placed on top of the kerbs, to keep the sliding track continuously supported. Note that the length of the steel bridge (25 m) is not sufficient to cross a full span of the concrete bridge and to locate both supports on the adjacent spans; this is further detailed in Sections 6.3.3 and 6.3.4.

The load is applied by a 6000 kN hydraulic jack (1180 × 1050 × 710 mm, dead weight: 23.3 kN), placed on top of the concrete deck and supported by jacking timbers (1000 × 100 × 100 mm), see Figure 6.11a. The extended jack is also visible in Section 6.3.4 Figure 6.17. The hydraulics and power generator needed to operate the jack are shown in Figure 6.11b. In addition to the required load capacity, the height dimension (710 mm) and the maximum stroke (250 mm) of the jack are also of importance. The height of the jack is restricted by the desire to limit the distance between the steel bridge and the concrete deck as much as possible. In addition, the stroke should be large enough in relation to the expected deformations of the concrete deck as well as the steel bridge. To distribute the load between the two spreader beams, a 60 mm thick steel plate with dimensions 3000 × 1500 mm (dead weight: 21.2 kN) is positioned between the jack and the steel spreader beams, see Figure 6.11a. To assist in all operations, two large 1000 kN cranes are positioned on the northern bridge, one for span 2, the other for span 4, see Figure 6.11b.

Figure 6.10: Steel bridge support beam(s) placed on sand filling and gap between the northern and the southern bridge filled with smaller steel work

(a) Hydraulic jack (6000 kN) and steel plate supported by jacking timbers

(b) Hydraulics for jack and power generator

Figure 6.11: Jack with hydraulics and power generator

6.3.3. LOADING SETUP CONNECTED T-BEAMS

THE loading setup for tests 1–3 is shown in Figures 6.12–6.13 (the same setup is used for tests 2–3). The initial support reaction forces of the steel bridge (prior to loading) are given in Table 6.2. The reaction forces of the steel bridge will spread through the support beam(s) and the sand fill, and will gradually decrease during the transfer of the load from the steel bridge to the concrete bridge by the hydraulic jack. The maximum possible force by the jack is limited by the requirement to prevent uplifting of the steel bridge supports, and can be readily determined from the initial support reactions, see Table 6.2. Due to the different types of ballast used, the height of the ballast stacks differs, to a maximum height of about 4 m. For safety reasons, the highest stacks are tied down to the adjacent stacks using tensioning chains.

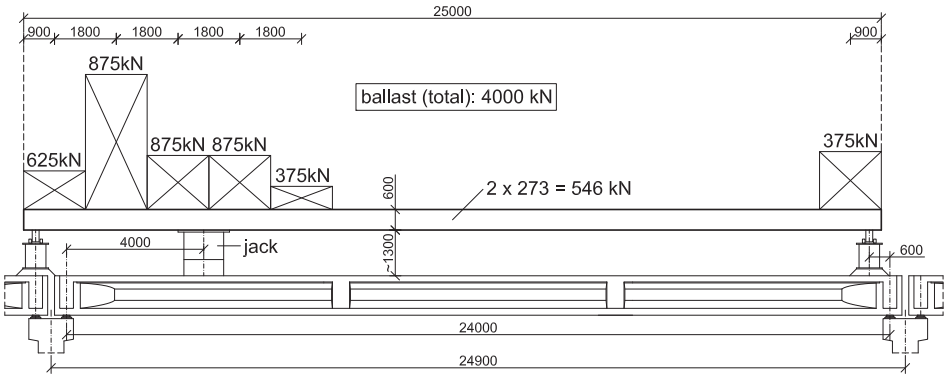

Figure 6.12: Loading setup test 1 (see also Figure 6.6) (measurements in mm)

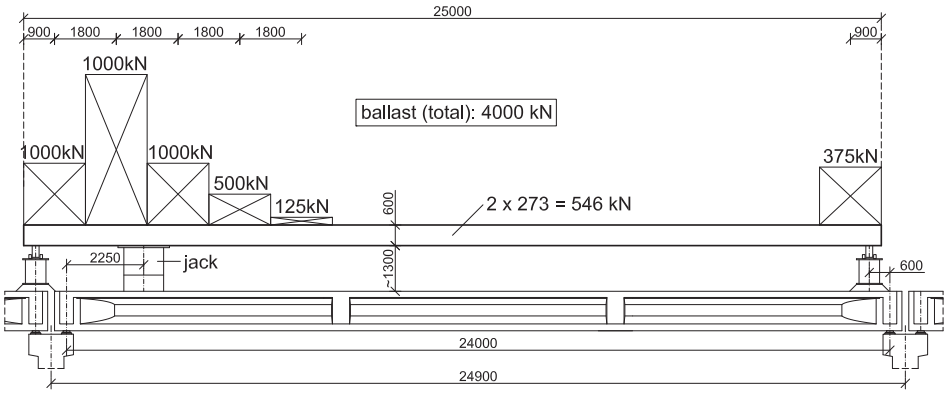

Figure 6.13: Loading setup test 2 and 3 (measurements in mm)

Table 6.2: Initial support reaction forces steel bridge and max. possible force jack, connected beam test 1–3

test	ballast (total) kN	steel bridge kN	total kN	support reaction 1 kN	support reaction 2 kN	max. force jack without support uplift (kN)
1	4000	546	4546	3324 (73%)	1222 (27%)	4164
2–3	4000	546	4546	3454 (76%)	1092 (24%)	3968

6.3.4. LOADING SETUP DISCONNECTED T-BEAMS

THE loading setup for test 4–7 is shown in Figures 6.14–6.15 (the same setup is used for tests 4–6). The initial support reaction forces of the steel bridge (prior to loading) are given in Table 6.3. The maximum possible load by the jack, as explained in the previous section, is also given in Table 6.3. The details of the sawing of the integrated deck slab and the cross-beams are given in Section 6.3.1. As a precaution, a safety system is put into place to prevent a disconnected beam falling to the ground below, see Figures

6.16–6.17. This system consists of two steel beams, a so called static steel beam ('S') and a dynamic steel beam ('D'), their positions are indicated in Figures 6.14–6.15. The purpose of the static steel beam is to support the T-beams after testing until the bridge is demolished. The purpose of the dynamic steel beam is to catch the tested T-beam should it break completely during testing. The connection between the steel and the concrete beams is accomplished by chains for which holes are drilled through the deck, see Figure 6.16. The chains connecting the concrete beam to the static steel beam are tensioned, whereas the dynamic steel beam chains are loosened so that, during testing, a maximum deflection of the concrete T-beam of 100 mm is allowed. However, in tests 4, 5 and 7 insufficient clearance is used and the chains needed to be adjusted during testing which also necessitates a partial or complete unloading before reloading. The supports of the static and dynamic steel beams are located beyond the tested beams (T-beams 9–12), see Figure 6.2 and Figure 6.17. Finally, to prevent damage, the jack itself is also connected to the steel bridge by using chains, see Figure 6.11a and Figure 6.17.

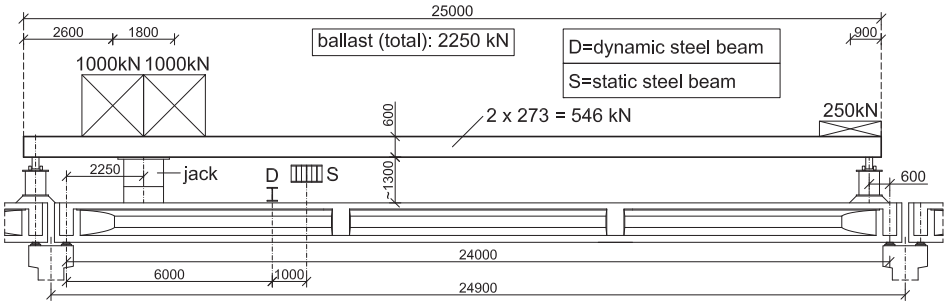

Figure 6.14: Loading setup test 4–6 (measurements in mm)

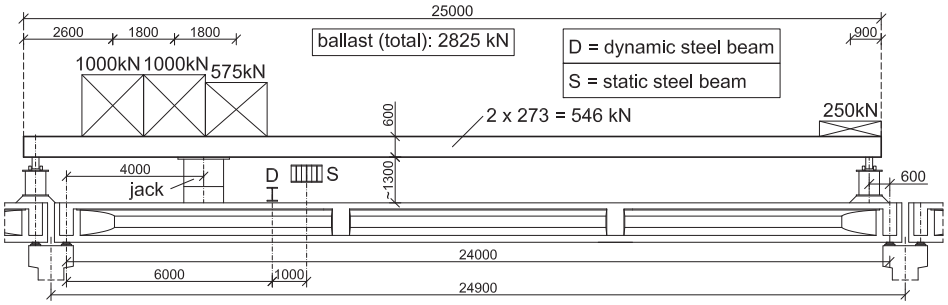

Figure 6.15: Loading setup test 7 (measurements in mm)

Table 6.3: Initial support reaction forces steel bridge and max. possible force jack, disconnected beam test 4–7

test	ballast (total) kN	steel bridge kN	total kN	support reaction 1 kN	support reaction 2 kN	max. force jack without support uplift (kN)
4–6	2250	546	2796	2019 (72%)	777 (28%)	2320
7	2825	546	3371	2456 (73%)	915 (27%)	3076

(a) Static steel beam with chains (top side)

(b) Chains around T-beams (bottom side)

Figure 6.16: Static steel beam with tensioned chains

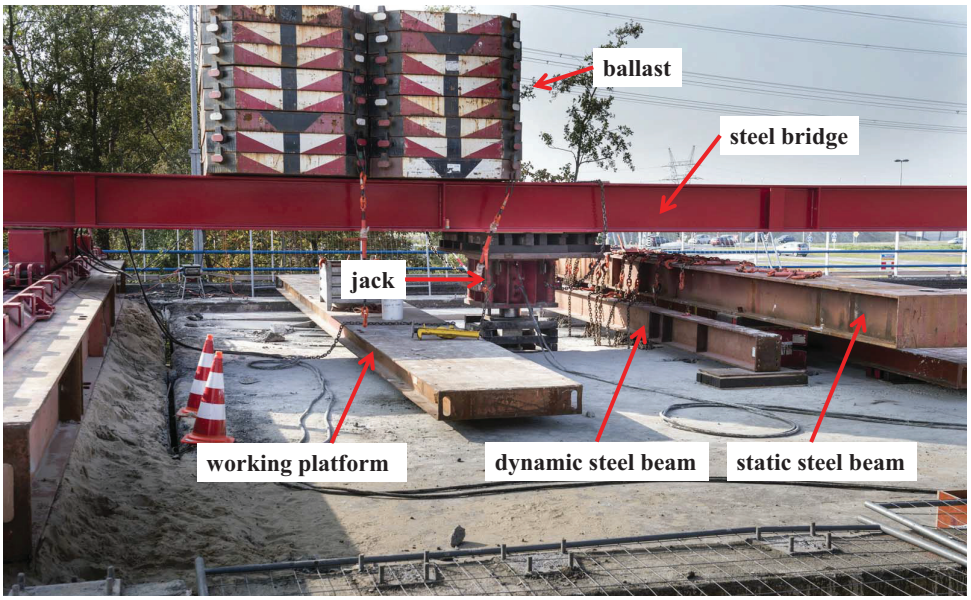

Figure 6.17: Safety and loading system disconnected beam tests

6.3.5. INSTRUMENTATION

THIS section summarises the instrumentation used for tests 1–7; more details can be found in the measurement report (Koekkoek 2017). All deformations are measured using linear potentiometers (LP). The sensor IDs and the measurements used in each test, including the measurement range for each sensor, are given in Tables 6.4–6.6. For the T-beam numbering and test locations, see also Figures 6.1–6.2. The typical sensor layout for the connected beam tests is shown in Figure 6.21, and for the disconnected beam tests in Figure 6.22.

The applied load is measured using a load cell which is positioned underneath the hydraulic jack, see Figure 6.18a. To equalise the surface and avoid stress concentrations, a thin layer of sand and a plywood plate are first placed on top of the concrete deck followed by a steel loading plate (400 × 400 mm) and the load cell, see Figure 6.18a. The gap between the top side of the load cell and the bottom of the jack is filled by a stack of steel blocks (not shown in Figure 6.18a).

The vertical deformations of the deck, at the position of the load and at the position of the intermediate cross-beam, are measured by sensors attached to aluminium frames positioned on the ground below the bridge, see Figure 6.19. In the connected beam tests, the vertical deformations of the adjacent beams (two on each side), at the position of the load and at the supports, are also measured, see Figures 6.19 and 6.20a. The deformations of the elastomeric bearings are measured using a sensor connected to the side face of the pier, see Figure 6.20a. The horizontal distance between the centre of the bearing and the sensor is 200 mm, see Figure 6.21. Therefore, this sensor will measure the vertical deformation of the bearing including the effect of its rotation. Since the deformations on the opposite side will be negligible, only the bearings on the loaded side of the span are measured.

In all tests, except test 5 and 6, a sensor is attached to the side face of the bottom flange of the T-beam, see Figure 6.18b and Figures 6.21–6.22. This sensor is located at the position of the load, to measure the displacement over a distance of 1 m (average longitudinal strain). The purpose of this sensor is to register when cracking occurs.

In test 1, additional sensors are placed to measure the relative vertical deformation of the integrated deck slab, see Figure 6.20b. These sensors are located on both sides of the loaded beam, at the positions indicated in Figure 6.21, and are also visible in Figure 6.19a.

(a) Load cell

(b) Average longitudinal strain (1 m) bottom flange T-beam

Figure 6.18: Load cell and average strain measurement

(a) Aluminium measurement frames (test 1)

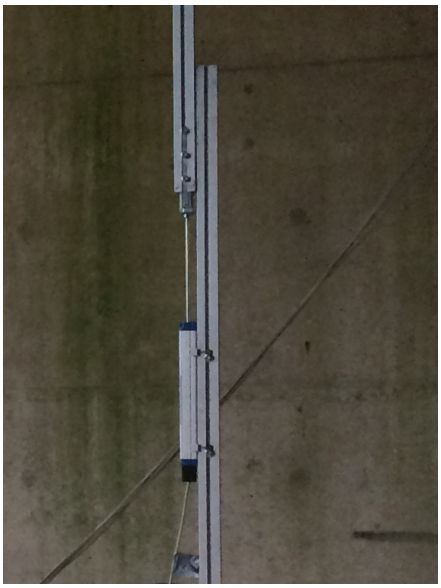

(b) Detail of LP sensor

Figure 6.19: Measurements of vertical deck deformations

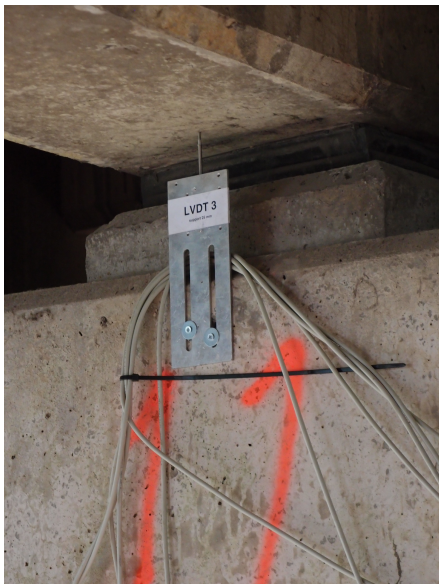

(a) Support deformation LP sensor

(b) Relative vertical slab deformation (loaded beam in the middle)

Figure 6.20: Measurements of support and relative vertical slab deformation

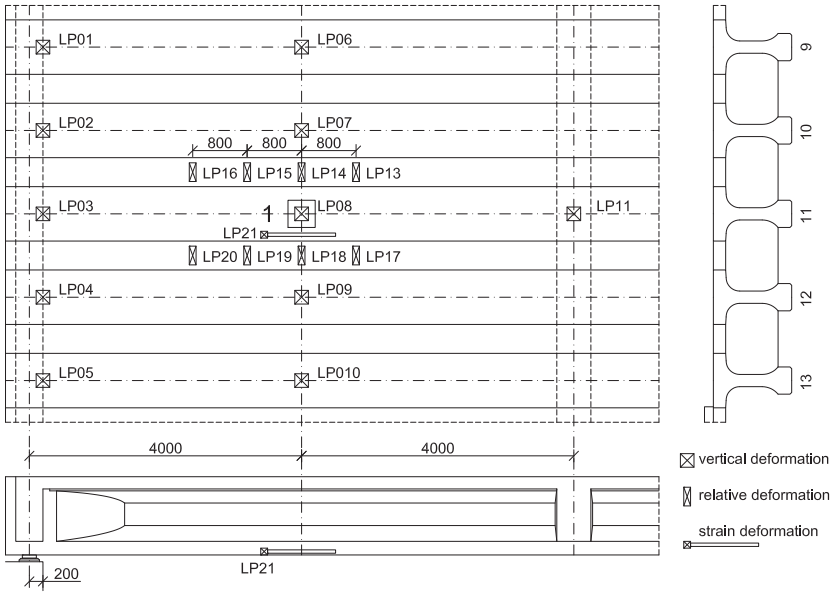

Figure 6.21: Sensor layout connected beam test 1 (span 4) (measurements in mm)

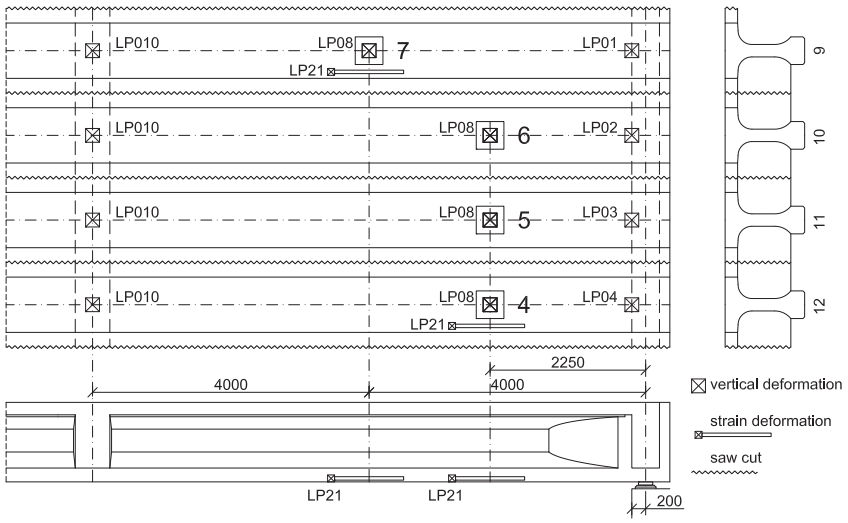

Figure 6.22: Sensor layout disconnected beam tests 4–7 (span 2) (measurements in mm)

Table 6.4: Measurements connected beam test 1–3

test 1	sensor ID	measurement	range
	F	applied load	0–5000 kN
	LP01–LP05	support deformation T-beam 9–13	0–25 mm
	LP06–LP10	vertical deformation T-beam 9–13	0–200 mm
	LP11	vertical deformation T-beam 11 at cross-beam	0–200 mm
	LP13–LP16	relative vertical slab deformation T-beam 10–11	0–25 mm
	LP17–LP20	relative vertical slab deformation T-beam 11–12	0–25 mm
	LP21	average longitudinal strain (1 m) T-beam 11	0–25 mm
test 2	sensor ID	measurement	range
	F	applied load	0–5000 kN
	LP01–LP05	support deformation T-beam 4–8	0–25 mm
	LP06–LP10	vertical deformation T-beam 4–8	0–200 mm
	LP11	vertical deformation T-beam 6 at cross-beam	0–200 mm
	LP12	average longitudinal strain (1 m) T-beam 6	0–25 mm
test 3	sensor ID	measurement	range
	F	applied load	0–5000 kN
	LP01–LP05	support deformation T-beam 1–5	0–25 mm
	LP06–LP10	vertical deformation T-beam 1–5	0–200 mm
	LP11	vertical deformation T-beam 1 at cross-beam	0–200 mm
	LP21	average longitudinal strain (1 m) T-beam 1	0–25 mm

Table 6.5: Measurements disconnected beam test 4–6

test 4	sensor ID	measurement	range
	F	applied load	0–5000 kN
	LP04	support deformation T-beam 12	0–25 mm
	LP08	vertical deformation T-beam 12	0–200 mm
	LP10	vertical deformation T-beam 12 at cross-beam	0–200 mm
	LP21	average longitudinal strain (1 m) T-beam 12	0–25 mm
test 5	sensor ID	measurement	range
	F	applied load	0–5000 kN
	LP03	support deformation T-beam 11	0–25 mm
	LP08	vertical deformation T-beam 11	0–200 mm
	LP10	vertical deformation T-beam 11 at cross-beam	0–200 mm
test 6	sensor ID	measurement	range
	F	applied load	0–5000 kN
	LP02	support deformation T-beam 10	0–25 mm
	LP08	vertical deformation T-beam 10	0–200 mm
	LP10	vertical deformation T-beam 10 at cross-beam	0–200 mm

Table 6.6: Measurements disconnected beam test 7

test 7	sensor ID	measurement	range
	F	applied load	0–5000 kN
	LP01	support deformation T-beam 9	0–25 mm
	LP08	vertical deformation T-beam 9	0–200 mm
	LP10	vertical deformation T-beam 9 at cross-beam	0–200 mm
	LP21	average longitudinal strain (1 m) T-beam 9	0–25 mm

In addition to the sensors, photo and video cameras together with LED lighting are fixed to the underside of the bridge deck, between the T-beams at the load position, see Figure 6.20b. Due to the close spacing of the T-beams, two video cameras are positioned side-by-side to cover a larger area. On the other side of the loaded beam, a third camera is used to continuously take photographs. To attach the equipment to the underside of the bridge deck a mobile manlift is utilised, see Figure 6.23.

Finally, a pilot radar interferometry measurement is used in tests 1 and 2, to investigate the possibility to replace contact measurements by non-contact measurements. With a radar station positioned on the ground below the bridge, see Figure 6.24, the vertical deformations of the deck are measured, at specific locations, by attaching reflectors to the underside of the deck. However, the radar measurements did not yield sufficiently accurate results and were only applied in tests 1–3. These will therefore not be treated further. More details about the radar interferometric system are given in the measurements report (Koekkoek 2017).

Figure 6.23: Use of mobile manlift (attaching equipment for test 1)

Figure 6.24: Interferometric radar station

6.3.6. PLANNING AND EXECUTION

To execute full-scale collapse tests on an existing bridge requires a significant amount of planning and preparation. However, as is the case with the Vecht bridge, and in many other cases a limited amount of time is available before testing (Bagge et al. 2018). In addition, because of the unique nature of the tests, unexpected challenges can arise during the execution. Some of the experiences from the Vecht bridge collapse tests in terms of planning and execution of the tests are summarised in this section for future reference.

Planning

For the full-scale collapse tests on the Vecht bridge, only four months were available for the planning and preparations before the actual testing took place in October 2016. Initially, individual T-beams were planned to be cut out and transported to the laboratory at TU Delft. However, this proved to be too expensive and it was therefore decided to perform all tests on-site. In total ten full-scale collapse tests were planned to be executed, four connected beam tests and six disconnected beam tests. Under normal circumstances 2–3 weeks would preferably be needed to perform all tests. However, as the Vecht bridge was part of a major infrastructural project, there would only be one week available for the execution of all tests. This time constraint resulted in the need to speed up the normal testing procedure, by utilizing two steel loading bridges that could be set up simultaneously, and to make use of sliding tracks to change their loading positions (see Section 6.3.2). In addition, by simplifying and/or limiting the amount of measurements, the time needed for each test could be further reduced. In this regard, the bridge deformations were planned to be measured by using an interferometric radar station.

Execution

For several reasons, the execution of ten tests in one week proved to be unfeasible. Due to a lack of experience with radar interferometry measurements, a second and more traditional backup system, with LP sensors, was also installed. In this way, it was also possible to compare the measurements between the two systems. This however meant additional sensor installation work for each test. In addition, attaching and/or positioning all the cameras, power and USB cables, LED lightning, LP sensors and radar reflectors proved to be much more time-consuming than originally thought. This was further complicated by the need to use mobile man lifts (see Figure 6.23) and by the fact that during the sliding of the steel bridge and ballast (see Figure 6.6), it was considered unsafe to work underneath the bridge deck. In addition, after a test had finished, the T-beam was generally severely damaged, and the sensors had to be carefully removed and checked. Also, it was considered unsafe to manoeuvrer the mobile man lift underneath the damaged area, and as a consequence it often needed to be repositioned. For three of the four disconnected beam tests, the safety system, designed to catch the T-beam using chains (see Figure 6.17), needed to be adjusted to allow for a larger deflection during testing. In the end, all these factors meant that three out of the ten tests planned were cancelled, i.e. two disconnected beam tests and one edge beam test, all at x = 4.00 m.

6.4. TEST RESULTS CONNECTED T-BEAMS

THE results of the connected beam tests 1–3 are summarised in Table 6.7 and the corresponding load versus deflection diagrams are given in Figure 6.25. The detailed results of tests 1–3 are given in Sections 6.4.1–6.4.3. For the sensor IDs of tests 1–3, see Table 6.4. The vertical deflection δ in Figure 6.25 is taken from sensor LP08.

Table 6.7: Results of tests 1–3: ultimate deflection (δ_u), ultimate load (F_u) and failure mode

test	a	a/d[a]	beam	δ_u	F_u	failure mode
	mm		number	mm	kN	
1	4000	4.8	11	21	3004	punching deck & shear T-beam
2	2250	2.8	6	14	3444	punching deck & shear T-beam
3	2250	2.8	1	11	2506	no failure (see Section 6.4.3)

[a] see also Table 6.1 Section 6.2

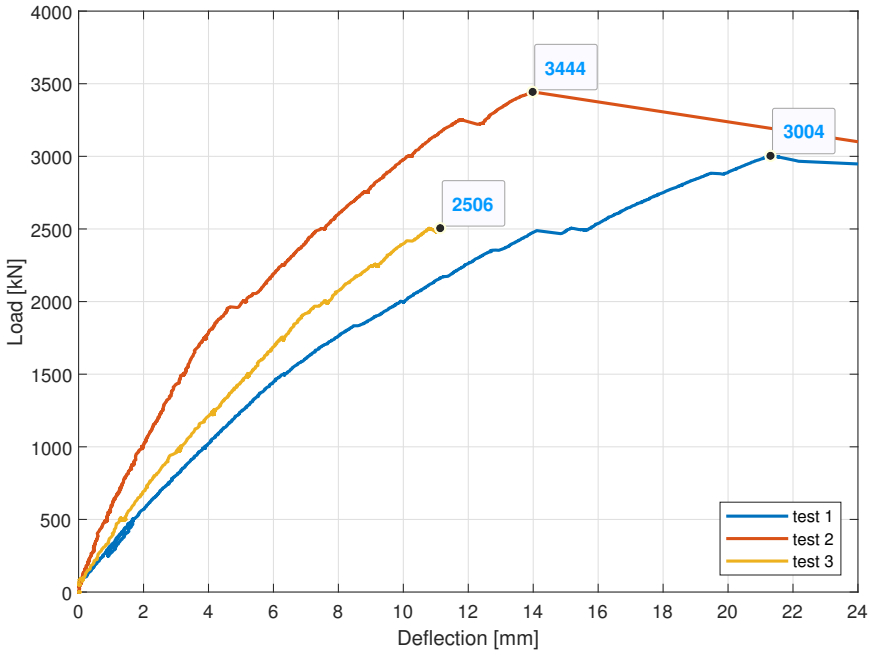

Figure 6.25: Load - deflection connected beam tests 1–3

The linear elastic deformations of the steel bridge, at the load position, are calculated from the loading setup, see Figures 6.12–6.13. The deformation $\delta_{sb,start}$ is the initial deformation of the steel bridge prior to loading the jack, as a result of its dead weight and ballast. The deformation $\delta_{sb,end}$ is the deformation with the jack pressing against the steel bridge, calculated from the force F_u reduced by the dead weight of the jack and the steel plate ($-23.3 - 21.2 =$ = -44.5 kN see Section 6.3.2). The total jack extension at fail-

ure (δ_{jack}) can then be determined as the sum of the deformation of the steel and the concrete bridge, see Equation 6.1 and Table 6.8.

$$\delta_{jack} = (\delta_{sb,start} - \delta_{sb,end}) + \delta_u \tag{6.1}$$

Table 6.8: Results of tests 1–3: steel bridge deformations, ultimate deflection and total jack extension

test	steel bridge deformations			δ_u	δ_{jack}[a]
	$\delta_{sb,start}$ mm	$\delta_{sb,end}$ mm	$\delta_{sb,start}$-$\delta_{sb,end}$ mm	mm	mm
1	115	12	103	21	124
2	67	9	58	14	72
3	67	25	42	14	56

[a] theoretical (minimum) value without tolerances for execution

6.4.1. TEST 1

THE results of test 1 are given in Figures 6.26–6.28. Note that the load measurement starts at 33 kN. In Figure 6.26a the support deformations show a linear behaviour. However, at a load of 2489 kN, a sudden change in deformation is observed, see Figure 6.26 and Figure 6.28a. A significant bending crack is first observed at a load of approximately 1500 kN, see Figure 6.28a. In Figure 6.27, the relative vertical slab deformations start to show some irregularities between a load of 1000–2000 kN. This is due to the position of the sensors (see Figure 6.20b), and is the result of concrete spalling from the integrated deck slab. The loading scheme for test 1 is shown in Figure 6.28b, with load increments of 500 kN used until failure. Test 1 results in a shear failure of the T-beam, see Figure 6.29. However, the shear failure of the T-beam is preceded by a punching failure of the deck. The punching perimeter on the top side is shown in Figure 6.30a and is just slightly larger than the loading plate (400 × 400 mm). The punching perimeter on the bottom side extends to the full width of the integrated deck slab on both sides of the loaded beam, see Figure 6.30b. As a consequence of the punching failure the load transfer to the adjacent T-beams is largely lost, and the punching failure is immediately followed by a shear failure of the T-beam. Note that the web is severely damaged, and that the prestressing tendons are visible. The centre of the severely damaged web is located approximately 1 m from the load position towards the end support (estimated from photos). In addition to shear cracks towards the end support, a single large shear crack is also observed in the opposite direction towards the intermediate cross-beam, see Figure 6.31 (also visible in Figure 6.29). Prior to failure, the video and photos show a larger opening of the shear cracks compared to the bending cracks (not measured).

6.4.2. TEST 2

THE results of test 2 are given in Figures 6.32–6.33. In Figure 6.32a the support deformations of the adjacent T-beams show a linear behaviour, whereas the support deformation of the loaded T-beam, starting from a load of approximately 2000 kN, shows

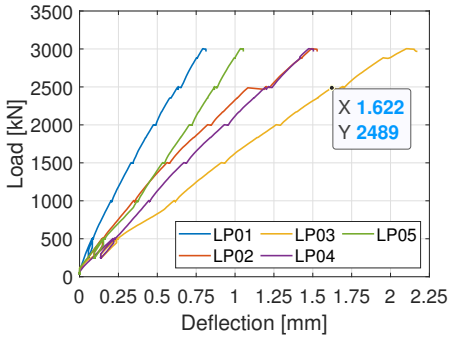

(a) Support deformations: LP01-05

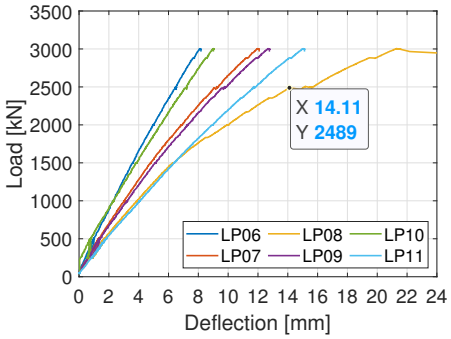

(b) T-beam deformations: LP06-11

Figure 6.26: Connected beam test 1: support and T-beam deformations

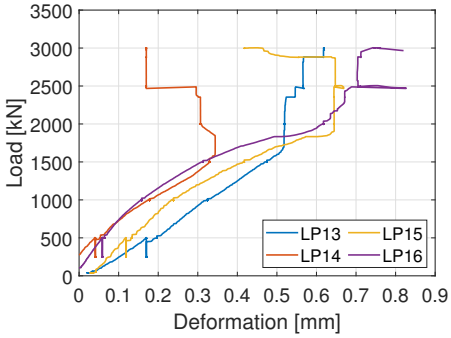

(a) Relative deformations: LP13-16

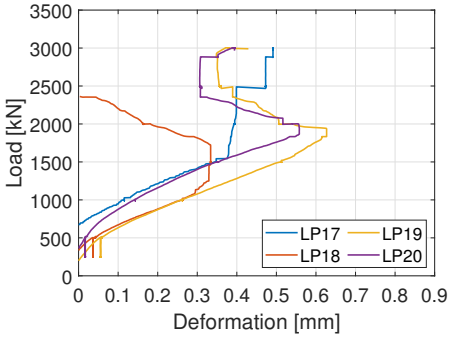

(b) Relative deformations: LP17-20

Figure 6.27: Connected beam test 1: relative deformations integrated deck slab

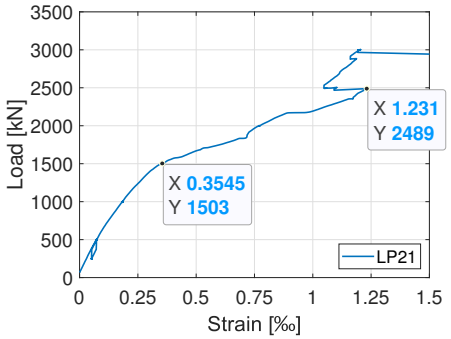

(a) Average longitudinal strain: LP21

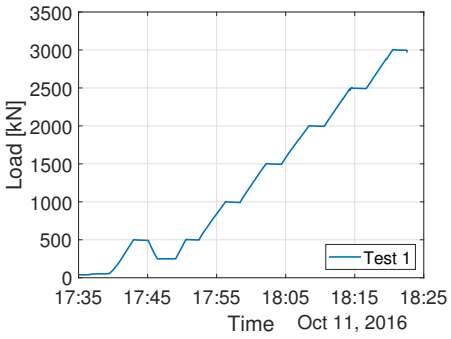

(b) Loading scheme

Figure 6.28: Connected beam test 1: average strain and loading scheme

Figure 6.29: Shear failure T-beam test 1 (intermediate cross-beam on the left side, end support on the right side)

(a) Punching failure top side (measurements in cm)

(b) Punching failure bottom side

Figure 6.30: Punching failure deck slab test 1

(a) Shear cracks towards end support

(b) Shear crack towards intermediate cross-beam

Figure 6.31: Shear cracks towards end support and intermediate cross-beam T-beam test 1

a highly nonlinear behaviour. A bending crack is first observed at a load of approximately 1800 kN, see Figure 6.33a. The loading scheme for test 2 is shown in Figure 6.33b, with initial load increments of 500 kN, followed by load increments of 250 kN until failure. Similar to test 1, test 2 results in a shear failure of the T-beam, see Figure 6.34. However, the shear failure of the T-beam is again preceded by a punching failure of the deck. The punching perimeter on the top side is just slightly larger than the loading plate (400 × 400 mm). The punching perimeter on the bottom side extends over the full width of the integrated deck slab on both sides of the loaded beam, see Figure 6.35. The centre of the severely damaged web is located approximately 1 m from the load position towards the end support (estimated from photos). Similar to test 1, a single large shear crack is observed in the opposite direction towards the intermediate cross-beam, see Figure 6.34. Finally, a torsion crack is observed in the end cross-beam, between T-beam 6 and 7, see Figure 6.35. Prior to failure, the video and photos show a larger opening of the shear cracks compared to the bending cracks (not measured).

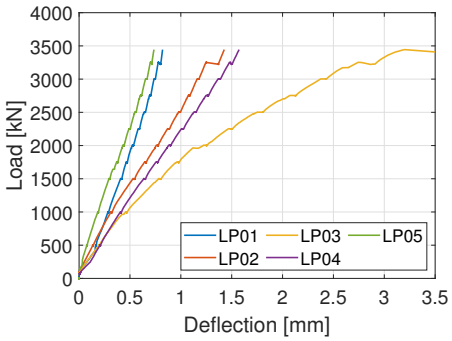

(a) Support deformations: LP01-05

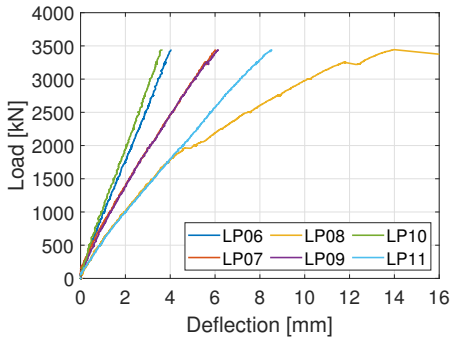

(b) T-beam deformations: LP06-11

Figure 6.32: Connected beam test 2: support and T-beam deformations

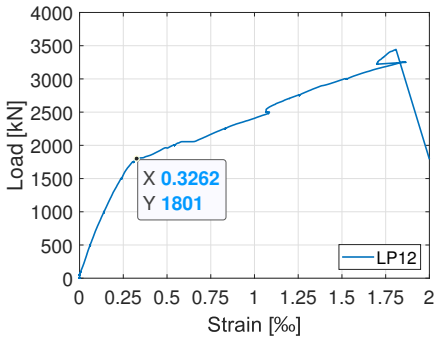

(a) Average longitudinal strain: LP12

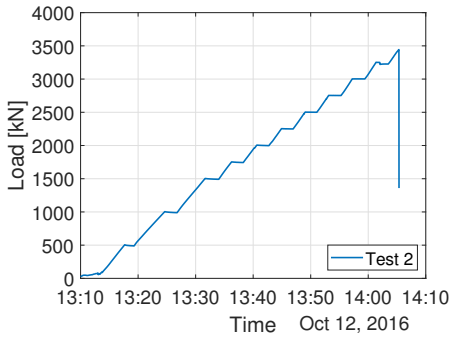

(b) Loading scheme

Figure 6.33: Connected beam test 2: average strain and loading scheme

Figure 6.34: Shear failure T-beam test 2 (intermediate cross-beam on the left side, end support on the right side)

Figure 6.35: Punching failure deck slab and shear failure T-beam test 2, torsion crack end cross-beam (between T-beam 6 and 7)

6.4.3. TEST 3

THE results of test 3 are given in Figures 6.36–6.37. Because of safety concerns, the edge beam is not loaded beyond 2506 kN which did not result in a failure of the deck or the T-beam. The loading scheme for test 3 is shown in Figure 6.37b, with initial load increments of 500 kN, followed by load increments of 250 kN. The edge beam has an increased stiffness due to the presence of the concrete kerb (see Figure 6.1 and Figure 6.4). However, the edge beam deformations are still higher compared to test 2, see Figure 6.25. A bending crack is first observed at a load of approximately 1900 kN, see Figure 6.37a. The final photo also shows a small shear crack, in the web near the bottom flange, from the load position to the end support.

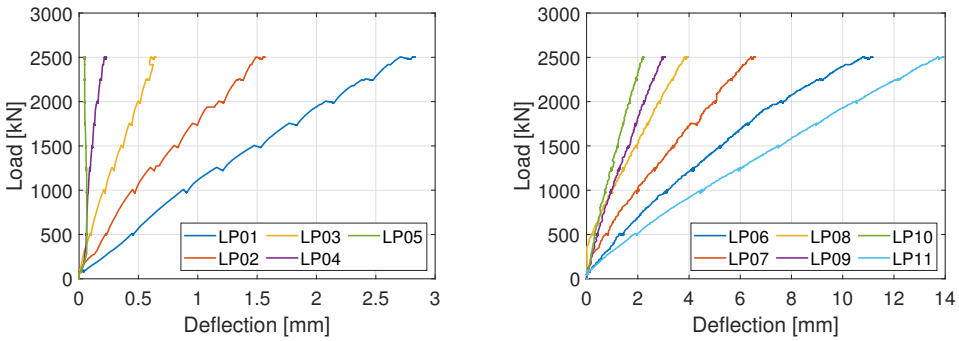

(a) Support deformations: LP01-05

(b) T-beam deformations: LP06-11

Figure 6.36: Connected beam test 3: support and T-beam deformations

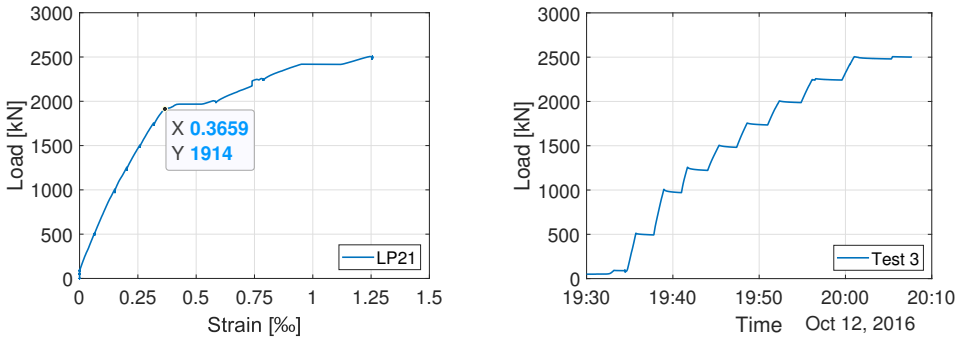

(a) Average longitudinal strain: LP21

(b) Loading scheme

Figure 6.37: Connected beam test 3: average strain and loading scheme

6.5. TEST RESULTS DISCONNECTED T-BEAMS

THE results of the disconnected beam tests 4–7 are summarised in Table 6.9 and the corresponding load versus deflection diagrams are given in Figure 6.38. Note that for clarity, the unloading branches in tests 4, 5 and 7 are omitted in Figure 6.38. The detailed results of tests 4–7, including the unloading branches, are given in the Sections 6.5.1–6.5.4. For the sensor IDs of tests 4–7 see Tables 6.5–6.6. The vertical deflection δ in Figure 6.38 is taken from sensor LP08. Note that in the tests with unloading, the reloading branches reconnect with the previous loading branches with only marginal deviations. The scatter in the ultimate load F_u in tests 4–6, with equal a/d, is approximately 6%.

Table 6.9: Results of tests 4–7: ultimate deflection (δ_u), ultimate load (F_u) and failure mode

test	a	a/d[a]	beam	δ_u	F_u	failure mode
	mm		number	mm	kN	
4	2250	2.8	12	79	1678	flexural shear T-beam
5	2250	2.8	11	65	1703	flexural shear T-beam
6	2250	2.8	10	74	1774	flexural shear T-beam
7	4000	4.8	9	132	1022	flexural shear T-beam

[a] see also Table 6.1 Section 6.2

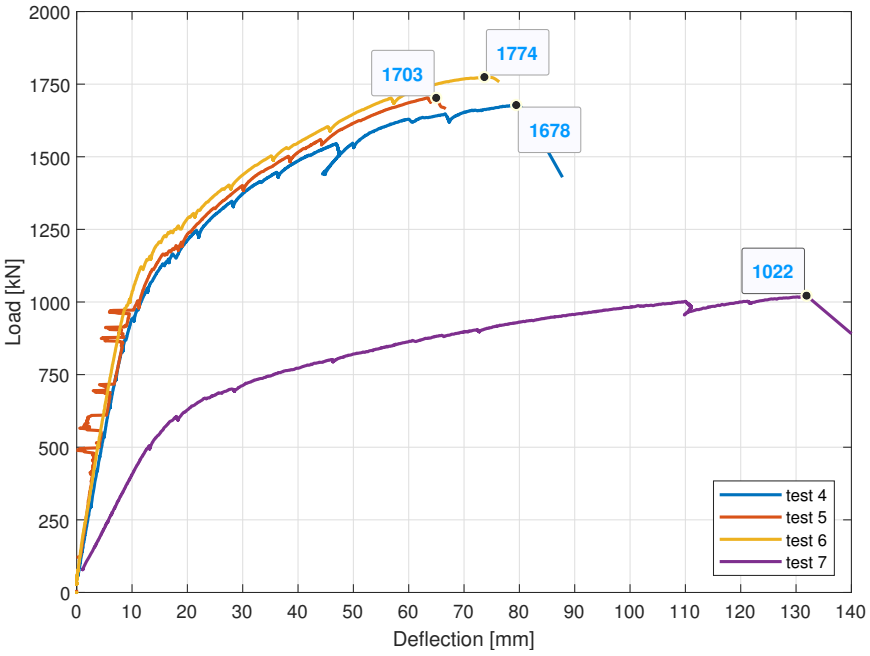

Figure 6.38: Load - deflection disconnected beam tests 4–7

The calculated linear elastic deformations of the steel bridge and the total jack extension

at failure for tests 4–7 are given in Table 6.10. The definitions of $\delta_{sb,start}$, $\delta_{sb,end}$ and δ_{jack} are explained in Section 6.4.

Table 6.10: Results of tests 4–7: steel bridge deformations, ultimate deflection and total jack extension

test	steel bridge deformations			δ_u	δ_{jack}[a]
	$\delta_{sb,start}$ mm	$\delta_{sb,end}$ mm	$\delta_{sb,start}$-$\delta_{sb,end}$ mm	mm	mm
4	46	17	29	79	108
5	46	17	29	65	94
6	46	16	30	74	104
7	88	54	34	132	166

[a] theoretical (minimum) value without tolerances for execution

6.5.1. TEST 4

THE results of test 4 are given in Figures 6.41–6.42. Note that at a load of 1546 kN an unloading to 294 kN is applied to adjust the safety chains (see Section 6.3.4). In Figure 6.41a the support deformation shows a highly nonlinear behaviour. A bending crack is first observed at a load of approximately 871 kN, see Figure 6.42a. The loading scheme for test 4 is shown in Figure 6.42b, with initial load increments of 250 kN, followed by load increments of 100 kN. After the unloading, the load is again increased without interruption to 1348 kN, followed by load increments of 100 kN until failure. Test 4 results in a flexural shear failure of the T-beam, see Figure 6.39. Due to the close proximity of tendon 7 in the top flange (see Chapter 5 Figure 5.6), the unreinforced concrete filling at the anchorage is broken out, see Figure 6.40. This occurred in all tests with the load position at 2.25 m, i.e. tests 4–6. Prior to failure, the video and photos show comparable widths of the shear and bending cracks (not measured).

6.5.2. TEST 5

THE results of test 5 are given in Figure 6.43 and Figure 6.44a. Note that at a load of 1559 kN an unloading to 232 kN is applied to adjust the safety chains (see Section 6.3.4). In Figure 6.43a, the support deformation shows a highly nonlinear behaviour, and does not appear to unload correctly as it remains more or less constant during the initial unloading phase. During this test unused sensors were lying in the water that caused voltage fluctuations in the measurement of LP08 and LP10, see Figure 6.43. The unused sensors were subsequently unplugged solving the problem for LP08, but LP10 remained unstable. Therefore, the measurement of LP10 is only plotted to a load of 910 kN. The loading scheme is shown in Figure 6.44a, with initial load increments of 1000 kN, 200 kN and 100 kN. After the unloading, the load is again increased without interruption to 1203 kN, followed by load increments of 200 kN and 100 kN until failure. Test 5 resulted in a flexural shear failure of the T-beam, see Figure 6.39. In tests 4–6, the unreinforced concrete filling at the anchorage of tendon 7 broke out, see Section 6.5.1 and Figure 6.40.

Figure 6.39: Flexural shear failure T-beam test 4 (top) and test 5 (bottom)

Figure 6.40: Broken out unreinforced concrete filling at anchorage of tendon 7 in tests 4–6 (see Chapter 5 Figure 5.6). View towards span, the load position is just visible at the top side of the photo

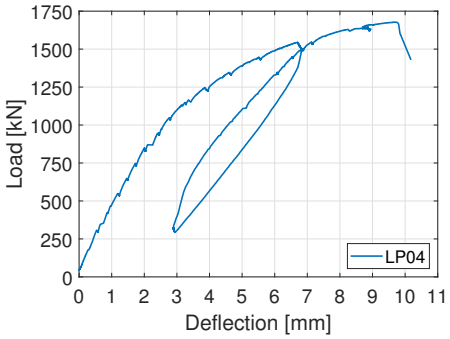

(a) Support deformations: LP04

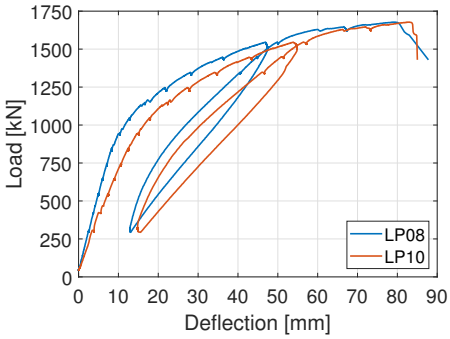

(b) T-beam deformations: LP08, LP10

Figure 6.41: Disconnected beam test 4: support and T-beam deformations

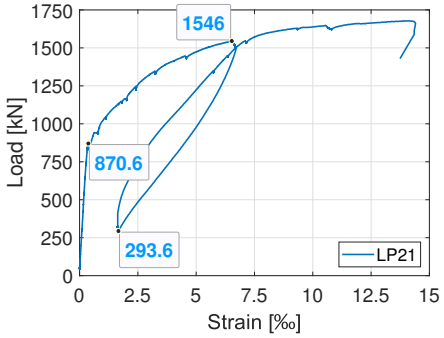

(a) Average longitudinal strain: LP21

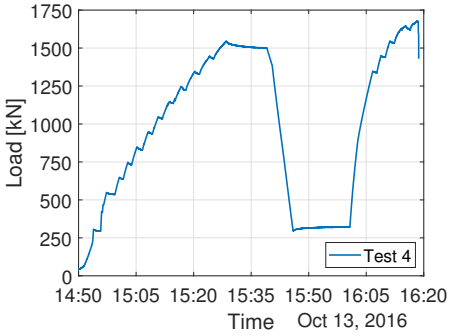

(b) Loading scheme

Figure 6.42: Disconnected beam test 4: average strain and loading scheme

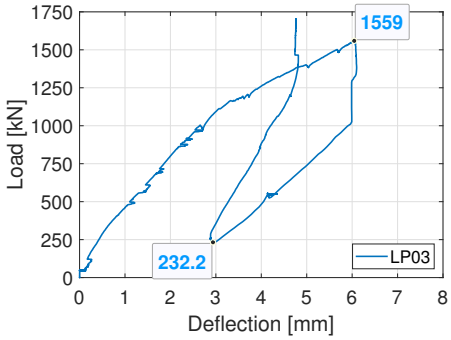

(a) Support deformations: LP03

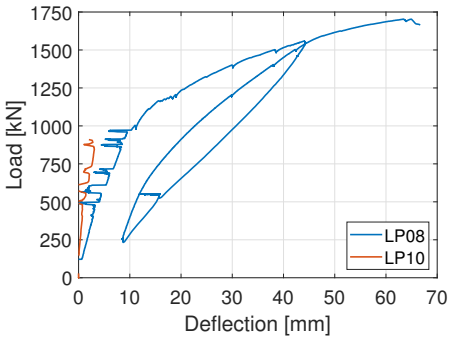

(b) T-beam deformations: LP08, LP10

Figure 6.43: Disconnected beam test 5: support and T-beam deformations

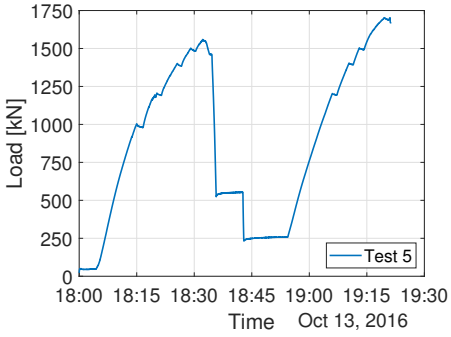

(a) Loading scheme test 5

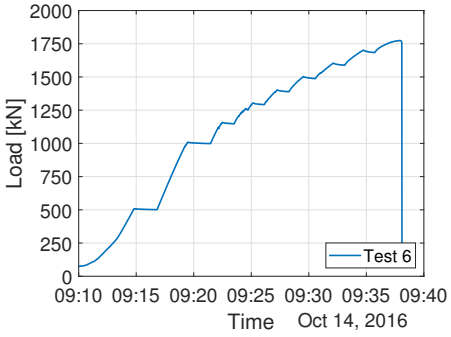

(b) Loading scheme test 6

Figure 6.44: Disconnected beam tests 5–6: loading scheme

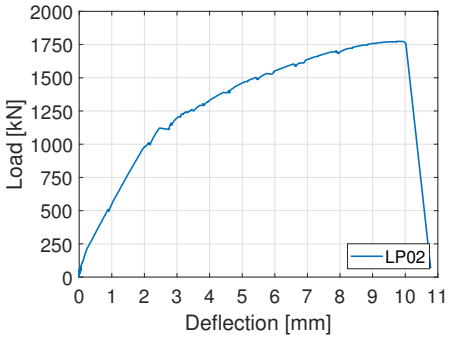

(a) Support deformations: LP02

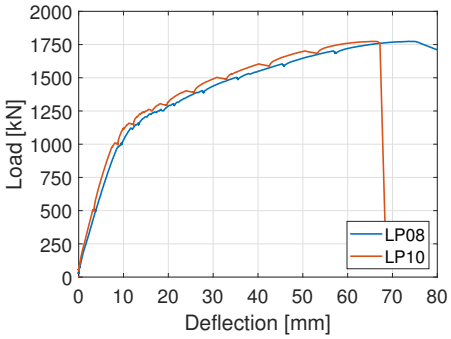

(b) T-beam deformations: LP08, LP10

Figure 6.45: Disconnected beam test 6: support and T-beam deformations

6.5.3. TEST 6

THE results of test 6 are given in Figure 6.44b and Figure 6.45. In Figure 6.45a, the support deformation shows a highly nonlinear behaviour. The loading scheme for test 6 is shown in Figure 6.44b, with initial load increments of 500 kN, followed by load increments of 150 kN and 100 kN until failure. Test 6 results in a flexural shear failure of the T-beam, similar to tests 4 and 5, see Figure 6.46. In tests 4–6, the unreinforced concrete filling at the anchorage of tendon 7 broke out, see Section 6.5.1 and Figure 6.40. Prior to failure, the photos show comparable widths of the shear and bending cracks (not measured).

6.5.4. TEST 7

THE results of test 7 are given in Figures 6.48–6.49. Note that the load measurement starts at 78 kN and that at a load of 1002 kN a complete unloading is applied to adjust the safety chains (see Section 6.3.4). In tests 4 and 5, the load is not reduced to zero

since the safety chains are adjusted from the top side. However, in test 7 the safety chains needed to be adjusted from underneath the bridge deck, using a mobile manlift (see Section 6.3.5 Figure 6.23), and therefore the load had to be completely removed. In Figure 6.48a, the support deformation shows a highly nonlinear behaviour. A bending crack is first observed at a load of approximately 505 kN, see Figure 6.49a. The loading scheme for test 7 is shown in Figure 6.49b, with an initial load increment of 500 kN, followed by load increments of 100 kN. After the unloading, the load is again increased in two steps of 450 kN, followed by load increments of 100 kN until failure.

Figure 6.46: Flexural shear failure T-beam test 6 (top) and test 7 (bottom)

(a) Detail of shear crack (view towards span)

(b) Support uplift and shift

Figure 6.47: Shear fracture and support uplift T-beam test 7

Test 7 results in a flexural shear failure of the T-beam, see Figure 6.46. In this test the T-beam almost completely separated into two parts being kept together only by the prestressing tendons, see also Figure 6.47a. Prior to failure, the video shows multiple shear

and bending cracks (not measured). Post failure, an uplift and shift of the elastomeric bearing is observed, see Figure 6.47b. In addition, a torsion crack is observed in the end cross-beam on the opposite side. Note that this end cross-beam is not sawn, see Section 6.3.1.

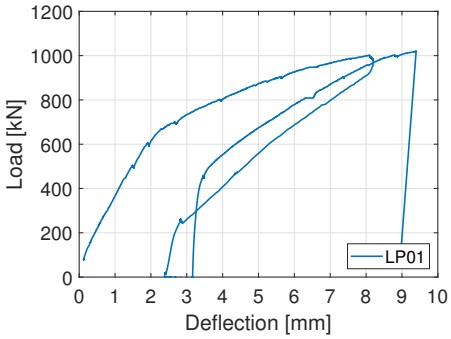

(a) Support deformations: LP01

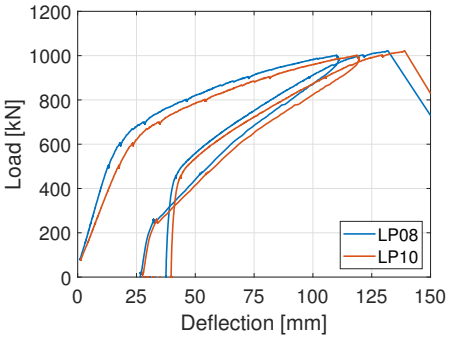

(b) T-beam deformations: LP08, LP10

Figure 6.48: Disconnected beam test 7: support and T-beam deformations

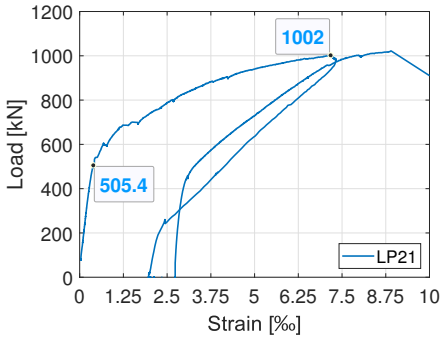

(a) Average longitudinal strain: LP21

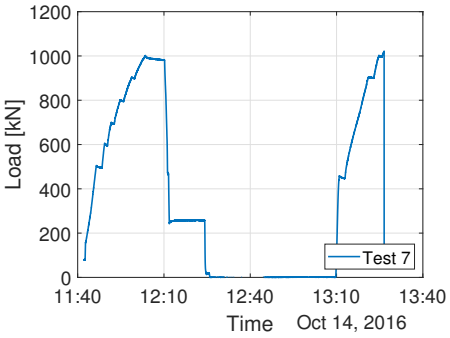

(b) Loading scheme

Figure 6.49: Disconnected beam test 7: average strain and loading scheme

6.6. SUMMARY

THE test objectives, considerations for full-scale collapse tests, observations during the execution and the results of the seven collapse tests are summarised in this section.

Test objectives:

- In total seven collapse tests are carried out on the Vecht bridge on two different spans of the southern bridge, using a single concentrated load at the centre of the

T-beam.

- Three experiments are carried out with the original structural system unchanged; these are referred to as the connected beam tests.
- In four experiments, the integrated deck slab is sawn in the longitudinal direction so that the individual T-beams can be tested; these are referred to as the disconnected beam tests.
- In order to compare the results of the disconnected beam tests to the connected beam tests, the same load positions are chosen; one at 2.25 m and the second at 4.00 m.
- The load position at 2.25 m is assumed to be governing for a (flexural) shear failure of the T-beam.
- The load position at 4.00 m is selected for studying arching effects, in case of connected T-beams, as it is centred exactly between the cross-beams.

Considerations for the design of the full-scale collapse tests:

- The loading system consists of a steel bridge with ballast. A sliding track facilitates the changing of loading position on the same span. A 6000 kN hydraulic jack is used to apply the load.
- The steel bridge has a span length of 24.3 m, and a maximum load capacity of approximately 4000 kN.
- The hydraulic jack is chosen for its capacity as well as its stroke capability (250 mm).
  - In the connected beam tests, due to the relatively high load needed, the total jack extension is governed primarily by the steel bridge deformation.
  - In the disconnected beam tests, the total jack extension is governed primarily by the concrete T-beam deformation.
- For the disconnected beam tests, a comprehensive safety system is used to prevent beams falling to the ground below. This system consists of a static and a dynamic steel beam connected to the concrete T-beam(s) using chains.

Observations made during the execution of the full-scale collapse tests:

- In the case of collapse tests, several dynamic aspects need to be taken into account.
  - The uplift of the steel bridge, due to the high jack forces, can be considered as a temporary excitation in a dynamic system. At failure, the elastic energy is suddenly released which causes a significant downward movement, i.e. vibration, of the steel bridge as well as a noticeable movement of the concrete bridge. This situation is different from proof loading in which the load is gradually reduced back to zero (Lantsoght et al. 2017a,b, Waarts et al. 2015).
  - To prevent plastic behaviour or even damage, the dynamic loading should be considered when checking the cross-section of the steel bridge. For the Vecht bridge tests, only the static loading was taken into account with a safety factor of 1.5.

  - During several disconnected beam tests, the chains for the connection with the dynamic steel beam needed to be adjusted to allow for a larger deflection, resulting in unforeseen unloading. The safety system used could be optimised to allow for larger deflections.

- In the connected beam tests 1 and 2, the (premature) punching of the deck can possibly be avoided, or postponed, by using a larger loading plate or by using multiple concentrated loads. However, higher loading may also require a higher capacity of the loading setup (see Table 6.2).
- For on-site testing of individual beams, the saw cut proved sufficiently wide and no contact between a loaded beam and the adjacent beams is observed. In addition, the uncut end cross-beam, opposite to the load location, sufficiently prevents tilting of the loaded beam. However, for post analysis, it also creates a semi-clamped end which needs to be taken into account[1].
- In future tests, an additional measurement of the jack stroke could be considered to check its deformation during testing.
- In the first connected beam test, the measurements of the relative vertical deformations of the integrated deck slab largely failed due to concrete spalling from the integrated deck slab.

Results connected beam tests 1–3:

- Test 1 and 2 resulted in an instantaneous punching of the deck slab and subsequent shear failure of the T-beam, with a failure load of 3004 kN and 3444 kN.
- In Test 3 no failure occurred since the edge T-beam is not loaded beyond 2506 kN because of safety concerns.

Results disconnected beam tests 4–7:

- All disconnected beam tests resulted in a flexural shear failure of the T-beam.
- In the identical tests 4–6, with the load position at 2.25 m, the ultimate load is 1678 kN, 1703 kN and 1774 kN, with an average of 1718 kN (scatter in the ultimate load ≈ 6%).
- In test 7, with the load position at 4.00 m, the ultimate load is 1022 kN, i.e. 59% of the average ultimate load of tests 4–6.
- In tests 4–6, the unreinforced concrete filling at the anchorage of tendon 7 is broken out.

[1] this is treated in Chapter 7

7

CASE STUDY: THE VECHT BRIDGE NONLINEAR ANALYSIS

In this chapter the full-scale collapse tests, as treated in Chapter 6, are analysed using nonlinear finite element analysis (NLFEA). In addition, a baseline simply supported T-beam is also analysed. A numerical parameter study, in which the element size and the solution method are varied, is carried out to investigate their respective sensitivity and to optimise the analyses. Modelling aspects, related to the large bridge deck model are treated, including the use of solid versus shell elements, the application of prestressing and mesh optimisations.

Parts of this chapter have been published in (Ensink et al. 2019).

7.1. INTRODUCTION

THE case study of the Vecht bridge is split into three parts, and is treated in Chapters 5–7. A detailed description of the Vecht bridge and its structural components is given in Chapter 5. For the results of the full-scale collapse tests the reader is referred to Chapter 6. In this chapter the details and the results of the nonlinear finite element analysis (NLFEA) are treated. An overview of all analyses is given in Section 7.2.2.

7.2. FINITE ELEMENT ANALYSIS

THIS section introduces the finite element software and gives an overview of the different adopted FEM models and analyses as well as a brief description of the Python scripting used.

7.2.1. DIANA 10.3 FINITE ELEMENT SOFTWARE

FINITE element modelling is an important tool for engineers and researchers. Within the scope of this research a large number of finite element models are created with the finite element software DIANA version 10.3 (DIANA 2019)[1].

DIANA (DIsplacement ANAlyzer) is a finite element software package with extensive element and material model libraries as well as a wide range of nonlinear analysis capabilities. From version 10.0 onwards, the graphical user interface (GUI) has been redesigned so that now all tasks can be performed from within the same program, from pre-processing to performing the analysis to post-processing. In addition, Python scripting is supported meaning that all tasks can be written to a text file, to rerun and reproduce the same analysis. Python scripting also enables the use of variables or parameters, within the script, for creating standardised models and/or analyses.

7.2.2. FEM MODELS AND ANALYSES

THE collapse tests (see Chapter 6 Table 6.1) are analysed with a nonlinear finite element analysis for each test, see Table 7.1. Test 3 is not included as this test did not result in a failure of the deck or the T-beam (see Chapter 6 Section 6.4.3). Note that in tests 4–7 the T-beams are not completely disconnected. Additional baseline analyses are therefore carried out of a simply supported T-beam, see Table 7.2. For all analyses three different FEM models are utilised, designated with FEM model A, B and C:

FEM model A: Bridge deck with fully connected T-beams

Model of the bridge deck consisting of 15 prestressed T-beams and four cross-beams. FEM model A represents span 4 of the Vecht bridge, see Chapter 6 Figure 6.1. This model is used for the analysis of the connected beam tests 1–2, see Tabel 7.1.

FEM model B: Bridge deck with partially disconnected T-beams

Model of the bridge deck consisting of 15 prestressed T-beams and four cross-beams. This model represents span 2 of the Vecht bridge and includes the saw cuts of the in-

[1] System used: Intel Core i9-9900K, 128 GB 2666 MHz DDR4, M.2 1 TB PCIe Class 40 SSD (RAID 0), Nvidia Quadro P2200

tegrated deck slab and three of the four cross-beams to create partially disconnected T-beams, see Chapter 6 Figure 6.2. Note that a small part of the integrated deck slab as well as the end cross-beam at the non-loaded side are *not* sawn (see Chapter 6 Section 6.3.1). FEM model B is used for the disconnected beam tests 4–7, see Tabel 7.1.

FEM model C: Simply supported T-beam

Model of an individual, simply supported, prestressed T-beam of the Vecht bridge. This model is used for reference and is primarily used for the numerical parameter study, see Table 7.2.

Table 7.1: Overview of nonlinear analyses (test simulations)

analysis	FEM model	test	a mm	loaded beam[a]	model description
A-T1	A	1	4000	11	bridge deck (connected T-beams)
A-T2	A	2	2250	6	bridge deck (connected T-beams)
B-T4	B	4	2250	12	bridge deck (disconnected T-beams)
B-T5	B	5	2250	11	bridge deck (disconnected T-beams)
B-T6	B	6	2250	10	bridge deck (disconnected T-beams)
B-T7	B	7	4000	9	bridge deck (disconnected T-beams)

[a] see Section 6.2 Figures 6.1–6.2

Numerical parameter study

The numerical parameter study consists of an investigation of the most relevant parameters used in the nonlinear analysis, i.e. the element size and the solution method, to investigate their respective sensitivity and optimise the analyses. This study is performed using FEM model C and is treated in Section 7.7.

Table 7.2: Overview of nonlinear analyses (numerical parameter study)

analysis	FEM model	a mm	model description
C1	C	2250	simply supported T-beam
C2	C	4000	simply supported T-beam

Analysis designation

In the following sections, the analysis designation, as given in Tables 7.1–7.2, is further extended with a number, representing the element size, and a letter combination, representing the solution method used, for example:

'C1-100-FNR'

refers to analysis 'C1', see Table 7.2, using a general element size of 100 mm and the Full Newton-Raphson (FNR) solution method. Other solution method abbreviations used are given in Section 7.7.2. In some cases two different element sizes are adopted: a fine mesh near the load position and a coarse mesh for the remaining parts of the model. In

these cases the fine/coarse mesh is included in the designation by a double number, for example:

'A-T1-60/180-QNR'

refers to analysis 'A-T1', see Table 7.1, using a local fine element size of 60 mm and a general coarse element size of 180 mm as well as the Quasi Newton-Raphson (QNR) solution method.

7.2.3. PYTHON SCRIPTING

TO create the FEM models given in Section 7.2.2 a single comprehensive parametric Python script is adopted to automate the modelling process. The key advantages of using a single script is that it speeds up the modelling process and that it creates uniformity across all models. The Python script evolved continuously during the course of the research in order to create variations of the different models as needed. In this section only a brief description of the main features of the script are given. The models are created using different parameters to control the modelling and/or analysis process, the main parameters related to the geometry are:

- number of T-beams, cross-sectional and longitudinal dimensions, spacing etc.;
- dimensions of integrated deck slab, cross-beams, supports, etc.;
- embedded reinforcements: location, diameter, spacing, etc.

In addition to the geometry settings, many toggle switches are included in the script to turn features on and off, such as reinforcements, prestressing, loads, meshing, linear or nonlinear analysis etc.

7.3. FEM MODELS - GENERAL

THIS section describes the general aspects of the FEM models A, B and C, introduced in Section 7.2.2, such as the (nonlinear) material properties and material models used, as well as some general modelling and analysis details. The material modelling, meshing, convergence and other nonlinear settings, used throughout all analyses, are, as much as possible, in accordance with the Dutch 'Guidelines for Nonlinear Finite Element Analysis of Concrete Structures', referred to as RTD 1016-1 (Hendriks et al. 2017). If alternative choices are made, these will be indicated.

7.3.1. MATERIAL PROPERTIES

THE material (strength) properties are based on the material investigation. For more details the reader is referred to Chapter 5 Section 5.3.

Concrete

The tensile (G_f) and compressive (G_c) fracture energy are determined in accordance with RTD 1016-1 (Hendriks et al. 2017) and Model Code 2010 (fib 2012), see Equations 7.1–7.2 (G_f in N/m, f_{cm} in N/mm^2).

$$G_f = 73 f_{cm}^{0.18} \tag{7.1}$$

$$G_c = 250 G_f \tag{7.2}$$

The mean tensile strength and Young's modulus are determined in accordance with NEN-EN 1992-1-1 (NNI 2011a), see Equations 5.21 and 7.3.

$$E_{cm} = 22[f_{cm}/10]^{0.3} \times 10^3 \tag{7.3}$$

The concrete FEM material properties used are summarised in Table 7.3. For high strength concrete, the variation of the fracture energy, as obtained from experiments, is reported in fib bulletin 42 (fib 2008) and shown in Figure 7.1. With reference to Figure 7.1, the fracture energy G_f obtained using Equation 7.1, see Table 7.3, seems reasonable in relation to the large aggregates (Chapter 5 Figure 5.9) and the relatively high compressive strength f_{cm} of the T-beam.

Reinforcement and prestressing steel

The reinforcement and prestressing steel FEM material properties are given in Table 7.4. For reinforcement steel diameters other than ø10 mm the ultimate strain is in accordance with NEN-EN 1992-1-1 (NNI 2011a)[2]. In the nonlinear analyses the values for ultimate strain, as given in Table 7.4, are reduced to $0.9\epsilon_u$ or $0.9\epsilon_{uk}$.

Reinforced elastomeric bearing (supports)

As a first approximation, the vertical stiffness of the reinforced elastomeric bearings (see Chapter 5 Section 5.2.6) is determined by using a general rule of thumb, according to the Dutch guideline for assessing existing bridges, RTD 1006 (Rijkswaterstaat 2013), which assumes a 1 mm vertical compression as a result of the self-weight. This rule of thumb results in a vertical stiffness of the bearing of approximately 167 MN/m.
Alternatively, the vertical stiffness of reinforced elastomeric bearings can be determined using the formulations from the old Dutch code NEN 6723 (NNI 1995), see Equations 7.4–7.5 (equations for rectangular bearings).

$$\delta = \frac{h^3 \sigma}{G b^2 T} + \frac{\sigma h}{C} \tag{7.4}$$

$$T = \left(1 - 0.631 \frac{b}{l} \tanh\left(\frac{\pi l}{2b}\right)\right) \tag{7.5}$$

Where:

δ compression rubber sheet (mm)

σ average compressive stress (N/mm^2)

b width rubber sheet (mm)

[2] In the Dutch guideline for assessing existing bridges, RTD 1006 (Rijkswaterstaat 2013), the ductility of steel grade QR24 is classified as Class B.

Table 7.3: Concrete FEM material properties

T-beam			
mean compressive strength	f_{cm}	87.7	N/mm^2
mean tensile strength	f_{ctm}	4.83	N/mm^2
fracture energy[a]	G_f	0.163	Nmm/mm^2
compressive fracture energy	G_c	40.83	Nmm/mm^2
Poisson's ratio	ν	0.15	-
Young's modulus	E_{cm}	42200	N/mm^2
integrated deck slab and cross-beam			
mean compressive strength	f_{cm}	60.3	N/mm^2
mean tensile strength	f_{ctm}	4.13	N/mm^2
fracture energy[a]	G_f	0.153	Nmm/mm^2
compressive fracture energy	G_c	38.17	Nmm/mm^2
Poisson's ratio	ν	0.15	-
Young's modulus	E_{cm}	37715	N/mm^2
kerb			
mean compressive strength	f_{cm}	55.4	N/mm^2
mean tensile strength	f_{ctm}	3.98	N/mm^2
fracture energy[a]	G_f	0.150	Nmm/mm^2
compressive fracture energy	G_c	37.59	Nmm/mm^2
Poisson's ratio	ν	0.15	-
Young's modulus	E_{cm}	36768	N/mm^2

[a] alternatively referred to as mode I fracture energy, i.e. G_f^I

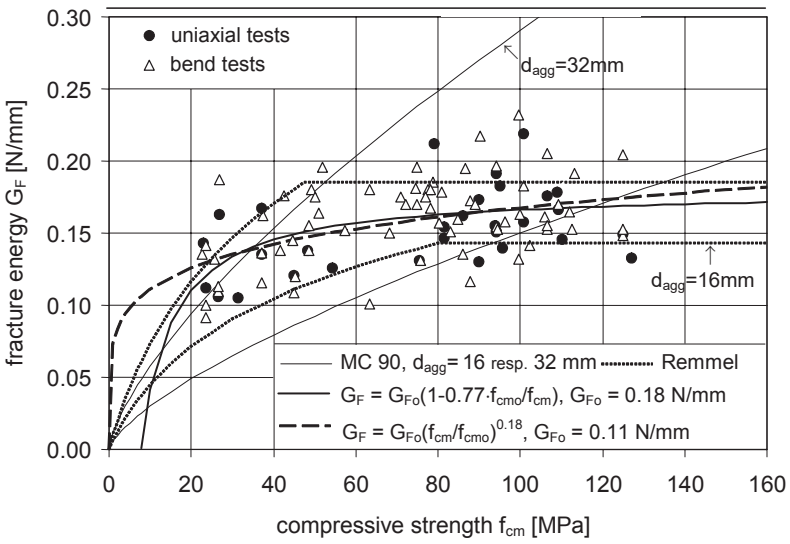

Figure 7.1: Relation between compressive strength and fracture energy - experimental results and corresponding relations, f_{cm0} = 10 N/mm^2 (taken from (fib 2008))

Table 7.4: Reinforcement and prestressing steel FEM material properties

reinforcement steel			
mean yield strength	f_{ym}	288	N/mm^2
ultimate tensile strength	f_u	352	N/mm^2
Young's modulus	E_s	200000	N/mm^2
ultimate strain (ø10 mm)[a]	ϵ_u	10.0	%
ultimate strain (other diameters)	ϵ_{uk}	5.0	%
prestressing steel			
mean yield strength	f_{ym}	1505	N/mm^2
ultimate tensile strength	f_u	1770	N/mm^2
Young's modulus	E_p	195000	N/mm^2
ultimate strain[a]	ϵ_u	7.5	%

[a] minimum value for ϵ_u, see Table 5.2

h thickness rubber sheet (mm)

l length rubber sheet (mm)

C volumetric compressive modulus, equal to 1000 N/mm^2

G shear modulus rubber, equal to 0.9 N/mm^2

T ratio coefficient, dependent on l and b

The dimensions of the bearings are: l = 306 mm, b = 206 mm and h = 15.5 mm (layer thickness). Using Equation 7.5 results in T = 0.58. With $\sigma = F/(l \times b)$ and $F = K \times \delta$, Equation 7.4 can be rewritten to Equation 7.6 to determine the vertical stiffness of a single rubber layer (K). Using Equation 7.6 results in K = 345 MN/m for each layer, giving a total vertical stiffness, for two layers, of 173 MN/m.

$$K = \left(\frac{h^3}{Gb^2 T l b} + \frac{h}{AC} \right)^{-1} \tag{7.6}$$

Both the rule of thumb and the Dutch code NEN 6723 (NNI 1995) give comparable results, and therefore initially a stiffness of 173 MN/m is assumed in the nonlinear analysis. The support measurements of tests 1–7[3] are then compared to the nonlinear analysis results (Appendices A–B). In order to obtain comparable deformations, the vertical support stiffness in the NLFEA models has to be increased significantly, by a factor of 2.75, to a value of 475 MN/m.

This difference could indicate a significant underestimation by the initially used standard analytical formula. In this regard it is also worth mentioning that the bearing are 54 year old. Based on previous results from testing rubber bearings in the laboratory at TU Delft (Reinders 2016), a more realistic stiffness can be obtained by using the analytical formula by Banks, Pinter and Yeoh (Banks et al. 2002), which in this case would result in

[3] Note that due to the position of the support measurement (Chapter 6 Figure 6.20a), the vertical support stiffness cannot be directly determined.

a stiffness of 398 MN/m.

In particular in tests 4–7, a nonlinear relation between the load and the support displacement is observed (see Chapter 6 Section 6.5). This is the combined effect of cracking of the T-beam and the nonlinear behaviour of the rubber bearing (Amir and van der Veen 2013). However, from the support measurements it is not possible to isolate one of these effects. Therefore, in all analyses a linear support stiffness of 475 MN/m is assumed. The supports are modelled using a 2D plane interface, and the distributed spring stiffness, in vertical (K_z) and horizontal ($K_{x,y}$) direction(s), is given by Equations 7.7–7.8.

$$K_z = \frac{K}{lb} = \frac{475 \times 10^3}{306 \times 206} = 7.54 \text{ N/mm}^3 \tag{7.7}$$

$$K_{x,y} = \frac{G}{h} = \frac{0.9}{2 \times 15.5} = 0.029 \text{ N/mm}^3 \tag{7.8}$$

Concentrated load (plywood)

A plywood plate is placed on top of the concrete deck underneath the loading plate, for details see Chapter 6 Section 6.3.5. The plywood plate has a thickness h of 18 mm and is modelled using a 2D plane interface. Assuming a Young's modulus of $E = 300$ N/mm^2 and a shear modulus of $G = 172.5$ N/mm^2, the distributed spring stiffness, in vertical and horizontal direction(s), is given by Equations 7.9–7.10.

$$K_z = \frac{E}{h} = \frac{300}{18} = 16.7 \text{ N/mm}^3 \tag{7.9}$$

$$K_{x,y} = \frac{G}{h} = \frac{172.5}{18} = 9.58 \text{ N/mm}^3 \tag{7.10}$$

7.3.2. CONSTITUTIVE MODELLING

FOR concrete a smeared crack approach is adopted using a total strain rotating crack model (DIANA 2019), as recommended by RTD 1016-1 (Hendriks et al. 2017). Compared to a fixed crack model, the rotating crack model is considered to result in a lower bound failure load and is less susceptible to stress-locking. An overview of all constitutive models used for concrete is given in Table 7.5.

Table 7.5: Concrete constitutive modelling (DIANA 2019)

aspect	model used
tensile behaviour	Hordijk softening
compressive behaviour	parabolic stress-strain diagram
tension-compression interaction	Vecchio and Collins 1993
compression-compression interaction	-
Poisson's ratio	damage based
equivalent length (crack-band width)	Rots

Note that compression-compression interaction is not taken into account which is a conservative approach. The equivalent length, or crack-band width h_{eq}, is automatically

determined by DIANA, using the model by Rots, and is based on the element size (for solid elements it is calculated as $\sqrt[3]{V}$ with V the volume of the element and for quadratic 2D elements as $\sqrt{A}$ with A the area of the element). For the concrete tensile behaviour, the exponential softening curve by Hordijk is adopted. This curve is dependent on the tensile strength f_{ctm}, the fracture energy G_{f} and the crack-band width h_{eq}, see Figure 7.2a. For the compressive behaviour, a parabolic diagram is used. This diagram is dependent on the compressive strength f_{cm}, the fracture energy G_{c} and the crack-band width h_{eq} and therefore also includes a softening branch, see Figure 7.2b. The reduction of the compressive strength, as a result of lateral cracking, is taken into account by the tension-compression interaction model by Vecchio and Collins 1993 (DIANA 2019). The maximum reduction is 60%, i.e. a minimum of 40% of the compressive strength always remains. Finally, a damage-based reduction of the Poisson's ratio, due to cracking, is also adopted.

For the reinforcement and prestressing steel an elasto-plastic material model with strain hardening is adopted, see Figure 7.3. The yield strength, tensile strength and the ultimate strain are determined by the material investigation, see Chapter 5 Section 5.3 and Table 7.4. An overview of the constitutive models used for the reinforcement and prestressing steel is given in Table 7.6. Note that bond-slip, between concrete and reinforcement, is not taken into account.

7.3.3. ELEMENT TYPES AND SIZES

FOR all FEM models A, B and C, see Section 7.2.2, 3D solid elements are used. In FEM models A and B, some parts of the structure are modelled using 2D curved shell elements[4], to limit the amount of elements and thereby reduce computing time. Using 3D solid elements for the complete structure in these cases is not feasible, due to computing limitations, but also not necessary since the 2D shell elements are generally used outside the area of interest (see Sections 7.4–7.5). In all cases, quadratic elements are used with full integration, except for the quadratic 2D shell elements which by default use a reduced integration. In 3D, hexahedrons or brick elements are used, whereas in 2D, quadrilaterals are used, see Figure 7.4. Depending on the complexity of the geometry and the mesher, these are sometimes supplemented with tetrahedrals or triangles, in 3D or 2D respectively.

Maximum element size

For the exponential concrete tensioning softening curve by Hordijk (see Figure 7.2a), a maximum value for the crack-band width can be determined to avoid a snap-back in the softening curve, according to Equation 7.11 (DIANA 2019).

$$h_{\text{eq,max}} = 0.739 \frac{E G_{\text{f}}}{f_{\text{ctm}}^2} \tag{7.11}$$

With the material properties given in Table 7.3, Equation 7.11 results in a maximum crack-band width of 218 mm (concrete of T-beam) and 250 mm (concrete of integrated deck slab and cross-beam). For equilateral elements the crack-band width is equal to

[4]Curved shells are used for their compatibility with embedded bar reinforcement (DIANA 2019).

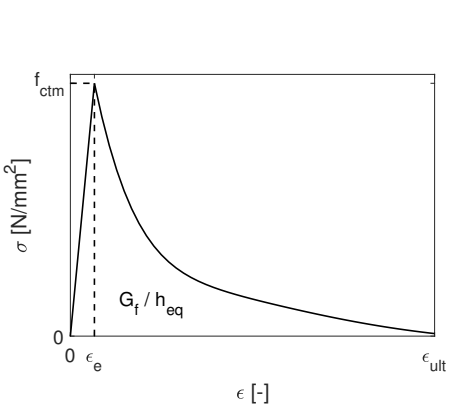

(a) Concrete tension softening (Hordijk)

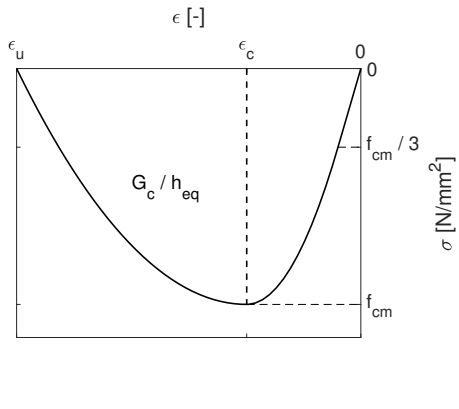

(b) Parabolic compression with softening

Figure 7.2: Concrete in tension and compression

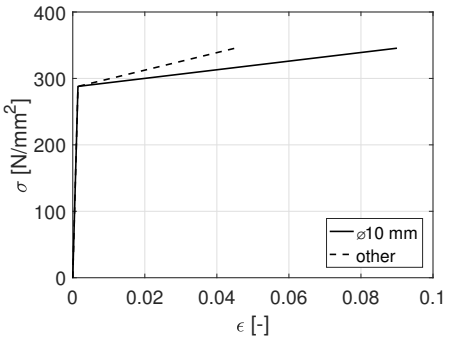

(a) Stress-strain reinforcement steel

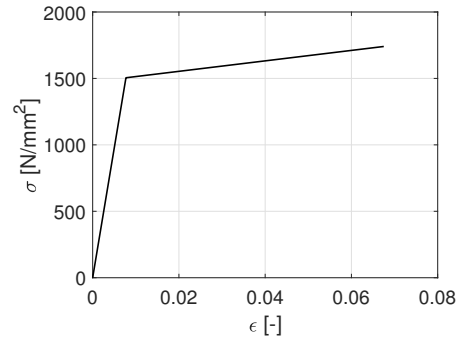

(b) Stress-strain prestressing steel

Figure 7.3: Stress-strain diagram reinforcement and prestressing steel (see also Table 7.4)

Table 7.6: Reinforcement and prestressing steel constitutive modelling (DIANA 2019)

aspect	model used
tensile and compressive behaviour	Von Mises plasticity
hardening hypothesis	strain hardening
bond-slip	full bond

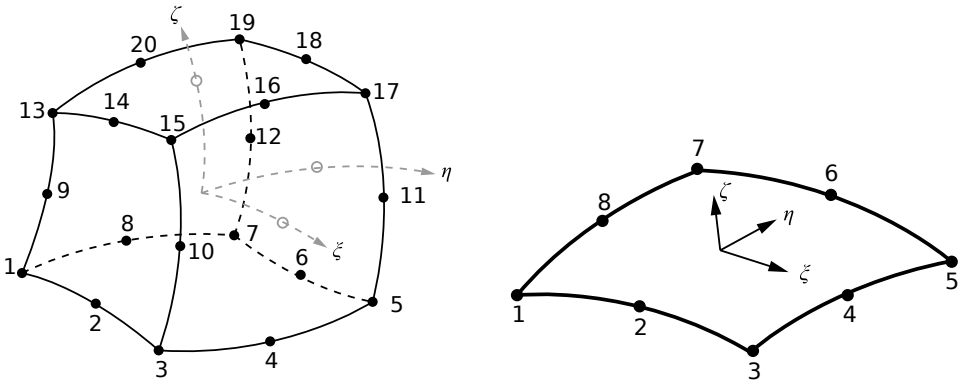

(a) 20-node brick element (DIANA: CHX60) (b) 8-node curved shell element (DIANA: CQ40S)

Figure 7.4: Base element types used in 3D and 2D (figures taken from DIANA manual (DIANA 2019))

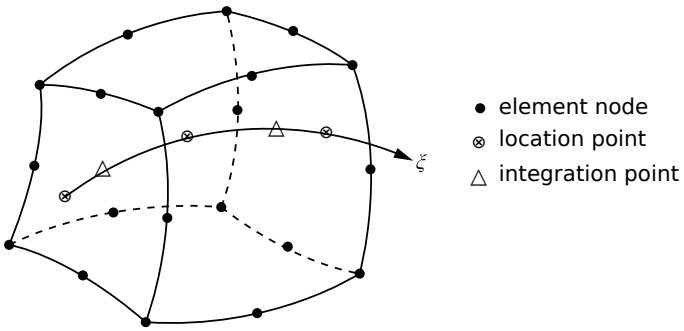

Figure 7.5: Example of embedded reinforcement, bar in 3D brick element (taken from (DIANA 2019))

the element size, therefore these values also represent the maximum element size.

Additionally, the choice for the maximum element size is related to the modelled structure. For beams and slabs using solid elements, RTD 1016-1 (Hendriks et al. 2017), recommends a minimum of 6 elements for the height. The T-beam has a height of 1150 mm, therefore this recommendation results in a maximum element size of 192 mm. Due to its acting width, the integrated deck slab is considered as part of the top flange of the T-beam. Otherwise, a maximum element size of 180/6 = 30 mm would be recommended to model the integrated deck slab, which is not feasible. In conclusion, a maximum element size of 200 mm will be used and, in addition, the element size dependency will be investigated in Section 7.7.

Embedded reinforcement

Reinforcement can be modelled in DIANA independently from the surrounding structural elements either with bars, i.e. lines, or grids, i.e. sheets. As part of the meshing procedure, the intersections of the reinforcement with the 2D or 3D elements are identified and the reinforcement is automatically 'embedded' and thus become part of the intersected or mother elements in which it is located, see Figure 7.5. The embedded

reinforcement does not influence the space occupied and does not increase the weight of the mother element, but it does increase the stiffness of the mother element. In this research, all reinforcement and prestressing tendons are modelled as embedded reinforcement using individual bars with full bond. The curved prestressing tendons are approximated by straight lines at 750 mm interval with the vertical coordinates determined using the polynomials as described in Chapter 5 Section 5.4. In addition, the horizontal curvature, of tendons 1, 3, 4 and 6, although limited, is also taken into account using the coordinates provided on the original drawings. In general, using individual bars, instead of grids, and more precise coordinates for embedded reinforcements becomes more relevant when using a finer mesh.

7.3.4. LOADING AND CONVERGENCE

THE loading consists of the self-weight, the transverse prestressing of the bridge deck, the longitudinal prestressing of the T-beam(s) and a displacement load, see Table 7.7. The self-weight of the concrete is taken from the material investigation, see Chapter 5 Section 5.3 Table 5.1. The prestressing loads are applied to the embedded reinforcement, representing the prestressing tendons, using an initial stress of $\sigma_{pw} = 0.8\sigma_{pi} = 0.8 \times 1084 = 867\ \mathrm{N/mm^2}$, see Chapter 5 Section 5.4 Equation 5.1. When using an imposed deformation or displacement load, a support is needed at the same node(s), and therefore a phased analysis is required. In the first phase, the self-weight and the prestressing load(s) are applied. Then, in the second phase, the additional support is activated to apply the displacement load.

Table 7.7: Load cases in DIANA

load case	name used in DIANA	load type
LC1	1 SW	self-weight
LC2	2 TP	transverse prestressing (slab and cross-beams)
LC3	3 LP	longitudinal prestressing (T-beam)
LC4	4 load	displacement load

The convergence tolerances used in the nonlinear phased analyses are based on the recommendations of RTD 1016-1 (Hendriks et al. 2017) and are given in Table 7.8. To improve convergence, different convergence norms are set to be satisfied simultaneously whenever possible [5]. In the first phase, both energy, displacement and force norms are set for convergence. The second phase is then split into two parts, i.e. phase 2a and phase 2b. In phase 2a, both the energy and force norms are set for convergence and this analysis phase is extended for as long as possible. When convergence of both norms is no longer achieved, phase 2b is initiated where only one, either energy or force norm, is required for convergence.

For the displacement load in phase 2a and phase 2b, an automatic step size routine is utilized [6]. Using this routine, a maximum and minimum step size can be defined as

[5] This is more strict than RTD 1016-1 (Hendriks et al. 2017).
[6] In DIANA this feature is referred to as: cutback based automatic incremental loading (DIANA 2019).

Table 7.8: Convergence settings

phase	energy norm tolerance	displacement norm tolerance	force norm tolerance	satisfy all norms	load case(s)
1	10^{-3}	10^{-2}	10^{-2}	YES	LC1, LC2, LC3
2a	10^{-3}	-	10^{-2}	YES	LC4
2b	10^{-3}	-	10^{-2}	NO	LC4

well as the total displacement load. When non-convergence occurs, the routine automatically adjusts, i.e. decreases, the step size and tries again until either: 1) convergence is reached and loading is continued, or 2) the minimum step size is reached and the analysis is aborted. Conversely, when few iterations are needed the step sizes are automatically increased. If non-convergence occurs and the analysis is aborted, it can be continued from the last converged step. In this case, several very small user-defined steps are used to try to regain convergence. If convergence is regained, the analysis is again continued using the automatic step size routine. This procedure is repeated until the ultimate failure load is reached. The ultimate failure load is defined as the highest load obtained in a converged step. In the following sections, the non-converged steps will be reported and indicated in the load-displacement curves.

7.4. FEM MODEL A: BRIDGE DECK (CONNECTED T-BEAMS)

THIS section gives a detailed description of FEM model A. This model represents a bridge deck span with connected T-beams and is used for analyses A-T1 and A-T2, see Section 7.2.2 Table 7.1. For the general aspects used throughout all models see Section 7.3. FEM models A–C are created using the same parametric Python script to construct the model; for more details see Section 7.2.3.

7.4.1. GEOMETRY, ELEMENTS AND MESHING

AN overview of FEM model A is given in Figure 7.6. In this model, five T-beams, centered around the loaded beam, are modelled with 3D solid elements and the remaining T-beams are modelled with 2D shell elements (see also Section 7.3.3). Note that in the connected beam tests, measurements are taken of the loaded beam and the adjacent beams (two on either side), see Chapter 6 Section 6.3.5. Table 7.9 gives an overview of the 2D/3D modelling and the adopted element size(s) for analyses A-T1 and A-T2. The full length of a T-beam, including the integrated deck slab and the corresponding parts of the cross-beam(s), is modelled in either 2D or 3D, see Figure 7.7. The vertical 2D shell elements, used for modelling the T-beam, use a spatial thickness function, see Figure 7.8a. The accuracy of the resulting varying thickness depends on the selected element size. At the solid-shell transition, the shell elements connect to the center lines of the connecting solid parts, i.e. the integrated deck slab and the cross-beam(s), see Figure 7.7. For this connection the 'auto-tying' option is selected. This option ensures compatibility at the transition, by connecting the translational degrees of freedom of the solid nodes to the translational and rotational degrees of freedom of the shell nodes (DIANA

2019). At the intersection of the shell T-beam and the shell cross-beam, the latter takes precedence, see Figure 7.7. In case of a shell T-beam, the integrated deck slab is overlapping with the top flange of the T-beam. In addition, the shell cross-beam is overlapping with the shell T-beam. To compensate the excess weight, the weight of the shell slab and the shell cross-beam is reduced. In addition, the Young's modulus of the shell T-beam is calibrated, i.e. increased by 2.5%, to give the same deflection as the solid T-beams[7]. To prevent badly shaped elements in the mesh, the transition piece near the end block is partly omitted and only the part on the straight web is modelled, see Figure 7.8b. For the shell T-beam the transition piece is completely omitted.

Table 7.9: FEM model A, 2D/3D modelling and element size

analysis	beam number[a] 3D solid	beam number[a] 2D shell	element size 3D solid mm	element size 2D shell mm
A-T1	9–13	1–8 & 14–15	90	180
A-T2	4–8	1–3 & 9–15	90	180

[a] for the beam numbering see Chapter 6 Figure 6.1

7.4.2. SUPPORT AND CONCENTRATED (LIVE) LOAD MODELLING

FOR the 3D solid beams, a 2D surface interface is used to model the rubber bearings and to connect the bottom side of the T-beam to a rectangular steel (base) plate (2D shell, l×b = 206 × 306 mm, see also Chapter 5 Section 5.2.6). The support interface stiffness is given in Section 7.3.1 by Equations 7.7–7.8. A tying is adopted to connect the translations X, Y and Z, of the steel (base) plate, to a single master node. The master node is subsequently constrained in all directions, X, Y and Z, thereby constraining the entire steel (base) plate. This simplifies the boundary conditions needed and results in the support reaction to be automatically available in post-processing as a single integrated value, in each direction, from the master node.

Similarly, for the 2D shell beams, a 1D line interface is adopted with a thickness (width) of 306 mm and a stiffness given in Section 7.3.1 by Equations 7.7–7.8. A tying is again adopted to connect the translations X, Y and Z, of the steel (base) plate, to a single master node. The master node is subsequently constrained in all directions, X, Y and Z, thereby constraining the entire steel (base) plate.

The concentrated (live) load is applied by a 100 mm thick steel loading plate (2D shell, 400 × 400 mm), to represent the steel plate with load cell used in the experiments (see Chapter 6 Section 6.3.5 Figure 6.18a). A 2D surface interface is used to model the plywood and to connect the top side of the T-beam to the steel loading plate. The interface stiffness is given in Section 7.3.1 by Equations 7.9–7.10. The displacement controlled load is applied to a single node at the center of the loading plate.

[7] For this calibration a model consisting of three T-beams is constructed in 3D. The maximum deflection at midspan of the 3D model is used to calibrate the same model constructed in 2D.

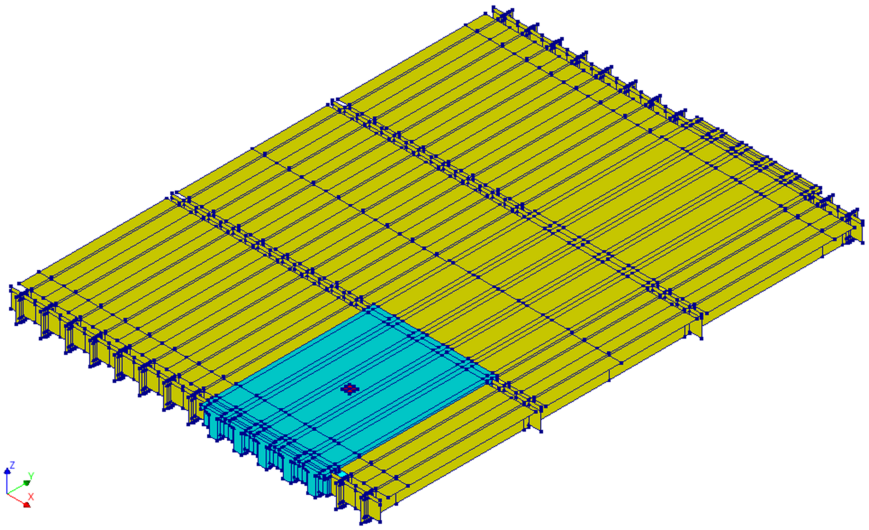

Figure 7.6: Geometry FEM model A (nonlinear parts indicated in blue), top view

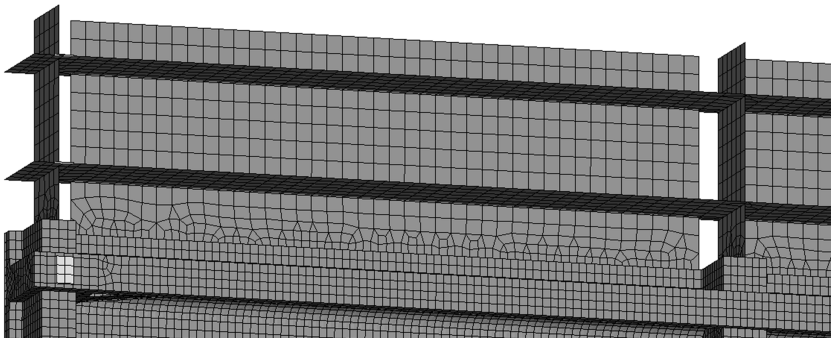

Figure 7.7: Mesh FEM model A, detail of solid-shell transition, bottom view

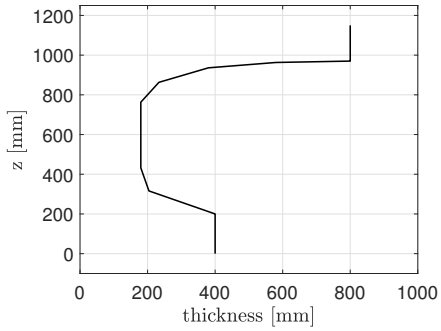

(a) Spatial thickness function, shell T-beam

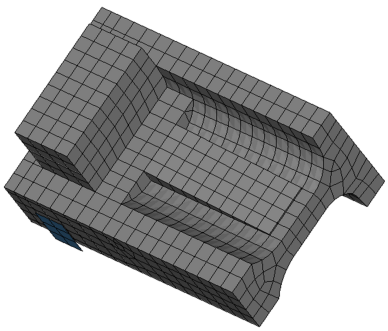

(b) Detail of transition piece, solid T-beam

Figure 7.8: Details of FEM model A

7.4.3. REINFORCEMENT AND PRESTRESSING

THE reinforcement layout is taken from the original drawings and all reinforcement and prestressing tendons are modelled using bars (embedded reinforcement) with full bond, see Section 7.3.3. The reinforcement is only applied in the parts of the model with 3D solid elements having nonlinear material properties (see Figure 7.6). For a more detailed description of the reinforcement see also Chapter 5 Sections 5.2.3–5.2.5. The (nonlinear) material properties are given in Section 7.3.1 Table 7.4 and in Section 7.3.2 Figure 7.3a. The reinforcements consist of stirrups and longitudinal bars (T-beam, integrated deck slab and cross-beams(s)) as well as splitting reinforcement (anchorage zone(s) prestressing tendons). For a single T-beam, the applied reinforcements are shown in Figure 7.9. In FEM model A, five T-beams, modelled with 3D solids (see Table 7.9), are applied with reinforcements up until the first intermediate cross-beam as is shown in Figure 7.6 and in Figure 7.9. For a single T-beam, the reinforcement representing prestressing tendons 1–7, is shown in Figure 7.10. All 15 T-beams, using either solids or shells, are provided with prestressing tendons 1–7. For the prestressing load see Section 7.3.4. The (nonlinear) material properties are given in Section 7.3.1 Table 7.4 and in Section 7.3.2 Figure 7.3b. The transverse prestressing consists of 59 straight tendons located in the integrated deck slab and the cross-beams. The locations are taken from the original drawings. For a more detailed description of the transverse prestressing, see also Chapter 5 Sections 5.2.4–5.2.5. For FEM model A, the reinforcement representing the transverse prestressing tendons 8–66, is shown in Figure 7.11. For the prestressing load, see Section 7.3.4. The (nonlinear) material properties are given in Section 7.3.1 Table 7.4 and in Section 7.3.2 Figure 7.3b.

7.4.4. COMPOSED LINE AND SURFACE ELEMENTS

COMPOSED line elements integrate the stresses of the surrounding 3D solid elements and embedded reinforcements to 1D sectional forces N_x, Q_y, Q_z, M_x, M_y and M_z. The stresses are integrated over the plane perpendicular to the reference line (DIANA 2019). In FEM model A, composed line elements are applied in the five T-beams modelled with 3D solids (see Table 7.9), see Figure 7.12. The composed line elements are modelled as a horizontal line, at the center of gravity of the cross-section of the T-beam, between the end cross-beam and the intermediate cross-beam, in the nonlinear part of the model (see Figure 7.6). The selected integrated parts are: the T-beam, the integrated deck slab and the regular longitudinal reinforcement. Note that the longitudinal prestressing tendons are not selected. Otherwise, because of equilibrium, the sectional forces resulting from the prestressing load(s) become zero.

Likewise, composed surface elements integrate the stresses of the surrounding 3D solid elements and embedded reinforcements to 2D distributed sectional forces N_{xx}, N_{yy}, N_{xy}, Q_{xz}, Q_{yz}, M_{xx}, M_{yy} and M_{xy}. In FEM model A, composed surface elements are applied in the integrated deck slab between the T-beams modelled with 3D solids (see Table 7.9), see Figure 7.12. The composed surface elements are modelled as a horizontal plane, at the center of gravity of the integrated deck slab, between the end cross-beam and the intermediate cross-beam, in the nonlinear part of the model (see Figure 7.6). The selected integrated parts are: the integrated deck slab, the regular reinforcement and the transverse prestressing tendons.

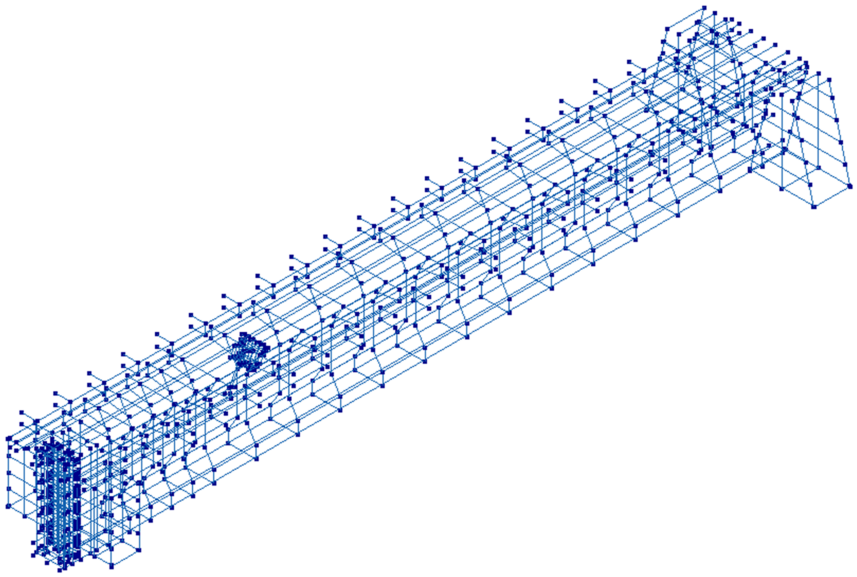

Figure 7.9: Embedded (regular) reinforcements FEM model A
(end cross-beam (left), intermediate cross-beam (right))

Figure 7.10: Embedded reinforcements prestressing tendons 1–7 T-beam

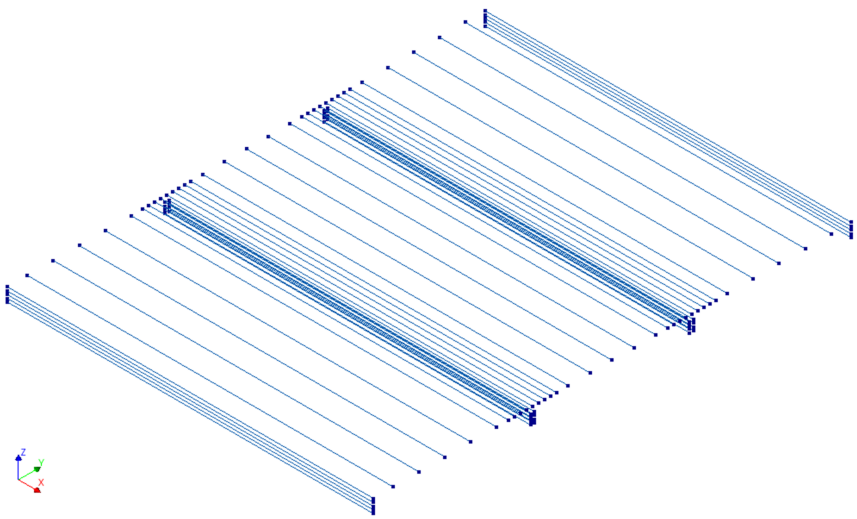

Figure 7.11: Embedded reinforcements transverse prestressing tendons 8–66 FEM model A

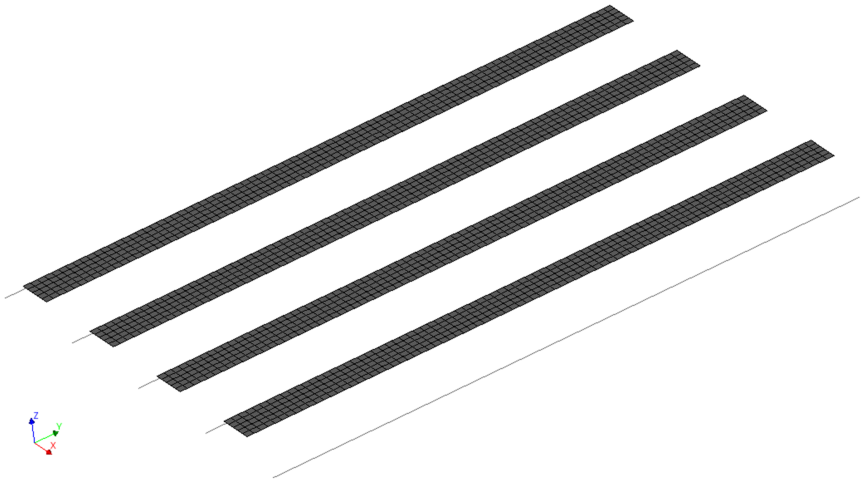

Figure 7.12: Composed line and surface elements FEM model A, top view

7.5. FEM MODEL B: BRIDGE DECK (DISCONNECTED T-BEAMS)

THIS section gives a detailed description of FEM model B. This model represents a bridge deck span with disconnected T-beams and is used for analyses B-T4, B-T5, B-T6 and B-T7, see Section 7.2.2 Table 7.1. For the general aspects used throughout all models, see Section 7.3. FEM models A–C are created using the same parametric Python script to construct the model; for more details see Section 7.2.3.

7.5.1. GEOMETRY, ELEMENTS AND MESHING

AN overview of FEM model B is given in Figure 7.13. In this model, 8 T-beams are modelled with 3D solid elements and the remaining T-beams are modelled with 2D shell elements (see also Section 7.3.3). Table 7.10 gives an overview of the 2D/3D modelling and the adopted element size(s) for analyses B-T4, B-T5, B-T6 and B-T7. The general aspects related to the 2D shell elements, described in Section 7.4.1 for FEM model A, also apply to FEM model B. The saw cuts, in the integrated deck slab and cross-beams, are modelled by a 2 mm gap (see also Chapter 6 Figure 6.2). For the support and concentrated (live) load modelling the reader is referred to Section 7.4.2. At the clamped end, a composed line element is adopted for post-processing of the hogging bending moment. For a detailed description of composed elements, the reader is referred to Section 7.4.4.

7.5.2. REINFORCEMENT AND PRESTRESSING

THE general aspects of the reinforcement layout, described in Section 7.4.3 for FEM model A, also apply to FEM model B. The reinforcement is applied to the loaded part of the T-beam and to the clamped end, see Figure 7.14. The nonlinear (reinforced) parts are shown in Figure 7.13. The T-beam prestressing tendons 1–7 are described in Section 7.4.3 (see Figure 7.10). All 15 T-beams are provided with prestressing tendons 1–7. The saw cuts, in the integrated deck slab and cross-beams, also cause the trans-

Table 7.10: FEM model B, 2D/3D modelling and element size

analysis	beam number[a] 3D solid	beam number[a] 2D shell	element size 3D solid mm	element size 2D shell mm
B-T4	6–13	1–5 & 14–15	60[b]/180	180
B-T5	6–13	1–5 & 14–15	60[b]/180	180
B-T6	6–13	1–5 & 14–15	60[b]/180	180
B-T7	6–13	1–5 & 14–15	60[b]/180	180

[a] for the beam numbering see Chapter 6 Figure 6.2, [b] fine mesh applied to loaded T-beam and clamped end cross-beam, see nonlinear parts in Figure 7.13

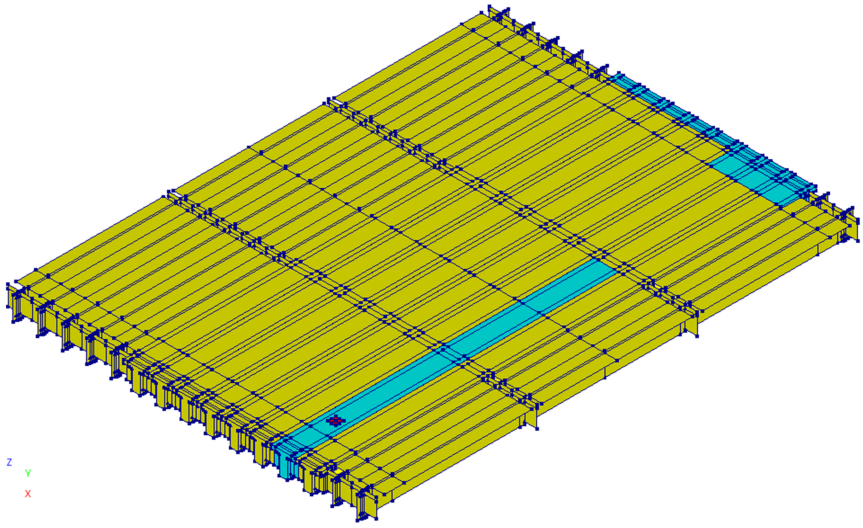

Figure 7.13: Geometry FEM model B (nonlinear parts indicated in blue), top view

verse prestressing tendons to be sawn. The distance between the saw cuts is 1225 mm (equal to the T-beam spacing). Therefore, the affected transverse prestressing tendons have insufficient transmission length and have lost all tension. The affected transverse prestressing tendons are therefore modelled as (regular) reinforcements. At the clamped end, 5 transverse prestressing tendons at the end cross-beam remain intact (for the prestressing load see Section 7.3.4). The transverse prestressing tendons 8–66, adopted in FEM model B, are given in Figure 7.15.

7.6. FEM MODEL C: SIMPLY SUPPORTED T-BEAM

THIS section gives a detailed description of FEM model C of an individual simply supported T-beam of the Vecht bridge. This model is used for analyses C1 and C2, see Section 7.2.2 Table 7.2. For the general aspects used throughout all models, see Section 7.3. FEM models A–C are created using the same parametric Python script to construct

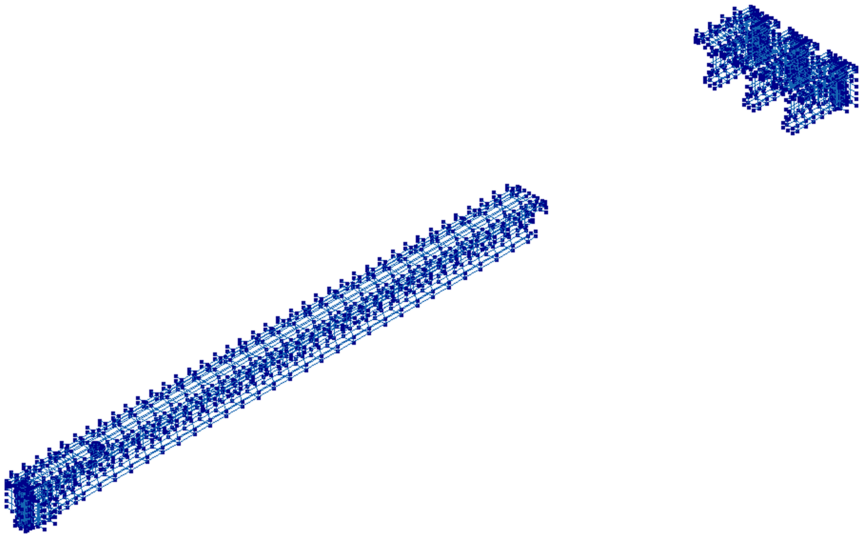

Figure 7.14: Embedded (regular) reinforcements FEM model B

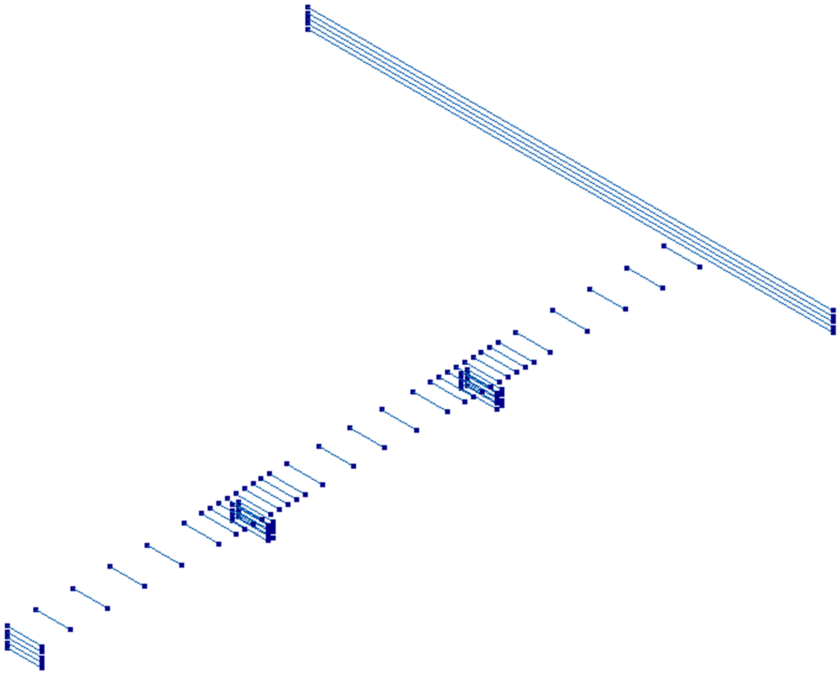

Figure 7.15: Embedded reinforcements transverse prestressing tendons 8–66 FEM model B

the model, for more details see Section 7.2.3. An overview of FEM model C is given in Figure 7.16. FEM model C consists of 3D solid elements only. For the support and concentrated (live) load modelling the reader is referred to Section 7.4.2. The general aspects of the reinforcement layout, described in Section 7.4.3 for FEM model A, also apply to FEM model C. The reinforcement is applied to the loaded part of the T-beam, see Figure 7.17. The nonlinear (reinforced) parts are shown in Figure 7.16.

7.7. NUMERICAL PARAMETER STUDY

IN this section a numerical parameter study is performed by investigating the influence of:

- element size: 50 mm, 100 mm or 200 mm;
- solution method: full Newton-Raphson, Modified Newton-Raphson or Quasi-Newton.

The basis for this investigation is FEM model C, i.e. a simply supported T-beam, using the two load positions 'a' equal to the experiments (see Chapter 6 Section 6.2).

7.7.1. ELEMENT SIZE

THE element size dependency is investigated with element sizes 50 mm, 100 mm and 200 mm. Note that an element size larger than 200 mm is not recommended for this investigation, see Section 7.3.3. Conversely, an element size smaller than 50 mm is not feasible due to computing limitations. An overview of the analyses is given in Table 7.11. The loading procedure and convergence settings are given in Section 7.3.4 using the minimum and maximum step size given in Table 7.11. The various element sizes are shown in cross-sectional view in Figure 7.18. Note that by doubling the element size, the number of degrees of freedom (DOF) decreases by a factor of approximately 4–5, see Table 7.11. Analysis C2-50/100-QNR failed at the start of phase 2b due to a convergence problem. Alternatively, an analysis is run with an element size of 60 mm (C2-60/100-QNR, see Table 7.11).

Table 7.11: Overview analyses for element size dependency investigation

analysis	FEM model	a mm	element size mm	DOF	min/max step size mm
C1-50/100-QNR[a]	C	2250	50/100	1.20E+06	0.0625/0.5[b]
C1-100-QNR	C	2250	100	2.36E+05	0.0625/0.5[b]
C1-200-QNR	C	2250	200	6.26E+04	0.0625/0.5[b]
C2-50/100-QNR[a]	C	4000	50/100	1.20E+06	0.0625/0.5
C2-60/100-QNR[a]	C	4000	60/100	7.44E+05	0.0625/0.5
C2-100-QNR	C	4000	100	2.36E+05	0.0625/0.5
C2-200-QNR	C	4000	200	6.26E+04	0.0625/0.5

[a] fine mesh size applied to 2/3 of the model, [b] in phase 2b the maximum step size is reduced to 0.25 mm

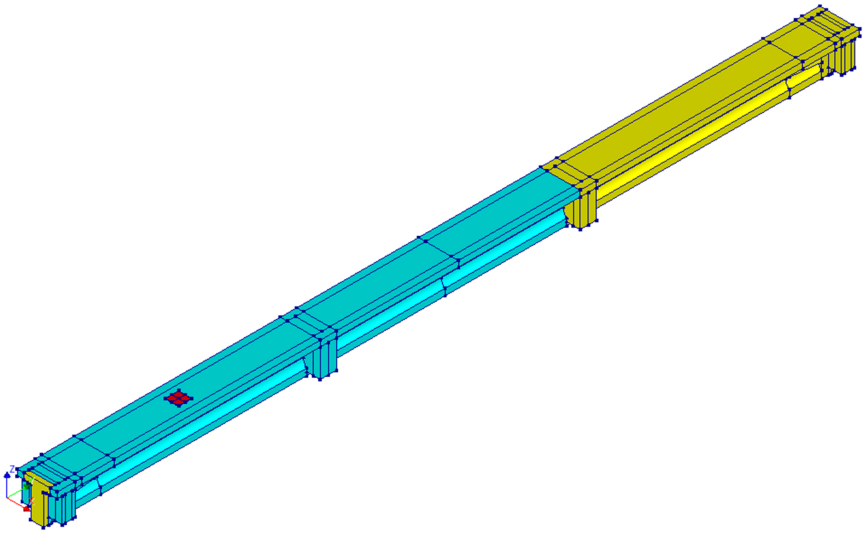

Figure 7.16: Geometry FEM model C (nonlinear parts indicated in blue), top view

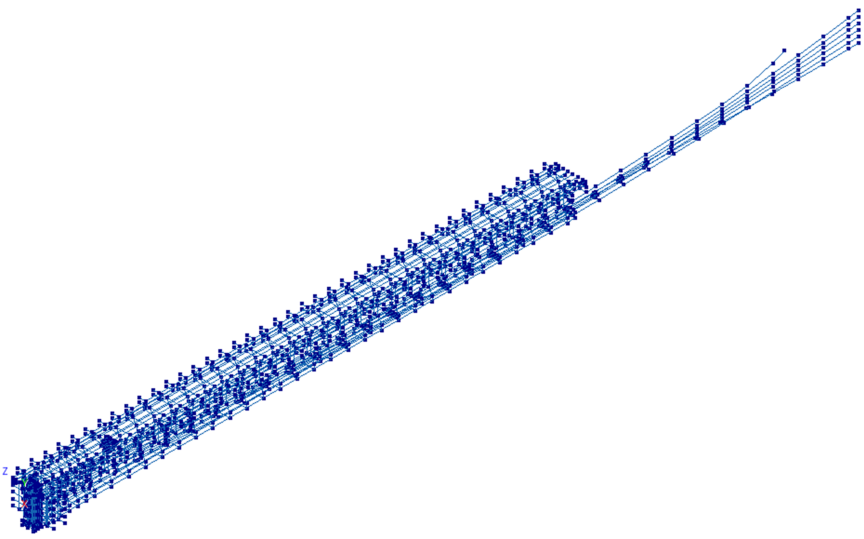

Figure 7.17: Embedded (regular) reinforcements and prestressing tendons 1–7 FEM model C

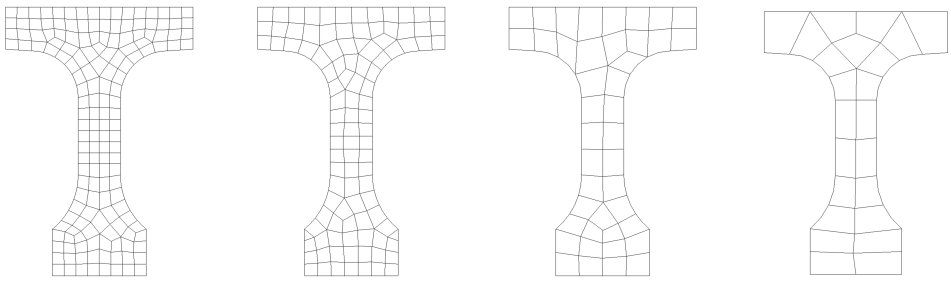

(a) 50 mm (b) 60 mm (c) 100 mm (d) 200 mm

Figure 7.18: Element size T-beam cross-section

Table 7.12: Results various element sizes

analysis	a mm	δ_{2a} mm	F_{2a} kN	δ_u mm	F_u kN	non-converged steps
C1-50/100-QNR	2250	23.9	1124	63.3	1512	0
C1-100-QNR	2250	20.9	1043	54.2	1420	0
C1-200-QNR	2250	17.9	980	71.4	1550	0
C2-60/100-QNR	4000	47.7	805	175.2	1151	0
C2-100-QNR	4000	43.3	758	166.8	1142	0
C2-200-QNR	4000	40.8	727	185.2	1155	0

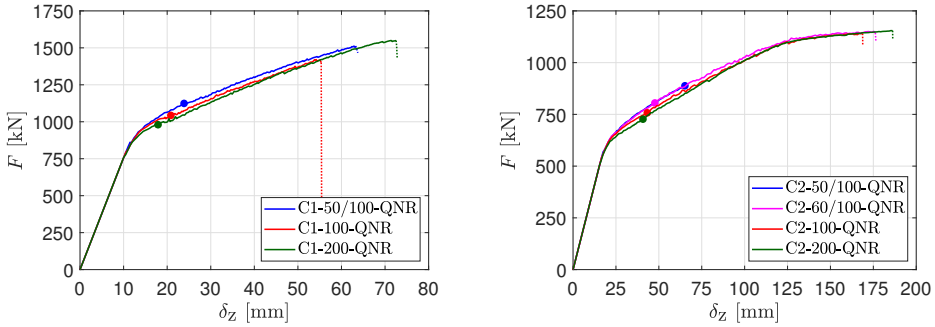

(a) Analyses C1 (b) Analyses C2

Figure 7.19: Analyses C1 (left) and C2 (right) load-deflection with various element sizes (bullet indicates start of phase 2b see Table 7.8, dashed line = non-converged (post-peak))

The results of the investigation are shown in Figure 7.19 (load-deflection) and Figures 7.21–7.22 (cracking behaviour). Figure 7.20 shows the color segments, used in all FEM principal strain plots, related to the various parts of the Hordijk softening curve. The results are also summarised in Table 7.12. In all analyses all load steps, up until the ultimate failure load, are converged (for convergence settings see Table 7.8). The convergence graph of analysis C1-50/100-QNR and C1-200-QNR is shown in Figures 7.23–7.24. For analyses C1, the maximum stress in the prestressing tendons is equal to 1532 N/mm^2 (C1-50/100-QNR), 1505 N/mm^2 (C1-100-QNR) and 1512 N/mm^2 (C1-200-QNR), see also Figure 7.3b. It appears analysis C1-100-QNR does not converge at the onset of plasticity, and therefore the ultimate failure load seems underestimated, see Figure 7.19a. From Table 7.12 and Figure 7.19 it can be concluded that phase 2a is extended when the element size is reduced. In addition, the force norm is better satisfied in phase 2b (see Table 7.8); compare Figure 7.23 to Figure 7.24.

Conclusion element size

The optimal element size to be used in this research is between 50–100 mm, in order to obtain sufficiently detailed cracking patterns for failure analysis and for comparison to the experiments. In addition, a smaller element size performs better in relation to the force norm in both phase 2a and phase 2b.

7.7.2. SOLUTION METHOD

THE performance of the incremental-iterative solution method is investigated with three methods: full (regular) Newton-Raphson (FNR), modified Newton-Raphson (MNR) and Quasi-Newton (QNR) with the Broyden-Fletcher-Goldfarb-Shanno (BFGS) method (DIANA 2019). An overview of the analyses is given in Table 7.13. In all models, an element size of 100 mm is adopted. In addition, a fixed step size is used equal to 0.3 mm for analyses C1 and 0.5 mm for analyses C2. These step sizes are selected based upon the average step sizes of analyses C1-100-QNR and C2-100-QNR, see Section 7.7.1. The analyses using a fixed step size are marked with (f), i.e. fixed step size, see Table 7.13. With the exception of the adaptive step size, the loading procedure and convergence settings are given in Section 7.3.4. For analyses using fixed step sizes, an isolated non-converged step in phase 2a is accepted. However, after two successive non-converged steps, phase 2b is initiated.

Table 7.13: Overview analyses for solution method investigation

analysis	FEM model	a mm	element size mm	solution method	step size mm
C1-100-FNR(f)	C	2250	100	FNR	0.3
C1-100-MNR(f)	C	2250	100	MNR	0.3
C1-100-QNR(f)	C	2250	100	QNR	0.3
C2-100-FNR(f)	C	4000	100	FNR	0.5
C2-100-MNR(f)	C	4000	100	MNR	0.5
C2-100-QNR(f)	C	4000	100	QNR	0.5

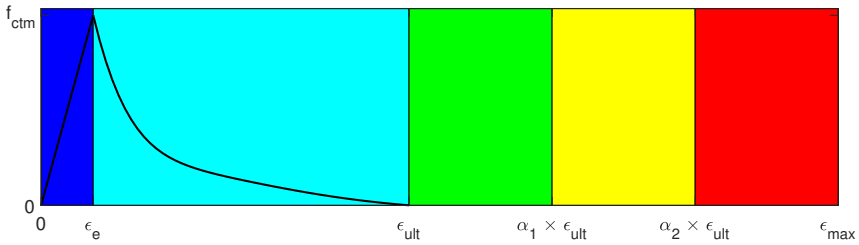

Figure 7.20: Total strain Hordijk softening curve with color segments used in FEM crack plots (not to scale)

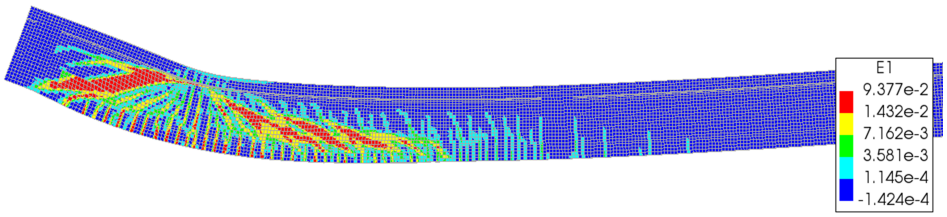

(a) C1-50-QNR, δ_u = 63.3 mm, F_u = 1512 kN
(color segments: $\alpha_1 = 2$, $\alpha_2 = 4$, see Figure 7.20)

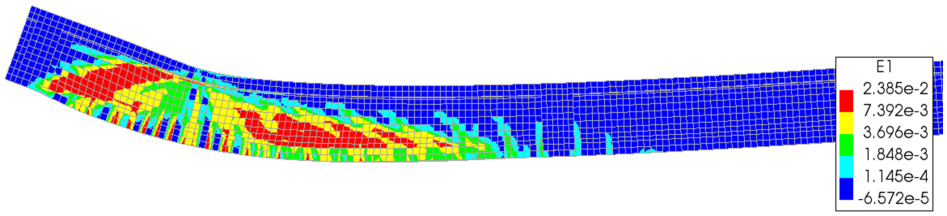

(b) C1-100-QNR, δ_u = 54.2 mm, F_u = 1420 kN
(color segments: $\alpha_1 = 2$, $\alpha_2 = 4$, see Figure 7.20)

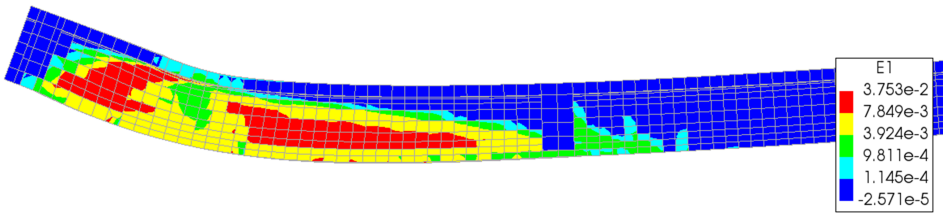

(c) C1-200-QNR, δ_u = 71.4 mm, F_u = 1550 kN
(color segments: $\alpha_1 = 4$, $\alpha_2 = 8$, see Figure 7.20)

Figure 7.21: Analyses C1 maximum principal strain E_1 at failure load

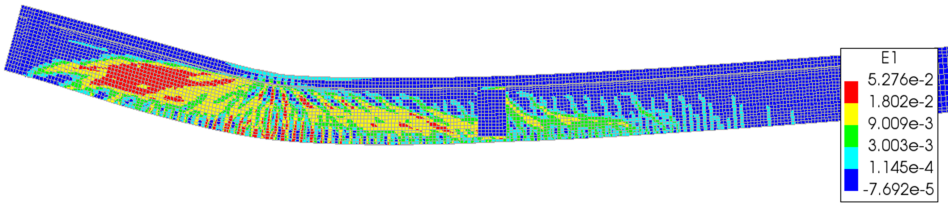

(a) C2-60/100-QNR, δ_u = 175.2 mm, F_u = 1151 kN
(color segments: α_1 = 3, α_2 = 6, see Figure 7.20)

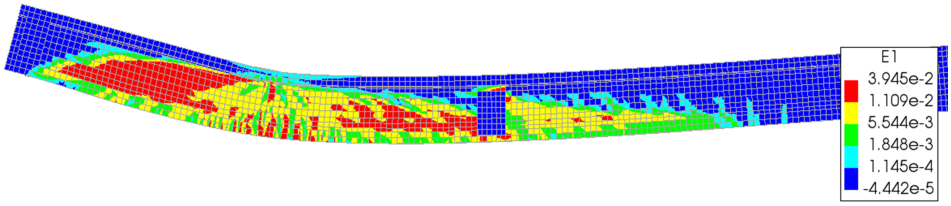

(b) C2-100-QNR, δ_u = 166.8 mm, F_u = 1142 kN
(color segments: α_1 = 3, α_2 = 6, see Figure 7.20)

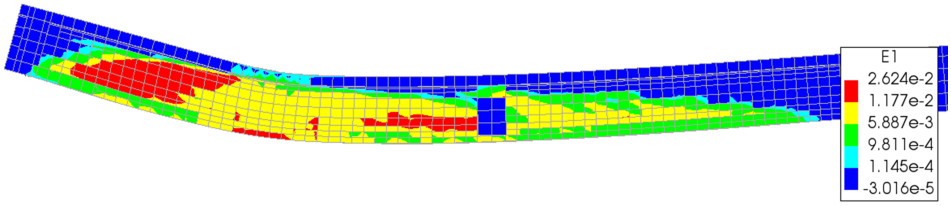

(c) C2-200-QNR, δ_u = 185.2 mm, F_u = 1155 kN
(color segments: α_1 = 6, α_2 = 12, see Figure 7.20)

Figure 7.22: Analyses C2 maximum principal strain E_1 at failure load

The results of the investigation are given in Figure 7.25 (load-deflection). The solution method convergence performance is summarised in Table 7.14 which also includes analyses C1-100-QNR and C2-100-QNR (see Section 7.7.1). Finally, the solution method iteration speed and run time are given in Table 7.15. The lower iteration speed for analyses C2, as compared to analyses C1, can be explained by the increase in nonlinear activity (larger cracked area), see Figures 7.21–7.22. In all cases, the Quasi-Newton method performs best in relation to the force norm. This method is able to extend phase 2a further than the other two methods, see Table 7.14 and Figure 7.25e–f. In terms of iteration speed, the Modified-Newton and the Quasi-Newton methods are very comparable, with the latter showing a 10% higher speed. The full Newton-Raphson method shows a decrease in speed of approximately 49% as compared to the other two methods. This can be explained by the fact that this method derives the tangent stiffness matrix in every iteration. Considering all analyses, the average number of iterations needed for each step (iter/step) is 24.0 in phase 1–2a and 10.4 in phase 2b. This illustrates the numerical 'cost' of satisfying both force and energy norms simultaneously. Contrary to the Quasi-Newton

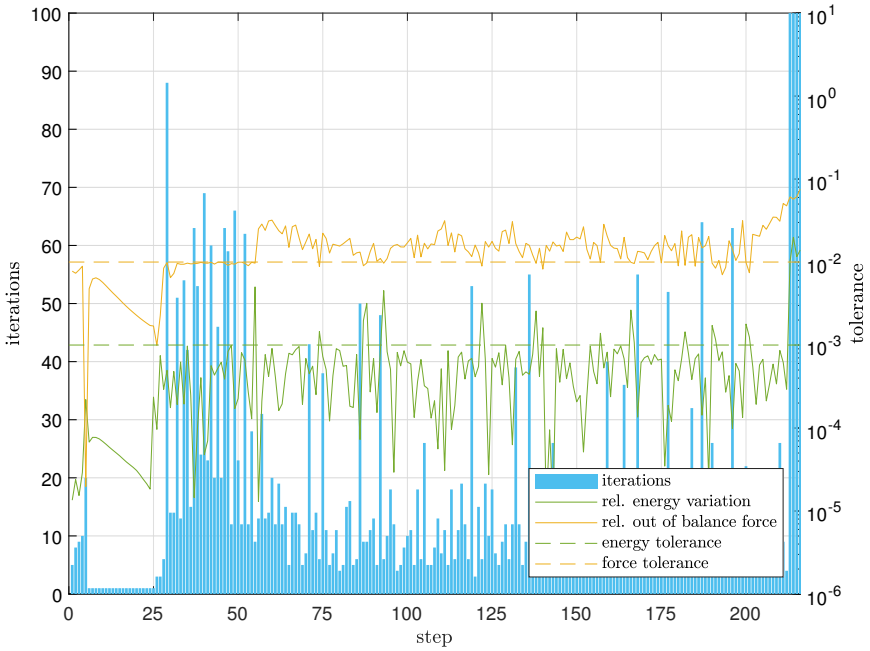

Figure 7.23: C1-50/100-QNR, convergence (Quasi-Newton)

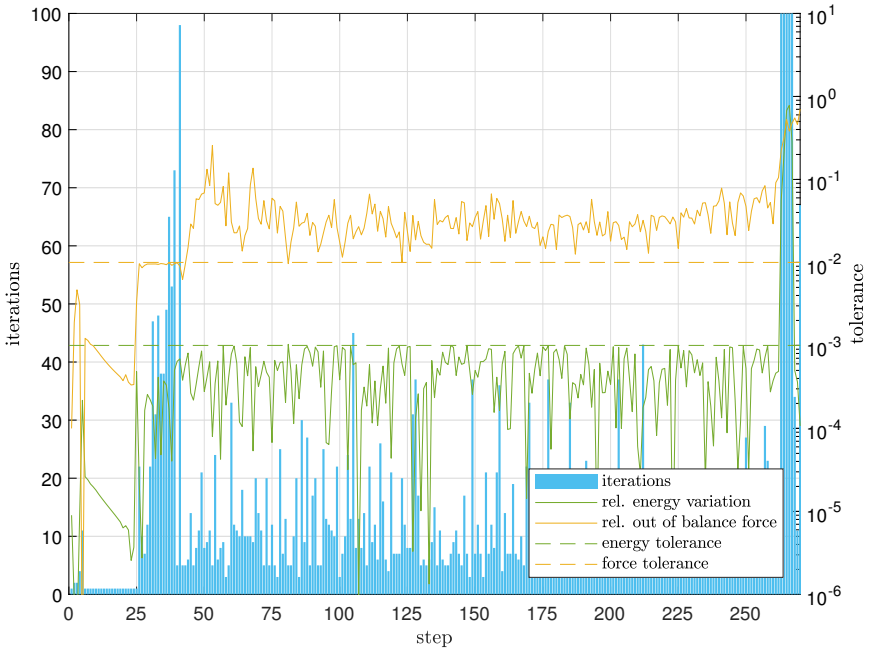

Figure 7.24: C1-200-QNR, convergence (Quasi-Newton)

method, the convergence graph of the Modified-Newton and the full Newton-Raphson method, show a similar constantly increasing deviation from the force norm in phase 2b, compare Figures 7.23–7.24 to Figure 7.26.

Table 7.14: Solution method convergence performance

analysis	phase 1–2a			phase 2b		
	steps	iter/step (average)	non-converged	steps	iter/step (average)	non-converged
C1-100-FNR(f)	72	15.4	1.4%	111	13.5	4.5%
C1-100-MNR(f)	75	21.1	4.0%	89	12.5	1.1%
C1-100-QNR(f)	180	23.7[a]	1.7%	5	6.4	0%
C1-100-QNR	52[b]	20.2	0%	139[c]	11.9	0%
C2-100-FNR(f)	81	27.3	3.7%	256	6.9	2.7%
C2-100-MNR(f)	74	29.2	8.1%	148	8.5	0%
C2-100-QNR(f)	107	31.4[d]	7.5%	234	11.4	0%
C2-100-QNR	99[e]	23.6	0%	251	11.7	0%

[a] first 75 steps: iter/step (average) = 16.3 (for comparison to other methods)

[b] resizing steps not included, i.e. 5 times with 100 iter/step (see Table 7.11)

[c] resizing steps not included, i.e. 3 times with 100 iter/step (see Table 7.11)

[d] first 81 steps: iter/step (average) = 21.7 (for comparison to other methods)

[e] resizing steps not included, i.e. 6 times with 100 iter/step (see Table 7.11)

Table 7.15: Solution method iteration speed and run time (min = minutes)

analysis	iter/min (average)	phase 1–2a min	phase 2b min	total min
C1-100-FNR(f)	10.34	107.23	144.92	252.15
C1-100-MNR(f)	20.25	78.15	54.94	133.09
C1-100-QNR(f)	unknown	-	-	-
C2-100-FNR(f)	9.29	238.03	190.14	428.17
C2-100-MNR(f)	17.26	125.19	72.88	198.07
C2-100-QNR(f)	18.92	177.58	140.99	318.57

Conclusion solution method

The optimal incremental-iterative solution method to be used in this research is the Quasi-Newton (QNR) with BFGS method. This method performs best in terms of achieving convergence especially in combination with an adaptive step size. Of the three methods, the QNR with BFGS method also requires the least amount of iterations for each step (except for analyses C2 phase 2b, see Table 7.14). Considering run time, the QNR with BFGS method shows an iteration speed (iter/min) comparable to the modified Newton-Raphson method, see Table 7.15. Finally, the QNR with the BFGS method does not exhibit the deviation from the force norm, in phase 2b, observed with both the Modified-Newton and the full Newton-Raphson method.

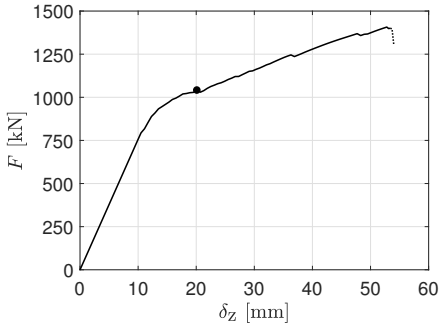

(a) C1-100-FNR(f)
(Full Newton-Raphson)

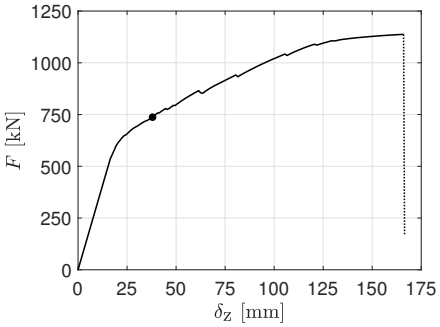

(b) C2-100-FNR(f)
(Full Newton-Raphson)

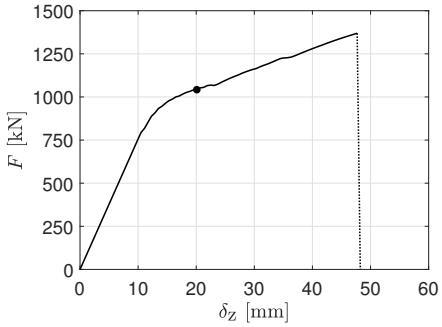

(c) C1-100-MNR(f)
(Modified Newton-Raphson)

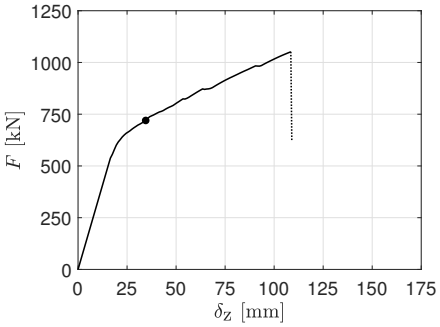

(d) C2-100-MNR(f)
(Modified Newton-Raphson)

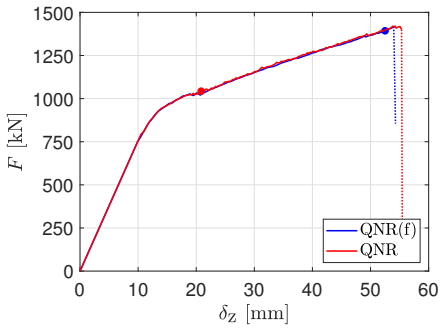

(e) C1-100-QNR(f) and C1-100-QNR
(Quasi-Newton)

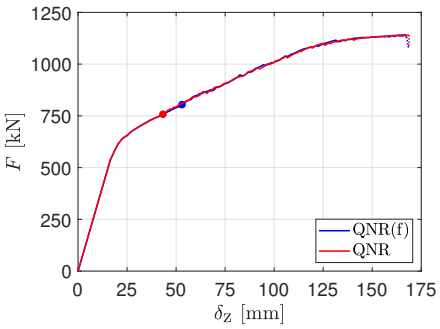

(f) C2-100-QNR(f) and C2-100-QNR
(Quasi-Newton)

Figure 7.25: Analyses C1 (left) and C2 (right) load-deflection using various solution methods
(bullet indicates start of phase 2b see Table 7.8, dashed line = non-converged (post-peak))

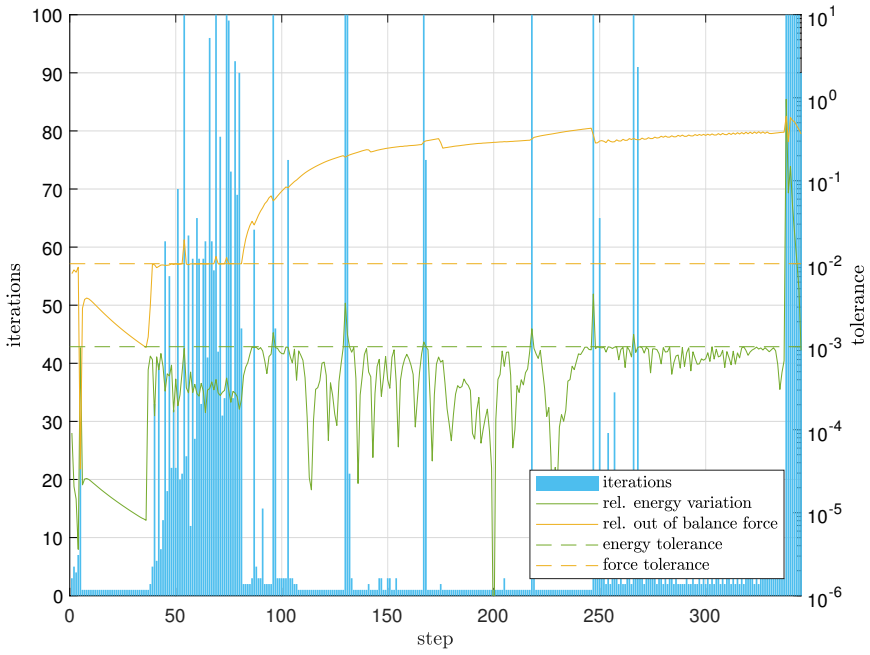

Figure 7.26: C2-100-FNR, convergence (Full Newton-Raphson)

7.8. RESULTS CONNECTED T-BEAMS (FEM MODELS A)

THIS section gives the results of the connected T-beams analyses A-T1 and A-T2, see Section 7.2.2 Table 7.1. For a detailed description of FEM model A the reader is referred to Section 7.4.

7.8.1. ANALYSIS A-T1

THE main results of analysis A-T1-90/180-QNR are summarized in Table 7.16 with the load versus deflection diagram given in Figure 7.27. The non-converged steps, reported in Table 7.16, are cross-marked in Figure 7.27. More detailed results of the analysis, such as the convergence graph and the comparison to the test measurements, are given in Appendix A Section A.1. The ultimate failure load is 87% compared to the test result (see Chapter 6 Section 6.4). The (linear) support and beam stiffnesses, as well as the T-beam cracking moment, are consistent with the test results, see Appendix A Section A.1. However, some limited stiffness deviation is observed in the supports of T-beam 9–10, see Appendix A Figures A.3a–b.

Table 7.16: Analysis A-T1-90/180-QNR results

analysis	δ_{2a} mm	F_{2a} kN	δ_u mm	F_u kN	total steps	non-converged steps
A-T1-90/180-QNR	13.2	2509	20.5	2760	227	2 (0.9%)

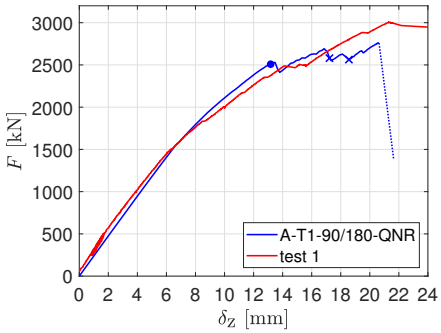

Figure 7.27: A-T1-90/180-QNR, load - deflection
(bullet indicates start of phase 2b see Table 7.8, dashed line = non-converged (post-peak))

Principal strains (cracking)

The cracking evolution of the loaded T-beam is shown in Figure 7.28 and in Figure 7.29, showing the loaded T-beam and the adjacent T-beams in cross-sectional view at the load position. The first cracking occurs at the bottom side of the T-beam's top flange, due to transverse sagging bending moments, see Figure 7.29a. These cracks then extend from the load position in the longitudinal directions. Next, T-beam bending cracks are initiated followed by cracking at the top side of the adjacent T-beam's top flange, due to transverse hogging bending moments, see Figures 7.29b–c. The T-beam bending cracks remain concentrated near the load position throughout the analysis, see Figure 7.28a–d. Next, a flexural shear crack develops from the load position in the direction of the intermediate cross-beam, see Figure 7.28a. The initial shear crack angle, of approximately 65°, rotates to an angle of 45°. Next, in the thin web of the T-beam, a large and sudden almost horizontal shear tension crack is initiated from the flexural shear crack, see Figure 7.28b. The initiation of this crack causes the first drop in the load - deflection diagram, see Figure 7.27. The location of this shear tension crack coincides with the compressive strut from the loading point towards the intermediate cross-beam, see Figure 7.31. Note that the minimum values of E_3, reported in Figure 7.31, do not exceed ϵ_u (see Figure 7.30) and are located on the top side of the T-beam, underneath the loading plate (not visible in Figure 7.31). The shear tension crack continues to grow and widen until failure, see Figures 7.28b–d. At the same time, punching in the integrated deck slab and the top flange of the T-beam is initiated, see Figure 7.28c and Figure 7.29d (first non-converged step). Just prior to failure, a secondary shear tension crack is initiated from the load position in the direction of the end support, see left side of Figure 7.28d (second non-converged step). Finally, the deck slab punching failure is shown in Figures 7.28d–e and Figure 7.29e, causing an immediate overload and failure of the T-beam. Figure 7.28e also shows the cracking at the anchorage of cable 7.

T-beam sectional forces

The sectional forces of the loaded T-beam, resulting from the composed line elements (see Section 7.4.4), are given in Figures 7.33–7.35 (normal force), 7.36 (shear force) and 7.37 (bending moment). Note that Figures 7.34–7.35 include the increase of the force

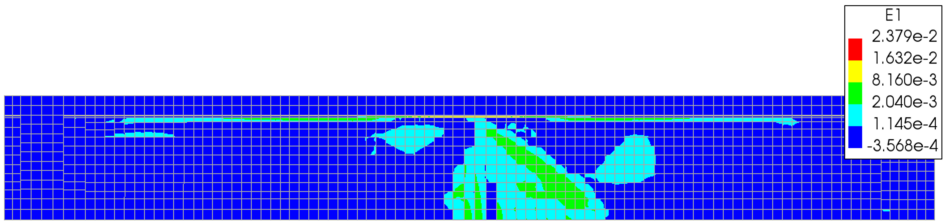

(a) F = 2531 kN, δ_z = 13.5 mm, T-beam flexural shear crack (side view)

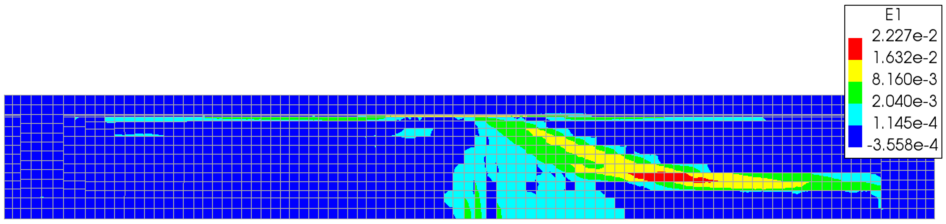

(b) F = 2412 kN, δ_z = 13.8 mm, T-beam shear tension crack (side view)

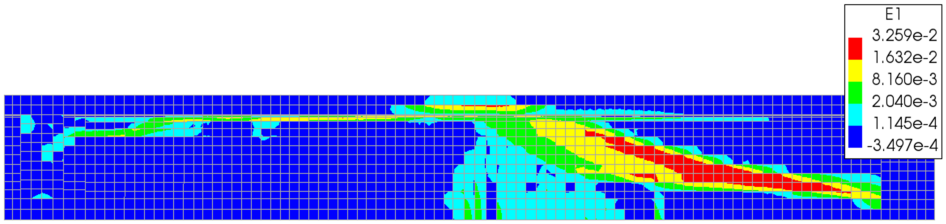

(c) F = 2580 kN, δ_z = 17.2 mm, deck slab punching initiation (side view)

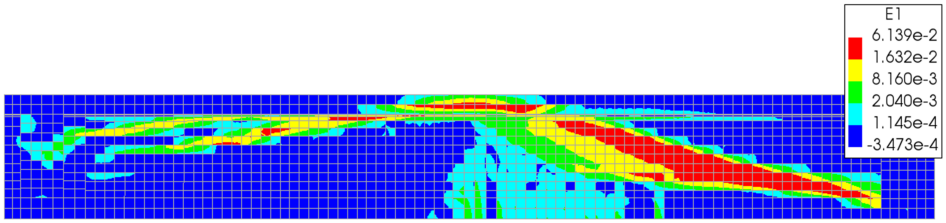

(d) F_u = 2760 kN, δ_u = 20.5 mm, T-beam shear tension crack, deck slab punching failure (side view)

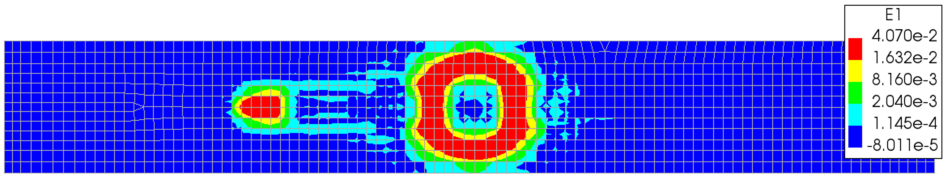

(e) F_u = 2760 kN, δ_u = 20.5 mm, deck slab punching failure (top view)

Figure 7.28: A-T1-90/180-QNR, maximum principal strain E_1 T-beam 11 (loaded beam)
(end cross-beam on the left side, intermediate cross-beam on the right side)
(color segments: α_1 = 4, α_2 = 8, see Figure 7.20)

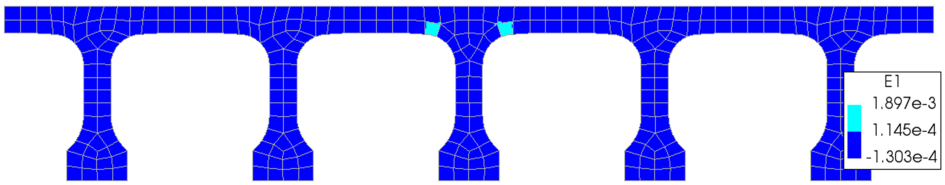

(a) F = 1425 kN, δ_z = 6.1 mm, T-beam top flange crack initiation

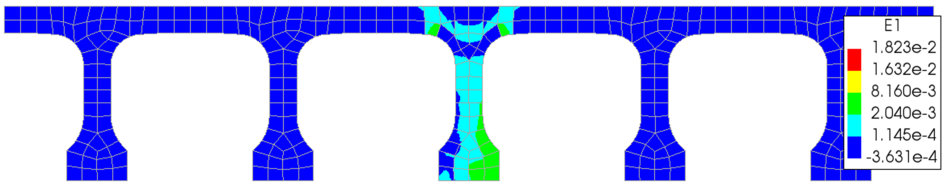

(b) F = 2135 kN, δ_z = 10.2 mm, T-beam bending crack

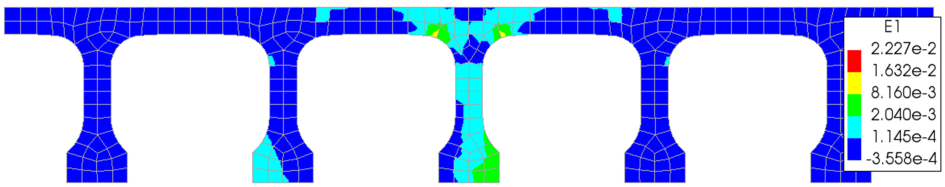

(c) F = 2412 kN, δ_z = 13.8 mm, adjacent T-beam cracking, deck slab cracking (top side)

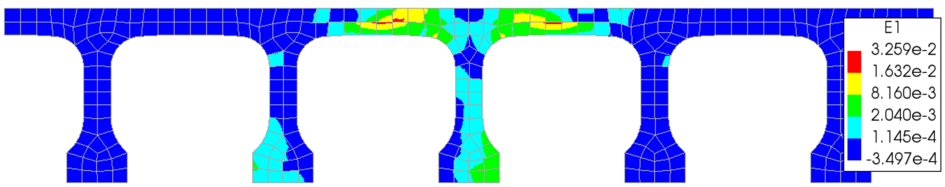

(d) F = 2580 kN, δ_z = 17.2 mm, deck slab punching initiation

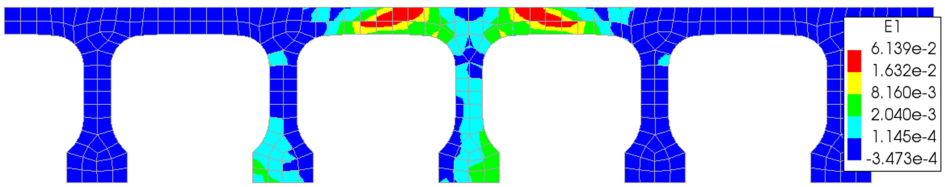

(e) F_u = 2760 kN, δ_u = 20.5 mm, deck slab punching failure

Figure 7.29: A-T1-90/180-QNR, maximum principal strain E_1 T-beam 9–13 (cross-section at load position) (color segments: $\alpha_1 = 4$, $\alpha_2 = 8$, see Figure 7.20)

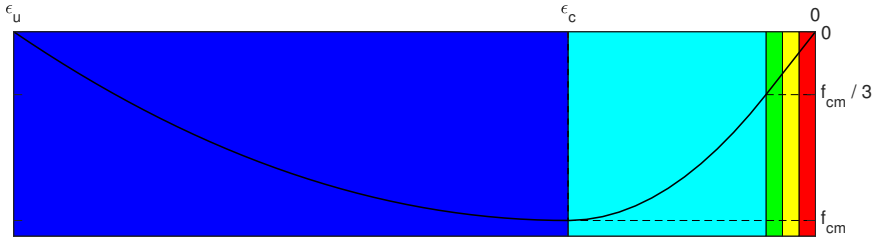

Figure 7.30: Total strain parabolic compression curve with color segments used in FEM crack plots (reduction of the compressive strength, as a result of lateral cracking, not included in this figure, see Section 7.3.2)

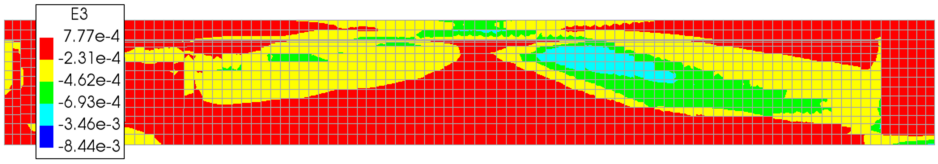

Figure 7.31: A-T1-90/180-QNR, minimum principal strain E_3 T-beam 11 (loaded beam), F_u = 2760 kN, δ_u = 20.5 mm (color segments see Figure 7.30)

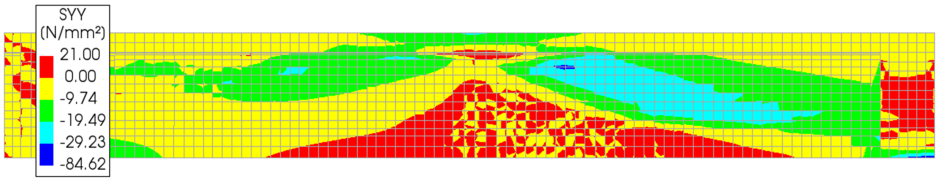

Figure 7.32: A-T1-90/180-QNR, stress S_{YY} T-beam 11 (loaded beam), F_u = 2760 kN, δ_u = 20.5 mm

in the prestressing tendons (ΔN_p) whereas Figure 7.33 shows the normal force N_x only. The initial sectional forces, as a result of the self-weight and the prestressing load(s), are given in Appendix A Section A.1 Figure A.5 and are equivalent to the linear analysis, see Chapter 5 Section 5.4 Figure 5.11b–d. The initial normal force and shear force correspond well to the linear analysis, compare Figures A.5a–b to Figures 5.11b–c. However, the initial bending moment is higher, by approximately 25–35%, as compared to the linear analysis (compare Figure A.5c to Figure 5.11d). It appears that the bending moment is more susceptible to the differences in modelling approach as compared to the normal force and the shear force.

With increased loading, the compressive normal force in the loaded T-beam initially decreases (tension) by approximately 630 kN and then increases significantly (compression) by approximately 1740 kN (loading point), compared to the initial value, see Figure 7.35 [8]. The initial compressive normal force, at the loading point, is recovered at a load of F = 2443 kN (89% F_u), see Figure 7.33b and Figure 7.35. Conversely, the compressive

[8] The 'loading point' in Figures 7.34–7.35 is defined as the location of $|N_x|_{max}$ shown in Figure 7.33c. The 'end cross-beam' is equal to the left side of Figure 7.33. The 'intermediate cross-beam' is equal to the right side of Figure 7.33.

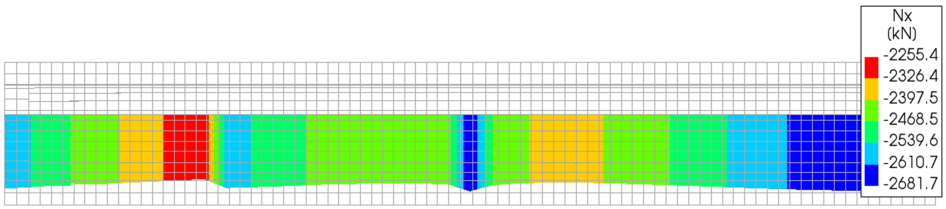

(a) F = 1877 kN, δ_z = 8.5 mm

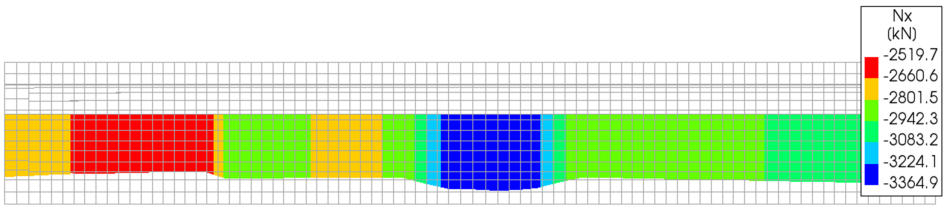

(b) F = 2443 kN, δ_z = 12.5 mm

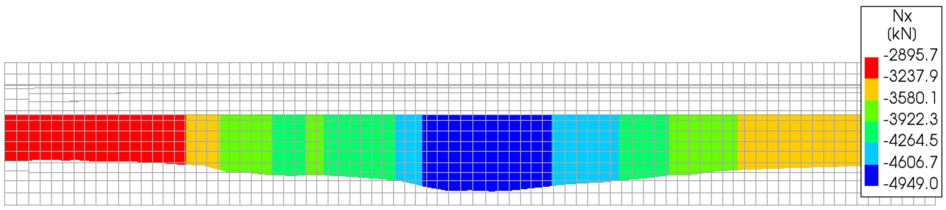

(c) F_u = 2760 kN, δ_u = 20.5 mm ($|N_x|_{max}$ = 4949 kN)

Figure 7.33: A-T1-90/180-QNR, normal force N_x T-beam 11 (loaded beam)

normal force in the adjacent T-beam 10 decreases (tension) by approximately 740 kN (loading point), compared to the initial value, see Figure 7.34. A similar behaviour is observed in the adjacent T-beam 12. The normal forces in the loaded T-beam, as a result from the point load, are therefore counteracted by the adjacent T-beams. The increase in compressive normal force, in the loaded T-beam, is relatively localised and diminishes towards the cross-beams, see Figure 7.33 and Figure 7.35.

Towards the end support the shear force, as a result of the point load, is reduced by the shear force of the self-weight and prestressing load(s), see left side of Figure A.5b. Initially, the shear force on either side of the loading point is almost equal, see Figure 7.36a. After the initiation of the shear tension crack, the shear force towards the intermediate cross-beam is reduced, see Figure 7.36b. Note that the maximum shear force of the analysis is shown in Figure 7.36c. The shape of the shear force graph corresponds well to the linear analysis, compare Figure 7.36 to Figure 5.17c.

After the initiation of the shear tension crack, the hogging bending moment at the intermediate cross-beam is also reduced, see Figure 7.37b.

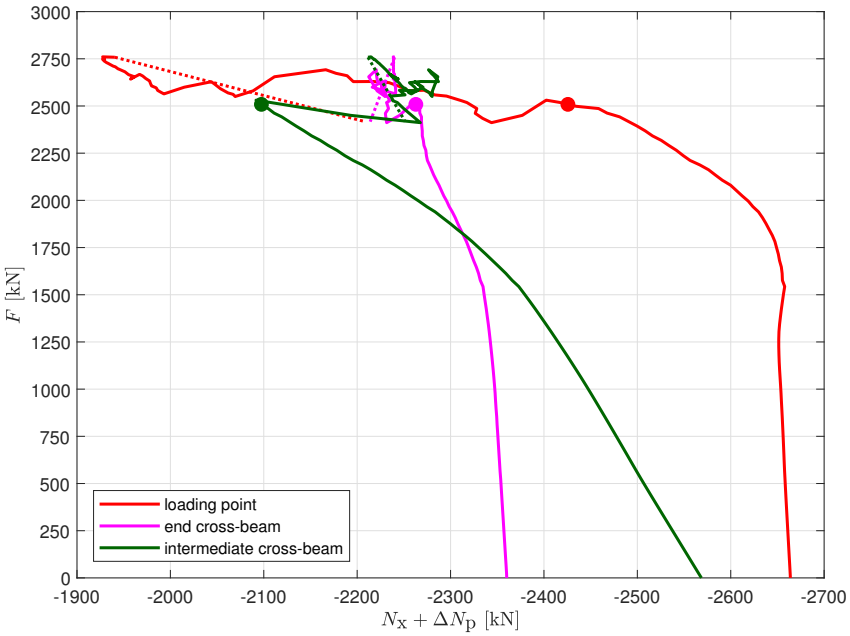

Figure 7.34: A-T1-90/180-QNR, normal force $N_x + \Delta N_p$ T-beam 10 (adjacent beam)
(bullet indicates start of phase 2b see Table 7.8, dashed line = non-converged (post-peak))

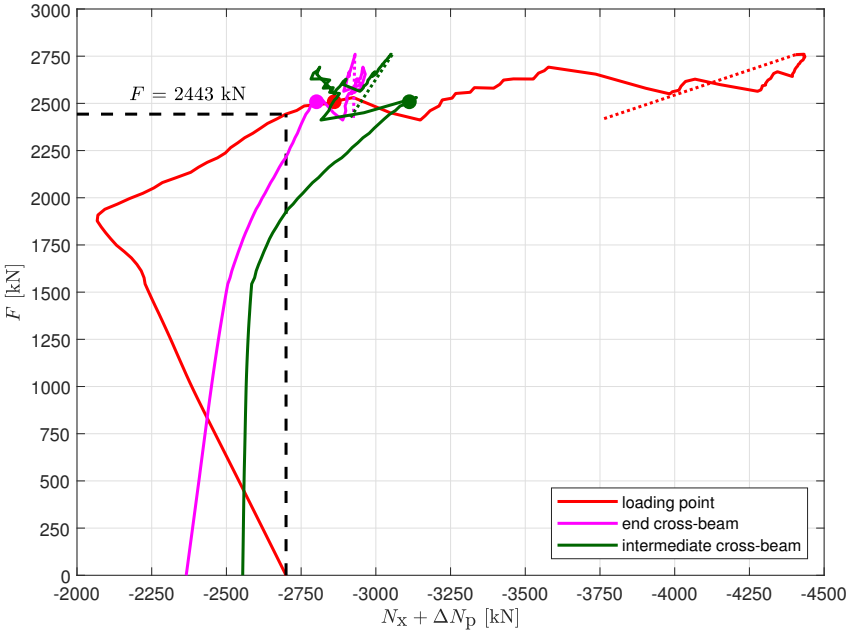

Figure 7.35: A-T1-90/180-QNR, normal force $N_x + \Delta N_p$ T-beam 11 (loaded beam)
(bullet indicates start of phase 2b see Table 7.8, dashed line = non-converged (post-peak))

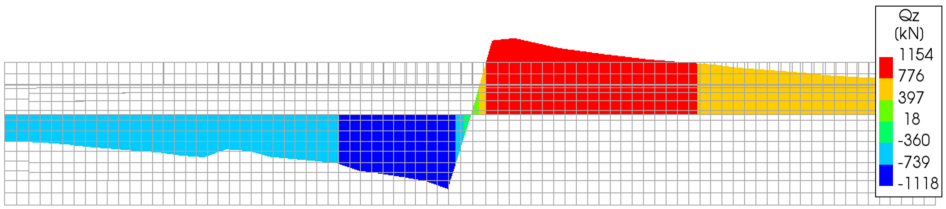

(a) F = 2531 kN, δ_z = 13.5 mm

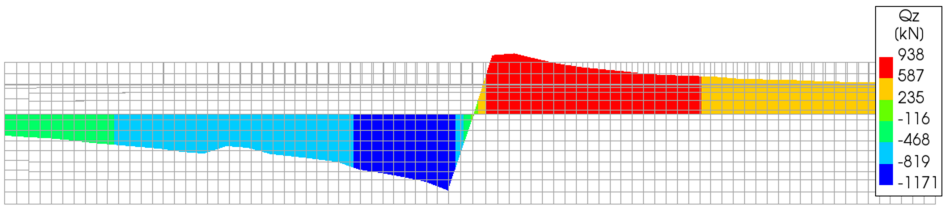

(b) F = 2412 kN, δ_z = 13.8 mm

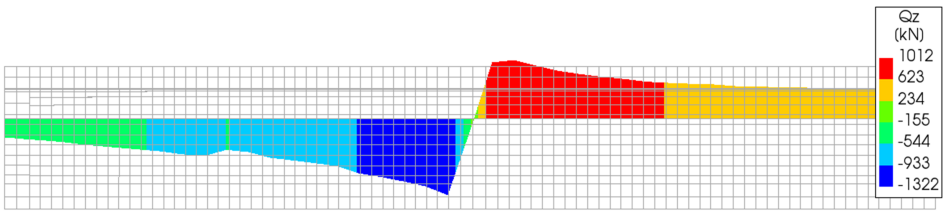

(c) F = 2692 kN, δ_z = 16.9 mm ($|Q_z|_{\max}$ = 1322 kN)

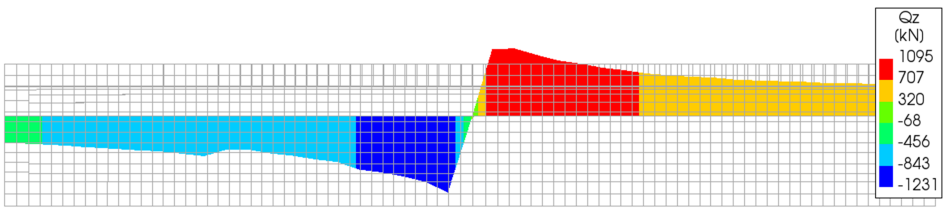

(d) F_u = 2760 kN, δ_u = 20.5 mm

Figure 7.36: A-T1-90/180, shear force Q_z T-beam 11 (loaded beam)
(end cross-beam on the left side, intermediate cross-beam on the right side)

Reinforcement and prestressing tendons stresses (yielding)

The stresses of the reinforcement, at the ultimate load, are given in Figure 7.38. All prestressing tendons remain linear elastic (see also Figure 7.3b). Stress peaks are visible at the location of the bending cracks and the shear tension crack towards the end support, see Figure 7.38a. Yielding does take place in the regular reinforcement. The T-beam stirrups, longitudinal and splitting reinforcements (anchorages of tendons 1–7) and the cross-beam reinforcement show a maximum stress of S_{xx} = 337 N/mm^2, see

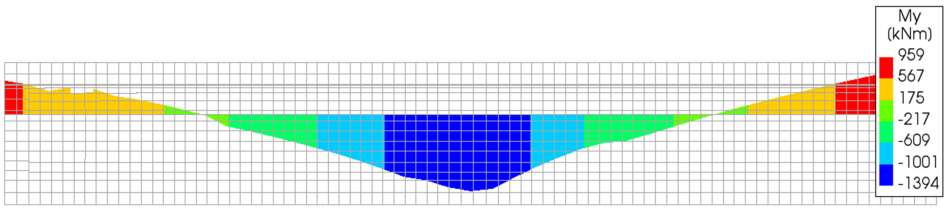

(a) F = 2531 kN, δ_z = 13.5 mm

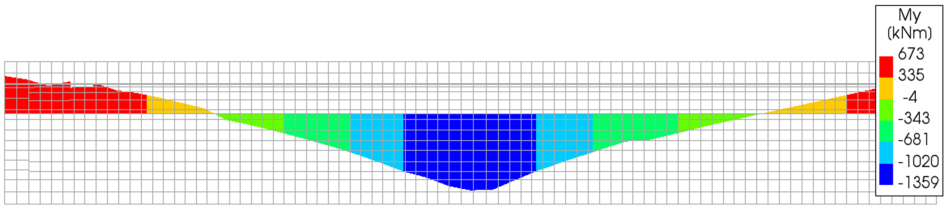

(b) F = 2412 kN, δ_z = 13.8 mm

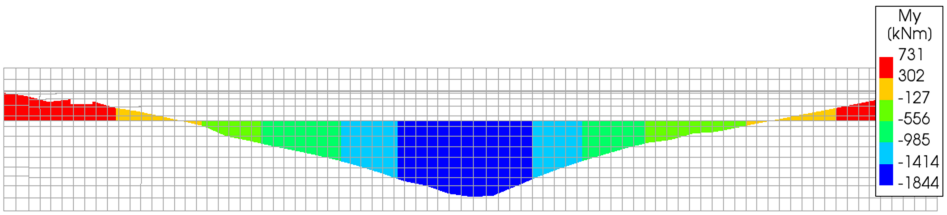

(c) F_u = 2760 kN, δ_u = 20.5 mm ($|M_y|_{max}$ = 1844 kNm)

Figure 7.37: A-T1-90/180, bending moment M_y T-beam 11 (loaded beam)
(end cross-beam on the left side, intermediate cross-beam on the right side)

Figure 7.38b. However, no fracture occurs as the ultimate strain $0.9\epsilon_u$ or $0.9\epsilon_{uk}$ is not exceeded (see also Figure 7.3a). At the ultimate load, the top side regular longitudinal reinforcement is just starting to yield in compression.

Stresses, in-plane forces and (relative) displacements concrete deck slab

The initial transverse stresses S_{XX} in the integrated deck slab, as a result of the self-weight and the (transverse) prestressing load(s), are given in Appendix A Section A.1 Figures A.6–A.7 and at the failure load in Figures A.8–A.9[9]. The stresses of the loaded T-beam and the adjacent T-beams, in cross-sectional view at the load position, are shown in Figure 7.39. Initially, as a result of the transverse prestressing (see also Figure 7.11), an average transverse compressive stress in the integrated deck slab, at the position of the load, is present of approximately S_{XX} = -2.9 N/mm^2, see Figure 7.39a. The distributed in-plane forces of the integrated deck slab, resulting from the composed surface elements (see Section 7.4.4), are given in Figure 7.41. The initial transverse in-plane force, at the

[9] Note that the shell elements have three layers in the thickness direction. For Figures A.6 and A.8 the output of layer 3 is selected (top side). For Figures A.7 and A.9 the output of layer 1 is selected (bottom side).

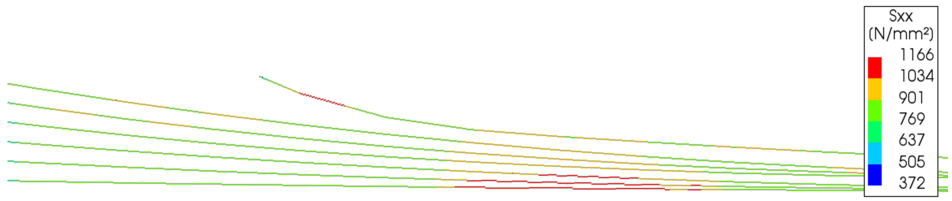

(a) Prestressing tendons 1–7

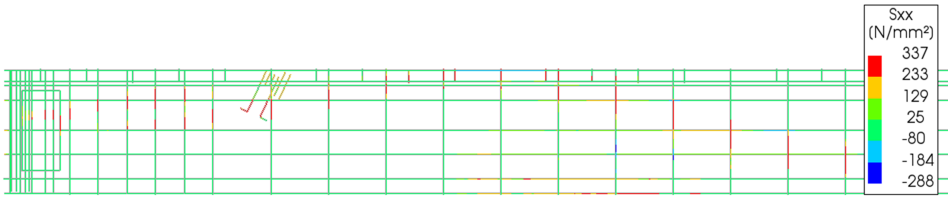

(b) Regular reinforcements

Figure 7.38: A-T1-90/180-QNR, stress S_{xx} embedded reinforcements T-beam 11 (loaded beam), F_u = 2760 kN, δ_u = 20.5 mm

position of the load, is equal to approximately N_{xx} = -2.9 × 180 = -522 N/mm, see Figure 7.41a. The distribution of the in-plane force N_{xx} in the longitudinal direction, along the edge of the composed surface elements closest to the loading point (see Figure 7.41), is given in Figure 7.42. At the ultimate load, the average transverse compressive stress in the integrated deck slab, at the load position, increases to a maximum of approximately S_{XX} = -13.9 N/mm^2, see Figure 7.39b. The corresponding in-plane force increases to approximately N_{xx} = -13.9 × 180 = -2500 N/mm, see Figure 7.41b and Figure 7.42. The evolution of the vertical displacement of the loaded T-beam and the adjacent T-beams, in cross-sectional view at the load position, is shown in Figure 7.40. At the edge of the bridge, close to the end support, the compressive stresses in the deck branch out to the center line of the adjacent T-beams, see Figure A.8.

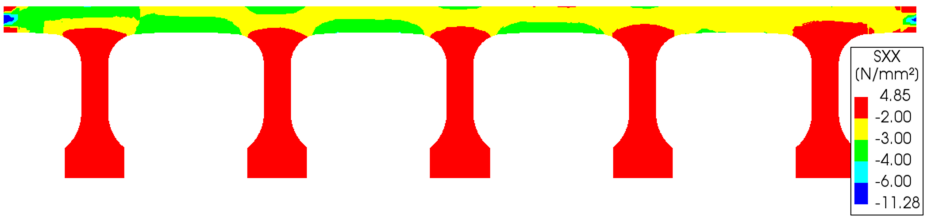

(a) Self-weight and prestressing load(s)

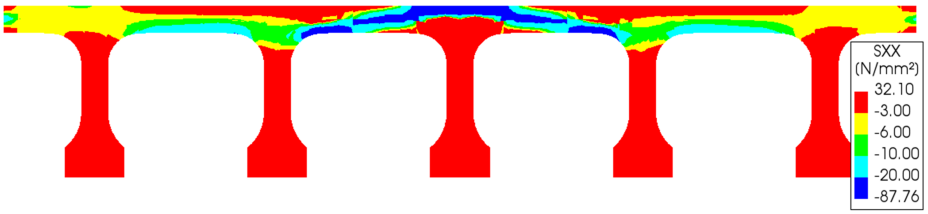

(b) F_u = 2760 kN, δ_u = 20.5 mm

Figure 7.39: A-T1-90/180-QNR, stress S_{XX} T-beam 9–13 (cross-section at load position)

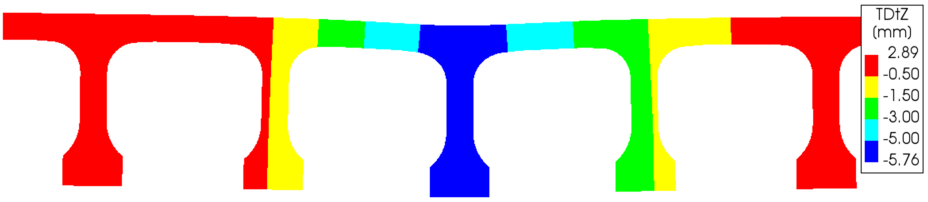

(a) F = 2412 kN, δ_z = 13.8 mm

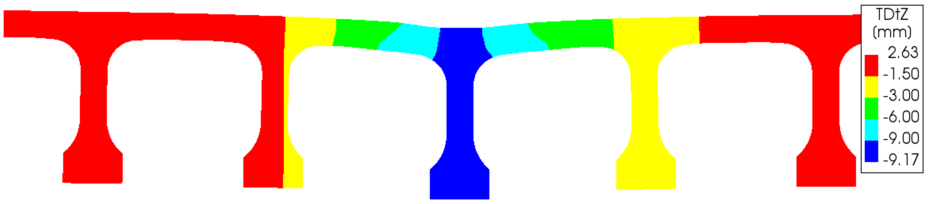

(b) F = 2580 kN, δ_z = 17.2 mm

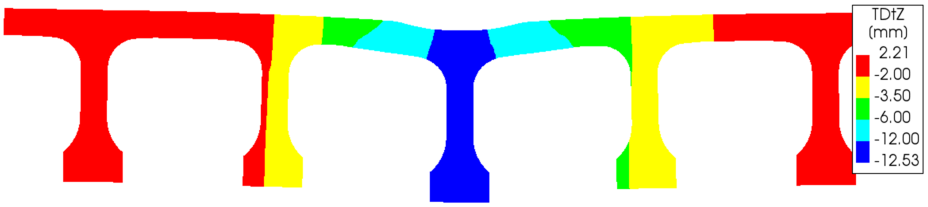

(c) F_u = 2760 kN, δ_u = 20.5 mm

Figure 7.40: A-T1-90/180-QNR, deformation δ_z T-beam 9–13 (cross-section at load position)

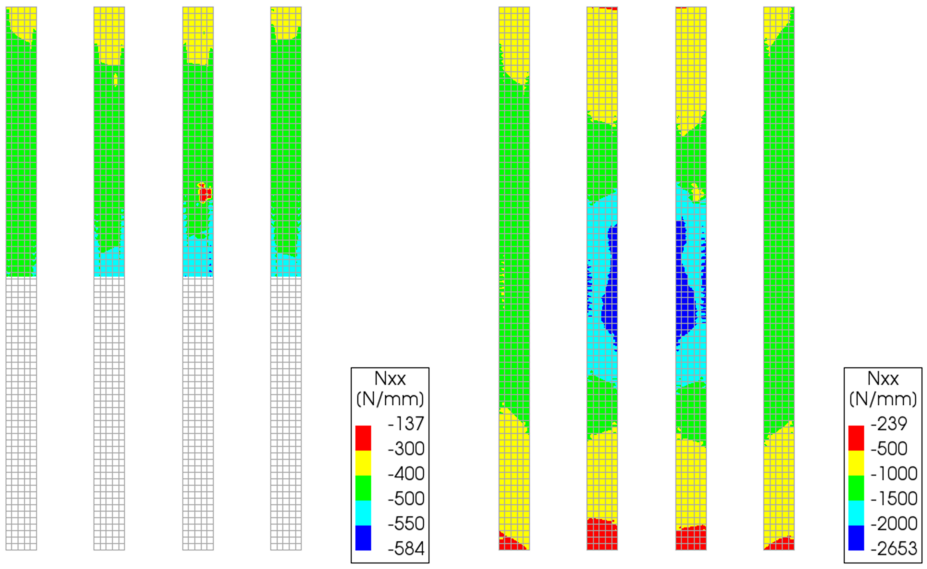

(a) Self-weight and prestressing load(s)

(b) F_u = 2760 kN, δ_u = 20.5 mm

Figure 7.41: A-T1-90/180-QNR, in-plane force N_{xx} (transverse direction)

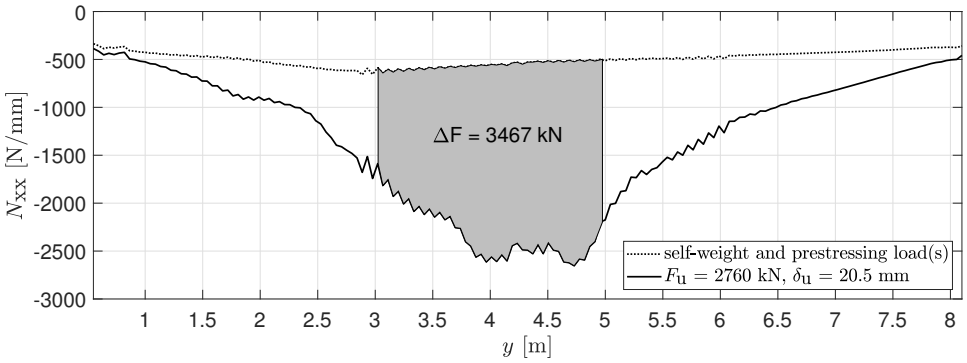

Figure 7.42: A-T1-90/180-QNR, in-plane force N_{xx}, horizontal axis in span direction with load at y = 4.00 m (see also Figure 7.41), grey area indicates integrated membrane force ΔF (see Chapter 8 Section 8.2.4)

7.8.2. ANALYSIS A-T2

THE main results of analysis A-T2-90/180-QNR are summarized in Table 7.17 with the load versus deflection diagram given in Figure 7.43. All load steps of the analysis are converged. More detailed results of the analysis, such as the convergence graph and the comparison to the test measurements, are given in Appendix A Section A.2. The ultimate failure load is 95% compared to the test result (see Chapter 6 Section 6.4). The (linear) support and beam stiffnesses, as well as the T-beam cracking moment, are consistent with the test results, see Appendix A Section A.2. However, some limited stiffness deviation is observed in the supports of T-beam 5 and 8, see Appendix A Figures A.12b,e.

Table 7.17: Analysis A-T2-90/180-QNR results

analysis	δ_{2a} mm	F_{2a} kN	δ_u mm	F_u kN	total steps	non-converged steps
A-T2-90/180-QNR	10.5	2915	16.4	3256	192	0

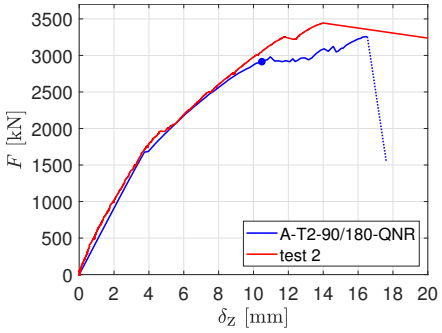

Figure 7.43: A-T2-90/180-QNR, load - deflection
(bullet indicates start of phase 2b see Table 7.8, dashed line = non-converged (post-peak))

Principal strains (cracking)

The cracking evolution of the loaded T-beam is shown in Figure 7.46 and in Figure 7.47, showing the loaded T-beam and the adjacent T-beams in cross-sectional view at the load position. The first cracking occurs at the bottom side of the T-beam's top flange, due to transverse sagging bending moments, see Figure 7.47a. These cracks then extend from the load position in the longitudinal directions. Towards the end support, they continue in the thin part of the web, between the top flange and the transition piece (see also Figure 7.8b), see Figure 7.46a. At the same time, T-beam bending cracks are initiated followed by cracking at the top side of the adjacent T-beam's top flange, due to transverse hogging bending moments, see Figures 7.47b–c. The T-beam bending cracks continue to extend from the load position throughout the analysis, mainly in the span direction, see Figure 7.46a–d. Next, a flexural shear crack develops from the load position in the direction of the intermediate cross-beam, see Figure 7.46b. The initial shear crack angle, of approximately 45°, ultimately rotates to an angle of 20°, see Figure 7.46d. Next, a shear tension crack develops from the load position in the direction of the end sup-

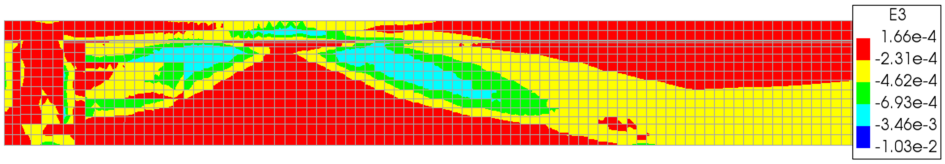

Figure 7.44: A-T2-90/180-QNR, minimum principal strain E_3 T-beam 6 (loaded beam), F_u = 3256 kN, δ_u = 16.4 mm (color segments see Figure 7.30)

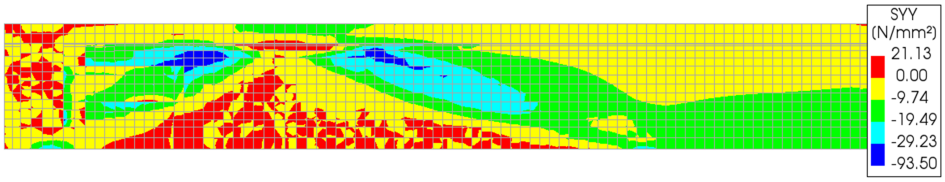

Figure 7.45: A-T2-90/180-QNR, stress S_{YY} T-beam 6 (loaded beam), F_u = 3256 kN, δ_u = 16.4 mm

port, see Figure 7.46c. At the same time, punching in the integrated deck slab and the top flange of the T-beam is initiated, see Figure 7.46c and Figure 7.47d. Finally, the deck slab punching failure is shown in Figure 7.46d–e and Figure 7.47e, causing an immediate overload and failure of the T-beam. The minimum principal strains E_3, at the ultimate load, are shown in Figure 7.44. The location of the flexural shear crack, shown in Figure 7.46d coincides with the compressive strut shown in Figure 7.44. Note that the minimum values of E_3, reported in Figure 7.44, do not exceed ϵ_u and are located on the top side of the T-beam, underneath the loading plate (not visible in Figure 7.44).

7

T-beam sectional forces

The sectional forces of the loaded T-beam, resulting from the composed line elements (see Section 7.4.4), are given in Figures 7.48–7.50 (normal force), 7.51 (shear force) and 7.52 (bending moment). Note that Figures 7.49–7.50 include the increase of the force in the prestressing tendons (ΔN_p) whereas Figure 7.48 shows the normal force N_x only. For the initial sectional forces, as a result of the self-weight and the prestressing load(s), the reader is referred to Appendix A Section A.1 Figure A.5.

With increased loading, the compressive normal force in the loaded T-beam initially decreases (tension) by approximately 370 kN and then increases significantly (compression) by approximately 2010 kN (loading point), compared to the initial value, see Figure 7.50 [10]. The initial compressive normal force, at the loading point, is recovered at a load of F = 2356 kN (72% F_u), see Figure 7.48b and Figure 7.50. Conversely, the compressive normal force in the adjacent T-beam 5 initially increases slightly (compression) by approximately 80 kN and then decreases (tension) by approximately 760 kN (loading point), compared to the initial value, see Figure 7.49. A similar behaviour is observed

[10] The 'loading point' in Figures 7.49–7.50 is defined as the location of $|N_x|_{max}$ shown in Figure 7.48c. The 'end cross-beam' is equal to the left side of Figure 7.48. The 'intermediate cross-beam' is equal to the right side of Figure 7.48.

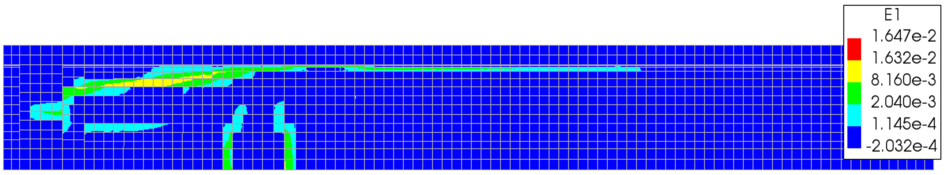

(a) F = 2288 kN, δ_z = 6.5 mm, T-beam shear tension crack (side view)

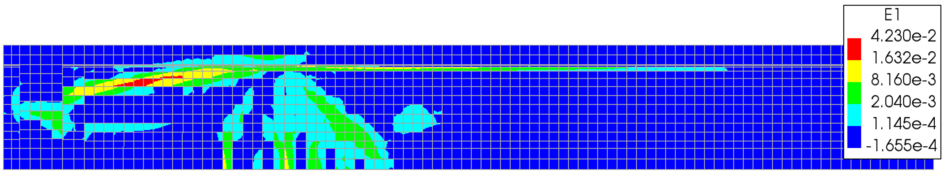

(b) F = 2899 kN, δ_z = 10.4 mm, T-beam flexural shear crack (side view)

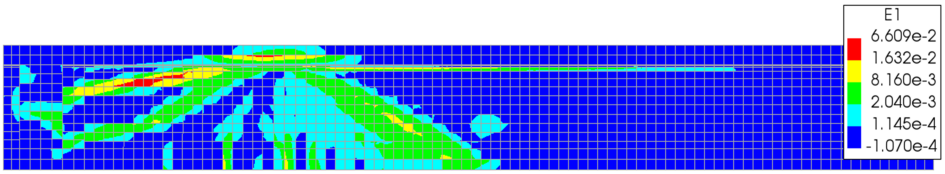

(c) F = 2915 kN, δ_z = 11.7 mm, T-beam shear tension crack, deck slab punching initiation (side view)

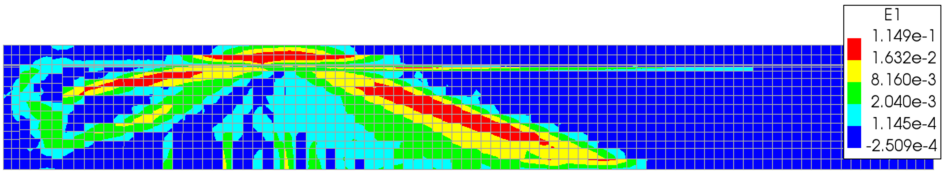

(d) F_u = 3256 kN, δ_u = 16.4 mm, deck slab punching failure (side view)

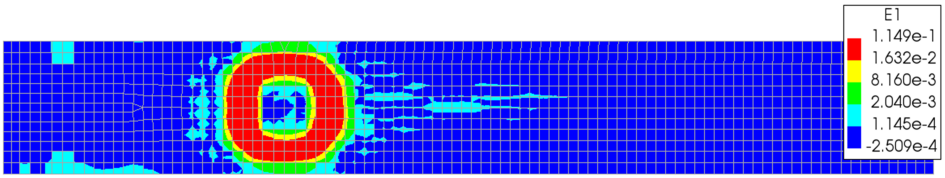

(e) F_u = 3256 kN, δ_u = 16.4 mm, deck slab punching failure (top view)

Figure 7.46: A-T2-90/180-QNR, maximum principal strain E_1 T-beam 6 (loaded beam)
(end cross-beam on the left side, intermediate cross-beam on the right side)
(color segments: α_1 = 4, α_2 = 8, see Figure 7.20)

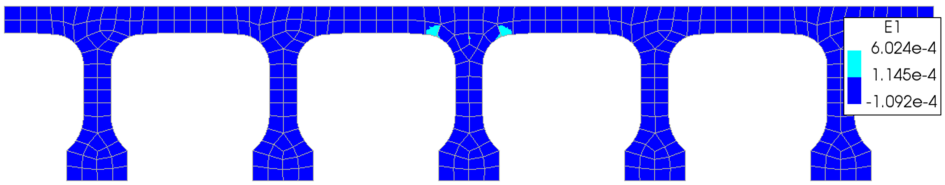

(a) F = 1190 kN, δ_z = 2.6 mm, T-beam top flange crack initiation

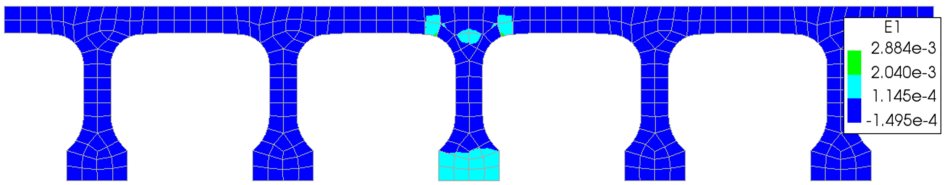

(b) F = 1686 kN, δ_z = 4.0 mm, T-beam bending crack

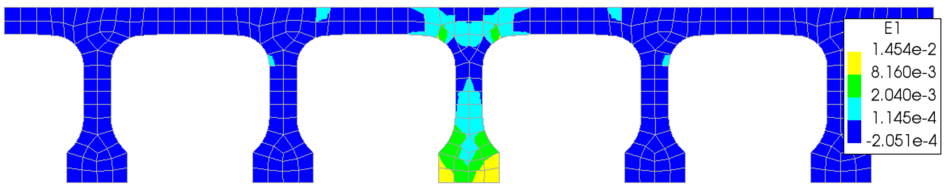

(c) F = 2472 kN, δ_z = 7.5 mm, deck slab cracking (top side)

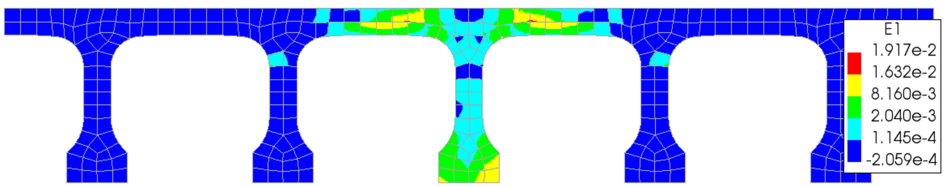

(d) F = 2915 kN, δ_z = 11.7 mm, deck slab punching initiation

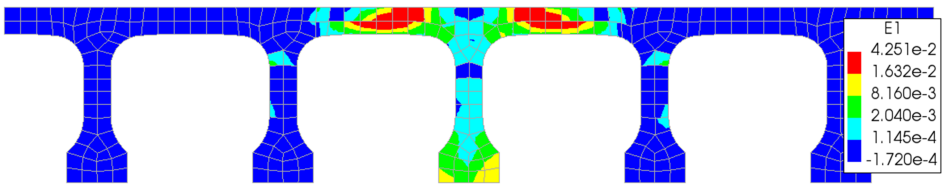

(e) F_u = 3256 kN, δ_u = 16.4 mm, deck slab punching failure

Figure 7.47: A-T2-90/180-QNR, maximum principal strain E_1 T-beam 4–8 (cross-section at load position) (color segments: α_1 = 4, α_2 = 8, see Figure 7.20)

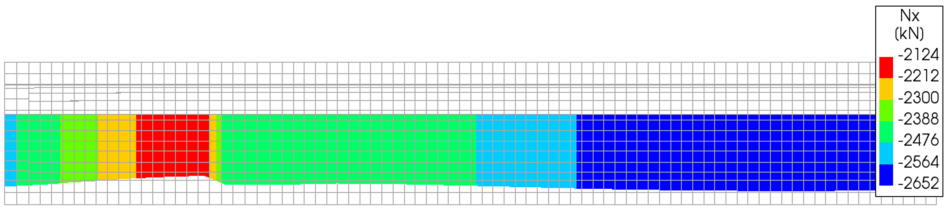

(a) F = 1676 kN, δ_z = 3.7 mm

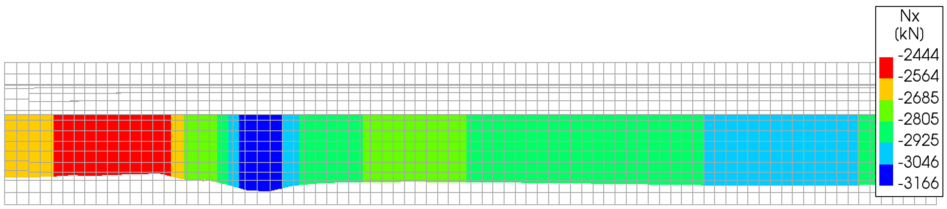

(b) F = 2356 kN, δ_z = 6.9 mm

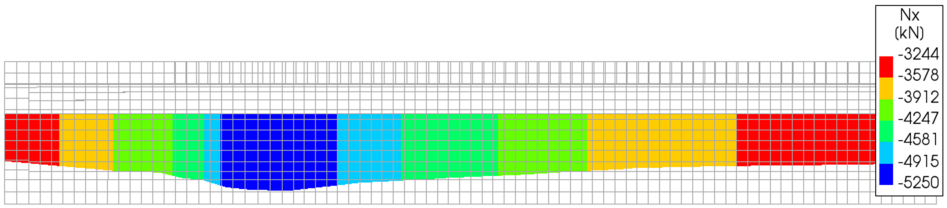

(c) F_u = 3256 kN, δ_u = 16.4 mm ($|N_x|_{max}$ = 5250 kN)

Figure 7.48: A-T2-90/180-QNR, normal force N_x T-beam 6 (loaded beam)

in the adjacent T-beam 7. Similar to analysis A-T1, see Section 7.8.1, the normal forces in the loaded T-beam, as a result from the point load, are counteracted by the adjacent T-beams. The increase in compressive normal force, in the loaded T-beam, is relatively localised and diminishes towards the cross-beams, see Figure 7.48 and Figure 7.50.

Towards the end support the shear force, as a result of the point load, is reduced by the shear force of the self-weight and prestressing load(s), see left side of Figure A.5b. Initially, the shear force on either side of the loading point is almost equal. After the initiation of the second shear tension crack, the shear force towards the end support is reduced, see Figure 7.51a. The maximum shear force of the analysis is reached at the failure load, see Figure 7.51b. The shape of the shear force graph corresponds well to the linear analysis, compare Figure 7.51 to Figure 5.17c.

Reinforcement and prestressing tendons stresses (yielding)

The stresses of the reinforcement, at the ultimate load, are given in Figure 7.53. All prestressing tendons remain linear elastic (see also Figure 7.3b). Stress peaks are visible at the location of the bending cracks and the shear tension cracks towards the end support, see Figure 7.53a. Yielding does take place in the regular reinforcement. The T-beam

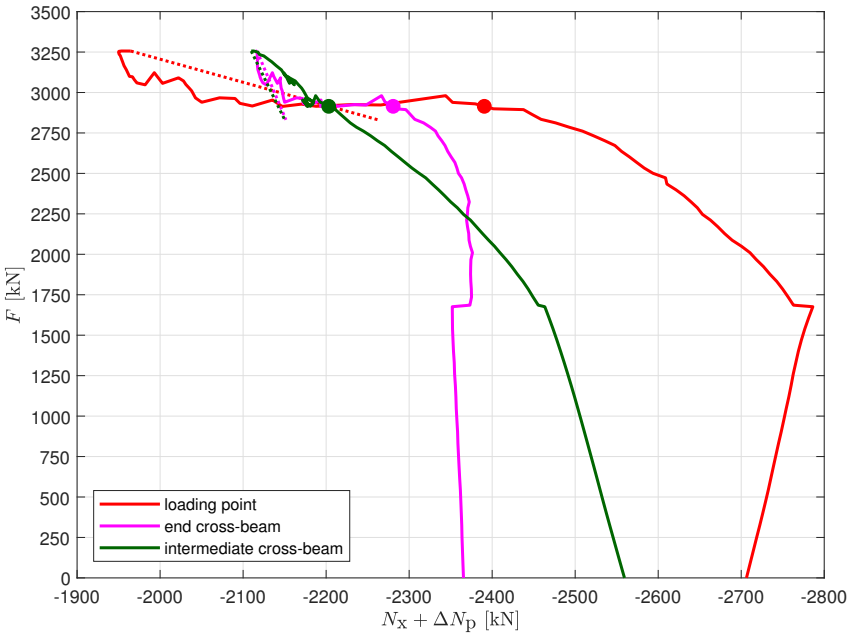

Figure 7.49: A-T2-90/180-QNR, normal force $N_x + \Delta N_p$ T-beam 5 (adjacent beam)
(bullet indicates start of phase 2b see Table 7.8, dashed line = non-converged (post-peak))

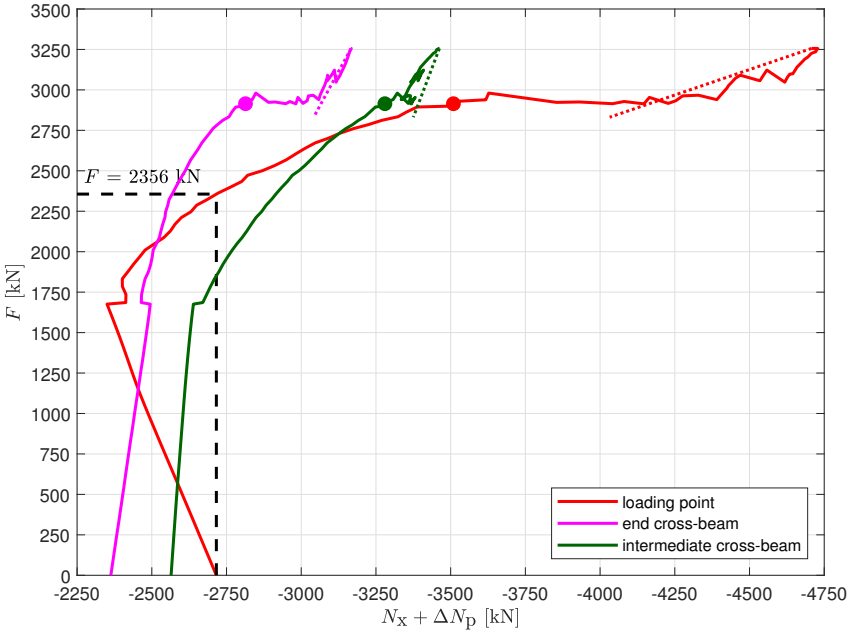

Figure 7.50: A-T2-90/180-QNR, normal force $N_x + \Delta N_p$ T-beam 6 (loaded beam)
(bullet indicates start of phase 2b see Table 7.8, dashed line = non-converged (post-peak))

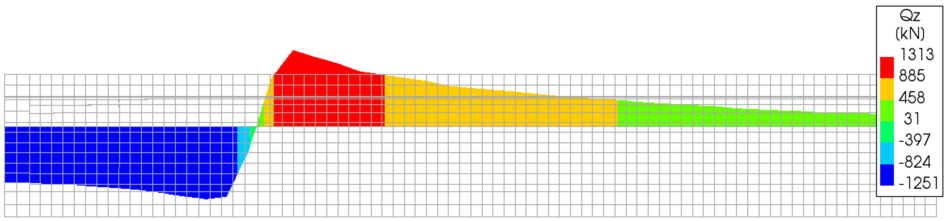

(a) F = 2923 kN, δ_z = 11.2 mm

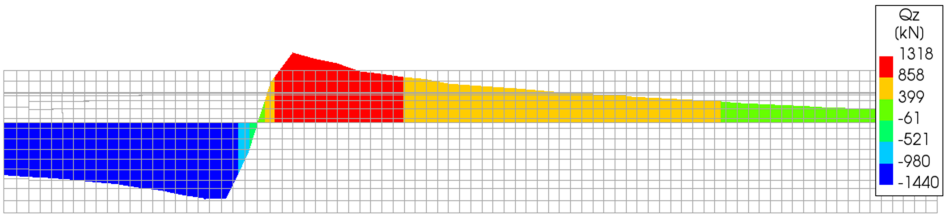

(b) F_u = 3256 kN, δ_u = 16.4 mm ($|Q_z|_{max}$ = 1440 kN)

Figure 7.51: A-T2-90/180, shear force Q_z T-beam 6 (loaded beam)
(end cross-beam on the left side, intermediate cross-beam on the right side)

stirrups, longitudinal and splitting reinforcements (anchorages of tendons 1–7) and the end cross-beam reinforcement show a maximum stress of S_{xx} = 338 N/mm^2, see Figure 7.53b. However, no fracture occurs as the ultimate strain $0.9\epsilon_u$ or $0.9\epsilon_{uk}$ is not exceeded (see also Figure 7.3a). At the ultimate load, the top side regular longitudinal reinforcement is just starting to yield in compression.

7

Stresses, in-plane forces and (relative) displacements concrete deck slab

The initial transverse stresses S_{XX} in the integrated deck slab, as a result of the self-weight and the (transverse) prestressing load(s), are given in Appendix A Section A.2 Figures A.14–A.15 and at the failure load in Figures A.16–A.17[11]. The stresses of the loaded T-beam and the adjacent T-beams, in cross-sectional view at the load position, are shown in Figure 7.54. Initially, as a result of the transverse prestressing (see also Figure 7.11), an average transverse compressive stress in the integrated deck slab, at the position of the load, is present of approximately S_{XX} = -3.1 N/mm^2, see Figure 7.54a. The distributed in-plane forces of the integrated deck slab, resulting from the composed surface elements (see Section 7.4.4), are given in Figure 7.56. The initial transverse in-plane force, at the position of the load, is equal to approximately N_{xx} = -3.1 × 180 = -558 N/mm, see Figure 7.56a. The distribution of the in-plane force N_{xx} in the longitudinal direction, along the edge of the composed surface elements closest to the loading point (see Figure 7.56), is given in Figure 7.57. At the ultimate load, the average transverse compressive stress in the integrated deck slab, at the load position, increases to a maximum of approximately S_{XX} = -12.5 N/mm^2, see Figure 7.54b. The corresponding in-plane force increases to

[11] Note that the shell elements have three layers in the thickness direction. For Figures A.14 and A.16 the output of layer 3 is selected (top side). For Figures A.15 and A.17 the output of layer 1 is selected (bottom side).

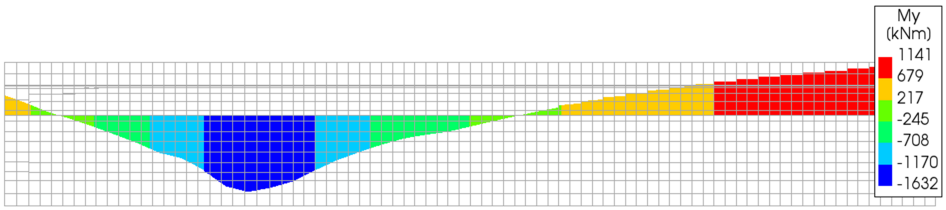

(a) F = 2923 kN, δ_z = 11.2 mm

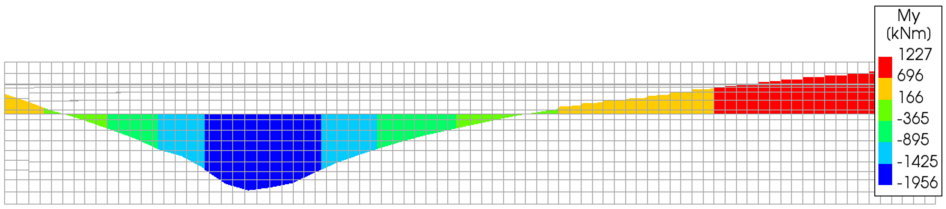

(b) F_u = 3256 kN, δ_u = 16.4 mm ($|M_y|_{max}$ = 1956 kNm)

Figure 7.52: A-T2-90/180, bending moment M_y T-beam 6 (loaded beam)
(end cross-beam on the left side, intermediate cross-beam on the right side)

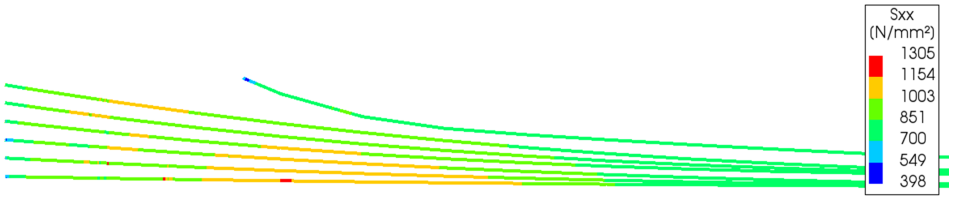

(a) Prestressing tendons 1–7

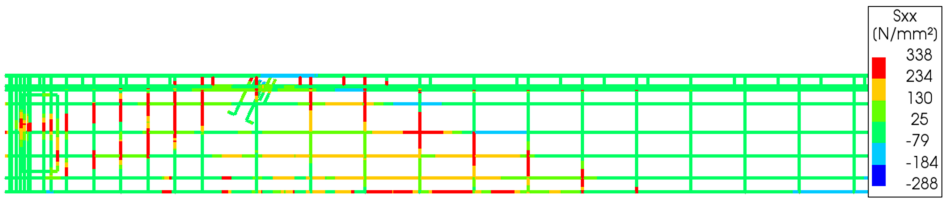

(b) Regular reinforcements

Figure 7.53: A-T2-90/180-QNR, stress S_{xx} embedded reinforcements T-beam 6 (loaded beam), F_u = 3256 kN, δ_u = 16.4 mm

approximately N_{xx} = -12.5 × 180 = -2250 N/mm, see Figure 7.56b and Figure 7.57. The evolution of the vertical displacement of the loaded T-beam and the adjacent T-beams, in cross-sectional view at the load position, is shown in Figure 7.55.

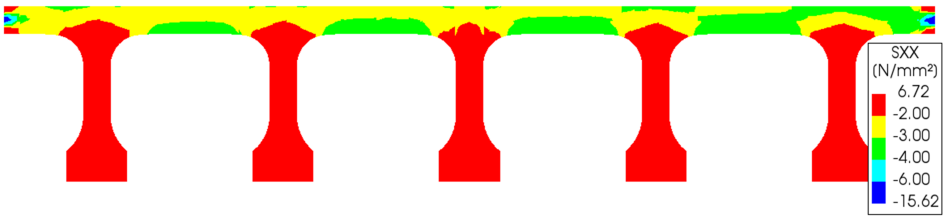

(a) Self-weight and prestressing load(s)

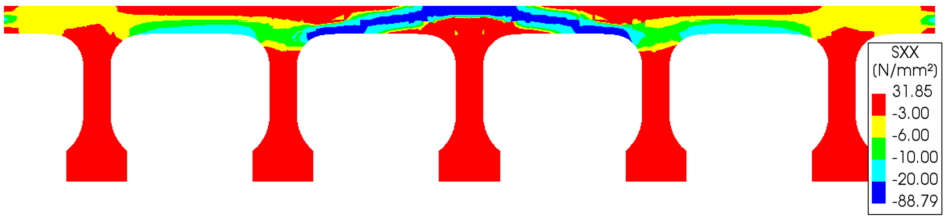

(b) F_u = 3256 kN, δ_u = 16.4 mm

Figure 7.54: A-T2-90/180-QNR, stress S_{XX} T-beam 4–8 (cross-section at load position)

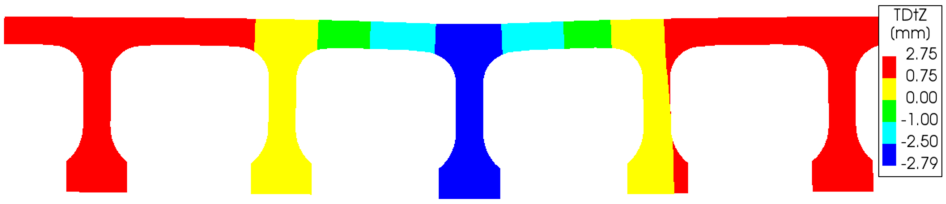

(a) F = 2472 kN, δ_z = 7.5 mm

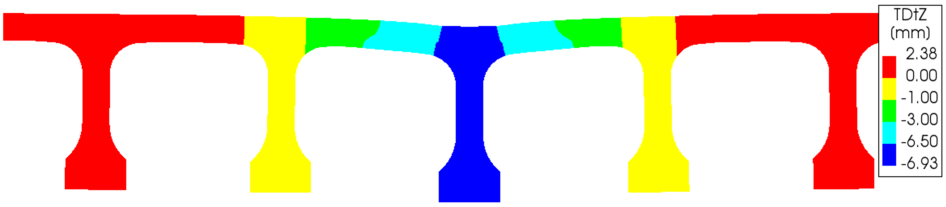

(b) F = 2915 kN, δ_z = 11.7 mm

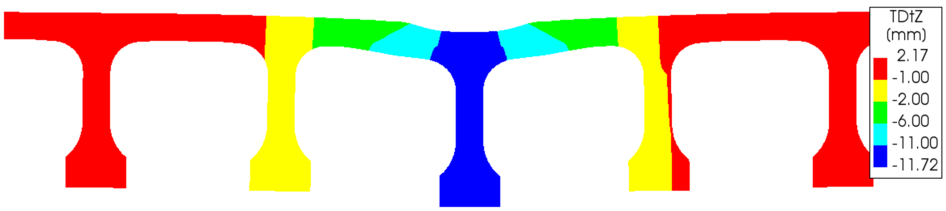

(c) F_u = 3256 kN, δ_u = 16.4 mm

Figure 7.55: A-T2-90/180-QNR, deformation δ_z T-beam 4–8 (cross-section at load position)

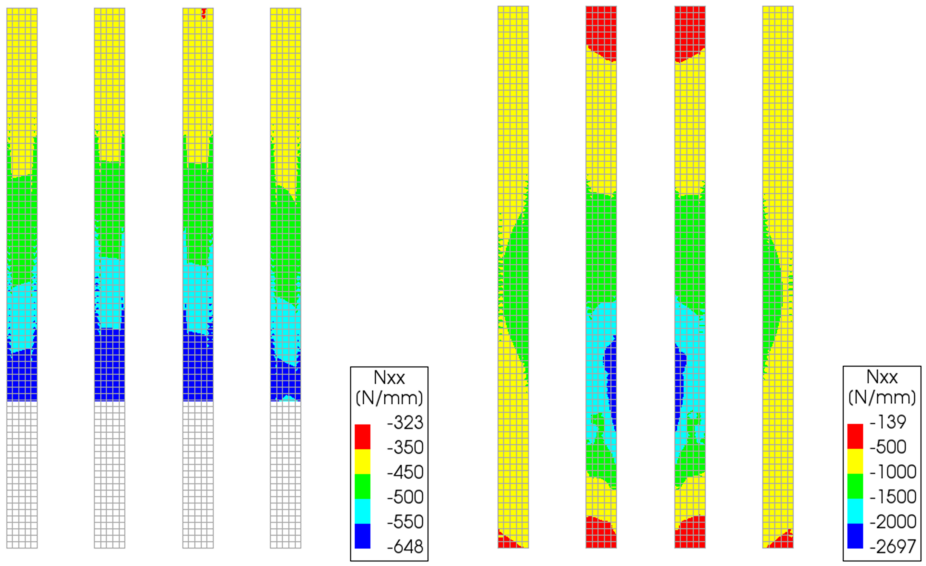

(a) Self-weight and prestressing load(s)

(b) F_u = 3256 kN, δ_u = 16.4 mm

Figure 7.56: A-T2-90/180-QNR, in-plane force N_{xx} (transverse direction)

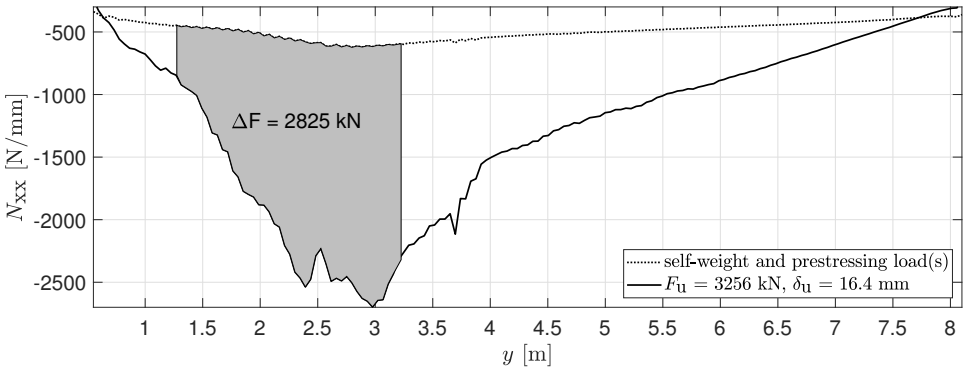

Figure 7.57: A-T2-90/180-QNR, in-plane force N_{xx}, horizontal axis in span direction with load at y = 2.25 m (see also Figure 7.56), grey area indicates integrated membrane force ΔF (see Chapter 8 Section 8.2.4)

7.9. RESULTS DISCONNECTED T-BEAMS (FEM MODELS B)

THIS section gives the results of the disconnected T-beams analyses B-T4, B-T5, B-T6 and B-T7, see Section 7.2.2 Table 7.1. For a detailed description of FEM model B the reader is referred to Section 7.5.

7.9.1. ANALYSIS B-T4

THE main results of analysis B-T4-60/180-QNR are summarized in Table 7.18 with the load versus deflection diagram given in Figure 7.58. All load steps of the analysis are converged. More detailed results of the analysis, such as the convergence graph and the comparison to the test measurements, are given in Appendix B Section B.1. The ultimate failure load is 89% compared to the test result (see Chapter 6 Section 6.5). The (linear) support stiffness, as well as the T-beam cracking moment, are consistent with the test results, see Appendix B Section B.1. However, some stiffness deviation is observed at the position of the intermediate cross-beam, see Appendix B Figure B.3b.

Table 7.18: Analysis B-T4-60/180-QNR results

analysis	δ_{2a} mm	F_{2a} kN	δ_u mm	F_u kN	total steps	non-converged steps
B-T4-60/180-QNR	20.9	1148	50.6	1486	218	0

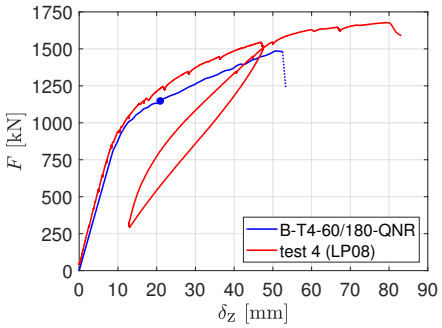

Figure 7.58: B-T4-60/180-QNR, load - deflection
(bullet indicates start of phase 2b see Table 7.8, dashed line = non-converged (post-peak))

Principal strains (cracking)

The cracking evolution of the loaded T-beam is shown in Figure 7.60 and in Figure 7.61, showing the clamped end. The first cracking occurs at the clamped end due to the hogging bending moment. In addition, horizontal cracking starts in the T-beam, near the load position, between the transition piece and the T-beam's top flange (see also Figure 7.8b). Next, bending cracks are initiated in the T-beam, followed by flexural shear cracks, see Figure 7.60a. At the same time, torsion cracks are initiated in the end cross-beam. In addition, the full width of the disconnected T-beam is now cracked on the top side, see Figure 7.61a. Next, horizontal shear tension cracks are initiated in the T-beam, below the

transition piece, see Figure 7.60b. Finally, the T-beam fails due to a large flexural shear crack developing from the loading point to the end support, see Figure 7.60c.

T-beam sectional forces (clamped end)

The sectional forces of the loaded T-beam at the clamped end, resulting from the composed line elements (see Section 7.5.1), are given in Figure 7.59. Both the shear force and the bending moment remain linear up until a load of approximately F = 1100 kN, when the full width of the disconnected T-beam is cracked on the top side, see Figure 7.61a.

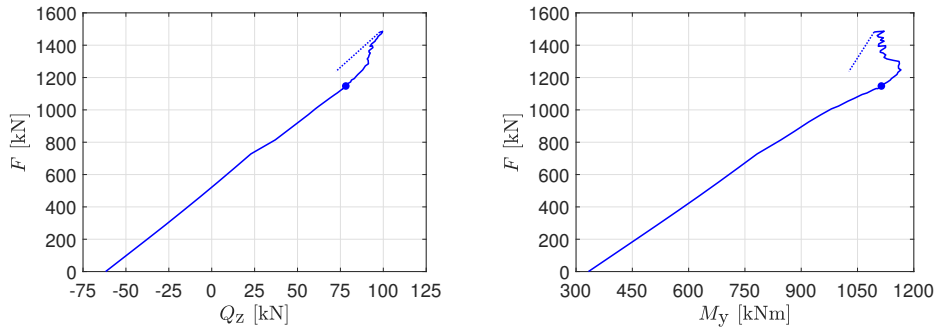

(a) Shear force Q_z

(b) Bending moment M_y

Figure 7.59: B-T4-60/180-QNR, shear force Q_z and bending moment M_y T-beam 12 (clamped end) (bullet indicates start of phase 2b see Table 7.8, dashed line = non-converged (post-peak))

Reinforcement and prestressing tendons stresses (yielding)

The stresses of the reinforcement, at the ultimate load, are given in Figure 7.62. Yielding of the prestressing tendons is initiated at a load level of F = 1300 kN, in the two tendons closest to the bottom of the cross-section. All other tendons remain linear elastic throughout the analysis. At the ultimate load, the maximum stress in the tendons is S_{xx} = 1519 N/mm^2, see Figure 7.62a.

In the regular reinforcement yielding is initiated at a load level of F = 866 kN, in the longitudinal reinforcement closest to the bottom of the cross-section. At a load level of F = 1105 kN, the T-beam stirrups also start yielding at the location of the horizontal crack, between the transition piece and the T-beam's top flange (see also Figures 7.60a–b). At the ultimate load, the regular reinforcement shows a maximum stress of S_{xx} = 308 N/mm^2, see Figure 7.62b. In addition, the top side regular longitudinal reinforcement is just starting to yield in compression.

At the clamped end, the top side regular longitudinal reinforcement start yielding at a load level of F = 971 kN. In addition, as a result of the torsion cracks (see Figure 7.61), the stirrups and longitudinal reinforcements, at the end cross-beam, start yielding at a load level of F = 1185 kN. No fracture occurs in either the prestressing tendons or the regular reinforcement (see also Figure 7.3).

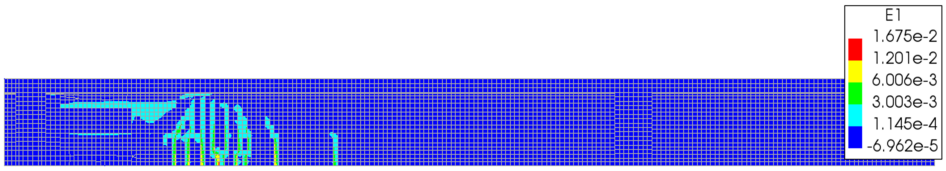

(a) F = 1072 kN, δ_z = 15.7 mm, T-beam bending cracks, initiation of flexural shear cracks

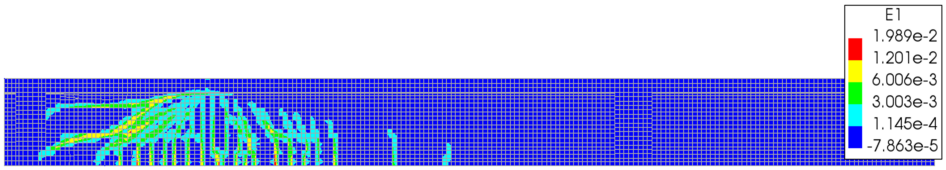

(b) F = 1185 kN, δ_z = 23.7 mm

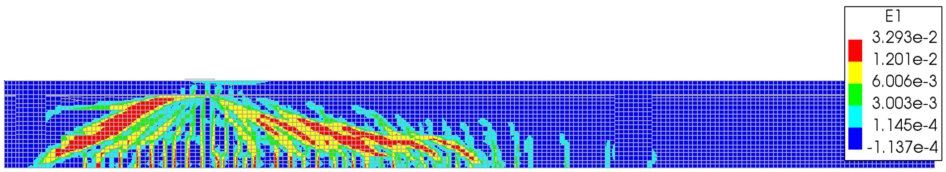

(c) F_u = 1486 kN, δ_u = 50.6 mm

Figure 7.60: B-T4-60/180-QNR, maximum principal strain E_1 T-beam 12
(end cross-beam on the left side, half span shown)
(color segments: $\alpha_1 = 2$, $\alpha_2 = 4$, see Figure 7.20)

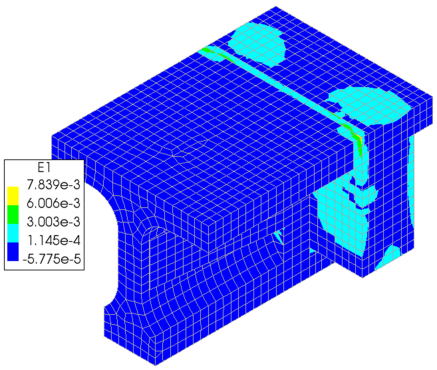

(a) F = 1105 kN, δ_z = 17.7 mm

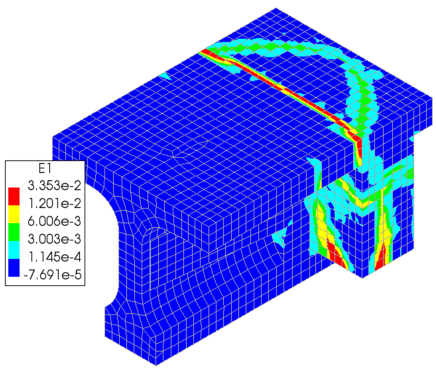

(b) F_u = 1486 kN, δ_u = 50.6 mm

Figure 7.61: B-T4-60/180-QNR, maximum principal strain E_1 T-beam 12 (clamped end)
(color segments: $\alpha_1 = 2$, $\alpha_2 = 4$, see Figure 7.20)

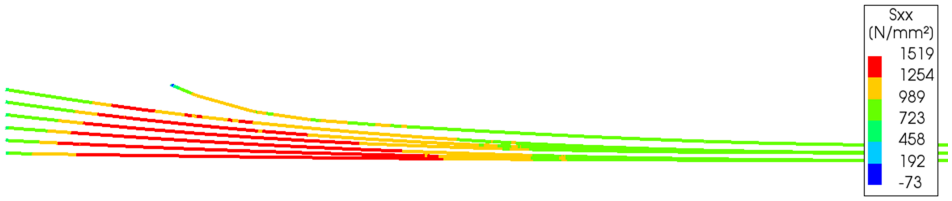

(a) Prestressing tendons 1–7

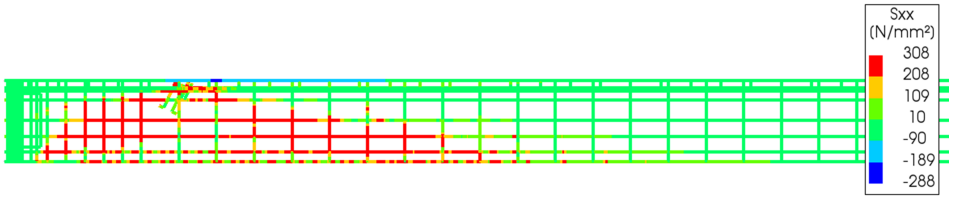

(b) Regular reinforcements

Figure 7.62: B-T4-60/180-QNR, stress S_{xx} embedded reinforcements T-beam 12, F_u = 1486 kN, δ_u = 50.6 mm

7.9.2. ANALYSIS B-T5

THE main results of analysis B-T5-60/180-QNR are summarized in Table 7.19 with the load versus deflection diagram given in Figure 7.63. All load steps of the analysis are converged. More detailed results of the analysis, such as the convergence graph and the comparison to the test measurements, are given in Appendix B Section B.2. The ultimate failure load is 88% compared to the test result (see Chapter 6 Section 6.5). The (linear) support stiffness is consistent with the test results, see Appendix B Section B.2. The comparison to the intermediate cross-beam deformation measurement (LP10) is unreliable (see also Chapter 6 Section 6.5.2), see Appendix B Figure B.5b.

Table 7.19: Analysis B-T5-60/180-QNR results

analysis	δ_{2a} mm	F_{2a} kN	δ_u mm	F_u kN	total steps	non-converged steps
B-T5-60/180-QNR	20.8	1146	53.3	1505	221	0

Principal strains (cracking)

The cracking evolution of the loaded T-beam is shown in Figure 7.65 and in Figure 7.66, showing the clamped end. The first cracking occurs at the clamped end due to the hogging bending moment. Next, horizontal cracking starts in the T-beam, near the load position, between the transition piece and the T-beam's top flange (see also Figure 7.8b). At the same time, bending cracks are initiated in the T-beam, see Figure 7.65a. Next, horizontal shear tension cracks are initiated in the T-beam, below the transition piece, followed by flexural shear cracks, see Figure 7.65b. At the same time, torsion cracks are initiated in the end cross-beam. In addition, the full width of the disconnected T-beam is now cracked on the top side, see Figure 7.66a. Finally, the T-beam fails due to a large

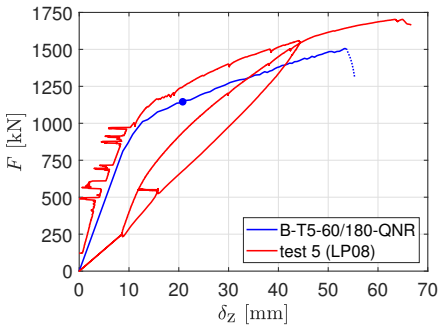

Figure 7.63: B-T5-60/180-QNR, load - deflection
(bullet indicates start of phase 2b see Table 7.8, dashed line = non-converged (post-peak))

flexural shear crack developing from the loading point to the end support, see Figure 7.65c.

T-beam sectional forces (clamped end)

The sectional forces of the loaded T-beam at the clamped end, resulting from the composed line elements (see Section 7.5.1), are given in Figure 7.64. Both the shear force and the bending moment remain linear up until a load of approximately F = 1100 kN, when the full width of the disconnected T-beam is cracked on the top side, see Figure 7.66a.

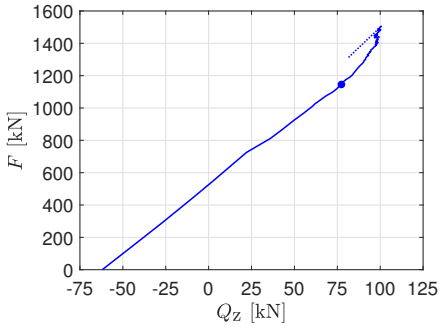

(a) Shear force Q_z

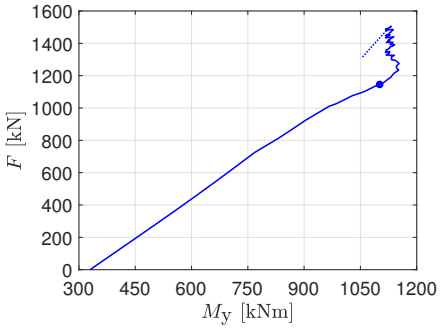

(b) Bending moment M_y

Figure 7.64: B-T5-60/180-QNR, shear force Q_z and bending moment M_y T-beam 11 (clamped end)
(bullet indicates start of phase 2b see Table 7.8, dashed line = non-converged (post-peak))

Reinforcement and prestressing tendons stresses (yielding)

The stresses of the reinforcement, at the ultimate load, are given in Figure 7.67. Yielding of the prestressing tendons is initiated at a load level of F = 1440 kN, in the tendon closest to the bottom of the cross-section. At the ultimate load, the maximum stress in the tendons is S_{xx} = 1529 N/mm^2, see Figure 7.67a. In addition, at the ultimate load, yielding is also initiated in the second tendon from the bottom.

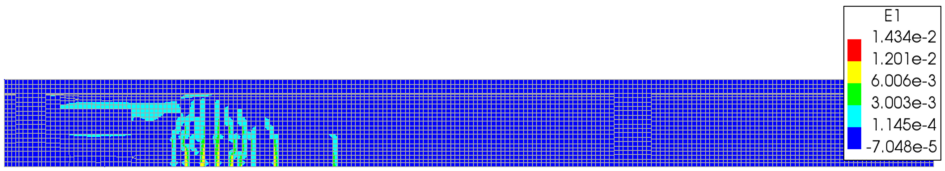

(a) F = 1077 kN, δ_z = 15.7 mm, T-beam bending cracks

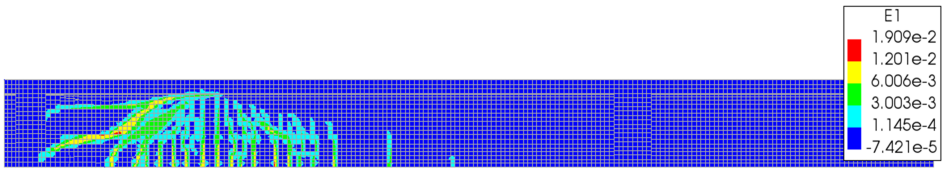

(b) F = 1174 kN, δ_z = 23.3 mm, T-beam flexural shear cracks

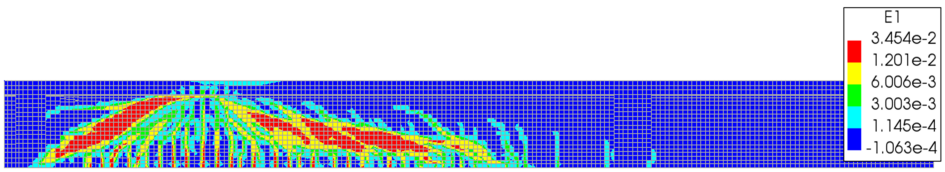

(c) F_u = 1505 kN, δ_u = 53.3 mm

Figure 7.65: B-T5-60/180-QNR, maximum principal strain E_1 T-beam 11
(end cross-beam on the left side, half span shown)
(color segments: $\alpha_1 = 2$, $\alpha_2 = 4$, see Figure 7.20)

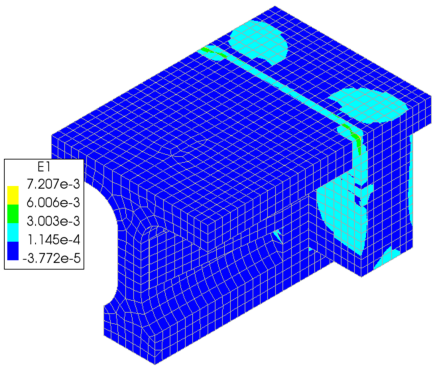

(a) F = 1101 kN, δ_z = 17.7 mm

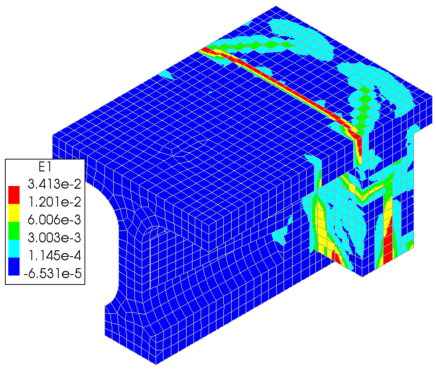

(b) F_u = 1505 kN, δ_u = 53.3 mm

Figure 7.66: B-T5-60/180-QNR, maximum principal strain E_1 T-beam 11 (clamped end)
(color segments: $\alpha_1 = 2$, $\alpha_2 = 4$, see Figure 7.20)

In the regular reinforcement yielding is initiated at a load level of F = 864 kN, in the longitudinal reinforcement closest to the bottom of the cross-section. At a load level of F = 1119 kN, the T-beam stirrups also start yielding at the location of the horizontal crack, between the transition piece and the T-beam's top flange (see also Figures 7.65a–b). At the ultimate load, the regular reinforcement shows a maximum stress of S_{xx} = 311 N/mm^2, see Figure 7.67b. In addition, the top side regular longitudinal reinforcement is starting to yield in compression.

At the clamped end, the top side regular longitudinal reinforcement start yielding at a load level of F = 1025 kN. In addition, as a result of the torsion cracks (see Figure 7.66), the stirrups and longitudinal reinforcements, at the end cross-beam, start yielding at a load level of F = 1234 kN. No fracture occurs in either the prestressing tendons or the regular reinforcement (see also Figure 7.3).

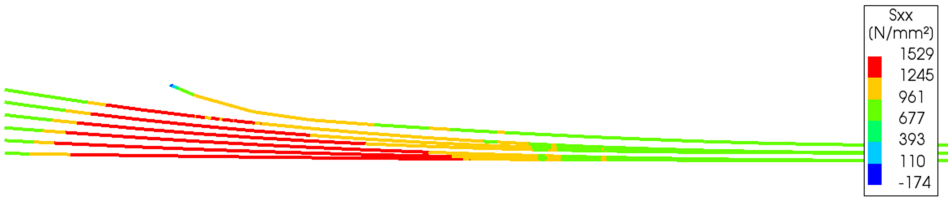

(a) Prestressing tendons 1–7

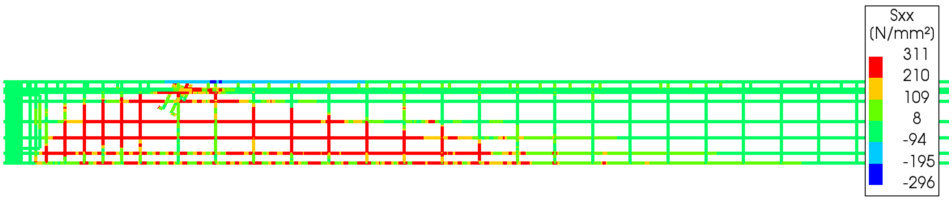

(b) Regular reinforcements

Figure 7.67: B-T5-60/180-QNR, stress S_{xx} embedded reinforcements T-beam 11, F_u = 1505 kN, δ_u = 53.3 mm

7.9.3. ANALYSIS B-T6

THE main results of analysis B-T6-60/180-QNR are summarized in Table 7.20 with the load versus deflection diagram given in Figure 7.68. All load steps of the analysis are converged. More detailed results of the analysis, such as the convergence graph and the comparison to the test measurements, are given in Appendix B Section B.3. The ultimate failure load is 84% compared to the test result (see Chapter 6 Section 6.5). The (linear) support stiffness shows some deviation with the test results, see Appendix B Section B.3. However, significant stiffness deviation is observed at the position of the intermediate cross-beam, see Appendix B Figure B.7b.

Principal strains (cracking)

The cracking evolution of the loaded T-beam is shown in Figure 7.69 and in Figure 7.70, showing the clamped end. The first cracking occurs at the clamped end due to the hog-

Table 7.20: Analysis B-T6-60/180-QNR results

analysis	δ_{2a} mm	F_{2a} kN	δ_u mm	F_u kN	total steps	non-converged steps
B-T6-60/180-QNR	20.5	1146	52.0	1498	216	0

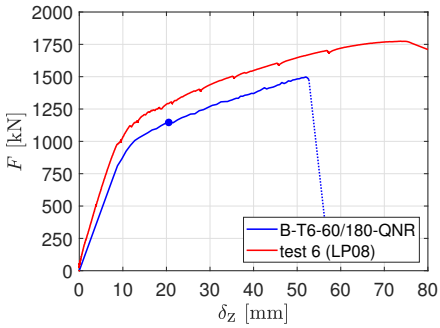

Figure 7.68: B-T6-60/180-QNR, load - deflection
(bullet indicates start of phase 2b see Table 7.8, dashed line = non-converged (post-peak))

ging bending moment. In addition, horizontal cracking starts in the T-beam, near the load position, between the transition piece and the T-beam's top flange (see also Figure 7.8b). Next, bending cracks are initiated in the T-beam, followed by horizontal shear tension cracks in the T-beam, below the transition piece, see Figure 7.69a. Next, flexural shear cracks are initiated, see Figure 7.69b. At the same time, torsion cracks are initiated in the end cross-beam. In addition, the full width of the disconnected T-beam is now cracked on the top side, see Figure 7.70a. Finally, the T-beam fails due to a large flexural shear crack developing from the loading point to the end support, see Figure 7.69c.

T-beam sectional forces (clamped end)

The sectional forces of the loaded T-beam at the clamped end, resulting from the composed line elements (see Section 7.5.1), are given in Figure 7.71. Both the shear force and the bending moment remain linear up until a load of approximately F = 1100 kN, when the full width of the disconnected T-beam is cracked on the top side, see Figure 7.70a.

Reinforcement and prestressing tendons stresses (yielding)

The stresses of the reinforcement, at the ultimate load, are given in Figure 7.72. Yielding of the prestressing tendons is initiated at a load level of F = 1371 kN, in the tendon closest to the bottom of the cross-section. At the ultimate load, the maximum stress in the tendons is S_{xx} = 1522 N/mm^2, see Figure 7.72a.

In the regular reinforcement yielding is initiated at a load level of F = 864 kN, in the longitudinal reinforcement closest to the bottom of the cross-section. At a load level of F = 1098 kN, the T-beam stirrups also start yielding at the location of the horizontal crack, between the transition piece and the T-beam's top flange (see also Figures

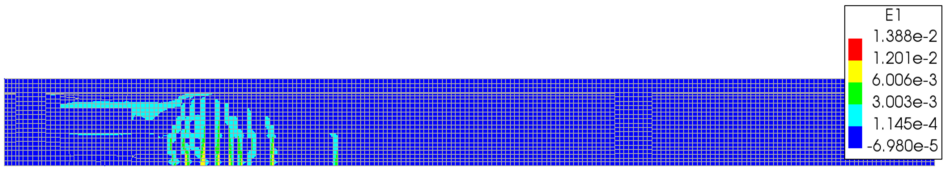

(a) F = 1066 kN, δ_z = 15.7 mm, T-beam bending cracks

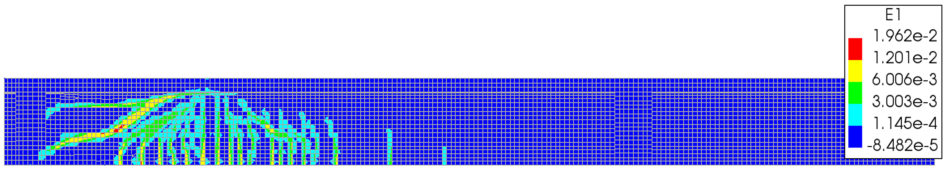

(b) F = 1183 kN, δ_z = 23.5 mm, T-beam flexural shear cracks

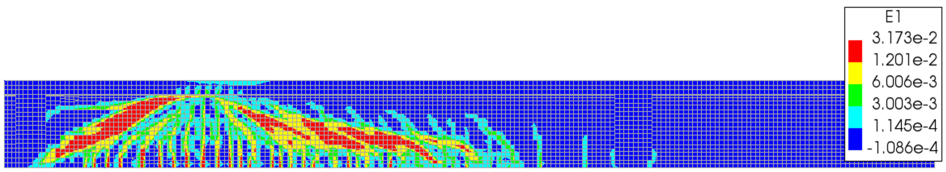

(c) F_u = 1498 kN, δ_u = 52.0 mm

Figure 7.69: B-T6-60/180-QNR, maximum principal strain E_1 T-beam 10
(end cross-beam on the left side, half span shown)
(color segments: $\alpha_1 = 2$, $\alpha_2 = 4$, see Figure 7.20)

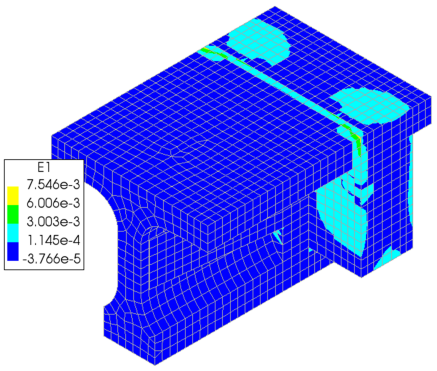

(a) F = 1120 kN, δ_z = 18.7 mm

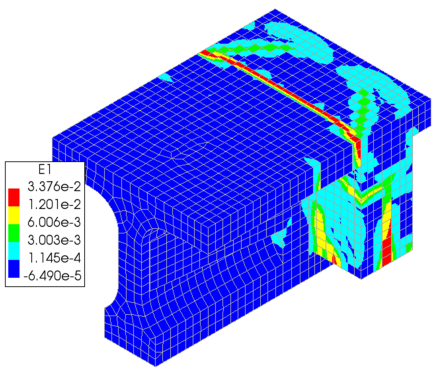

(b) F_u = 1498 kN, δ_u = 52.0 mm

Figure 7.70: B-T6-60/180-QNR, maximum principal strain E_1 T-beam 10 (clamped end)
(color segments: $\alpha_1 = 2$, $\alpha_2 = 4$, see Figure 7.20)

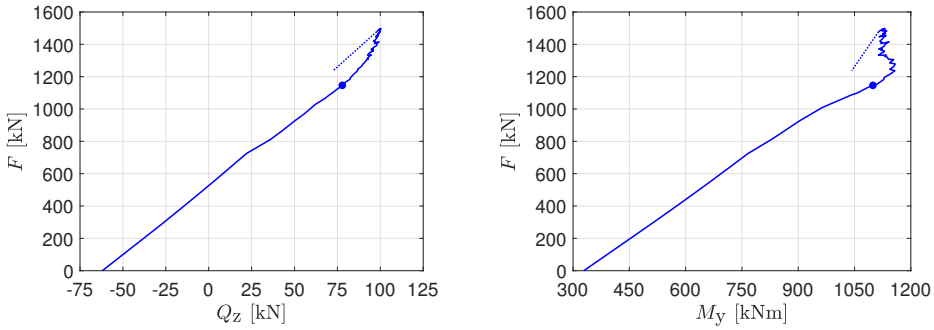

(a) Shear force Q_z

(b) Bending moment M_y

Figure 7.71: B-T6-60/180-QNR, shear force Q_z and bending moment M_y T-beam 10 (clamped end) (bullet indicates start of phase 2b see Table 7.8, dashed line = non-converged (post-peak))

7.69a–b). At the ultimate load, the regular reinforcement shows a maximum stress of S_{xx} = 309 N/mm^2, see Figure 7.72b. In addition, the top side regular longitudinal reinforcement is starting to yield in compression.

At the clamped end, the top side regular longitudinal reinforcement start yielding at a load level of F = 1029 kN. In addition, as a result of the torsion cracks (see Figure 7.70), the stirrups and longitudinal reinforcements, at the end cross-beam, start yielding at a load level of F = 1237 kN. No fracture occurs in either the prestressing tendons or the regular reinforcement (see also Figure 7.3).

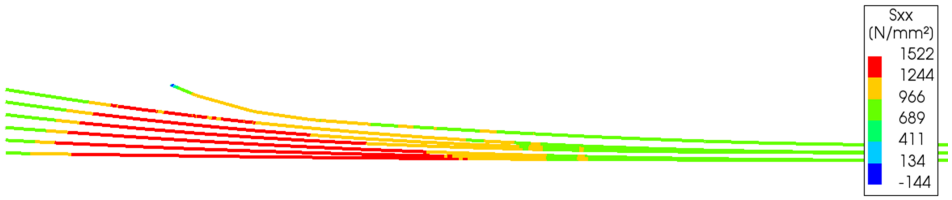

(a) Prestressing tendons 1–7

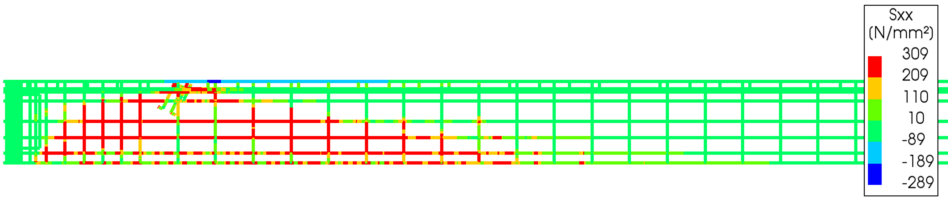

(b) Regular reinforcements

Figure 7.72: B-T6-60/180-QNR, stress S_{xx} embedded reinforcements T-beam 10, F_u = 1498 kN, δ_u = 52.0 mm

7.9.4. ANALYSIS B-T7

THE main results of analysis B-T7-60/180-QNR are summarized in Table 7.21 with the load versus deflection diagram given in Figure 7.73. All load steps of the analysis are converged. More detailed results of the analysis, such as the convergence graph and the comparison to the test measurements, are given in Appendix B Section B.4. The ultimate failure load is 118% compared to the test result (see Chapter 6 Section 6.5). The (linear) support stiffness shows some stiffness deviation with the test results, see Appendix B Section B.4. However, significant stiffness deviation is observed at the position of the intermediate cross-beam, see Appendix B Figure B.10b.

Table 7.21: Analysis B-T7-60/180-QNR results

analysis	δ_{2a} mm	F_{2a} kN	δ_u mm	F_u kN	total steps	non-converged steps
B-T7-60/180-QNR	54.2	904	162.6	1203	548	0

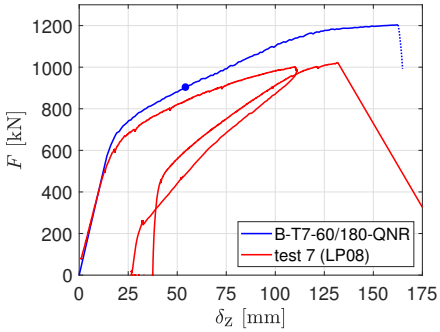

Figure 7.73: B-T7-60/180-QNR, load - deflection
(bullet indicates start of phase 2b see Table 7.8, dashed line = non-converged (post-peak))

Principal strains (cracking)

The cracking evolution of the loaded T-beam is shown in Figure 7.74 and in Figure 7.75, showing the clamped end. The first cracking occurs at the clamped end due to the hogging bending moment. Next, bending cracks are initiated in the T-beam, see Figure 7.74a. At the same time, torsion cracks are initiated in the end cross-beam. In addition, the full width of the disconnected T-beam is now cracked on the top side, see Figure 7.75a. Next, flexural shear cracks are initiated, see Figure 7.74b. Finally, the T-beam fails due to a large flexural shear crack developing from the loading point to the end support, see Figure 7.74c.

T-beam sectional forces (clamped end)

The sectional forces of the loaded T-beam at the clamped end, resulting from the composed line elements (see Section 7.5.1), are given in Figure 7.76. Both the shear force and the bending moment remain linear up until a load of approximately F = 750 kN, when

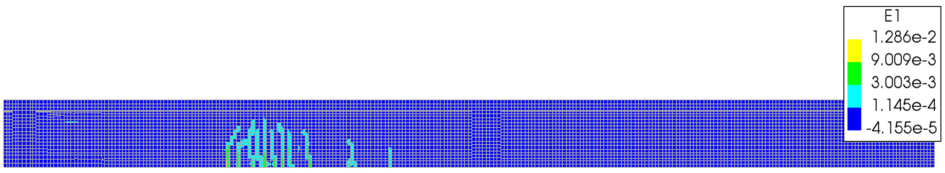

(a) F = 725 kN, δ_z = 23.4 mm, T-beam bending cracks

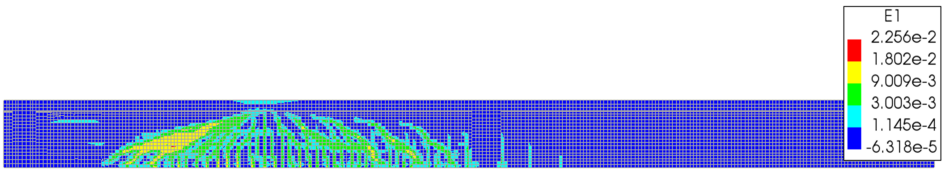

(b) F = 931 kN, δ_z = 60.2 mm, T-beam flexural shear cracks

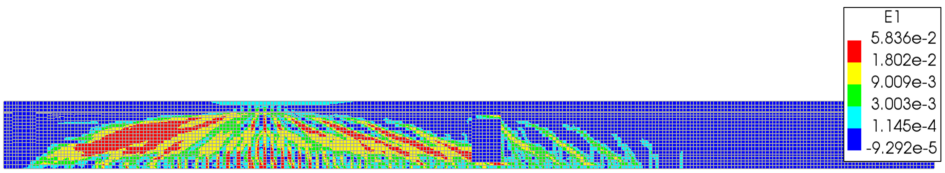

(c) F_u = 1203 kN, δ_u = 162.6 mm

Figure 7.74: B-T7-60/180-QNR, maximum principal strain E_1 T-beam 9
(end cross-beam on the left side, half span shown)
(color segments: α_1 = 3, α_2 = 6, see Figure 7.20)

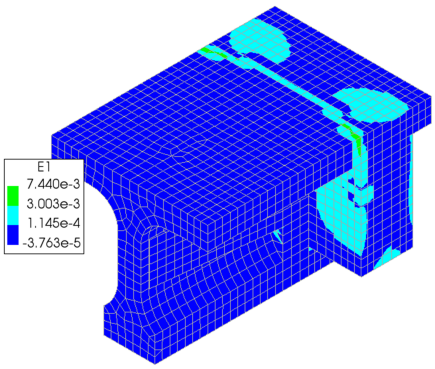

(a) F = 688 kN, δ_z = 19.9 mm

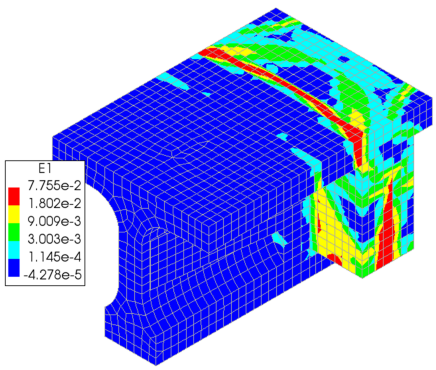

(b) F_u = 1203 kN, δ_u = 162.6 mm

Figure 7.75: B-T7-60/180-QNR, maximum principal strain E_1 T-beam 9 (clamped end)
(color segments: α_1 = 3, α_2 = 6, see Figure 7.20)

the full width of the disconnected T-beam is cracked on the top side, see Figure 7.75a.

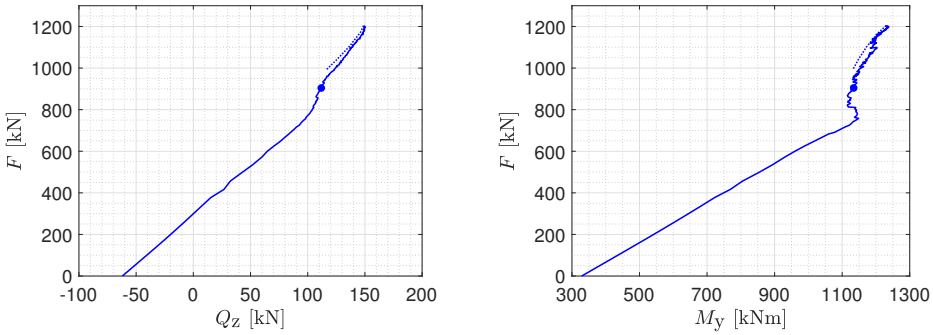

(a) Shear force Q_z

(b) Bending moment M_y

Figure 7.76: B-T7-60/180-QNR, shear force Q_z and bending moment M_y T-beam 9 (clamped end) (bullet indicates start of phase 2b see Table 7.8, dashed line = non-converged (post-peak))

Reinforcement and prestressing tendons stresses (yielding)

The stresses of the reinforcement, at the ultimate load, are given in Figure 7.77. Yielding of the prestressing tendons is initiated at a load level of F = 1010 kN, in the tendon closest to the top of the cross-section. At the ultimate load, the maximum stress in the tendons is S_{xx} = 1544 N/mm^2, see Figure 7.72a. In addition, at the ultimate load, yielding is observed in all tendons.

In the regular reinforcement yielding is initiated at a load level of F = 600 kN, in the longitudinal reinforcement closest to the bottom of the cross-section. At a load level of F = 785 kN, the T-beam stirrups also start yielding at the location of the flexural shear crack, towards the end support. In addition, the top side regular longitudinal reinforcement starts yielding in compression at a load level of F = 1146 kN. At the ultimate load, the regular reinforcement shows a maximum stress of S_{xx} = 331 N/mm^2, see Figure 7.77b.

At the clamped end, the top side regular longitudinal reinforcement start yielding at a load level of F = 626 kN. In addition, as a result of the torsion cracks (see Figure 7.75), the stirrups and longitudinal reinforcements, at the end cross-beam, start yielding at a load level of F = 763 kN. No fracture occurs in either the prestressing tendons or the regular reinforcement (see also Figure 7.3).

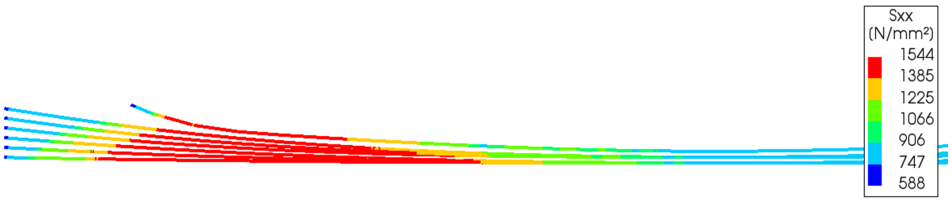

(a) Prestressing tendons 1–7

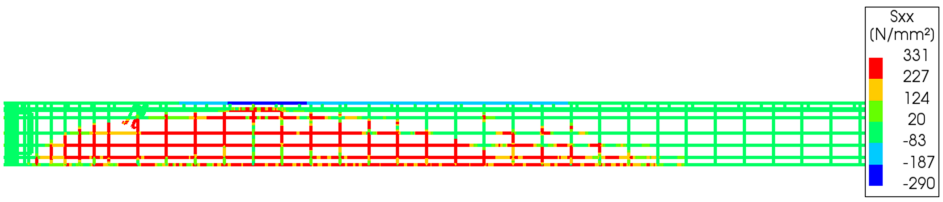

(b) Regular reinforcements

Figure 7.77: B-T7-60/180-QNR, stress S_{xx} embedded reinforcements T-beam 9, F_u = 1203 kN, δ_u = 162.6 mm

7.10. RESULTS SIMPLY SUPPORTED T-BEAMS (FEM MODELS C)

THIS section gives the results of the simply supported T-beams analyses C1 and C2, see Section 7.2.2 Table 7.2. For a detailed description of FEM model C the reader is referred to Section 7.6. As part of the numerical parameter study, the main results of these analyses are also reported in Section 7.7.1.

7.10.1. ANALYSIS C1

THE main results of analysis C1-50/100-QNR are summarized in Section 7.7.1 Table 7.12 with the load versus deflection diagram given in Section 7.7.1 Figure 7.19a. In this section the results are described in more detail.

Principal strains (cracking)

The cracking evolution of the T-beam is shown in Figure 7.78. The first cracking consists of horizontal cracks, near the load position, between the transition piece and the T-beam's top flange (see also Figure 7.8b). Next, bending cracks are initiated, followed by horizontal shear tension cracks, below the transition piece, see Figures 7.78a–b. Next, flexural shear cracks are initiated, see Figure 7.78b–c. Finally, the T-beam fails due to a large flexural shear crack developing from the loading point to the end support, see Figure 7.78d.

Reinforcement and prestressing tendons stresses (yielding)

The stresses of the reinforcement, at the ultimate load, are given in Figure 7.79. Yielding of the prestressing tendons is initiated at a load level of F = 1404 kN, in the tendon clos-

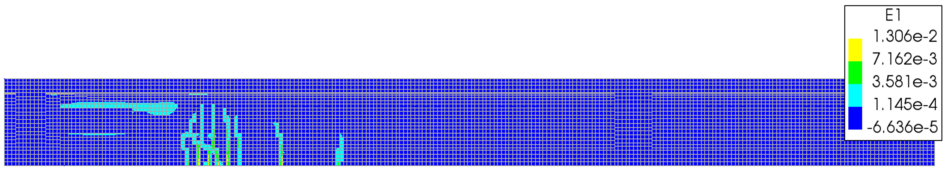

(a) F = 989 kN, δ_z = 15.9 mm, T-beam bending cracks

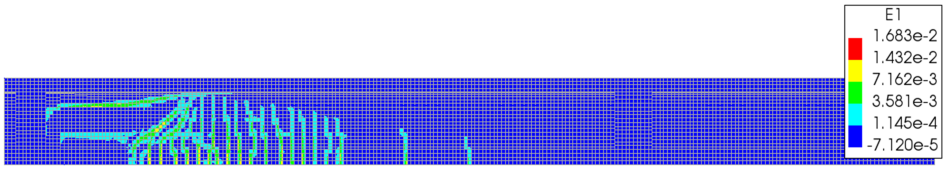

(b) F = 1124 kN, δ_z = 23.9 mm, T-beam flexural shear cracks

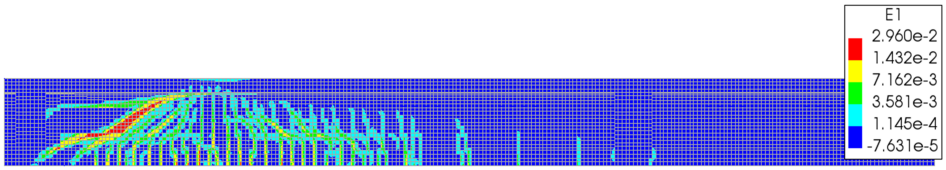

(c) F = 1264 kN, δ_z = 36.4 mm

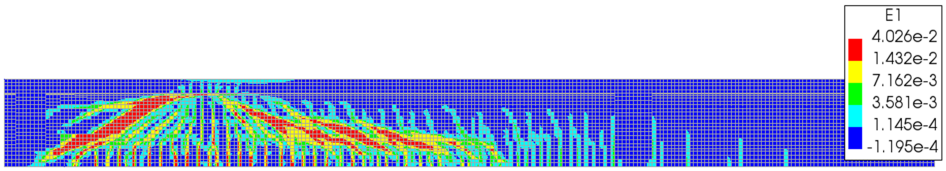

(d) F_u = 1512 kN, δ_u = 63.3 mm

Figure 7.78: C1-50/100-QNR, maximum principal strain E_1 (end cross-beam on the left side, half span shown) (color segments: $\alpha_1 = 2$, $\alpha_2 = 4$, see Figure 7.20)

est to the bottom of the cross-section. At the ultimate load, the maximum stress in the tendons is S_{xx} = 1532 N/mm^2, see Figure 7.79a.

In the regular reinforcement yielding is initiated at a load level of F = 856 kN, in the longitudinal reinforcement closest to the bottom of the cross-section. At a load level of F = 1068 kN, the T-beam stirrups also start yielding at the location of the horizontal crack, between the transition piece and the T-beam's top flange (see also Figures 7.78a–b). At the ultimate load, the regular reinforcement shows a maximum stress of S_{xx} = 312 N/mm^2, see Figure 7.79b. Just prior to failure, the top side regular longitudinal reinforcement is starting to yield in compression. No fracture occurs in either the prestressing tendons or the regular reinforcement (see also Figure 7.3).

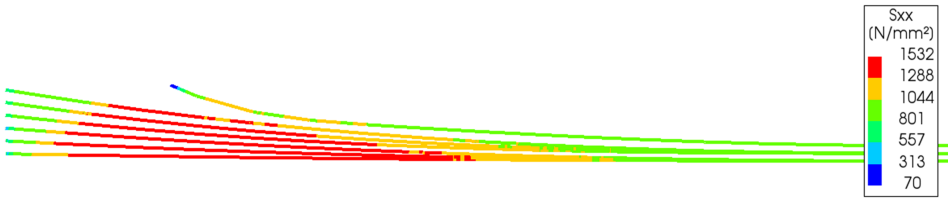

(a) Prestressing tendons 1–7

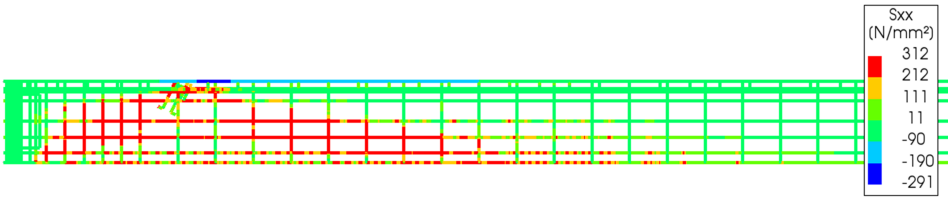

(b) Regular reinforcements

Figure 7.79: C1-50/100-QNR, stress S_{xx} embedded reinforcements, F_u = 1512 kN, δ_u = 63.3 mm

7.10.2. ANALYSIS C2

THE main results of analysis C2-60/100-QNR are summarized in Section 7.7.1 Table 7.12 with the load versus deflection diagram given in Section 7.7.1 Figure 7.19b. In this section the results are described in more detail.

Principal strains (cracking)

The cracking evolution of the T-beam is shown in Figure 7.80. The first cracking consists of bending cracks, see Figure 7.80a. Next, flexural shear cracks are initiated, see Figure 7.80a–b. Finally, the T-beam fails due to a large flexural shear crack developing from the loading point to the end support, see Figure 7.80c.

Reinforcement and prestressing tendons stresses (yielding)

The stresses of the reinforcement, at the ultimate load, are given in Figure 7.81. Yielding of the prestressing tendons is initiated at a load level of F = 965 kN, in the tendon closest to the top of the cross-section. At the ultimate load, the maximum stress in the tendons is S_{xx} = 1547 N/mm^2, see Figure 7.81a. In addition, at the ultimate load, yielding is observed in all tendons.

In the regular reinforcement yielding is initiated at a load level of F = 581 kN, in the longitudinal reinforcement closest to the bottom of the cross-section. At a load level of F = 750 kN, the T-beam stirrups also start yielding at the location of the flexural shear crack, towards the end support. In addition, the top side regular longitudinal reinforcement start yielding in compression at a load level of F = 1118 kN. At the ultimate load, the regular reinforcement shows a maximum stress of S_{xx} = 319 N/mm^2, see Figure 7.81b. No fracture occurs in either the prestressing tendons or the regular reinforcement (see also Figure 7.3).

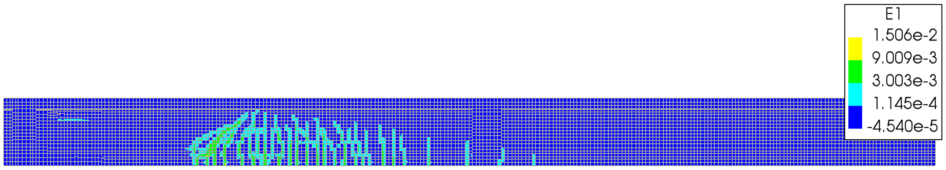

(a) F = 750 kN, δ_z = 37.9 mm, T-beam bending cracks

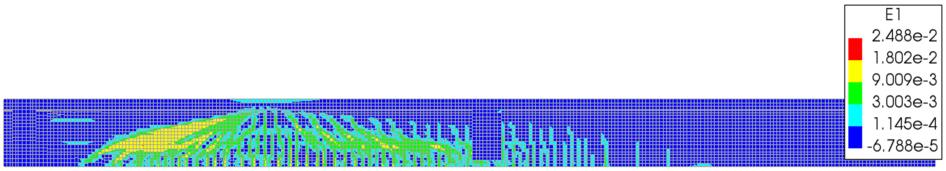

(b) F = 947 kN, δ_z = 80.2 mm, T-beam flexural shear cracks

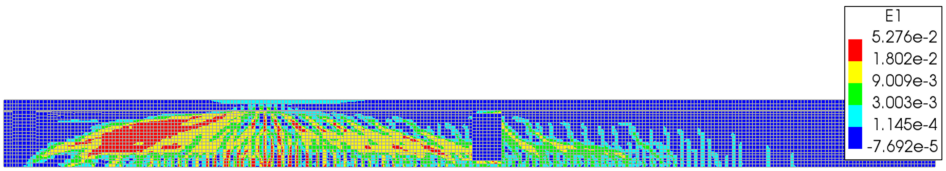

(c) F_u = 1151 kN, δ_u = 175.2 mm

Figure 7.80: C2-60/100-QNR, maximum principal strain E_1 (end cross-beam on the left side, half span shown) (color segments: $\alpha_1 = 3$, $\alpha_2 = 6$, see Figure 7.20)

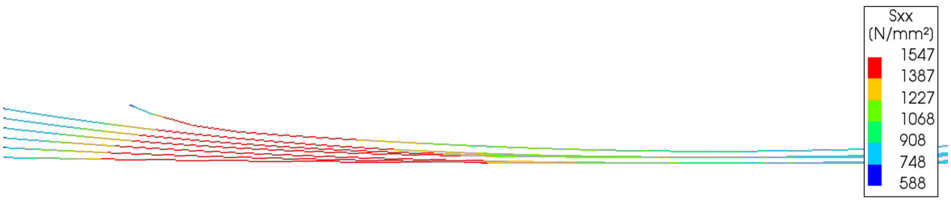

(a) Prestressing tendons 1–7

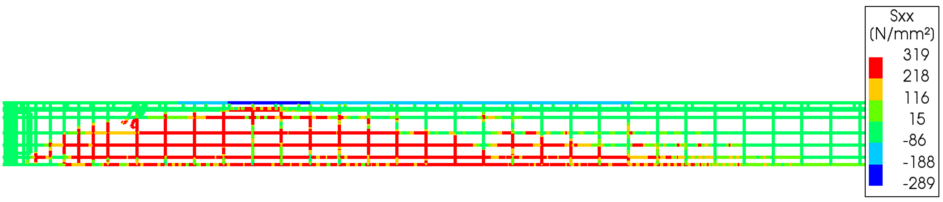

(b) Regular reinforcements

Figure 7.81: C2-60/100-QNR, stress S_{xx} embedded reinforcements, F_u = 1151 kN, δ_u = 175.2 mm

7.11. SUMMARY

THE modelling approach for the different FEM models, the results of the numerical parameter study and the results of the analyses of the Vecht bridge are summarised in this section.

Modelling and analysis:

- FEM models A–C are created using the same parametric Python script to construct each model.
- The material modelling, meshing, convergence and other nonlinear settings used, are in accordance with the Dutch 'Guidelines for Nonlinear Finite Element Analysis of Concrete Structures', i.e. RTD 1016-1 (Hendriks et al. 2017).
- The material properties for concrete, reinforcement steel and prestressing steel used are based on the material investigation.
- The vertical stiffness of the reinforced elastomeric bearings needed to be increased significantly, by a factor of 2.75, compared to the initial values based on standard analytical formulas, in order to obtain results comparable to the tests.
- A more realistic stiffness of the reinforced elastomeric bearings can be obtained by using the analytical formula by Banks, Pinter and Yeoh (Banks et al. 2002).
- 3D solid elements are used in combination with shell elements, wherever possible, to limit the number of elements and thereby computing time. In addition, outside the area of interest, linear elements without reinforcement are used.
- A maximum element size of 200 mm is derived in accordance with RTD 1016-1 (Hendriks et al. 2017) and in order to avoid a snap-back in the concrete softening curve.
- The reinforcements and prestressing tendons are modelled as embedded elements using individual bars with full bond.
- The curved prestressing tendons are approximated by straight lines at 750 mm intervals with the vertical coordinates determined using the polynomials as described in Chapter 5.
- The loading consists of the self-weight, the transverse prestressing of the bridge deck, the longitudinal prestressing of the T-beam(s) and a displacement load. For the latter a phased analysis is required.
- To improve convergence, different convergence norms are set to be satisfied simultaneously whenever possible. In addition, an automatic step size routine is utilized.
- In all analyses the ultimate failure load is defined as the highest load obtained in a converged step.
- For FEM models A–B, the stiffness of the shell T-beam is calibrated to give the same deflections as the T-beam modelled with solid elements.
- The transition piece near the end block is (partly) omitted to prevent badly shaped elements.

- Composed line elements are applied in the T-beam, at the area of interest, in order to obtain 1D sectional forces. Likewise, composed surface elements are applied in the integrated deck slab, in order to obtain 2D distributed sectional forces.

Results of the numerical parameter study:

- Using a model for a simply supported T-beam (FEM model C) and the two load positions of the tests, element sizes of 50 mm, 100 mm and 200 mm are investigated. In addition, three different solution methods are investigated: full Newton-Raphson (FNR), Modified Newton-Raphson (MNR) and Quasi-Newton (QNR).
- With one exception, 100% convergence is achieved, using the QNR method, and the difference in ultimate load, for all element sizes, is between 1–3%. In one case, the analysis does not convergence at the onset of plasticity.
- Better convergence is obtained for smaller element sizes. In addition, in the last phase, when either an energy or a force norm is required for convergence, the force norm is better satisfied for smaller element sizes.
- Of all solution methods, the QNR with the Broyden-Fletcher-Goldfarb-Shanno (BFGS) method performs best in relation to the force norm with the other two methods showing a constantly increasing deviation from the force norm in the last phase of the analysis.
- The QNR method with BFGS method performs best in achieving convergence, especially in combination with an adaptive step size. Generally, it also requires the least amount of iterations and shows an iteration speed (iter/min) comparable to the MNR method.

Results of the Vecht bridge analyses:

- The analyses of the connected T-beam tests (A-T1 and A-T2) show an ultimate failure load of 87–95% compared to the tests. Analysis A-T1 shows only two non-converged load steps, whereas analysis A-T2 shows zero non-converged load steps. In addition, the results of the analyses are consistent with the test measurements.
- Analyses A-T1 and A-T2 show a failure mode consistent with the tests, i.e. deck slab punching causing an immediate overload and failure of the T-beam.
- At loads exceeding 72–89% of the ultimate load, analyses A-T1 and A-T2 show indications of compressive arch action (CAA), with strut-like compressive stresses and increasing cross-sectional compressive normal forces in the T-beam, in both longitudinal directions, from the load position towards the end cross-beam and the intermediate cross-beam. The additional compressive normal forces in the loaded T-beam are balanced by tensile normal forces in the adjacent T-beams.
- Analyses A-T1 and A-T2 show compressive membrane action (CMA) in the transverse direction in the integrated deck slab and the top flange with compressive stresses approximately 4–5 times higher then the initial values.
- The analyses of the disconnected T-beam tests (B-T4, B-T5 and B-T6), with the load positioned at 2250 mm, show an ultimate failure load of 84–89% compared to

the tests with all load steps converged. In addition, the results of the analyses are consistent with the test measurements.

- Analyses B-T4, B-T5 and B-T6 show a failure mode consistent with the tests, i.e. a flexural shear failure of the T-beam.
- The analysis of the disconnected T-beam test B-T7, with the load positioned at 4000 mm, shows an ultimate failure load of 118% compared to the test with all load steps converged. The results of this analysis are not consistent with the test measurements.
- The analysis A-T7 has shown that the load-deflection behaviour is very sensitive to the stiffness of the connected end cross-beam, at the non-loaded side, as well as to the order of cracking (T-beam bending and shear cracks at the load position, hogging bending moment cracks due to the partial clamping effect and torsional cracks at the connected end cross-beam).
- The ultimate failure load of the simply supported T-beams (analyses C1 and C2) is very close to the ultimate failure load of the disconnected T-beams (analyses B-T4, B-T5, B-T6 and B-T7) with the difference in ultimate load between 4–5%.

8

SYSTEM BEHAVIOUR IN BRIDGES ANALYSIS OF THE CASE STUDY

In this chapter the additional load capacity, due to the effects of 'system behaviour' in prestressed concrete T-beam bridges, is analysed using the theory of arch action (Chapters 3–4) and the different parts of the case study of the Vecht bridge (Chapters 5–7). The analysis consists of the T-beam shear behaviour, the compressive membrane action in the slab (CMA), the compressive arch action in the T-beam (CAA) and the combined effects of CMA and CAA.

8.1. INTRODUCTION

IN this chapter the additional load capacity, due to the effects of 'system behaviour' in prestressed concrete T-beam bridges, is analysed using the results of the case study of the Vecht bridge as treated in the previous chapters. The analysis is aimed at the research objectives, as stated in Chapter 1 Section 1.2, and the research questions, as stated in Chapter 1 Section 1.3. For an overview of the different parts of the research, and how they connect, the reader is referred to Chapter 1 Figure 1.3.

8.2. ANALYSIS OF THE CASE STUDY

THE following aspects of system behaviour are analysed, based on the results of Chapters 5–7 and using the theory of arch action as treated in Chapters 3–4:

- shear behaviour and resistance of an individual, disconnected and connected T-beam (Sections 8.2.1–8.2.3);
- compressive membrane action (CMA) (Section 8.2.4);
- compressive arch action (CAA) (Section 8.2.5).
- combined CMA (slab) and CAA (T-beam) test 1 (Section 8.2.6).

The results of the analysis of system behaviour of the case study of the Vecht bridge are summarised in Section 8.3.

8.2.1. SHEAR RESISTANCE INDIVIDUAL T-BEAM

IN this section, the shear resistance of an individual T-beam of the Vecht bridge is analysed, using the results from the linear analyses (Chapter 5), the full-scale collapse tests (Chapter 6) and the nonlinear analyses (Chapter 7).

For a simply supported T-beam, the results are based on the linear and the nonlinear analysis. Note that in the full-scale collapse tests 4–7 the T-beams are not fully disconnected and therefore these results will be treated separately. For a simply supported T-beam, the comparison of the ultimate load, between the linear and the nonlinear analysis, at the two investigated load positions (a), is given in Table 8.1. The linear analysis results, with the corresponding cross-sectional verification, are also shown in Figure 8.1. At both load positions, the governing failure mode is flexural shear, with $F_{\max,V_{FS}} = 766$ kN (Figure 8.1a at $x = 2.20$ m) and $F_{\max,V_{FS}} = 710$ kN (Figure 8.1b at $x = 4.00$ m). Note that, at a load position of $a = 4.00$ m, the failure mode is very close to a flexural failure.

The next step is to determine the shear resistance at the critical cross-section from the ultimate loads given in Table 8.1. For the linear analysis, with the load positioned at $a = 2.25$ m, $F_{\max,V_{FS}} = 766$ kN, with the critical cross-section at $x = 2.20$ m. Combining the acting shear of the dead weight and the prestressing ($V_{dw} + V_{pw}$, see Chapter 5 Section 5.4 Figure 5.11c) and using the ratio between the load position and the span, the shear resistance of the linear analysis is determined by Equation 8.1 (for $V_{Rm,c}$ see Chapter 5 Section 5.6.2 Figure 5.18a).

$$V_{R,(8.1)} = (V_{dw} + V_{pw}) + V_F = (127 - 303) + (21.75/24.00) \times 766 = V_{Rm,c} = 518 \text{ [kN]} \quad (8.1)$$

Table 8.1: Ultimate load comparison between nonlinear analyses ($F_{u,NL}$) and linear analysis (F_{max}) (simply supported T-beam)

analysis	a mm	$F_{u,NL}$ [a] kN	$F_{max,V_{FS}}$ [b] kN	ratio	F_{max,M_u} [b,c] kN	ratio
C1-50/100-QNR	2250	1512		1.97		0.99
C1-100-QNR	2250	1420	766	1.85	1526	0.93
C1-200-QNR	2250	1550		2.02		1.02
average		1494		1.95		0.98
C2-60/100-QNR	4000	1151		1.62		1.09
C2-100-QNR	4000	1142	710	1.61	1054	1.08
C2-200-QNR	4000	1155		1.63		1.10
average		1149		1.62		1.09

[a] see Chapter 7 Section 7.7.1 Table 7.12, [b] see Chapter 5 Section 5.6.5 Figure 5.27

[c] in the linear analysis M_u is underestimated by approximately 10% (see Chapter 5 Section 5.6.4)

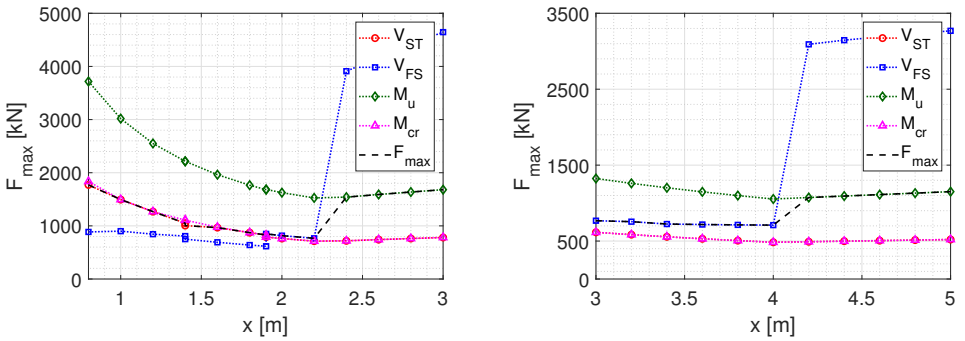

(a) $a = 2.25$ m (b) $a = 4.00$ m

Figure 8.1: Cross-sectional verification with fixed load positions (simply supported T-beam)

For the nonlinear analyses C1, with the load positioned at $a = 2.25$ m, $F_{u,NL} = 1494$ kN (average). For a direct comparison to the linear analysis, the critical cross-section is again taken at $x = 2.20$ m. Assuming the acting shear of the dead weight and the prestressing from the linear analysis (the shear force of the nonlinear analysis corresponds well to the linear analysis, see Chapter 7 Section 7.8.1), and using the ratio between the load position and the span, the shear resistance of the nonlinear analyses C1 is determined by Equation 8.2.

$$V_{R,(8.2)} = (V_{dw} + V_{pw}) + V_F = (127 - 303) + (21.75/24.00) \times 1494 = 1177 \text{ [kN]} \qquad (8.2)$$

Likewise, for the linear analysis, with the load positioned at $a = 4.00$ m, $F_{max,V_{FS}} = 710$ kN, with the critical cross-section at $x = 4.00$ m. Combining the acting shear of the dead weight and the prestressing ($V_{dw} + V_{pw}$, see Chapter 5 Section 5.4 Figure 5.11c) and using

the ratio between the load position and the span, the shear resistance of the linear analysis is determined by Equation 8.3 (for $V_{\mathrm{Rm,c}}$ see Chapter 5 Section 5.6.2 Figure 5.18a).

$$V_{R,(8.3)} = (V_{\mathrm{dw}} + V_{\mathrm{pw}}) + V_{\mathrm{F}} = (106 - 149) + (20.00/24.00) \times 710 = V_{\mathrm{Rm,c}} = 548 \text{ [kN]} \quad (8.3)$$

Likewise, for the nonlinear analyses C2, with the load positioned at a = 4.00 m, $F_{\mathrm{u,NL}}$ = 1149 kN (average). For a direct comparison to the linear analysis, the critical cross-section is again taken at x = 4.00 m. Assuming the acting shear of the dead weight and the prestressing from the linear analysis like before, and using the ratio between the load position and the span, the shear resistance of the nonlinear analyses C2 is determined by Equation 8.4.

$$V_{R,(8.4)} = (V_{\mathrm{dw}} + V_{\mathrm{pw}}) + V_{\mathrm{F}} = (106 - 149) + (20.00/24.00) \times 1149 = 914 \text{ [kN]} \quad (8.4)$$

In addition to a simply supported T-beam, the results of the disconnected T-beam tests 4–7 (partially clamped) and the corresponding nonlinear analyses are analysed. The comparison of the ultimate load, between the nonlinear analyses and the disconnected beam tests, at the two investigated load positions (a), is given in Table 8.2.

Table 8.2: Ultimate load comparison between nonlinear analyses ($F_{\mathrm{u,NL}}$) and tests ($F_{\mathrm{u,test}}$) (disconnected T-beam)

analysis	a mm	$F_{\mathrm{u,NL}}$ [a] kN	$F_{\mathrm{u,test}}$ [b] kN	ratio
B-T4-60/180-QNR	2250	1486	1678	0.89
B-T5-60/180-QNR	2250	1505	1703	0.88
B-T6-60/180-QNR	2250	1498	1774	0.84
average		1496	1718	0.87
B-T7-60/180-QNR	4000	1203	1022	1.18

[a] see Chapter 7 Section 7.9 Tables 7.18–7.21, [b] see Chapter 6 Section 6.5 Table 6.9

The next step is to determine the shear resistance at the critical cross-section from the ultimate loads given in Table 8.2. For the nonlinear analyses B-T4, B-T5 and B-T6, with the load positioned at a = 2.25 m, $F_{\mathrm{u,NL}}$ =1496 kN (average). The load distribution is complicated by the fact that the T-beam is not fully simply supported (see Chapter 7 Section 7.5). From analysis B-T6 (closest to the average failure load) the reaction forces at the ultimate load ($F_{\mathrm{u,NL}}$ = 1498 kN) are: R_{A} = 1486 kN (loaded side) and R_{B} = 335 kN (non-loaded side). These reaction forces include the dead weight. The reaction force, due to the dead weight on either side, is equal to approximately 166 kN (note that the difference between either sides is negligible). From these values, the ratio between the load and the support reaction R_{A}, at the loaded side, can be determined as: (1486-166)/1498 = 0.88. Note that for a simply supported beam, this ratio is: (21.75/24.00) = 0.91. The difference is due to the partial clamping effect of the connected end cross-beam at the non-loaded side. Using this factor, and assuming the acting shear as a result of the dead weight and the prestressing at the critical cross-section at x = 2.20 m from the linear analysis like

before, the shear resistance of the nonlinear analyses B-T4, B-T5 and B-T6 is determined by Equation 8.5.

$$V_{R,(8.5)} = (V_{dw} + V_{pw}) + V_F = (127 - 303) + 0.88 \times 1496 = 1140 \text{ [kN]} \tag{8.5}$$

From the experiments, tests 4–6, with the load positioned at a = 2.25 m, $F_{u,test}$ = 1718 kN (average). The critical cross-section is again taken at x = 2.20 m. Using the ratio between the load and the support reaction R_A from the nonlinear analysis and assuming the acting shear as a result of the dead weight and the prestressing like before, the shear resistance of the tests 4–6 is determined by Equation 8.6.

$$V_{R,(8.6)} = (V_{dw} + V_{pw}) + V_F = (127 - 303) + 0.88 \times 1718 = 1335 \text{ [kN]} \tag{8.6}$$

For the nonlinear analysis B-T7, with the load positioned at a = 4.00 m, $F_{u,NL}$ = 1203 kN. The load distribution is again complicated by the fact that the T-beam is not fully simply supported (see Chapter 7 Section 7.5). From analysis B-T7, the reaction forces at the ultimate load ($F_{u,NL}$ = 1203 kN) are: R_A = 1129 kN (loaded side) and R_B = 524 kN (non-loaded side). These reaction forces include the dead weight, which is equal to approximately 166 kN. From these values, the ratio between the load and the support reaction R_A, at the loaded side, can be determined as: (1129-166)/1203 = 0.80. Note that for a simply supported beam, this ratio is: (20.00/24.00) = 0.83. The difference is due to the partial clamping effect of the connected end cross-beam at the non-loaded side. Using this factor, and assuming the acting shear as a result of the dead weight and the prestressing at the critical cross-section at x = 4.00 m from the linear analysis like before, the shear resistance of the nonlinear analysis B-T7 is determined by Equation 8.7.

$$V_{R,(8.7)} = (V_{dw} + V_{pw}) + V_F = (106 - 149) + 0.80 \times 1203 = 918 \text{ [kN]} \tag{8.7}$$

Finally, from the experiment, test 7, with the load positioned at a = 4.00 m, $F_{u,test}$ = 1022 kN. The critical cross-section is again taken at x = 4.00 m. Using the ratio between the load and the support reaction R_A like before and assuming the acting shear as a result of the dead weight and the prestressing like before, the shear resistance of test 7 is determined by Equation 8.8.

$$V_{R,(8.8)} = (V_{dw} + V_{pw}) + V_F = (106 - 149) + 0.80 \times 1022 = 774 \text{ [kN]} \tag{8.8}$$

The results of the calculated shear resistances, from the linear analyses, the full-scale collapse tests and the nonlinear analyses (Equations 8.1–8.8), at the two investigated load positions (a) and critical cross-sections (x), are summarised in Figure 8.2.

In conclusion, with the load positioned at 2.25 m, compared to the linear analysis, the flexural shear resistance from the nonlinear analyses is increased by 120–127%, see Figure 8.2a. In addition, comparing the linear analysis to the tests, the flexural shear resistance is increased, on average, by 158%.

Likewise, with the load positioned at 4.00 m, compared to the linear analysis, the flexural shear resistance from the nonlinear analyses is increased by 67–68%, see Figure 8.2b. In addition, comparing the linear analysis to the test, the flexural shear resistance is increased by 41%. Note that in the nonlinear analyses, for the shear resistance at the

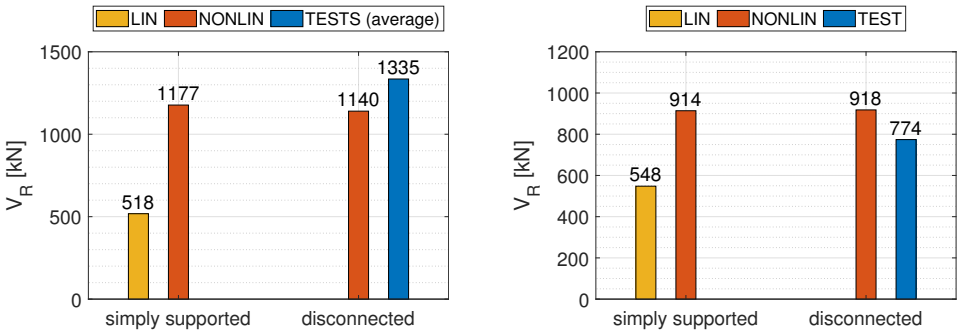

(a) a = 2.25 m, x = 2.20 m (Equations 8.1–8.2 and 8.5–8.6)

(b) a = 4.00 m, x = 4.00 m (Equations 8.3–8.4 and 8.7–8.8)

Figure 8.2: Summary of shear resistance individual T-beam

critical cross-section, similar results are obtained for a disconnected beam as compared to a simply supported beam.

Note that the experimental shear resistance, with the load positioned at 4.00 m, is based on just one experiment, i.e. test 7. In addition, during this experiment, a significant unloading was necessary to adjust the safety chains (see Chapter 6 Section 6.5.4). As this unloading took place very close to the ultimate load, this might have influenced the ultimate load capacity. In addition, the nonlinear analysis of test 7 (B-T7) has shown that the load-deflection behaviour is very sensitive to the stiffness of the connected end cross-beam, at the non-loaded side, as well as to the order of cracking (T-beam bending and shear cracks at the load position, hogging bending moment cracks due to the partial clamping effect and torsional cracks at the connected end cross-beam). Based on the shear resistance of 914 kN (Equation 8.4), resulting from the nonlinear analyses C2, test 7 shows a somewhat unexpected low shear resistance.

8.2.2. SHEAR RESISTANCE CONNECTED T-BEAM

IN this section, the shear resistance of a connected T-beam of the Vecht bridge is analysed, using the results from the linear analyses (Chapter 5), the full-scale collapse tests (Chapter 6) and the nonlinear analyses (Chapter 7).

For a connected T-beam, the comparison of the ultimate load, between the linear and the nonlinear analysis, at the two investigated load positions (a), is given in Table 8.3. In addition, the comparison of the ultimate load, between the nonlinear analyses and the connected beam tests 1–2, at the two investigated load positions (a), is given in Table 8.4. The linear analysis results, with the corresponding cross-sectional verification, are also shown in Figure 8.3. At both load positions, the governing failure mode is shear tension, with $F_{\max,V_{ST}}$ = 1693 kN (Figure 8.3a at x = 1.80 m) and $F_{\max,V_{ST}}$ = 1641 kN (Figure 8.3b at x = 4.20 m). Note that in the case of a = 4.00 m, the shear tension resistance is defined by the cracking moment (M_{cr}), see Figure 8.3b (see also Chapter 5 Section 5.6.3). The next step is to determine the shear resistance at the critical cross-section from the

Table 8.3: Ultimate load comparison between nonlinear analyses ($F_{u,NL}$) and linear analysis (F_{max}) (connected T-beam)

analysis	a mm	$F_{u,NL}$ [a] kN	$F_{max,V_{ST}}$ [b] kN	ratio	F_{max,M_u} [b,c] kN	ratio
A-T2-90/180-QNR	2250	3256	1693[d]	1.92	3642[c]	0.89
A-T1-90/180-QNR	4000	2760	1641	1.68	3417	0.81

[a] see Chapter 7 Section 7.8 Tables 7.16–7.17, [b] see Chapter 5 Section 5.6.5 Figure 5.29

[c] in the linear analysis M_u is underestimated by approximately 10% (see Chapter 5 Section 5.6.4)

[d] in the linear analysis the difference between T-beam number 5 and 6 and between the load position a = 2.20 m and a = 2.25 m is neglected

Table 8.4: Ultimate load comparison between nonlinear analyses ($F_{u,NL}$) and tests ($F_{u,test}$) (connected T-beam)

analysis	a mm	$F_{u,NL}$ [a] kN	$F_{u,test}$ [b] kN	ratio
A-T2-90/180-QNR	2250	3256	3444	0.95
A-T1-90/180-QNR	4000	2760	3004	0.92

[a] see Chapter 7 Section 7.8 Tables 7.16–7.17, [b] see Chapter 6 Section 6.4 Table 6.7

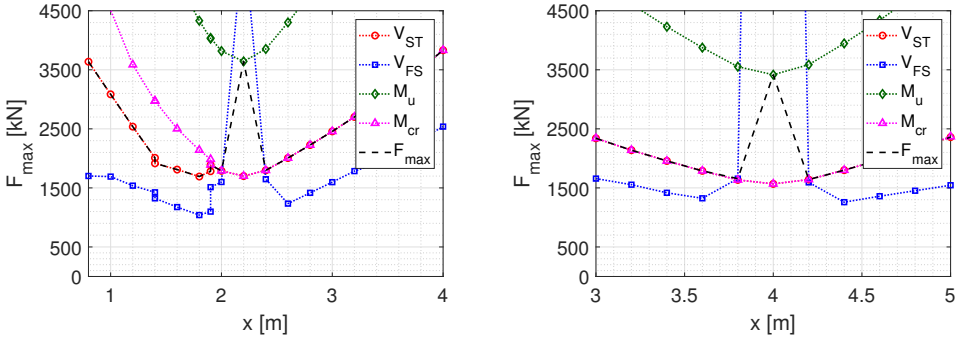

(a) a = 2.25 m (T-beam 5) (b) a = 4.00 m (T-beam 11)

Figure 8.3: Cross-sectional verification with fixed load positions (connected T-beam)

ultimate loads given in Tables 8.3–8.4. For the linear analysis of connected T-beam number 5, with the load positioned at a = 2.20 m, $F_{max,V_{ST}}$ = 1693 kN, with the critical cross-section at x = 1.80 m. Combining the acting shear of the dead weight and the prestressing ($V_{dw} + V_{pw}$, see Chapter 5 Section 5.4 Figure 5.11c) with the acting shear of the load, the shear resistance of the linear analysis is determined by Equation 8.9.

$$V_{R,(8.9)} = (V_{dw} + V_{pw}) + V_F = (132 - 172) + 942 = V_{R,ST} = 902 \text{ [kN]} \tag{8.9}$$

For the nonlinear analysis of connected T-beam number 6, with the load positioned at

a = 2.25 m, $F_{u,NL}$ = 3256 kN. In the nonlinear analysis, the critical cross-section is at x = 1.818 ≈ 1.80 m, i.e. similar to the linear analysis (Chapter 7 Section 7.8.2 Figure 7.51b). Assuming the acting shear of the dead weight and the prestressing from the linear analysis (the shear force of the nonlinear analysis corresponds well to the linear analysis, see Chapter 7 Section 7.8.1), the shear resistance of the nonlinear analysis A-T2 is determined by Equation 8.10[1].

$$V_{R,(8.10)} = (V_{dw} + V_{pw}) + V_F = (132 - 172) + 1480 = 1440 \text{ [kN]} \tag{8.10}$$

From the experiment, test 2, with the load positioned at a = 2.25 m, $F_{u,test}$ = 3444 kN. The critical cross-section is again taken at x = 1.80 m. Assuming the acting shear as a result of the dead weight and the prestressing like before, as well as taking the ratio between the acting shear (V_F) and the ultimate load (F_u) from the nonlinear analysis, the shear resistance of test 2 is determined by Equation 8.11.

$$V_{R,(8.11)} = (V_{dw} + V_{pw}) + V_F = (132 - 172) + (1480/3256) \times 3444 = 1525 \text{ [kN]} \tag{8.11}$$

Likewise, for the linear analysis of connected T-beam number 11, with the load positioned at a = 4.00 m, $F_{max,V_{ST}}$ = 1641 kN, with the critical cross-section at x = 4.20 m. Combining the acting shear of the dead weight and the prestressing ($V_{dw}+V_{pw}$, see Chapter 5 Section 5.4 Figure 5.11c) with the acting shear of the load, the shear resistance of the linear analysis is determined by Equation 8.12. Note that, for cross-sections $x > a$, V_F is negative.

$$V_{R,(8.12)} = (V_{dw} + V_{pw}) + V_F = (103 - 141) - 531 = V_{R,ST} = -569 \text{ [kN]} \tag{8.12}$$

For the nonlinear analysis of connected T-beam number 11, with the load positioned at a = 4.00 m, $F_{u,NL}$ = 2760 kN. In the nonlinear analysis, the critical cross-section is at x = 4.335 ≈ 4.20 m, i.e. similar to the linear analysis (Chapter 7 Section 7.8.1 Figure 7.36d). Assuming the acting shear of the dead weight and the prestressing from the linear analysis, the shear resistance of the nonlinear analysis A-T1 is determined by Equation 8.13[1].

$$V_{R,(8.13)} = (V_{dw} + V_{pw}) + V_F = (103 - 141) - 1057 = -1095 \text{ [kN]} \tag{8.13}$$

Finally, from the experiment, test 1, with the load positioned at a = 4.00 m, $F_{u,test}$ = 3004 kN. The critical cross-section is again taken at x = 4.20 m. Note that in test 1, prior to the shear punching failure, shear cracks occurred in the web of the T-beam in both longitudinal directions (Chapter 6 Section 6.4.1 Figure 6.31). Assuming the acting shear as a result of the dead weight and the prestressing like before, as well as taking the ratio between the acting shear (V_F) and the ultimate load (F_u) from the nonlinear analysis, the shear resistance of test 1 is determined by Equation 8.14.

$$V_{R,(8.14)} = (V_{dw} + V_{pw}) + V_F = (103 - 141) - (1057/2760) \times 3004 = -1188 \text{ [kN]} \tag{8.14}$$

[1] Note that in the nonlinear analysis the signs of the acting shear are reversed, see Chapter 7.

The results of the calculated shear resistances from the linear analyses, the full-scale collapse tests and the nonlinear analyses (Equations 8.9–8.14), at the two investigated load positions (a) and critical cross-sections (x), are summarised in Figure 8.4 (in absolute values).

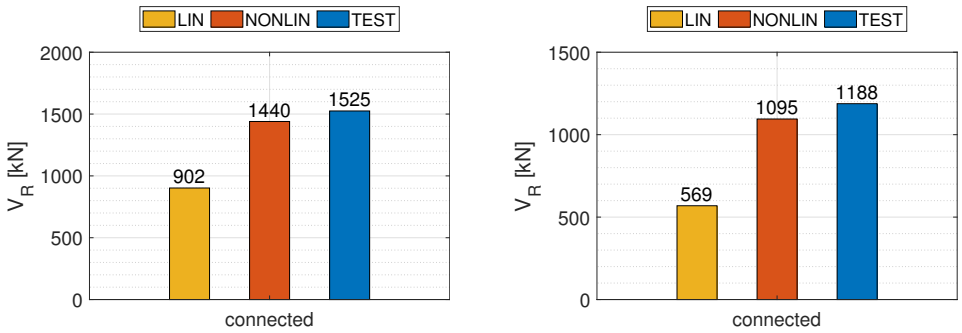

(a) a = 2.25 m, x = 1.80 m (Equations 8.9–8.11) (b) a = 4.00 m, x = 4.20 m (Equations 8.12–8.14)

Figure 8.4: Summary of shear resistance connected T-beam

Note that, due to the premature punching failure of the deck, the 'real' shear resistance of the connected T-beam, at the two investigated load positions, from both the nonlinear analysis as well as the tests, might be underestimated.

In conclusion, with the load positioned at 2.25 m, compared to the linear analysis, the shear tension resistance from the nonlinear analysis is increased by 60%, see Figure 8.4a. In addition, comparing the linear analysis to the test, the shear tension resistance is increased by 69%.

Likewise, with the load positioned at 4.00 m, compared to the linear analysis, the shear tension resistance from the nonlinear analysis is increased by 92%, see Figure 8.4b. In addition, comparing the linear analysis to the test, the shear tension resistance is increased by 109%.

8.2.3. SHEAR RESISTANCE INDIVIDUAL VERSUS CONNECTED T-BEAM

FOR several reasons, the results of the shear resistance of an individual T-beam, see Section 8.2.1, cannot be readily compared to the results of the shear resistance of a connected T-beam, see Section 8.2.2.

Firstly, the difference in load distribution causes the failure mode to switch from flexural shear, in case of an individual T-beam, to shear tension, in case of a connected T-beam, compare Figure 8.1 to Figure 8.3. The linear analysis shows that this difference in behaviour becomes more apparent for connected T-beams at a greater distance from the edge beam (see Chapter 5 Section 5.6.5, compare Figures 5.27–5.30). In addition to the change of failure mode, the load distribution also causes a (minor) shift of the location of the critical cross-sections, with x = 2.20 m and x = 4.00 m, in case of an individual T-beam (Figure 8.1), and x = 1.80 m and x = 4.20 m, in case of a connected T-beam (Figure 8.3).

Secondly, in case of a connected T-beam, due to the constraints provided by the surrounding members, the nonlinear analyses A-T1 and A-T2 show a significant additional compressive normal force in the loaded T-beam (see Chapter 7 Section 7.8), which will affect the shear resistance.

Despite the above-mentioned caveats, Figure 8.5 shows the increase in shear resistance of a connected T-beam compared to an individual T-beam. For the connected T-beam results, it is noted that the load distribution is strongly influenced by the presence of the cross-beams. For cross-sections closer to a cross-beam, the shear tension resistance tends to related to a maximum principal tensile stress (σ_1) in the web, whereas for cross-sections closer to the area in-between the cross-beams, the shear tension resistance tends to relate to a maximum principal tensile stress at the bottom fibre, i.e. the cracking moment (M_{cr}), see Chapter 5 Section 5.6.3 Figure 5.21.

The shear tension resistance of the linear analyses can possibly be improved by taking into account the additional compressive normal forces from the nonlinear analyses. With the load positioned at a = 2.25 m (analysis A-T2), the additional compressive normal force at failure equals 2010 kN (Chapter 7 Section 7.8.2 Figure 7.48). For the linear analysis of connected T-beam number 5, taking the additional compressive normal force into account, $F_{\max,V_{ST}}$ = 2017 kN (x = 1.80 m). Combining the acting shear of the dead weight and the prestressing ($V_{dw} + V_{pw}$), with the acting shear of the load, the shear resistance of the improved linear analysis is determined by Equation 8.15.

$$V_{R,(8.15)} = (V_{dw} + V_{pw}) + V_F = (132 - 172) + 1123 = V_{R,ST} = 1083 \text{ [kN]} \tag{8.15}$$

With the load positioned at a = 4.00 m (analysis A-T1), the additional compressive normal force at failure equals 1740 kN (Chapter 7 Section 7.8.1 Figure 7.33). For the linear analysis of connected T-beam number 11, taking the additional compressive normal force into account, $F_{\max,V_{ST}}$ = 2000 kN (x = 4.20 m). Combining the acting shear of the dead weight and the prestressing ($V_{dw} + V_{pw}$), with the acting shear of the load, the shear resistance of the improved linear analysis is determined by Equation 8.16.

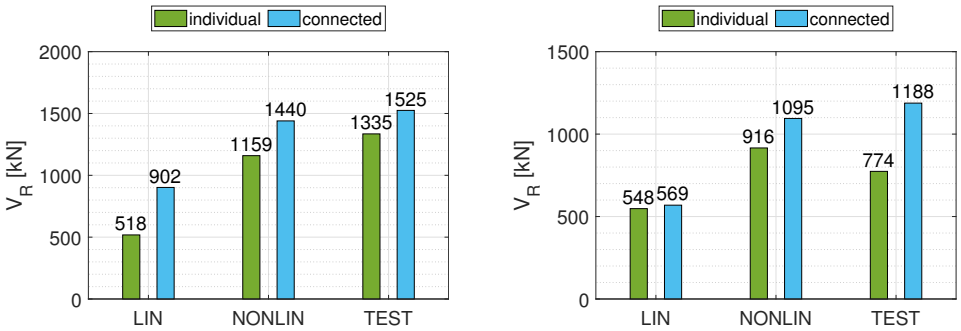

(a) a = 2.25 m (b) a = 4.00 m

Figure 8.5: Summary of shear resistance individual versus connected T-beam (results of Sections 8.2.1–8.2.2)

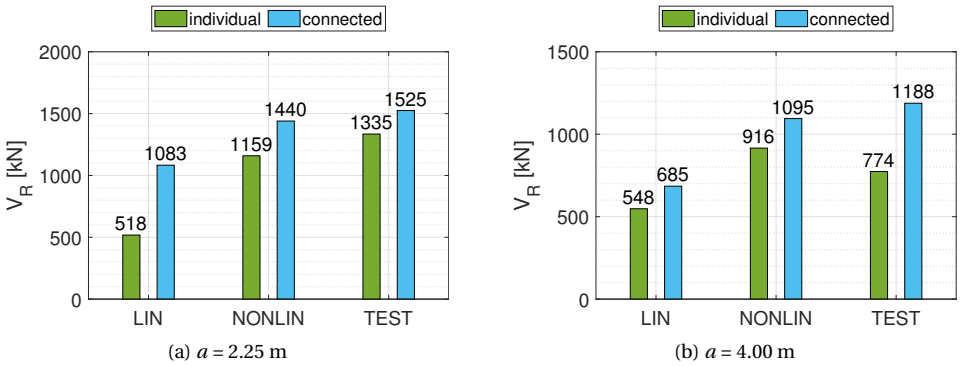

(a) $a = 2.25$ m (b) $a = 4.00$ m

Figure 8.6: Summary of shear resistance individual versus connected T-beam (linear analysis improved with additional compressive normal force)

$$V_{R,(8.16)} = (V_{\text{dw}} + V_{\text{pw}}) + V_{\text{F}} = (103 - 141) - 647 = V_{\text{R,ST}} = -685 \text{ [kN]} \tag{8.16}$$

With the results of the improved linear analysis, Figure 8.6 shows the increase in shear resistance of a connected T-beam compared to an individual T-beam. In both cases, the improved linear analysis shows an increase of the shear resistance of 20%.

In all cases and at both loading positions, due to the effects of system behaviour, the shear resistance of a connected T-beam is increased as compared to an individual T-beam, see Figures 8.5–8.6. Based on the experiments, tests 1–7, and the corresponding nonlinear analyses, the shear resistance is increased by 14–53%. As stated in the previous section, due to the premature punching failure of the deck, the 'real' shear resistance of the connected T-beam might be underestimated.

8.2.4. COMPRESSIVE MEMBRANE ACTION

In this section, the ultimate load related to compressive membrane action (CMA), of a connected T-beam of the Vecht bridge is analysed, using the analytical model for arch action, as derived in Chapter 4, and comparing the results to the full-scale collapse tests 1–2 (Chapter 6) and the corresponding nonlinear analyses (Chapter 7).

In both tests, the load is situated at the center of the T-beam. The main difference between test 1 and 2, is the location of the load in the longitudinal direction (Chapter 6 Section 6.2 Figure 6.1). In Figure 8.7, the cross-section of the deck and the assumed arch, at the location of the concentrated load, are indicated. As shown in Figure 8.7, the arch is assumed to develop from the loading point, in the top flange of the loaded T-beam and the integrated deck slab, to the adjacent T-beams on either side. The shape of the arch shown in Figure 8.7 is in accordance with the results of the nonlinear analysis, see Chapter 7 Section 7.8.1 Figure 7.39b (analysis A-T1) and Section 7.8.2 Figure 7.47b (analysis A-T2). The length of the arch is taken approximately equal to the distance between the cracks resulting from the transverse hogging bending moments on the top side of the slab, see Chapter 7 Section 7.8.1 Figure 7.29c (analysis A-T1) and Section 7.8.2

Figure 7.47c (analysis A-T2). Note that the sagging bending cracks on the bottom side are located on either side of the T-beam web. The location of the plastic hinges can therefore be modelled as shown in Figure 8.7 model (b). However, with the analytical model for arch action this is simplified to model (a). With these assumptions, the slab slenderness is equal to: $\lambda = L/h = 1950/180 = 10.83$. The transverse prestressing in the deck results in an initial compressive stress, at the position of the load, of approximately S_{XX} = -2.9 N/mm^2, see Chapter 7 Section 7.8.1 (analysis A-T1) and S_{XX} = -3.1 N/mm^2, see Section 7.8.2 (analysis A-T2).

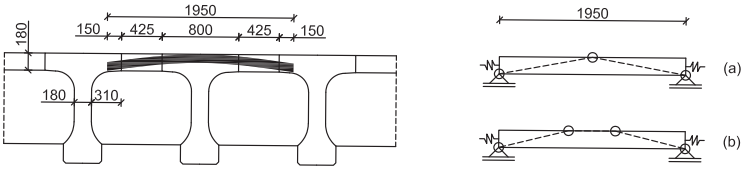

Figure 8.7: Assumed slab arching (CMA) in connected beam tests 1–2 (measurements in mm)

In both tests 1 and 2, the failure mode is punching of the deck slab (Chapter 6 Section 6.4). The failure load can therefore not be predicted by the analytical model for arch action (Chapter 4), as this model relates to the flexural CMA capacity. In order to predict the punching shear capacity of the deck slab, the presence of the loaded T-beam is temporarily neglected, resulting in a free span of the deck slab of 1950 mm. The punching shear capacity is then predicted using the results of the experimental program on transverse prestressed slabs by Amir (2014). These experiments are a 1:2 scale of the Van Brienenoord bridge, see also Chapter 2. The selected experimental tests, with a single concentrated load at midspan, and corresponding parameters and results are summarised in Table 8.5. In all tests, the slab has a free span of L = 1050 mm and a thickness of h = 100 mm. In addition, the top and bottom transverse reinforcement in the span is equal to ø6-200 mm (f_y = 525 N/mm^2).

The first step is to demonstrate the analytical model for arch action for the 1:2 scale experimental results summarised in Table 8.5. Assuming a linear horizontal stiffness[2] (k_{hor}), the calibration of the analytical model consist of obtaining a load versus displacement curve which includes a data point at a load of F_u = 338.7 kN at a vertical deflection of δ_u = 5.50 mm, see Table 8.5. The results of the first step calibration are given in Figure 8.8 (detailed results are given in Appendix C Sections C.1–C.2). For the acting width of the slab, a load distribution at an angle of 45°, from the load to the slab edges, is assumed resulting in a width of the slab equal to the span, i.e. B = 1050 mm. In Figure 8.8b, the influence of the transverse bending moments in the slab is taken into account assuming full plasticity of the reinforcement in the span, i.e. $N_{M_{u,span}} = {}^1/_4 \times \pi \times 6^2 \times (1050/200) \times 525 = 78 \times 10^3$ N, resulting in ζ_{span} = 0.067 (Equation 4.16), whereas in Figure 8.8a the transverse bending moments are neglected. The flexural CMA capacity is also derived in the thesis by Amir (2014), using the model by Park and Gamble (2000), resulting in an ultimate load capacity of approximately 410 kN. Figure 8.8 demonstrates that similar values

[2]Using a linear horizontal stiffness Chapter 4 Equation 4.1 simplifies to $\Delta F = k_{hor} \times \Delta u$.

Table 8.5: Punching shear capacity of transverse prestressed slabs with CMA, selected experimental results with a single concentrated load at midspan and corresponding parameters (Amir 2014)

test	λ	f_{cm}	TPL[a]	loading plate	Δu[b]	δ_u	F_u
	-	N/mm^2	N/mm^2	mm×mm	mm	mm	kN
BB01	10.50	65	2.50	200×200	0.368	5.80	348.7
BB02	10.50	65	2.50	200×200	0.414	4.92	321.4
BB07	10.50	65	2.50	200×200	0.152	5.77	345.9
average					0.311	5.50	338.7

[a] TPL = transverse prestressing level, [b] horizontal displacement, average from both sides

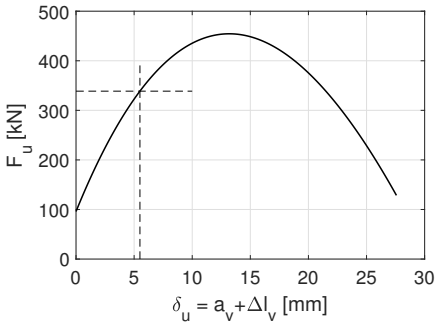

(a) k_{hor} = 995000 N/mm, $\zeta_{span} = \zeta_{supp} = 0$, δ_u = 13.17 mm, $F_{u,max}$ = 454.4 kN

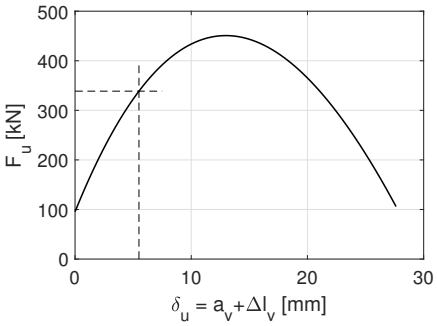

(b) k_{hor} = 1009000 N/mm, ζ_{span} = 0.067, ζ_{supp} = 0, δ_u = 12.99 mm, $F_{u,max}$ = 450.8 kN

Figure 8.8: Ultimate concentrated load, $L = B$ = 1050 mm, h = 100 mm (1:2 scale), f_{cm} = 65 N/mm^2, TPL = 2.5 N/mm^2, dashed line indicates punching failure at F_u = 338.7 kN (for detailed results see Appendix C Sections C.1–C.2)

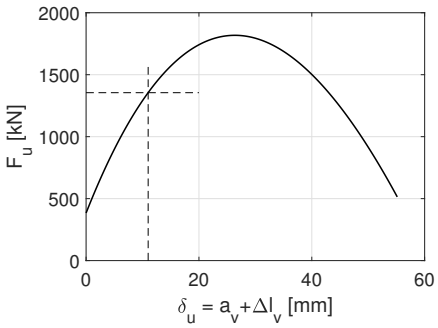

(a) k_{hor} = 1990000 N/mm, $\zeta_{span} = \zeta_{supp} = 0$, δ_u = 26.37 mm, $F_{u,max}$ = 1818 kN

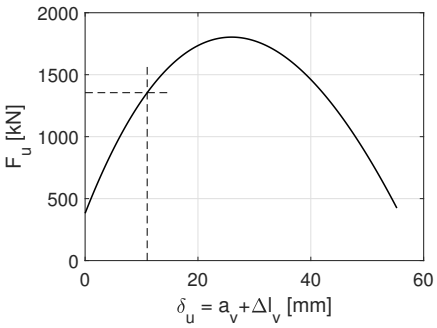

(b) k_{hor} = 2018000 N/mm, ζ_{span} = 0.067, ζ_{supp} = 0, δ_u = 25.98 mm, $F_{u,max}$ = 1803 kN

Figure 8.9: Ultimate concentrated load, $L = B$ = 2100 mm, h = 200 mm (1:1 scale), f_{cm} = 65 N/mm^2, TPL = 2.5 N/mm^2, dashed line indicates punching failure at F_u = 1355 kN (for detailed results see Appendix C Sections C.3–C.4)

are obtained by the analytical model for arch action. Note that the horizontal deformation (Δu) is not well predicted by the analytical model, as the obtained values are much higher (Appendix C Sections C.1–C.2) compared to the deformations from the experiments (Table 8.5). Figure 8.8 shows that the punching failure load is approximately equal to 75% of the flexural failure load. Note that with $\zeta_{span} = 0.067$ (Figure 8.8b), a somewhat higher stiffness is required in order to obtain the same load capacity for punching.

The next step is to repeat the analysis, using the real dimensions of the Van Brienenoord bridge and by applying a force scale factor of x^2, resulting in a punching load capacity of $F_u = 4 \times 338.7 \approx 1355$ kN. Note that an additional size factor, as reported by Amir (2014) and dependent on the transverse prestressing level (TPL), is ignored (0.98–1.08 for TPL = 2.5 N/mm^2). The results of the analysis are shown Figure 8.9 (detailed results are given in Appendix C Sections C.3–C.4).

The result of the two-step calibration is a horizontal stiffness for the Van Brienenoord bridge, equal to $k_{hor} \approx 1990000$–2018000 N/mm. The Vecht bridge is assumed to have at least a similar or, more likely, a much higher horizontal stiffness. This is because the calibration is based upon the setup of the 1:2 scale bridge, consisting of only 4 T-beams, and the Vecht bridge tests 1–2 are conducted with at least five adjacent T-beams (Chapter 6 Section 6.2 Figure 6.1). In addition, the setup of the 1:2 scaled bridge includes two cross-beams with a spacing of 10950 mm compared to 8000 mm in the case of the Vecht bridge (Chapter 5 Section 5.2.4 Figure 5.5).

As shown in Table 8.5 the main parameters for CMA are very similar to the Vecht bridge, i.e. the slab slenderness (λ) and the concrete compressive strength (f_{cm}). However, the transverse prestressing level is slightly lower as compared to the Vecht bridge. In the numerical parameter study by Amir (2014) the transverse prestressing level is investigated between 0.5–4.5 N/mm^2, and a linear relation was found between the punching failure load and the transverse prestressing level (TPL): $F_u = 25.139 \times \text{TPL} + 240.31$ [kN]. For the Vecht bridge, with an average transverse prestressing level of $S_{XX} = -3.0$ N/mm^2 (tests 1–2), this results in $F_u = 315.7$ kN. Note that the experiments resulted in higher failure loads as compared to the numerical study, with an average ratio of 1.12 for the selected tests listed in Table 8.5.

For the Vecht bridge, the slab thickness is increased by a factor of 1.8. Therefore, the resulting size factor for the ultimate load, including the increase of the punching perimeter, is equal to $2 \times 1.8 = 3.6$. The punching load capacity for the Vecht bridge is therefore equal to approximately $F_u = 3.6 \times 338.7 = 1219$ kN (average from tests). When taking into account the slightly higher transverse prestressing level, and using the ratio between the experiments and the numerical parameter study, the punching capacity increases to $F_u = 3.6 \times 1.12 \times 315.7 = 1273$ kN.

For the analysis of tests 1 and 2 of the Vecht bridge, the next step is to apply the analytical model for arch action using a horizontal stiffness, obtained from the calibration, of $k_{hor} \approx 1990000$ N/mm (Figure 8.9a). Note that, in the case of the Vecht bridge, due to the lower reinforcement ratio and yielding strength of the transverse reinforcement (Chapter 5 Section 5.2), the influence of the bending moments can be neglected. Conservatively, the lower concrete compressive strength of the integrated deck slab ($f_{cm} = 60.3$ N/mm^2) will be used in the analysis. Note that for the Vecht bridge, part of the punching cone is located in the top flange of the T-beam which has a 45% higher concrete compressive

strength (f_{cm} = 87.7 N/mm^2). For the acting width of the slab see also Chapter 7 Section 7.8.1 Figures 7.41–7.42 (analysis A-T1) and Section 7.8.2 Figures 7.56–7.57 (analysis A-T2). With these assumptions, the load versus vertical deflection is shown in Figure 8.10a (detailed results are given in Appendix C Section C.5).

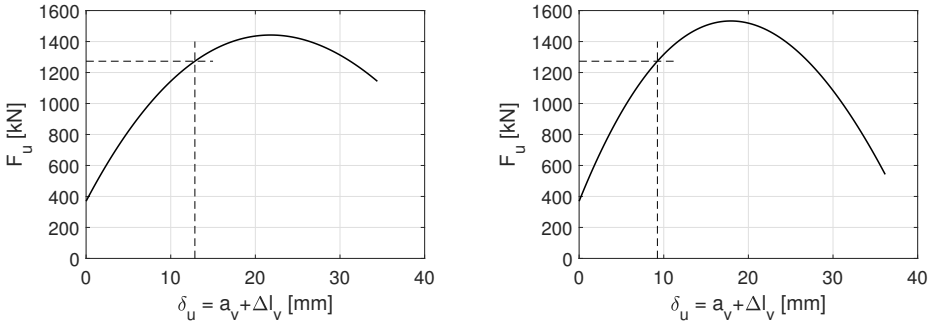

(a) k_{hor} = 1990000 N/mm, $\zeta_{span} = \zeta_{supp} = 0$, $F_{u,max}$ = 1442 kN (δ_u = 21.87 mm)

(b) k_{hor} = 2710000 N/mm, $\zeta_{span} = \zeta_{supp} = 0$, $F_{u,max}$ = 1533 kN (δ_u = 17.82 mm)

Figure 8.10: Ultimate concentrated load, $L = B$ = 1950 mm, h = 180 mm, f_{cm} = 60.3 N/mm^2, TPL = 3.0 N/mm^2, dashed line indicates punching failure at F_u = 1273 kN (for detailed results see Appendix C Sections C.5–C.6)

As detailed vertical slab deformations are not available from tests 1–2, the deformations are taken from the nonlinear analysis. Note that the global deformations of the T-beams need to be subtracted in order to obtain the local, relative, slab deformations. The maximum relative slab deformation at failure, between the loaded T-beam and the adjacent T-beams (at the ends of the arch), is approximately equal to δ_u = |-12.5+3.5| = 9.0 mm (analysis A-T1, Chapter 7 Section 7.8.1 Figure 7.40c), and δ_u = |-11.5+2.0| = 9.5 mm (analysis A-T2, Section 7.8.2 Figure 7.55c). Figure 8.10a shows that the relative slab deformation, at the punching failure load of 1273 kN, is equal to δ_u = 12.9 mm, i.e. approximately 40% higher as compared to the nonlinear analysis. As previously discussed, the horizontal stiffness for the Vecht bridge is expected to be higher. In addition, due to the presence of the loaded T-beam at midspan, the (relative) slab deformations are reduced. Assuming the punching failure load of 1273 kN is correct, a load versus displacement curve can be derived by increasing the horizontal stiffness, which includes a data point at a load of F_u = 1273 kN and a vertical deflection of δ_u = 9.25 mm (average from tests 1 and 2). The result of this final analysis is shown in Figure 8.10b (detailed results are given in Appendix C Section C.6). The horizontal stiffness is now increased by 36%. The punching failure load is approximately equal to 83–88% of the flexural failure load, see Figure 8.10. Note that at F_u = 1273 kN, for the case of Figure 8.10a, the membrane force is equal to ΔF = 3960 kN, and for the case of Figure 8.10b equal to ΔF = 3740 kN. With the assumption of an acting width symmetrically around the loading point, the numerically obtained values are ΔF = 3467 kN (analysis A-T1, Chapter 7 Section 7.8.1 Figure 7.42) and ΔF = 2825 kN (analysis A-T2, Chapter 7 Section 7.8.2 Figure 7.57). When a non-symmetrical acting width is assumed, the maximum numerical values are ΔF = 3536 kN

(analysis A-T1), with the centre of the acting width shifted by 0.29 m (Figure 8.11), and ΔF = 3247 kN (analysis A-T2), with the centre of the acting width shifted by 0.58 m (Figure 8.12). As the slab and T-beam are connected, a more comprehensive combined CMA (slab) and CAA (T-beam) analysis will be given in Section 8.2.6.

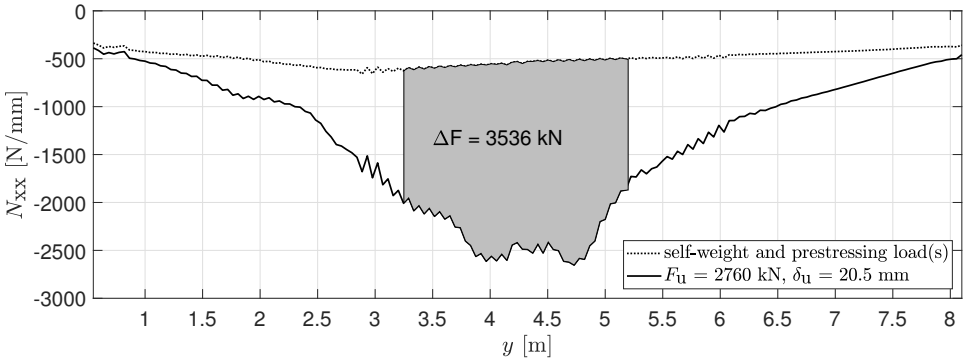

Figure 8.11: A-T1-90/180-QNR, in-plane force N_{xx}, horizontal axis in span direction with load at y = 4.00 m (see also Figure 7.41), grey area indicates maximum integrated membrane force ΔF

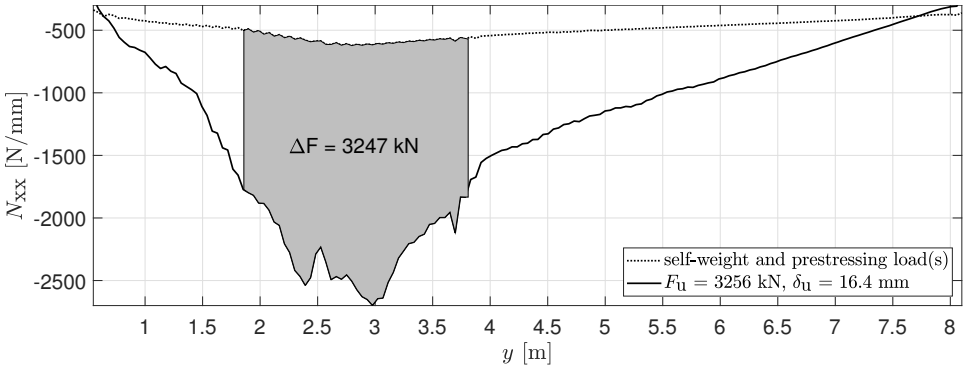

Figure 8.12: A-T2-90/180-QNR, in-plane force N_{xx}, horizontal axis in span direction with load at y = 2.25 m (see also Figure 7.56), grey area indicates maximum integrated membrane force ΔF

8.2.5. COMPRESSIVE ARCH ACTION

In this section, the ultimate load related to compressive arch action (CAA), of a connected T-beam of the Vecht bridge is analysed, using the analytical model for arch action, as derived in Chapter 4, and comparing the results to the full-scale collapse test (Chapter 6) and the corresponding nonlinear analysis (Chapter 7).

For the analysis of CAA the results of test 1 are utilised. In this test, the load is centered between the end cross-beam and the intermediate cross-beam, see Figure 8.13. As indicated in this figure, the arch is assumed to develop from the loading point to the inner edges of the cross-beams, which are assumed to provide a significant horizontal stiffness. This behaviour is also observed from the results of the nonlinear analysis, see Chapter 7 Section 7.8.1 Figures 7.31 and 7.32. With these assumptions, the beam slenderness is equal to: $\lambda = L/h = 7550/950 = 7.95$.

As a first approach for the analysis, some assumptions have to be made regarding the stiffness of the edge restraints. On the left side of the arch, at the end support, the horizontal stiffness is taken as the horizontal bending stiffness of the end cross-beam, whereas on the right side an 'infinite' stiffness is assumed (Figure 8.13). For simplicity, the horizontal stiffness is derived by taking the end cross-beam as a simply supported beam, spanning between the center lines of the adjacent T-beams, and loaded horizontally at midpoint by the arch, see left of Figure 8.13. Therefore, the clamped ends (continuous beam) and the rotation due to torsion of the end cross-beam are neglected.

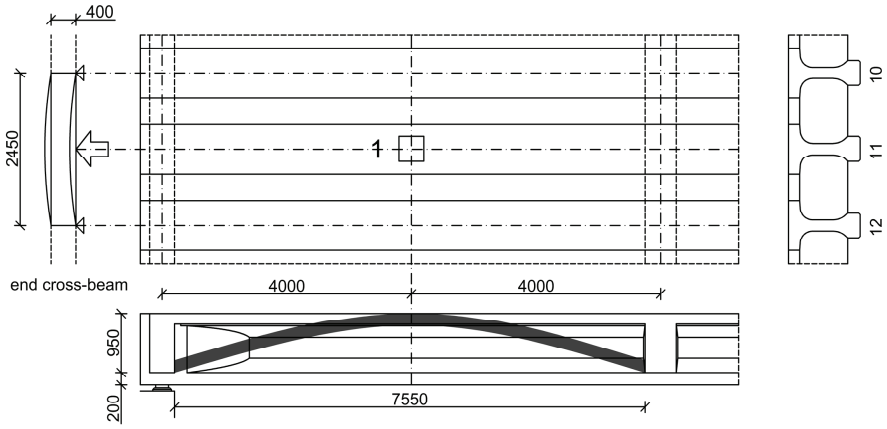

Figure 8.13: Assumed beam arching (CAA) in connected beam test 1 (measurements in mm)

With L = 2450 mm, b = 400 mm and h = 950 mm (Figure 8.13), E_{cm} = 37715 N/mm^2 (assumed uncracked, see Chapter 7 Section 7.3.1 Table 7.3), $I_c = \frac{1}{12}hb^3 = 5067 \times 10^6$ mm^4, the linear horizontal stiffness of the end cross-beam is given by Equation 8.17.

$$k_{hor} = \frac{48 E_{cm} I_c}{L^3} = \frac{48 \times 37715 \times 5067 \times 10^6}{2450^3} = 623705 \text{ [N/mm]} \tag{8.17}$$

Due to the symmetry of the arch action model, and with the assumption of an 'infinite' stiffness at the location of the intermediate cross-beam, the equivalent stiffness, at either end, is equal to: $k_{hor} = 2 \times 623705 = 1247410 \approx 1250000$ N/mm.

For the analysis, the T-beam cross-section including the acting width of the integrated deck slab is taken. To account for the lower concrete compressive strength of the deck, the acting width of the integrated deck slab is reduced, similar to the approach used for the ultimate bending moment (Chapter 5 Section 5.6.4). The resulting cross-sectional properties are shown in Appendix E Figure E.3a.

Test 1 resulted in punching of the deck thereby significantly reducing the height of the T-beam available for arching due to the damaged top flange. In a separate analysis, this is taken into account by omitting the part of the top flange with a width larger than 400 mm, i.e. approximately equal to the loading plate as well as the punching perimeter (Chapter 6 Section 6.4.1 Figure 6.30). With this approach, the height of the arch is reduced from 950 mm to approximately 742 mm. The resulting cross-sectional properties after punching are shown in Appendix E Figure E.3b.

The results of the analytical arch action model, for various prestressing levels, are summarised in Tables 8.6–8.7 (full arch height) and in Tables 8.8–8.9 (reduced arch height after punching). In Tables 8.7 and 8.9, the influence of the bending moments in the T-beam are taken into account by taking the average additional stress in the tendons 1–7 in the span from the nonlinear analysis (Chapter 7 Section 7.8.1 Figure 7.38a), i.e. $N_{M_{\mathrm{u,span}}} = \Delta\sigma_{\mathrm{p}} \times A_{\mathrm{p}} = 160 \times 7 \times 462 = 517 \times 10^3$ N, whereas in Tables 8.6 and 8.8 the bending moments are neglected. Detailed results of all calculations with 100% prestressing are given in Appendix D.

A key parameter for CAA is the level of restraint, i.e. the assumed horizontal stiffness k_{hor} used in the calculation. For the case of a T-beam with an integrated deck slab and 100% prestressing, see Table 8.6, the influence of the level of restraint is investigated by using halve and double the original stiffness. Using halve stiffness ($k_{\mathrm{hor}} = 625000$ N/mm^2), results in $F_{\mathrm{u}} = 2903$ kN with $\Delta u = 12.55$ mm and $\delta_{\mathrm{u}} = 59.52$ mm. Using double stiffness ($k_{\mathrm{hor}} = 2500000$ N/mm^2), results in $F_{\mathrm{u}} = 3146$ kN with $\Delta u = 3.30$ mm and $\delta_{\mathrm{u}} = 21.47$ mm. Therefore, using halve stiffness, the ultimate load is reduced by just 5%, whereas using double stiffness, the ultimate load is increased by just 3%.

From the results in Tables 8.6–8.9 and Appendix D the following general observations regarding CAA are made:

- The ultimate failure load is largely independent of the level of prestressing.
- With increasing prestressing (N_{p}), the membrane force (ΔF) decreases, whereas the total normal force (F_{tot}) remains almost constant. This indicates that CAA is a structural phenomenon which is mostly dependent on the level of restraint, the beam slenderness and the concrete compressive strength.
- With increased prestressing, the ductility decreases resulting in reduced horizontal (Δu) en vertical (δ_{u}) deformations.
- Typically, a bridge deck will be loaded by concentrated (wheel) loads as well as distributed loads. The CAA results demonstrate a significant load capacity for both types of loadings.
- Due to the relatively low additional force in the tendons in the span ($N_{M_{\mathrm{u,span}}}$), and the corresponding low ratio for ζ_{span} (Equation 4.16), the bending moment in the

Table 8.6: CAA results at ultimate load, T-beam with integrated deck slab (Appendix E Figure E.3a), L = 7550 mm, h = 950 mm, k_{hor} = 1250000 N/mm, $\zeta_{span} = \zeta_{supp} = 0$, various prestressing levels

prestressing	N_p [a]	ΔF	F_{tot}	Δu [b]	δ_u	z	F_u	q_u
%	kN	kN	kN	mm	mm	mm	kN	kN/m
0	0	10690	10690	8.55	45.59	518	2925	773
25	675	10060	10740	8.05	42.86	521	2960	782
50	1350	9500	10850	7.60	40.41	522	2996	792
75	2025	8875	10900	7.10	37.70	526	3030	801
100	2700	8310	11010	6.65	35.27	527	3066	811

[a] $N_p = \max(N_{p,span}, N_{p,supp})$, see Chapter 4 Section 4.6 Equation 4.29

[b] step size equal to 0.05 mm

Table 8.7: CAA results at ultimate load, T-beam with integrated deck slab (Appendix E Figure E.3a), L = 7550 mm, h = 950 mm, k_{hor} = 1250000 N/mm, ζ_{span} = 0.047 and $\zeta_{supp} = 0$

prestressing	N_p [a]	ΔF	F_{tot}	Δu [b]	δ_u	z	F_u	q_u
%	kN	kN	kN	mm	mm	mm	kN	kN/m
100	2700	8310	11010	6.65	35.27	523	3048	806

[a] $N_p = \max(N_{p,span}, N_{p,supp})$, see Chapter 4 Section 4.6 Equation 4.29

[b] step size equal to 0.05 mm

Table 8.8: CAA results at ultimate load, T-beam with reduced cross-section after punching (Appendix E Figure E.3b), L = 7550 mm, h = 742 mm, k_{hor} = 1250000 N/mm, $\zeta_{span} = \zeta_{supp} = 0$, various prestressing levels

prestressing	N_p [a]	ΔF	F_{tot}	Δu [b]	δ_u	z	F_u	q_u
%	kN	kN	kN	mm	mm	mm	kN	kN/m
0	0	5440	5440	4.35	38.74	415	1193	316
25	675	4815	5490	3.85	34.20	418	1215	322
50	1350	4190	5540	3.35	29.68	422	1238	328
75	2025	3565	5590	2.85	25.19	426	1261	334
100	2700	2940	5640	2.35	20.71	430	1283	340

[a] $N_p = \max(N_{p,span}, N_{p,supp})$, see Chapter 4 Section 4.6 Equation 4.29

[b] step size equal to 0.05 mm

Table 8.9: CAA results at ultimate load, T-beam with reduced cross-section after punching (Appendix E Figure E.3b), L = 7550 mm, h = 742 mm, k_{hor} = 1250000 N/mm, ζ_{span} = 0.094 and $\zeta_{supp} = 0$

prestressing	N_p [a]	ΔF	F_{tot}	Δu [b]	δ_u	z	F_u	q_u
%	kN	kN	kN	mm	mm	mm	kN	kN/m
100	2700	2815	5515	2.25	19.82	421	1229	325

[a] $N_p = \max(N_{p,span}, N_{p,supp})$, see Chapter 4 Section 4.6 Equation 4.29

[b] step size equal to 0.05 mm

span can be neglected.

- The reduced cross-section after punching results in a significant reduction of the ultimate load capacity, caused by the combined effect of the loss of the cross-sectional area of the top flange and the increase of the beam slenderness. After punching, for the current case with a concentrated load, the remaining cross-section is insufficient to carry the same load by arching ($F_{u,test}$ = 3004 kN versus $F_{u,CAA}$ = 1229 kN (Table 8.9)).

8.2.6. COMBINED CMA (SLAB) AND CAA (T-BEAM) TEST 1

FOR slabs CMA enhances both the flexural resistance as well as the punching shear resistance (Chapter 3). However, when considering a concentrated load, a slab will fail in punching. Likewise for beams, CAA enhances both the flexural resistance as well as the shear resistance. Analogously to slabs, it is reasonable to assume the same principle holds for beams and a shear failure will be governing for beams. However, the CAA-enhanced shear capacity of the T-beam is unknown.

In the previous section, the CAA load capacity of the T-beam is derived completely independent of the CMA load capacity of the slab. In this section, it is assumed that part of the load is carried by CMA and part of the load is carried by CAA. Note that the underlying principle in this combined CMA and CAA analysis, is assuming full plasticity and using the principle of superposition of both mechanisms. Firstly, it is assumed the difference between the punching failure load of the slab and the total failure load is carried by CAA. In Section 8.2.4, a punching failure load for tests 1–2 is derived of $F_{u,CMA}$ = 1273 kN at a relative slab deformation of $\delta_{u,CMA}$ = 9.25 mm. For test 1, the difference between the total failure load and the punching failure load equals to $F_{u,CAA}$ = 2760-1273 = 1487 kN (Chapter 7 section 7.8.1 Table 7.16). In addition, there should be compatibility between the deformations of both CMA and CAA at failure. The deformations are again taken from the nonlinear analysis. Note that the vertical deformation at the end support and at the intermediate cross-beam (assumed fictitious support see Chapter 3 Section 3.4.4 Figure 3.6) need to be subtracted in order to obtain the local, relative, T-beam deformations. The T-beam deformations, at various locations along its length, are shown in Figure 8.14a. At failure, the average deflection at the loading point, due to the deflections of the (fictitious) supports equals to approximately δ_{avg} = 6.34 mm. Therefore, for test 1, the maximum relative T-beam deformation at failure, between the loading point and the (fictitious) supports (at the ends of the arch), is approximately equal to: $\delta_{u,CAA}$ = 20.5-6.34 = 14.16 mm. Using this deformation the analytical model for arch action can be applied to derive a load versus displacement curve which includes a data point at a load of $F_{u,CAA}$ = 1487 kN and a vertical deflection of $\delta_{u,CAA}$ = 14.16 mm. As can be observed from the results in the previous section, a CAA failure load of the T-beam of 1487 kN corresponds to an almost zero vertical deflection, see Appendix D Sections D.1–D.2. The load capacity at zero deformation results from the prestressing force only (Chapter 4). Consequently, it is independent of the applied horizontal restraint. Therefore, with the assumed full CMA punching capacity of the slab, it is not possible to find an appropriate stiffness for CAA.

Alternatively, CAA can be calibrated independently from CMA by utilising the maximum acting shear in the T-beam as analysed in Section 8.2.2. By definition, the acting

shear, in the analytical model for arch action, equals $V_u = F_u/2$. Based on the nonlinear analysis, the acting shear at failure equals $V_u = 1095$ kN (Section 8.2.2 Figure 8.4b). With this information the analytical model for arch action can be applied to derive a load versus displacement curve which includes a data point at a load of $F_{u,CAA} = 2 \times 1095 = 2190$ kN and a vertical deflection of $\delta_{u,CAA} = 14.16$ mm. The results of the analysis are shown in Figure 8.14b (detailed results are given in Appendix D Section D.5). Note that the horizontal restraint is somewhat reduced compared to the previous section.

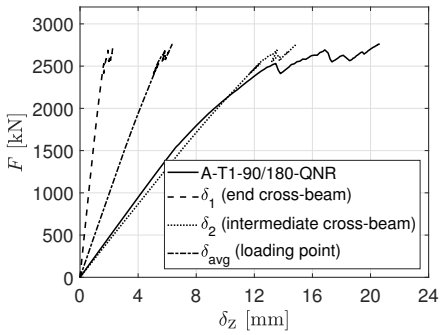

(a) A-T1-90/180-QNR, load-deflection at assumed arch ends (Figure 8.13)

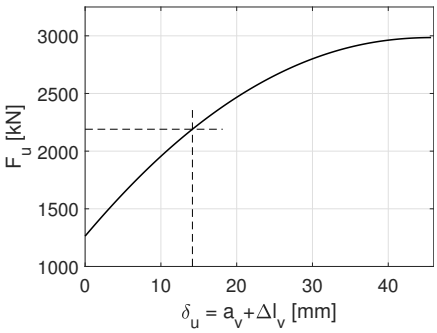

(b) Ultimate concentrated load, T-beam with integrated deck slab (Appendix E Figure E.3a), $\delta_u = 45.65$ mm, $F_u = 2985$ kN

Figure 8.14: Vecht bridge test 1, (relative) deformations T-beam (left), CAA analysis based on maximum acting shear, $k_{hor} = 907000$ N/mm, dashed line indicates shear failure at $F_u = 2190$ kN (right)

From the combined CMA (slab) and CAA (T-beam) analysis, based on the maximum acting shear, the following can be concluded:

- Assuming full plasticity, the combined analysis results in a subdivision of the load carried by CMA (slab) and CAA (T-beam) of $F_{u,CMA} = 570$ kN (21% of total load) and $F_{u,CAA} = 2190$ kN (79% of total load). However, for CAA this assumes a constant normal and shear force between the load and the supports which is not the case (Chapter 7 Section 7.8.1 Figure 7.33 and Figure 7.36).
- With the assumption of a free span, the initial CMA analysis (Section 8.2.4) resulted in a punching shear capacity of $F_{u,CMA} = 1273$ kN. The combined analysis results in a significantly lower CMA capacity of the slab of approximately $F_{u,CMA} = 570$ kN.
- It is possible that the required relative slab deformations, needed to achieve the maximum membrane force and corresponding punching shear capacity, are prevented by the presence of the T-beam at midspan. Contrary, the analysis in Section 8.2.4 shows a numerical membrane force relatively close to the analytical (87–95%), suggesting a high CMA presence.
- Figure 8.14b shows a ratio of 73% between the shear failure load and the flexural failure load. This indicates a substantial presence of CAA in the T-beam. Further evidence of this is shown in Chapter 7 Section 7.8.1 Figure 7.32 in which the maximum compressive stresses, in the direction of the intermediate cross-beam, are

approximately equal to 33 N/mm^2. Assuming the maximum effect due to lateral cracking (Figure 7.28d), the local concrete compressive strength can be approximated by $0.4 \times f_{cm} = 0.4 \times 87.7 = 35$ N/mm^2 (Section 7.3.2).

- If punching failure of the deck can be avoided or postponed, for instance in the case of multiple concentrated (axle) loads or a distributed load, the CMA capacity of the slab will increase. However, for the CAA capacity of the T-beam, considering the concrete compressive strength of the compressive strut is limited due to the presence of shear cracks (previous point), an increase in capacity is less likely.
- In the nonlinear analysis (A-T1), at the ultimate load of $F_u = 2760$ kN, the maximum membrane force of the T-beam is equal to $\Delta F = 1740$ kN (Chapter 7 Section 7.8.1). The CAA analysis results in a significant overestimated membrane force of $\Delta F = 2621$ kN (with $\Delta u = 2.89$ mm and $\delta_u = a_v + \Delta l_v = 14.16$ mm, see Appendix D Section D.5). This overestimation likely results from applying the full concrete compressive strength without taking into account the effect of lateral cracking.

8.3. SUMMARY AND CONCLUSIONS CASE STUDY

IN this section the main results and conclusions from the analysis of system behaviour of the case study are summarised.

Individual T-beam - Flexural shear resistance (Section 8.2.1)

- Combining the results of the linear and nonlinear analyses, as well as tests 4–7, the ultimate load is analysed to determine the maximum acting shear.
- With all individual beam tests, the failure mode is flexural shear.
- Compared to NEN-EN 1992-1-1 (NNI 2011a) and RTD 1006 (Rijkswaterstaat 2013), for a simply supported beam, the nonlinear analyses show an increase in flexural shear resistance of 127% ($a = 2.25$ m) and 67% ($a = 4.00$ m).
- Compared to NEN-EN 1992-1-1 (NNI 2011a) and RTD 1006 (Rijkswaterstaat 2013), for a disconnected beam, the nonlinear analyses show an increase in flexural shear resistance of 120% ($a = 2.25$ m) and 68% ($a = 4.00$ m). Therefore, it can be concluded that the nonlinear analyses show no significant difference ($\leq 3\%$) in flexural shear resistance of a simply supported T-beam compared to a disconnected T-beam. This consistency demonstrates that on-site testing of disconnected (T-) beams, which are only connected to the end cross-beam at the non-loaded side for safety, can be used to determine the (flexural) shear resistance.
- Tests 4–6, with $a = 2.25$ m, show an average increase in flexural shear resistance of 158% compared to NEN-EN 1992-1-1 (NNI 2011a) and RTD 1006 (Rijkswaterstaat 2013), and an increase of 13–17% compared to the nonlinear analyses.
- Test 7, with $a = 4.00$ m, shows an increase in flexural shear resistance of 41%, compared to NEN-EN 1992-1-1 (NNI 2011a) and RTD 1006 (Rijkswaterstaat 2013). However, the test resulted in an unexpected low failure load and corresponding low shear resistance (-16%), compared to the nonlinear analyses of both a simply

supported and a disconnected T-beam. From the nonlinear analysis, it is concluded that the connection to the end cross-beam, at the non-loaded side, results in a very sensitive load-deflection and cracking behaviour. In addition, despite the flexural shear failure in the test, the failure mode is also very close to a flexural failure. Finally, the adjustment of the safety chains during the experiment might have influenced the ultimate load capacity.

Connected T-beam - Shear tension resistance (Section 8.2.2)

- Combining the results of the linear and nonlinear analyses, as well as tests 1–2, the ultimate load is analysed to determine the maximum acting shear in the T-beam.
- At both load positions, the linear analyses indicate a shear tension failure of the T-beam. For the load position at a = 2.25 m, this is related to a maximum principal stress in the web, whereas for a = 4.00 m this is related to the cracking moment (Chapter 5 Section 5.6.3 Figure 5.21).
- At the position of the load, bending and flexural shear cracks are observed in both the tests and the nonlinear analyses, in the direction of the end support as well as in the span direction. However, these remain concentrated near the load position and, based on the nonlinear analysis, do not result in a flexural shear failure.
- Compared to NEN-EN 1992-1-1 (NNI 2011a) and RTD 1006 (Rijkswaterstaat 2013), for a connected T-beam, the nonlinear analyses show an increase in shear tension resistance of 60% (a = 2.25 m) and 92% (a = 4.00 m).
- Test 2 (a = 2.25 m) shows an increase of 69% and test 1 (a = 4.00 m) of 109% compared to NEN-EN 1992-1-1 (NNI 2011a) and RTD 1006 (Rijkswaterstaat 2013). In addition, the tests show an increase of 6–8% compared to the nonlinear analyses. Despite the significant increases, due to the premature punching failure of the deck, the 'real' shear resistance of the connected T-beam might be underestimated.
- Based on the linear analysis (Chapter 5), in addition to the area close to the supports, shear tension, with a maximum principal stress in the web, can also occur in the area surrounding the intermediate cross-beams.

Shear resistance - Individual versus connected T-beam (Section 8.2.3)

By adopting the exact same loading positions, the objective of the individual and connected T-beam tests is to enable a direct comparison of the shear resistances and to isolate the effect of system behaviour. However, a direct comparison of the two types of tests is complicated by the following aspects:

- Due to the difference in load distribution, the failure mode of an individual T-beam (flexural shear) is not the same as of a connected T-beam (shear tension). Based on the linear analysis, for connected T-beams, shear tension becomes more apparent for T-beams at a greater distance from the edge beam. In addition, for cross-sections closer to a cross-beam, the shear tension resistance tends to relate to a maximum principal tensile stress (σ_1) in the web, whereas for cross-sections

closer to the area in-between the cross-beams, the shear tension resistance tends to relate to a maximum principal tensile stress at the bottom fibre, i.e. the cracking moment (M_{cr}).

- The difference in load distribution can cause a (minor) shift of the location of the (theoretical) critical cross-section.
- Because of the unintended punching failure of the deck, the shear resistance of the connected T-beam tests might be underestimated.

Despite these aspects, from the direct comparison of the shear resistance of the individual to the connected T-beams the following is concluded:

- In all cases and at both load locations, the shear resistance of a connected T-beam is higher compared to an individual T-beam.
- For the load positioned at a = 2.25 m, the increase of shear resistance of a connected T-beam, compared to an individual T-beam, is equal to 74% (linear analysis), 24% (nonlinear analysis) and 14% (tests).
- For the load positioned at a = 4.00 m, the increase of shear resistance of a connected T-beam, compared to an individual T-beam, is equal to 4% (linear analysis), 53% (nonlinear analysis) and 20% (tests).
- In case of a connected T-beam, due to the constraints provided by the surrounding members, the nonlinear analyses show an additional compressive normal force in the T-beam which will affect the shear resistance. If this is taken into account, the analytical shear tension resistance can be improved, i.e. increased, for both loading positions by approximately 20%.

Compressive membrane action slab (CMA) (Section 8.2.4)

- Combining the results of tests 1–2 and the corresponding nonlinear analyses and adopting the analytical model for arch action (Chapter 4) the ultimate load related to compressive membrane action is analysed.
- In tests 1 and 2, the failure mode is punching of the deck slab which cannot be predicted by the analytical model for arch action as this model relates to the flexural CMA capacity. However, it is assumed that the punching failure load, and corresponding deflection, is a point on the failure curve obtained by the analytical model for arch action, which may hold true for a punching failure load close to the maximum flexural failure load.
- The punching shear capacity of the slab is predicted using the results of the experimental program on transverse prestressed slabs by Amir (2014), resulting in a capacity of F_u = 1273 kN.
- The analytical model for arch action is adopted using the concrete compressive strength of the integrated deck slab which is considerably lower than the T-beam. The assumption is to consider the lowest concrete compressive strength, present in the arch, to be the weakest link.

- For the acting width of the slab a load distribution of 45°, from the load to the slab edges, is assumed resulting in a width equal to the span. This acting width is compared to the results of the nonlinear analysis showing that the area of the maximum in-plane force N_{xx} is not exactly centred around the load, especially in the case of a load position closer to the (end) cross-beam (analysis A-T2). As CMA is dependent on relative slab deformations, a possible explanation is that these relative deformations can become larger in the area in-between the cross-beams.
- In the CMA analysis a free span of the deck slab is assumed in transverse direction spanning across the loaded T-beam. The shape of the resulting arch is in accordance with the results of the nonlinear analysis. However, the presence of the loaded T-beam in the middle of the arch will naturally result in lower relative slab deformations.

Compressive arch action T-beam (CAA) (Section 8.2.5)

- Combining the results of test 1 and the corresponding nonlinear analysis and adopting the analytical model for arch action (Chapter 4) the ultimate load related to compressive arch action is analysed.
- In the CAA analysis the arch is assumed to develop in span direction from the loading point to the inner edges of the cross-beams. The height of the arch is assumed to be equal to the height of the cross-beam(s). The resulting shape of the arch is in accordance with the results of the nonlinear analysis.
- For beams it is assumed that CAA enhances both the flexural resistance as well as the shear resistance. In addition, it is assumed that a shear failure will be governing which cannot be predicted by the analytical model for arch action. However, likewise to slabs, it is assumed that the shear failure load, and corresponding deflection, is a point on the failure curve obtained by the analytical model for arch action, which may hold true for a shear failure load close to the maximum flexural failure load.
- In test 1, the failure mode is punching of the deck slab resulting in a loss of load transfer to the adjacent T-beam(s). In a separate analysis this is taken into account by adopting a reduced cross-section of the T-beam after punching.
- Initially, the CAA load capacity of the T-beam is derived assuming a horizontal stiffness from the end cross-beam and the uncracked concrete compressive strength of the T-beam resulting in an ultimate load capacity of the T-beam of F_u = 3048 kN (full cross-section) and F_u = 1229 kN (reduced cross-section after punching). The latter indicates that the remaining cross-section after punching is insufficient to carry the full test load (3004 kN) by arching of a single T-beam.

Combined CMA (slab) and CAA (T-beam) test 1 (Section 8.2.6)

- Assuming full plasticity, and using the principle of superposition of both CMA and CAA, the difference between the total failure load and the punching failure load can be contributed to CAA and is equal to $F_{u,CAA}$ = 1487 kN. The initial CAA analysis indicates this capacity corresponds to an almost zero vertical deflection indicating a low presence of CAA in the T-beam.

- Alternatively, CAA can be calibrated independently from CMA by utilising the maximum acting shear in the T-beam taken from the nonlinear analysis. In the analytical model for arch action the acting shear equals to $V_u = F_u/2$. Using this approach results in a load contributed to CAA of $F_{u,CAA}$ = 2190 kN. However, this analysis assumes a constant normal and shear force, between the load and the supports, which is not the case for connected beams.
- The nonlinear analysis shows considerable (shear) cracking at failure and consequently concrete compressive stresses close to the reduced concrete strength taking into account the maximum effect for lateral cracking, i.e. $0.4 \times f_{cm}$.
- The analysis of the numerical membrane force for CMA shows a membrane force close to the analytical (87–95%), suggesting a high CMA presence.

Taking all of the above into account, the following approach seems most appropriate:

- For CMA assume an uncracked concrete compressive strength due to the bi-axial compressive stress state at the top side of the bridge deck.
- On the basis of the observed numerical membrane force, assume a close to maximum punching shear capacity for CMA (>85%) despite the slab spanning the loaded T-beam.
- For CAA assume a reduced concrete compressive strength due to the effects of lateral cracking similar to a situation of a compressive strut.
- Utilise the acting shear for the calibration of CAA. However, since the acting shear is not constant between the load and the supports, a more average value should perhaps be considered.

9

CONCLUSIONS AND RECOMMENDATIONS

This chapter summarizes the main conclusions of the research and gives recommendations for future research.

9.1. RESEARCH RECAP

ABOUT 70 prestressed concrete T-beam bridges, constructed in the Netherlands between 1953–1977, are still in use today with many located in the main highway network. Using traditional assessment methods it was concluded that about 50% of these bridges do not fulfil the current code requirements. In previous research the integrated deck slab with transverse prestressing was investigated and a substantially higher load capacity was found due to the presence of compressive membrane action (CMA). For the current research, the focus is on the load capacity of the main T-beams. For the Dutch T-beam bridge stock, the main characteristics and shear-related deficiencies are investigated in Chapter 2. The presence of 2–4 cross-beams in each span, as well as transverse prestressing, in both the cross-beams and the integrated deck slab, led to the concept of 'system behaviour', in which the capacity of a structure is increased due to the restraint provided by the connected members. This concept is investigated using the theory of compressive arching, for both the integrated deck slab (CMA) as well as the T-beams (CAA) (chapters 3–4). For the investigation, the main part of this research is related to a case study of a typical Dutch T-beam bridge called the Vecht bridge (chapters 5–7). Using a single concentrated load at the centre of a T-beam, seven full-scale collapse tests are conducted on this multispan bridge prior to its scheduled demolition. Three tests are conducted with the original structural system unchanged. On a separate span, four tests are conducted on individual T-beams, with the deck in-between the beams sawn in the longitudinal direction. The two types of tests allows for a direct comparison between the load capacity of an individual T-beam versus a connected T-beam. The case study is extensively analysed with conventional cross-sectional evaluations for shear and bending in Chapter 5 and using nonlinear analysis in Chapter 7. In addition, a generic analytical model for arch action is derived in Chapter 4, to investigate the effects of CMA and CAA. The results of the different parts of the research are then combined to analyse the 'system behaviour' in Chapter 8.

9.2. CONCLUSIONS

THE main conclusions related to the research questions (Chapter 1 Section 1.3) are summarised in this section and more detailed conclusions related to each subject are given in the following subsections. For the benefits and considerations of large-scale testing and nonlinear analysis the reader is also referred to the summaries in Chapter 6 Section 6.6 and Chapter 7 Section 7.11.

Main conclusions

- Using experimental, numerical and analytical methods, it has been demonstrated that for T-beam bridges a combination of compressive membrane action (CMA) and compressive arch action (CAA) contributes to the 'system behaviour', which differs significantly from the behaviour of an individual T-beam. This research has explained and quantified the contribution of the aforementioned mechanisms resulting in an increased capacity for these types of bridges. These effects are not considered in a traditional assessment (Chapters 4–8).
- Following a traditional assessment, using a linear model for the load effect and a

cross-sectional analysis for the verification, the governing failure mode for connected T-beams is shear tension. On the contrary, analysing an individual simply supported T-beam, the governing failure mode is either the ultimate bending moment at midpoint or flexural shear close to the support (Chapter 5 Section 5.6.5).

- Using an existing full-scale bridge in the experiments, the connected beam tests revealed an explosive failure for both the bridge deck (punching failure) and the T-beam (shear failure) (Chapter 6 Section 6.4).
- Using a full 3D nonlinear finite element model of the complete span with 15 beams, the experimentally observed failure mode(s) are confirmed. In addition, the model allowed insight in the development of the mechanisms of CMA and CAA. With the exception of the stiffness of the elastomeric bearings, no other parameters needed to be calibrated (Chapter 7).
- An optimal incremental-iterative solution method combined with an automatic adaptive step size method has been found resulting in nonlinear analyses in which all steps are converged, regardless of model size (Chapter 7 Sections 7.3.4 and 7.7.2).
- Compressive membrane action (CMA), and corresponding increased (punching) capacity, is found in the deck in case of a (concentrated) load at the centre of a T-beam (Chapter 8 Sections 8.2.4 and 8.2.6).
- Compressive arch action (CAA), and corresponding increased shear capacity, is found in the T-beam in case of a (concentrated) load positioned in-between the cross-beams (Chapter 8 Sections 8.2.5 and 8.2.6).
- A generic analytical model for arch action is derived capable of quantifying the effects of both CMA and CAA (Chapter 4).

9.2.1. COMPRESSIVE MEMBRANE ACTION (CMA)

WITH a concentrated load placed at the centre of a T-beam, the results of the nonlinear analyses, specifically the in-plane forces, demonstrate a significant presence of CMA in the integrated deck slab and the top flange of the T-beam. Note that in all previous CMA research the load is placed on the (integrated) deck slab. Based on the results, for the two different loading positions, a punching shear capacity of approximately 85% is expected as compared to a punching shear capacity with the load on the integrated deck slab. The reduced capacity can be explained by the lack of relative deflections, between the loading point and the ends of the arch, needed to achieve the maximum arching effect. In this case the deflection at the loading position is partly prevented by the presence of the T-beam. Additionally, the relative deflection is prevented in closer proximity to a cross-beam. However, the nonlinear analyses also demonstrate that in the latter case this is partly compensated by a non-symmetric acting width of the slab.

In conclusion, based on the results, CMA is expected to increase the load capacity for load positions, in the area in-between the cross-beams, at a relative distance of 25–75% of the centre-to-centre distance between the cross-beams. Due to the presence of the T-beam, transverse sagging bending moments cause cracking on the bottom side of the top flange, on either side of the T-beam web. Therefore, it is concluded that for

the application of an analytical model for arch action, these positions should be taken for the locations of the plastic hinges. Additionally, for the current case with different concrete compressive strengths for the integrated deck slab and the T-beam, the lowest value should be taken into account as the arch continues through both sections.

9.2.2. COMPRESSIVE ARCH ACTION (CAA)

IN the CAA analysis the arch is assumed to develop in the loaded T-beam in longitudinal direction, from the loading point to the inner edges of the cross-beams, which are assumed to provide a significant horizontal stiffness. This assumption is confirmed by the nonlinear analyses which demonstrate arch-shaped compressive struts, for the two investigated loading positions, in both longitudinal directions. In addition, the nonlinear analyses results show high compressive membrane forces at loads exceeding approximately 70–90%, depending on load position, of the ultimate load. The additional normal compressive forces in the loaded T-beam are balanced by tensile normal forces in the adjacent T-beams.

With respect to the load distribution, the linear and nonlinear analyses show that the intermediate cross-beam has the effect of an (internal) vertical support. Despite this effect, it is concluded that the formation of plastic hinges, at the ends of the arch, is limited by the general lack of hogging bending moments at the position of the cross-beams. Due to the connections with the integrated deck slab, along its longitudinal axis, the analysis has also shown that the sectional forces, including the axial membrane force, naturally dissipate away from the loading position further limiting the hogging bending moments as well as complicating the use of an analytical model.

For the application of an analytical model for arch action, the influence of the compression zone resultants as a result of bending moments, in both the span and the (fictitious) supports, is found to be negligible. Additionally, different concrete compressive strengths, for the integrated deck slab and the T-beam, can be taken into account using a similar approach as for the ultimate bending moment. However, contrary to CMA, for CAA the concrete compressive strength should be reduced taking into account the effect of lateral cracking. It is also concluded that for analytical modelling the horizontal restraint provided by the intermediate cross-beam will be much more significant as compared to the end cross-beam.

The punching failure of the deck (as observed in the experiments and confirmed by the nonlinear analyses) results in a loss of load transfer to the adjacent T-beam(s). It can be concluded that the remaining cross-section after punching is insufficient to carry the same load by arching of a T-beam. From the analysis it is concluded that this is caused by the combined effect of the loss of cross-sectional area at the top flange and the increase of the beam slenderness.

9.2.3. INDIVIDUAL VERSUS CONNECTED T-BEAM

THE shear resistance of an individual, disconnected and connected T-beam is analysed, using the results from the linear analysis, the full-scale collapse tests and the nonlinear analyses. A difference in failure mode is found, with flexural shear in case of an individual or disconnected T-beam, and shear tension in case of a connected T-beam.

The linear analysis shows that this difference becomes more apparent for connected T-beams at a greater distance from the edge beam. In addition, for connected T-beams, the failure mode is strongly dependent on the proximity to a cross-beam. For cross-sections closer to a cross-beam, the shear tension resistance tends to be related to a maximum principal tensile stress (σ_1) in the thin web, whereas for cross-sections closer to the area in-between the cross-beams, the shear tension resistance tends to relate to a maximum principal tensile stress at the bottom fibre, i.e. the cracking moment (M_{cr}). In all investigated cases, the shear resistance of a connected T-beam is found to be increased, between 14–53%, compared to an individual T-beam. In addition, due to the premature punching failure of the deck in tests 1–2, the 'real' shear resistance of the connected T-beams might still be underestimated. The shear tension resistance can be improved for connected T-beams by taking into account the additional compressive membrane force in the loaded T-beam increasing the resistance by 20%, for the two investigated loading positions.

9.3. RECOMMENDATIONS FOR FUTURE RESEARCH

BASED on the research presented in this dissertation the following recommendations are made for future research:

- The different geometries and bridge layouts, as investigated and tabulated in Chapter 2, should be further analysed to verify if the conditions for CMA and CAA to occur are met for the T-beam bridges in the Netherlands.
- The application of CMA and CAA to an edge beam should be further investigated. As a first step, the experimental result of test 3 (Chapter 6 Section 6.4) can be continued numerically to failure. As a second step, additional experiments are advised.
- A general mechanical model for CMA should be derived which includes two-way bending, a punching failure criterium, as well as the boundary conditions found in a bridge superstructure with the load at the centre of a T-beam.
- An overall multi-level assessment approach for T-beam bridges needs to be developed.

BIBLIOGRAPHY

Alampalli, S., Frangopol, D. M., Grimson, J., Halling, M. W., Kosnik, D. E., Lantsoght, E. O. L., Yang, D., and Zhou, Y. E. Bridge load testing: State-of-the-practice. *Journal of bridge engineering*, 26(3), 2021. https://doi.org/10.1061/(ASCE)BE.1943-5592.0001678.

Amir, S. *Compressive membrane action in prestressed concrete deck slabs*. PhD thesis, Delft University of Technology, 2014. 282 pp.

Amir, S. and van der Veen, C. Bearing capacity of transversely prestressed concrete decks. Stevin Report 25.5.13-06, Delft University of Technology, 2013.

Anonymous. Concrete structures at the Festival of Britain. South Bank, london, exibition. *Concrete and Constructural Engineering*, pages 199–206, July 1951.

Anonymous. Test of a prestressed concrete footbridge. *Concrete and Constructural Engineering*, pages 185–188, June 1952.

Bagge, N. *Structural assessment procedures for existing concrete bridges: Experiences from failure tests of the Kiruna Bridge*. PhD thesis, Luleå University of Technology, 2017. 310 pp.

Bagge, N., Popescu, C., and Elfgren, L. Failure tests on concrete bridges: Have we learnt the lessons? *Structure and Infrastructure Engineering*, 14(3):292–319, 2018. https://doi.org/10.1080/15732479.2017.1350985.

Banks, H. T., Pinter, G. A., and Yeoh, O. H. Analysis of bonded elastic blocks. *Mathematical and Computer Modelling*, 36(7-8):875–888, 2002. https://doi.org/10.1016/S0895-7177(02)00234-0.

Batchelor, B. d. *Concrete Bridge Engineering: Performance and Advances*, chapter 6, pages 189–213. Department of Civil Engineering, Queens University, Kingston, Ontario, Canada, 1987. Membrane Enhancement in Top Slabs of Concrete Bridges.

Bundesministerium für Verkehr, B. u. S. *Richtlinie zur Nachrechnung von Strassenbrürcken im Bestand (Nachrechnungsrichtlinie)*. Bundesministerium für Verkehr, Bau und Stadtentwicklung, 2011. 108 pp.

Burdette, E. G. and Goodpasture, D. W. Tests of four highway bridges to failure. In *Journal of the structural division*, volume 99, pages 335–348, 1973.

Cement. Het vervaardigen en plaatsen van freyssinet-kabels 12-5 en 12-7. *Cement*, (8): 469–472, 1956.

Cement. Access viaducts, medium-size precast beams. *Cement*, (XVIII):227, 1966.

CSA. *CAN/CSA-S6-06: Canadian Highway Bridge Design Code (CHBDC)*. Canadian Standards Association, 2006. 930 pp.

den Boef, D. Proefbelasting KW 'Vechtbrug A1', materiaalkundig onderzoek betondruksterkte. Technical Report RW2100-1/16-021.480, Witteveen+Bos, 2016. 79 pp.

DIANA. Diana user's manual – release 10.3. www.dianafea.com, 2019.

Ensink, S. W. H., van der Veen, C., Hordijk, D. A., Lantsoght, E. O. L., van der Ham, H., and de Boer, A. Full-size field test of prestressed concrete T-beam bridge. In *Euro-bridge*, 2018. Edinburgh, Scotland.

Ensink, S. W. H., Hendriks, M. A. N., and van der Veen, C. Non-linear analysis of prestressed concrete T-beams. In *Advances in Engineering Materials, Structures and Systems: Innovations, Mechanics and Applications - Proceedings of the 7th International Conference on Structural Engineering, Mechanics and Computation*, pages 1360–1365, 2019.

fib. *fib bulletin 42 Constitutive modelling of high strength/high performance concrete*, chapter 3, page 14. fib, 2008.

fib. *Model code 2010 Volume 1*. CEB-FIP, 2012. 311 pp.

Floyd, R., Pei, J., Murray, C., and Cranor, B. Understanding the behavior of prestressed girders after years of service. Technical Report FHWA-OK-16-03, Oklahoma Department of Transportations, Office of Research and Implementation, 2016. 166 pp.

Freyssinet. *Guide for Freyssinet methods*. Freyssinet international organization, 3rd edition, 1972.

Gijsbers, F., Steenbergen, R., and van der Veen, C. Werkset factoren plaatconstructies van gewapend beton zonder dwarskrachtwapening. Technical Report 2011:24, TNO / Delft University of Technology, 2011.

Gleich, P. *Das Erweitere Druckbogenmodell zur Beschreibung des Betontraganteils bei Querkraft*. PhD thesis, Technische Universität Dortmund, 2020. 324 pp.

Gleich, P. and Maurer, R. Bridge reassessment in Germany: shear capacity computation based on arch action model. *Engineering History and Heritage*, 170(3):112–124, 2017. https://doi.org/10.1680/jenhh.16.00024.

Gleich, P. and Maurer, R. Bridge Reassessments - Realistic Shear Capacity Evaluation Using Arch Action Model. In *High Tech Concrete: Where Technology and Engineering Meet*, 2018. Maastricht, The Netherlands.

Godart, B. Pathology, appraisal, repair and management of old prestressed concrete beam and slab bridges. *Structure and Infrastructure Engineering*, 11(4):501–518, 2015. https://doi.org/10.1080/15732479.2014.951865.

Goedhart, W. De IJ-oververbinding bij schellingwoude. Technical report, Rijkswaterstaat, Directie Bruggen, 1956.

Hendriks, M., de Boer, A., and Belletti, B. *Guidelines for nonlinear finite element analysis of concrete structures*. Rijkswaterstaat centre for infrastructure, report RTD 1016-1:2017, 2.1 edition, 2017. 69 pp.

Huber, P., Huber, T., and Kollegger, J. Influence of loading conditions on the shear capacity of post-tensioned beams with low shear reinforcement ratios. *Engineering structures*, (170):91–102, 2018. https://doi.org/10.1016/j.engstruct.2018.05.079.

Jeong, J. and Kim, W. Shear Resistant Mechanism into Base Components: Beam Action and Arch Action in Shear-Critical RC Members. *International Journal of Concrete Structures and Materials*, 8(1):1–14, 2014. https://doi.org/10.1007/s40069-013-0064-x.

Jiaquan, X., Zanping, W., Bing, H., Guanhua, F., Yufeng, Z., and Jianfei, Z. Practical Experimental Study on Ultimate Bearing Capacity of Actual Bridge in Huning Expressway Extension Project. *Modern Transportation Technology*, 3(5):77–84, 2006.

Kamp, C. Quick scan T-liggers 2017 samenvatting en advies. Technical Report RM192358, Movares, 2017. 19 pp.

Kiziltan, H. *Zum einfluss des druckbogens auf den schubwiderstand von spannbetonbalken*. PhD thesis, Technische Universität Dortmund, 2012. 219 pp.

Koekkoek, R. Measurement report loading of vechtbrug (25H-100). Stevin Report 25.5-17-03, Delft University of Technology, Faculty of Civil Engineering and Geosciences, 2017. 52 pp.

Kolodziejczyk, A. and Maurer, R. Arch action model applied to existing prestressed concrete bridges in Germany. *Engineering History and Heritage*, 170(3):99–111, 2017. https://doi.org/10.1680/jenhh.16.00025.

König, G. and Fischer, J. Model uncertainties concerning design equations for the shear capacity of concrete members without shear reinforcement. *CEB Bulletin*, (224):49–100, 1995.

Lantsoght, E. O. L., Koekkoek, R. T., van der Veen, C., Hordijk, D. A., and de Boer, A. Pilot proof-load test on viaduct De Beek: Case study. *Journal of Bridge Engineering*, 22(12), 2017a. https://doi.org/10.1061/(ASCE)BE.1943-5592.0001131.

Lantsoght, E. O. L., van der Veen, C., de Boer, A., and Hordijk, D. A. Proof load testing of reinforced concrete slab bridges in the Netherlands. *Structural Concrete*, 18(4):597–606, 2017b. https://doi.org/10.1002/suco.201600171.

Lu, X., Lin, K., Li, C., and Li, Y. New analytical calculation models for compressive arch action in reinforced concrete structures. *Engineering Structures*, 168:721–735, 2018. https://doi.org/10.1016/j.engstruct.2018.04.097.

Matlab. Matlab release 2019b. www.mathworks.com, 2019.

McClure, R. and West, H. Full-scale testing of a prestressed concrete segmental bridge. *Canadian Journal of Civil Engineering*, 11:505–515, 1984. https://doi.org/10.1139/l84-070.

McIlmoyle, R. *Prestressed Concrete Bridge Beams Being Tested in England*. Railway Age volume 123 no. 12, 1947.

Murray, C. and Floyd, R. Shear and anchorage failure of scale prestressed concrete I-girders and scale bridge section. In *Euro-bridge*, 2018. Edinburgh, Scotland.

Murray, C., Diaz Arancibia, M., Okumus, P., and Floyd, R. Destructive testing and computer modeling of a scale prestressed concrete I-girder bridge. *Engineering Structures*, 183:195–205, 2019. https://doi.org/10.1016/j.engstruct.2019.01.018.

Nemetschek. Scia engineer. www.scia.net, 2020.

NNI. *NEN 1009: Gewapend Betonvoorschriften GBV 1962*. Nederlands Normalisatie-Instituut, 1962. 112 pp.

NNI. *NEN 3865: Voorschriften Beton VB 1974, Deel E*. Nederlands Normalisatie-Instituut, 1977. 112 pp.

NNI. *NEN 6723: Regulations for concrete - Bridges (VBB 1995) - Structural requirements and calculation methods*. Nederlands Normalisatie-Instituut, 1995. 67 pp.

NNI. *NEN-EN 1992-1-1 Eurocode 2: Design of concrete structures - Part 1-1: General rules and rules for buildings*. Nederlands Normalisatie-Instituut, 2011a. 239 pp.

NNI. *NEN 8700: Assessment of existing structures in case of reconstruction and disapproval - Basic Rules*. Nederlands Normalisatie-Instituut, 2011b. 54 pp.

NNI. *NEN-EN 1991-2 Eurocode 1: Actions on structures - Part 2: Traffic loads on bridges*. Nederlands Normalisatie-Instituut, 2015. 180 pp.

NNI. Nederlands Normalisatie-Instituut. www.nen.nl, 2020.

Oh, B., Kim, K., and Lew, Y. Ultimate Load Behavior of Post-Tensioned Prestressed Concrete Girder Bridge through In-Place Failure Test. *ACI Structural Journal*, pages 172–180, March-April 2002. https://doi.org/10.14359/11542.

Park, R. and Gamble, W. L. *Reinforced concrete slabs*, chapter 12, pages 636–694. John Wiley & Sons, New York, 2nd edition, 2000.

Plos, M., Gylltoft, K., and Cederwall, K. Full-Scale Shear Tests on two Bridges. *IABSE reports*, (62):649–654, 1991. http://doi.org/10.5169/seals-47696.

Reinders, S. Service life monitoring of concrete bridges. Master's thesis, Delft University of Technology, 2016.

Rijkswaterstaat. Technical drawings vechtbrug (objectcode 25H 100). Technical report, Rijkswaterstaat, 1962.

Rijkswaterstaat. Inventarisatie kunstwerken (bruggen, tunnels en viaducten), version: 6. Technical report, Rijkswaterstaat, 2007. 47 pp.

Rijkswaterstaat. *Richtlijnen Beoordeling Kunstwerken (RBK)*. RTD 1006:2013, Rijkswaterstaat, 2013. 117 pp.

Rijkswaterstaat. Beeldarchief rijkswaterstaat. `www.rijkswaterstaat.nl/over-ons/onze-organisatie/ons-beeldarchief`, 2020.

Roosen, M. Beschrijving nader te onderzoeken T-liggers. Technical report, Rijkswaterstaat, 2015. 43 pp.

Roosen, M. *Shear failure of prestressed girders in regions without flexural cracks*. PhD thesis, Delft University of Technology, 2020. 269 pp.

Roosen, M. and Sliedrecht, H. Areaalbeoordeling objecten met T-liggers. Technical report, Rijkswaterstaat, 2018. 43 pp.

Sato, Y., Prayoonwet, W., and Oshima, Y. Investigation on structural behavior of existing prestressed post-tensioned concrete bridge superstructure. In *Proceedings of the fib symposium 2019, Concrete - Innovations in Materials, Design and Structures*, pages 1021–1028, 2019. Krakow, Poland.

SBR CUR. *CUR-Aanbeveling 77:2014 Rekenregels voor ongewapende onderwaterbetonvloeren (Design rules for unreinforced underwater concrete slabs)*. SBR CUR, 2014. 76 pp.

Taylor, S., Rankin, G., and Cleland, D. Guide to compressive membrane action. Technical paper 3, Concrete Bridge Development Group, 2002. 46 pp.

TNZ. *New Zealand Bridge Manual*. Transit New Zealand, 2 edition, 2003.

Tonnoir, B., Carde, C., and Banant, D. Curvature: An indicator of the mechanical condition of old prestressed concrete bridges. *Structural Engineering International*, 28(3): 357–361, 2018. `https://doi.org/10.1080/10168664.2018.1490585`.

UK HA. *BD 81/02: Use of Compressive Membrane Action in bridge decks, Design Manual for Roads and Bridges*. UK Highways Agency, 2002. 16 pp.

Waarts, P., Hordijk, D. A., Fennis, S., and Steenbergen, R. Proefbelasten van viaducten. *Cement*, (5):58–64, 2015.

Walraven, J. C. and Braam, C. R. *Prestressed concrete (course CIE3150/4160)*. Delft University of Technology, Faculty of Civil Engineering and Geosciences, 2018. 372 pp.

A

DETAILED RESULTS CONNECTED T-BEAMS

A

A.1. ANALYSIS A-T1

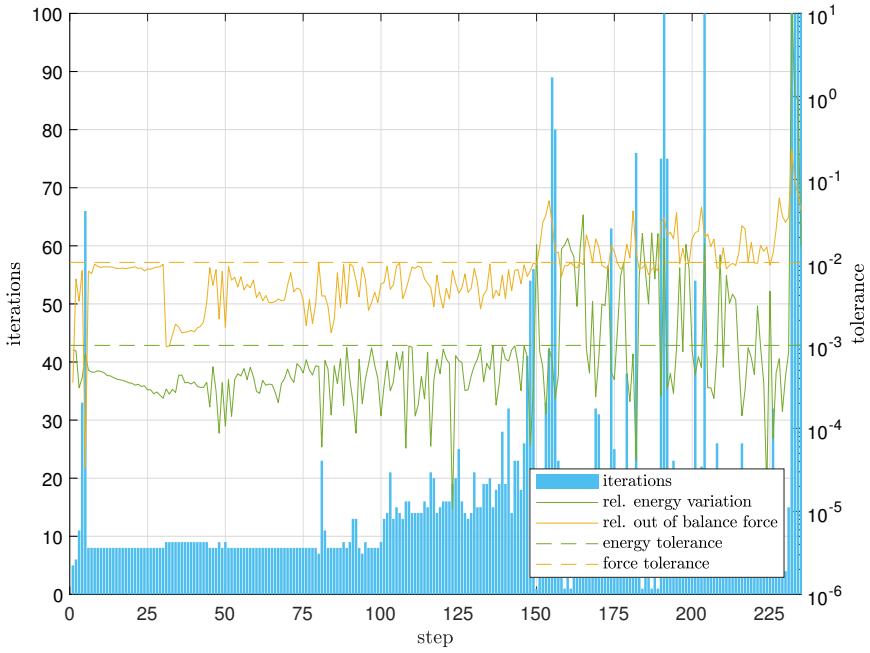

Figure A.1: A-T1-90/180-QNR, convergence

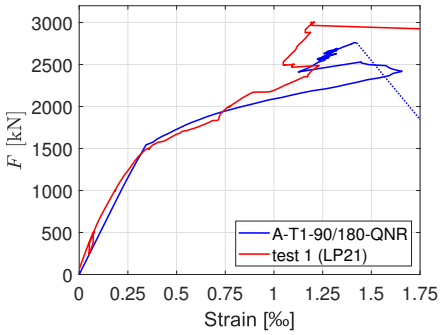

Figure A.2: Average longitudinal strain T-beam 11 (LP21)

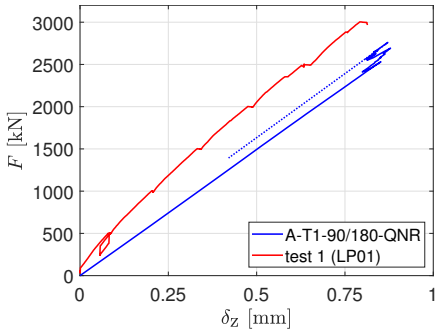

(a) T-beam 9

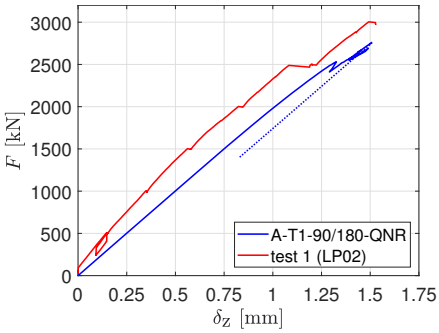

(b) T-beam 10

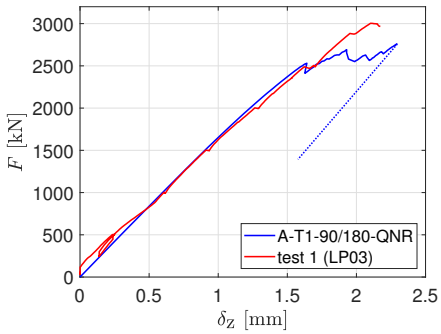

(c) T-beam 11

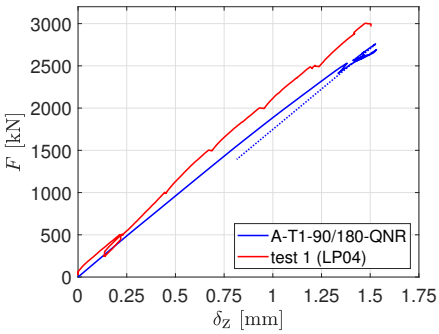

(d) T-beam 12

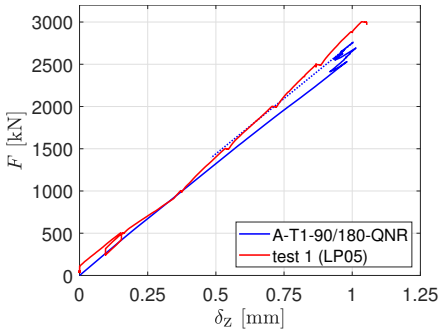

(e) T-beam 13

Figure A.3: Support deformations: T-beam 9–13 (LP01–05)
(dashed line = non-converged (post-peak))

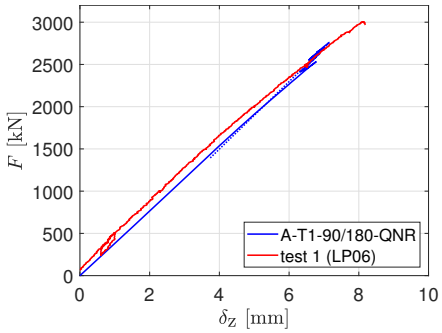

(a) T-beam 9

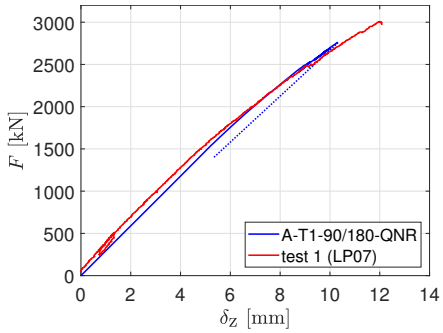

(b) T-beam 10

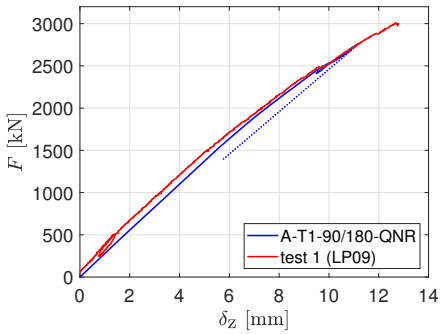

(c) T-beam 12

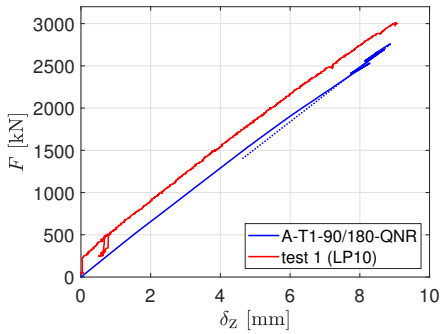

(d) T-beam 13

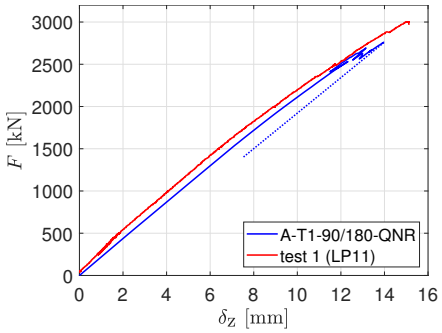

(e) T-beam 11, cross-beam

Figure A.4: Beam deformations: T-beam 9–10 (LP06–07), T-beam 12–13 (LP09–10) and T-beam 11 cross-beam (LP11) (dashed line = non-converged (post-peak))

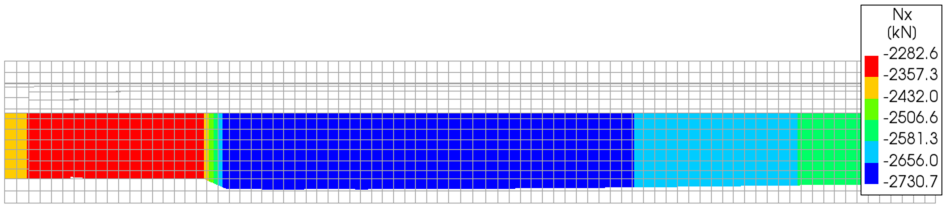

(a) Normal force N_x

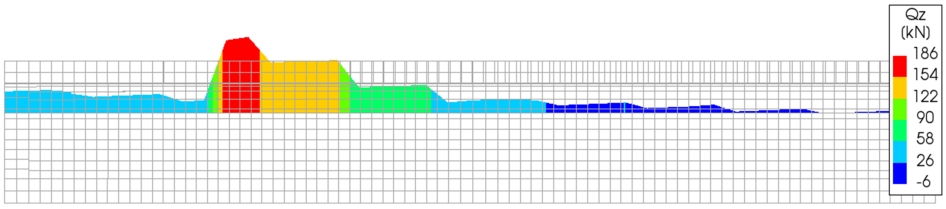

(b) Shear force Q_z

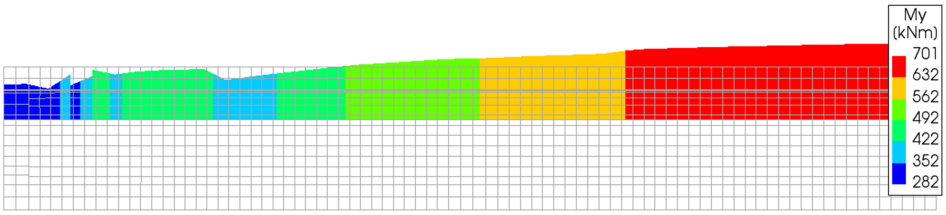

(c) Bending moment M_y

Figure A.5: A-T1-90/180-QNR, self-weight and prestressing load(s), sectional forces N_x, Q_z and M_y T-beam 11 (loaded beam)

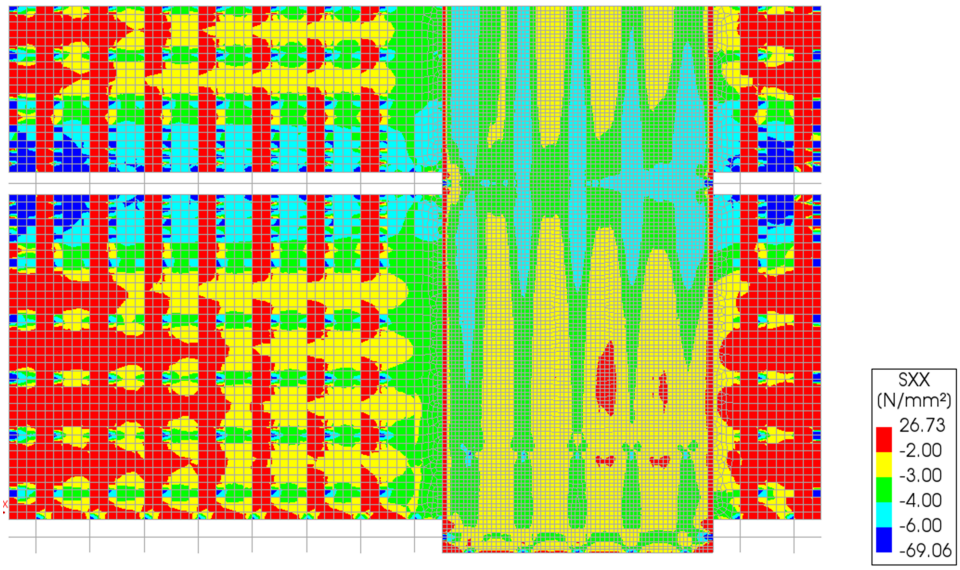

Figure A.6: A-T1-90/180-QNR, self-weight and prestressing load(s), stress S_{xx} (transverse direction) (top view, half of span shown, for complete model geometry see also Figure 7.6)

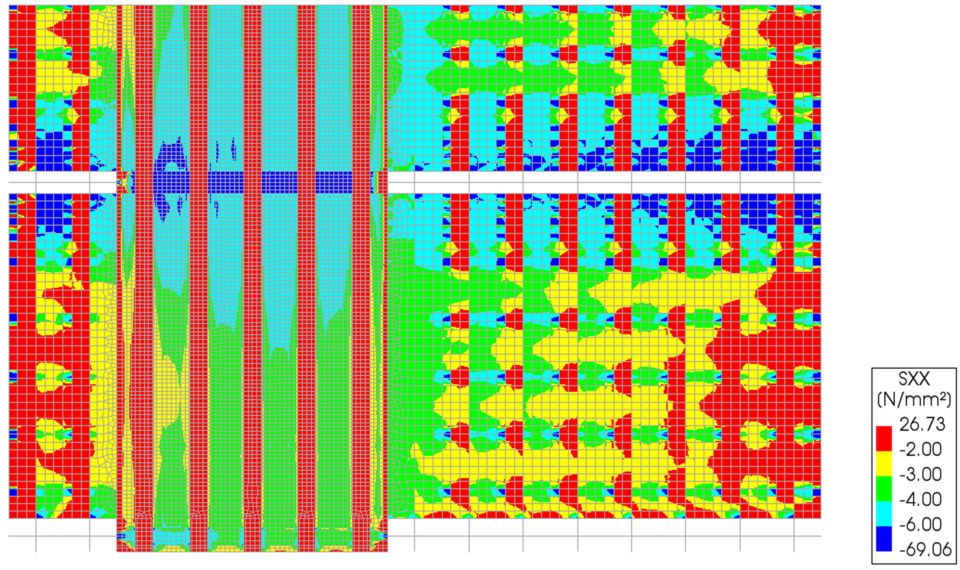

Figure A.7: A-T1-90/180-QNR, self-weight and prestressing load(s), stress S_{xx} (transverse direction) (bottom view, half of span shown, for complete model geometry see also Figure 7.6)

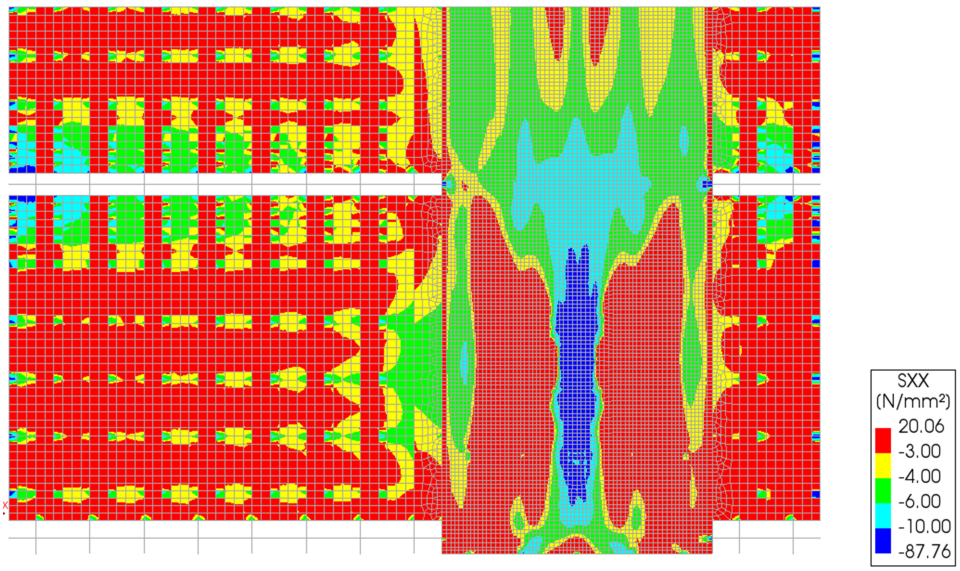

Figure A.8: A-T1-90/180-QNR, F_u = 2760 kN, δ_u = 20.5 mm, stress S_{xx} (transverse direction) (top view, half of span shown, for complete model geometry see also Figure 7.6)

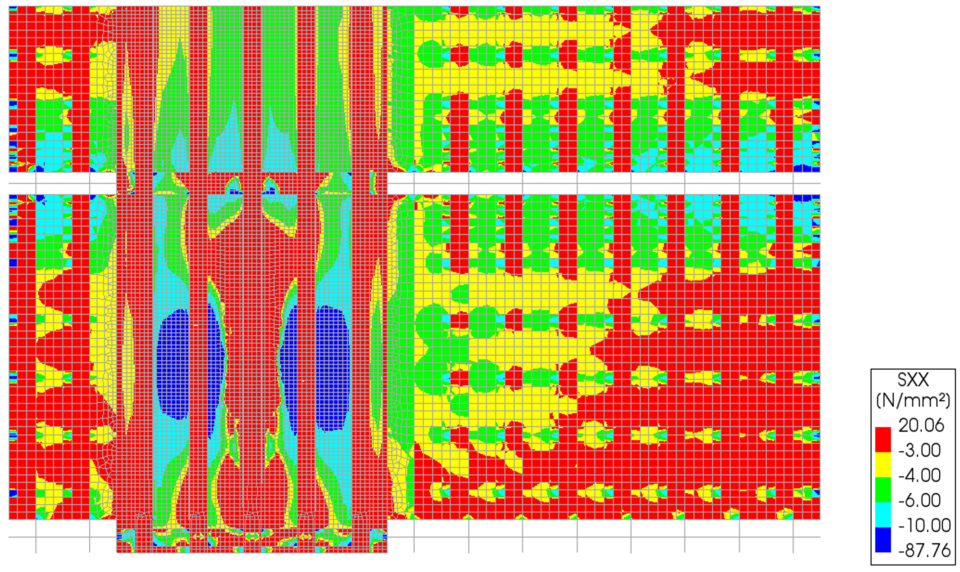

Figure A.9: A-T1-90/180-QNR, F_u = 2760 kN, δ_u = 20.5 mm, stress S_{xx} (transverse direction) (bottom view, half of span shown, for complete model geometry see also Figure 7.6)

A

A.2. ANALYSIS A-T2

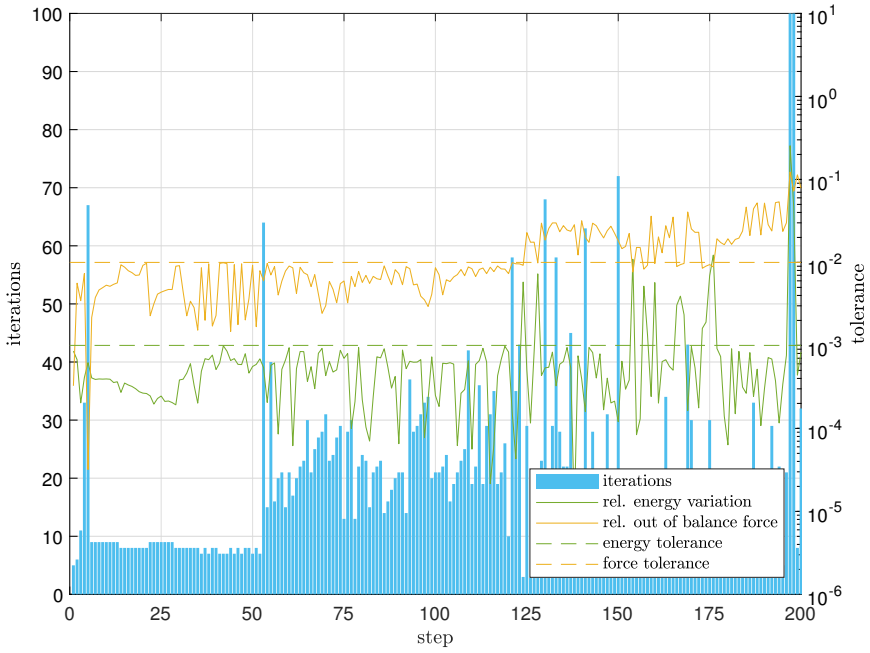

Figure A.10: A-T2-90/180-QNR, convergence

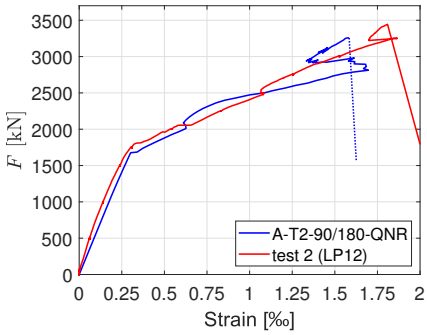

Figure A.11: Average longitudinal strain T-beam 6 (LP12)

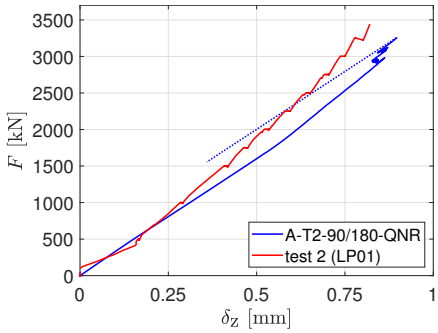

(a) T-beam 4

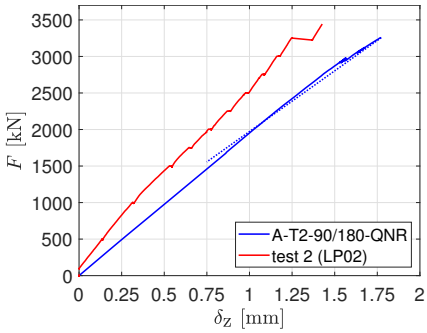

(b) T-beam 5

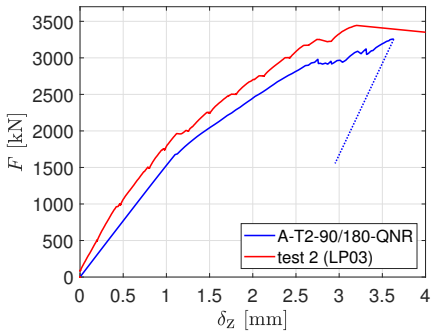

(c) T-beam 6

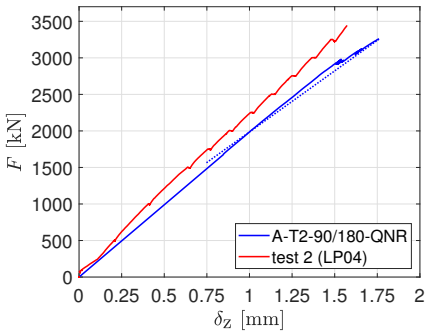

(d) T-beam 7

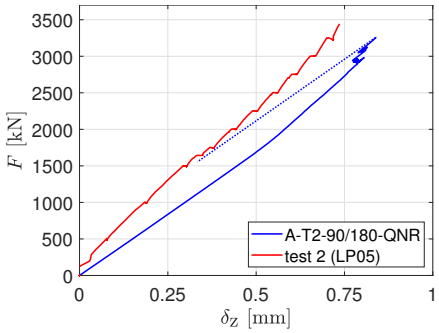

(e) T-beam 8

Figure A.12: Support deformations: T-beam 4–8 (LP01–05)
(dashed line = non-converged (post-peak))

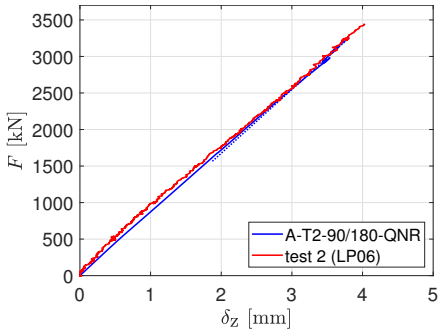

(a) T-beam 4

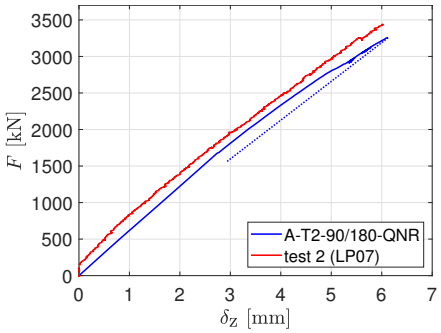

(b) T-beam 5

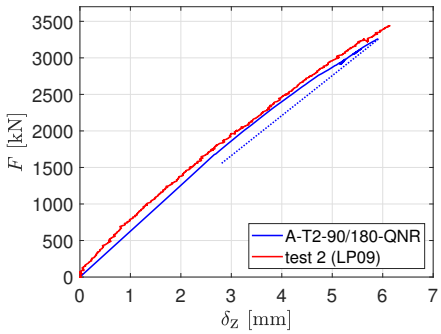

(c) T-beam 7

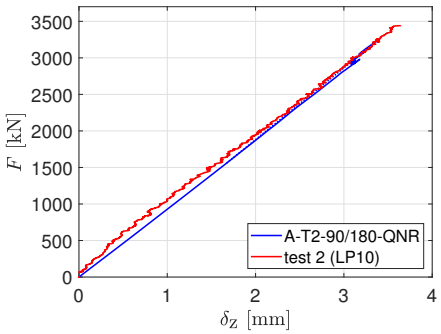

(d) T-beam 8

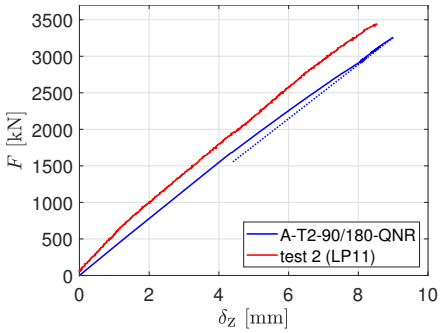

(e) T-beam 6, cross-beam

Figure A.13: Beam deformations: T-beam 4–5 (LP06–07), T-beam 7–8 (LP09–10) and T-beam 6 cross-beam (LP11) (dashed line = non-converged (post-peak))

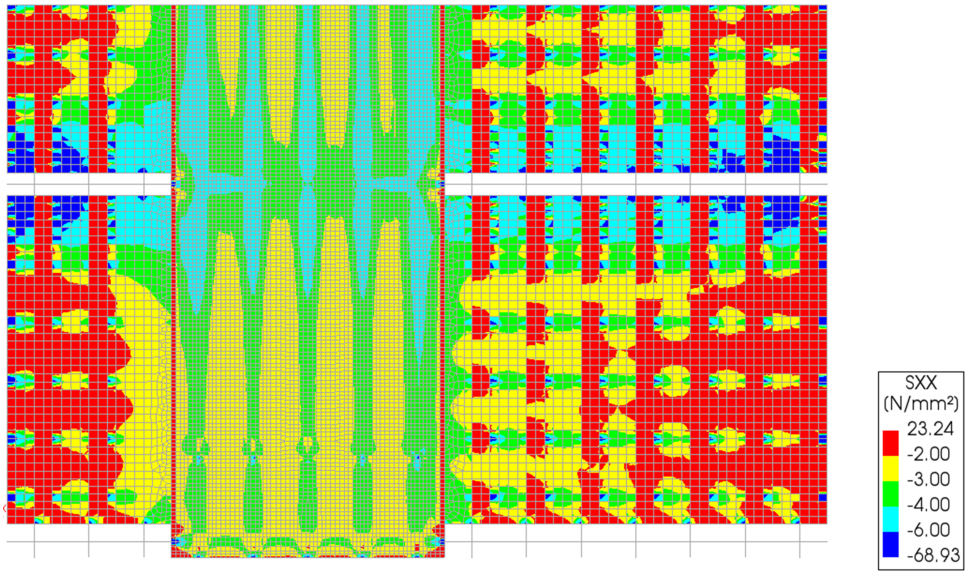

Figure A.14: A-T2-90/180-QNR, self-weight and prestressing load(s), stress S_{xx} (transverse direction) (top view, half of span shown, for complete model geometry see also Figure 7.6)

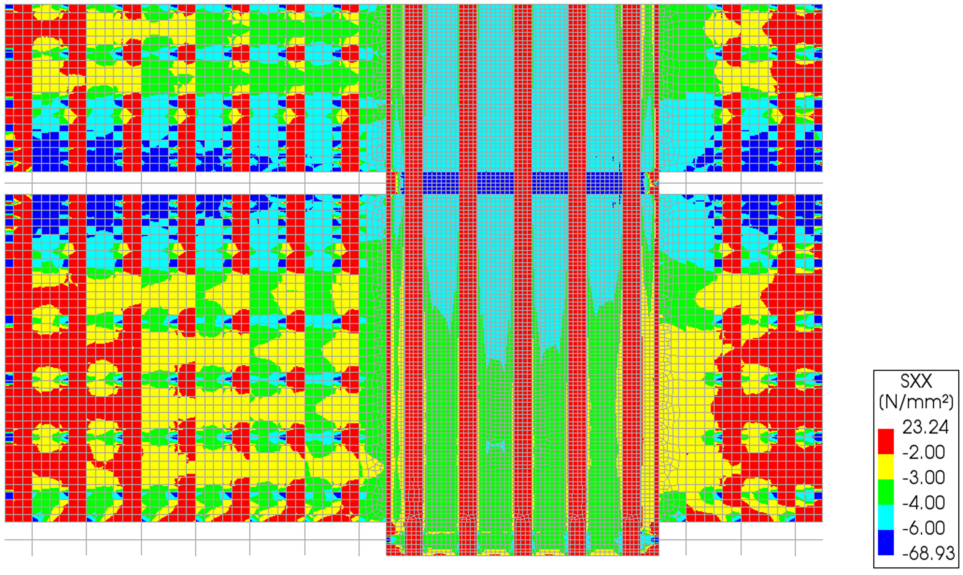

Figure A.15: A-T2-90/180-QNR, self-weight and prestressing load(s), stress S_{xx} (transverse direction) (bottom view, half of span shown, for complete model geometry see also Figure 7.6)

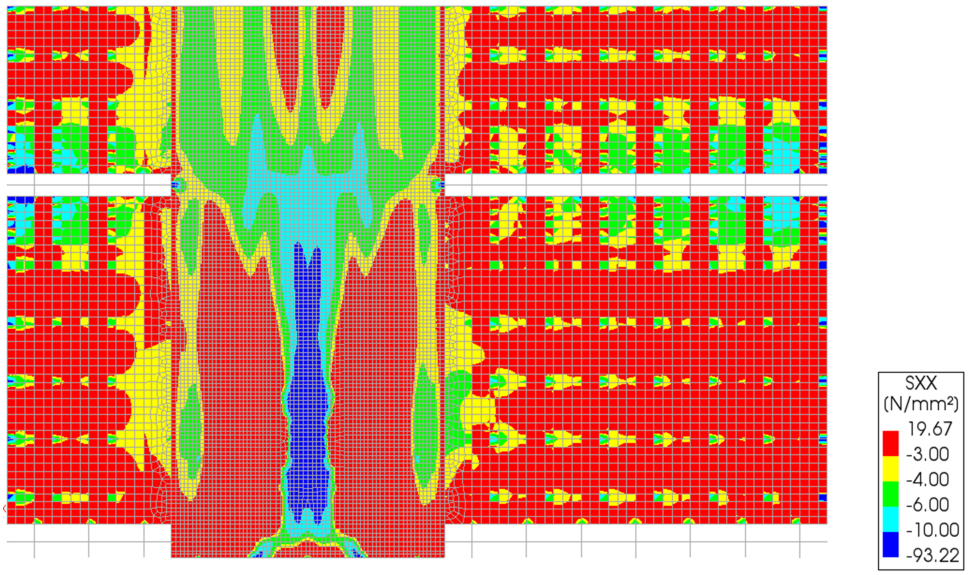

Figure A.16: A-T2-90/180-QNR, F_u = 3256 kN, δ_u = 16.4 mm, stress S_{xx} (transverse direction) (top view, half of span shown, for complete model geometry see also Figure 7.6)

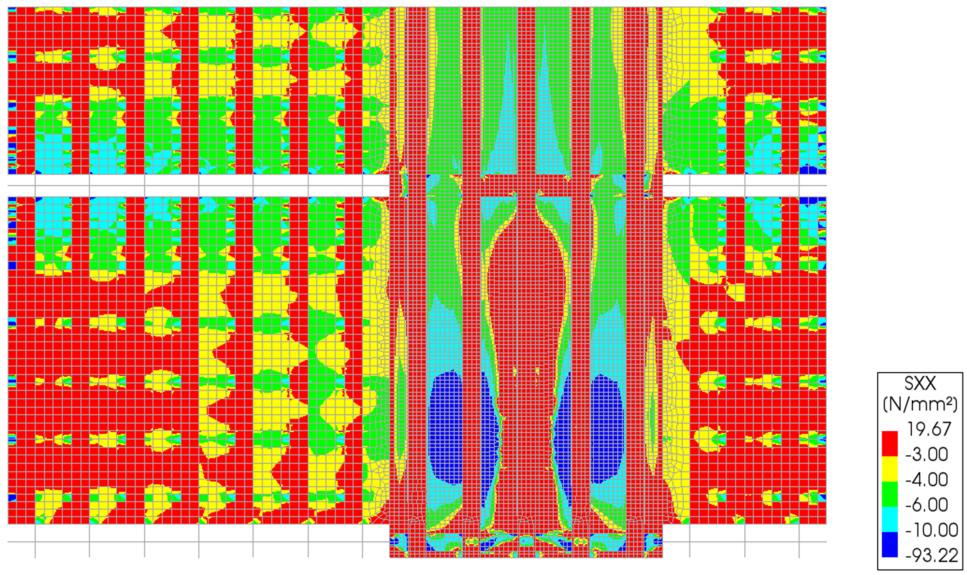

Figure A.17: A-T2-90/180-QNR, F_u = 3256 kN, δ_u = 16.4 mm, stress S_{xx} (transverse direction) (bottom view, half of span shown, for complete model geometry see also Figure 7.6)

B

DETAILED RESULTS DISCONNECTED T-BEAMS

B.1. ANALYSIS B-T4

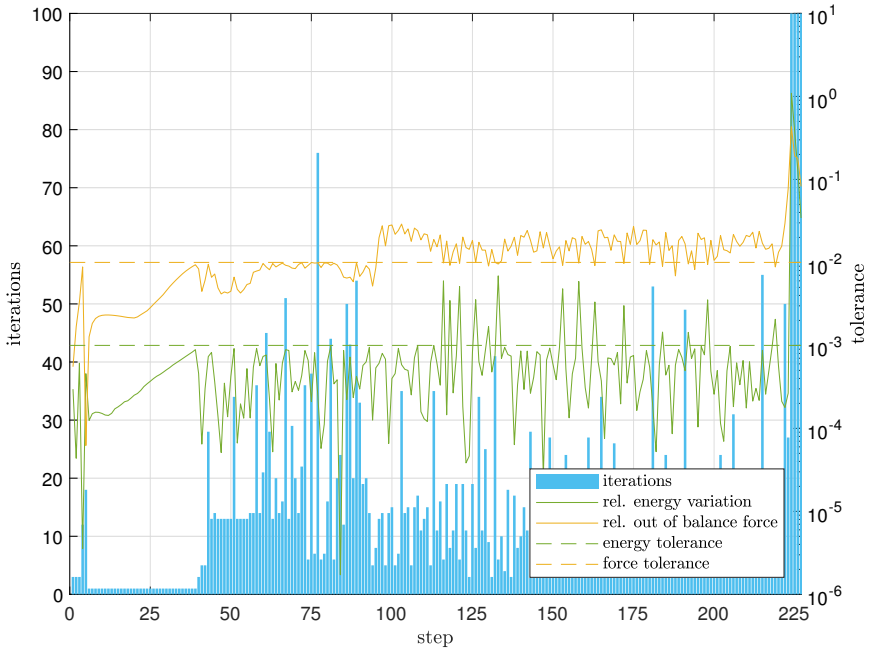

Figure B.1: B-T4-60/180-QNR, convergence

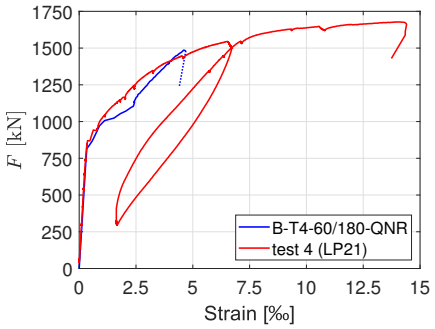

Figure B.2: Average longitudinal strain T-beam 12 (LP21)

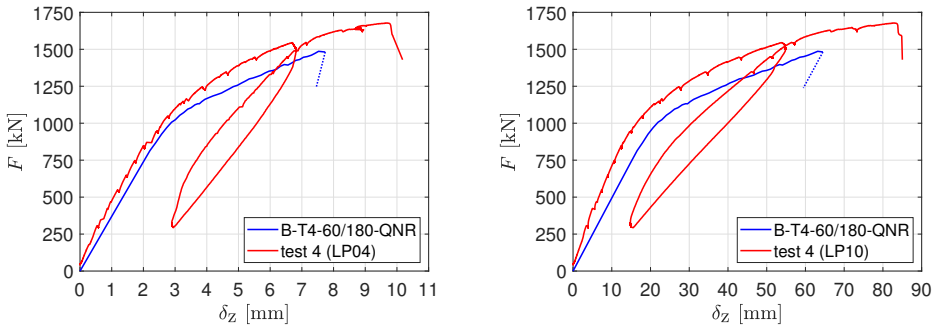

(a) Support deformation

(b) Cross-beam deformation

Figure B.3: Support and cross-beam deformation
(dashed line = non-converged (post-peak))

B.2. ANALYSIS B-T5

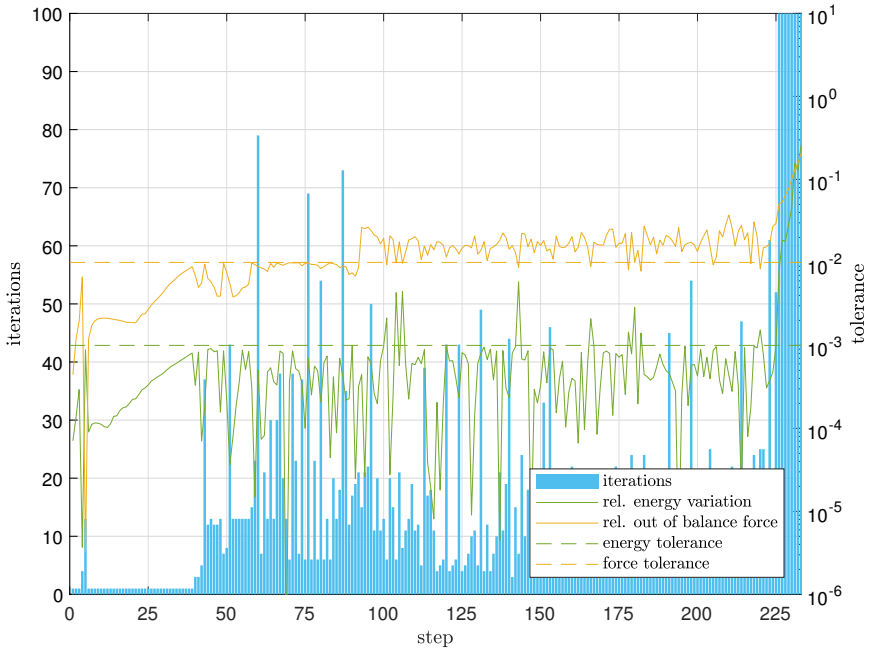

Figure B.4: B-T5-60/180-QNR, convergence

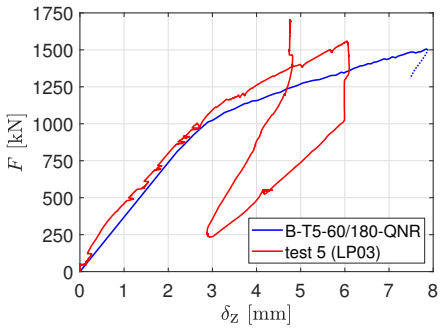

(a) Support deformation

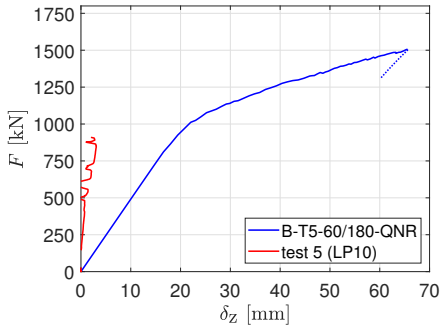

(b) Cross-beam deformation

Figure B.5: Support and cross-beam deformation
(dashed line = non-converged (post-peak))

B.3. ANALYSIS B-T6

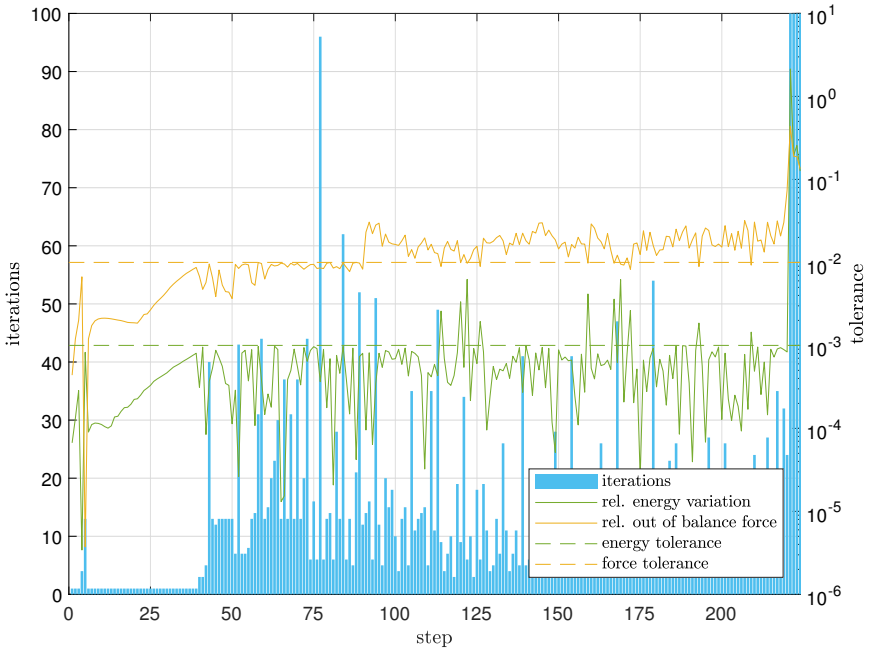

Figure B.6: B-T6-60/180-QNR, convergence

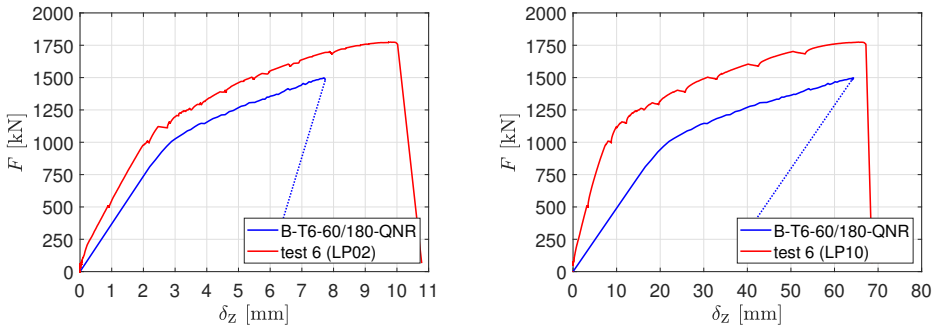

(a) Support deformation

(b) Cross-beam deformation

Figure B.7: Support and cross-beam deformation
(dashed line = non-converged (post-peak))

B.4. ANALYSIS B-T7

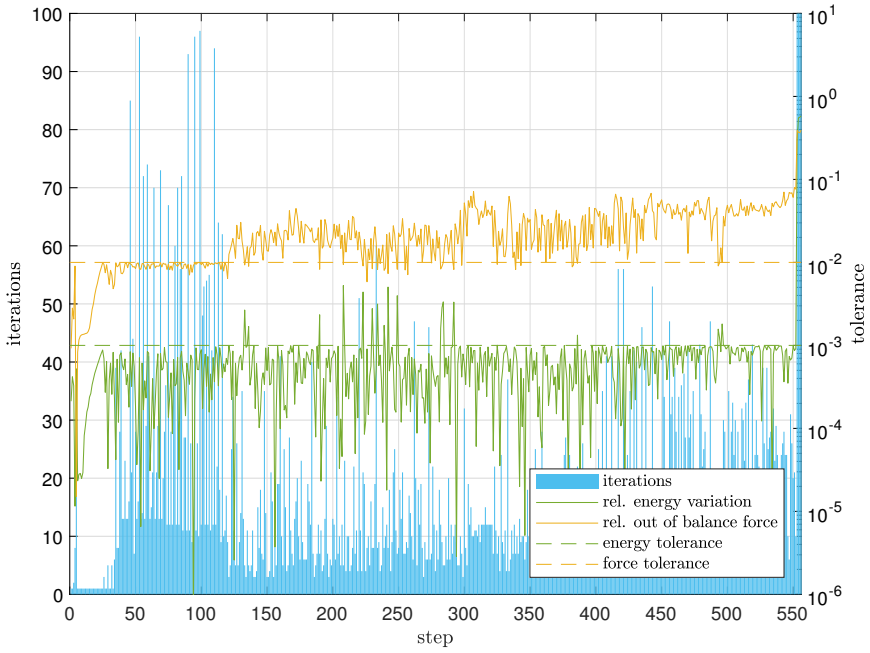

Figure B.8: B-T7-60/180-QNR, convergence

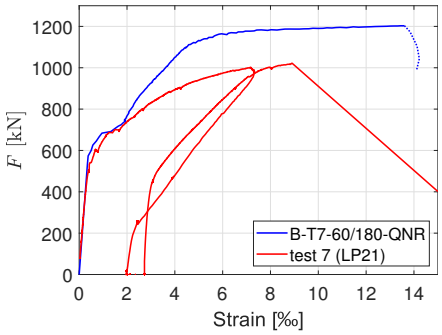

Figure B.9: Average longitudinal strain T-beam 9 (LP21)

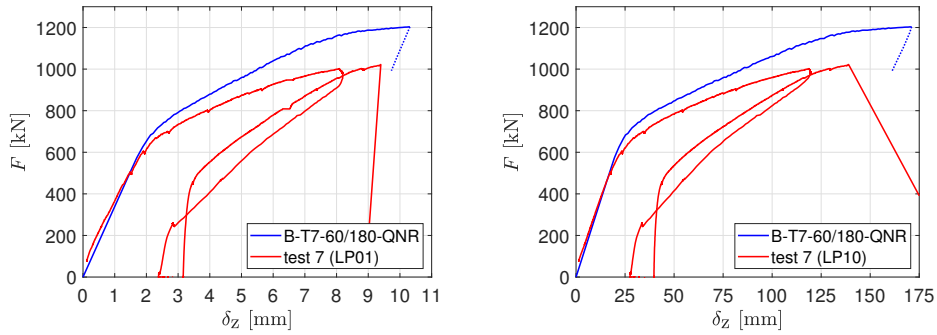

(a) Support deformation

(b) Cross-beam deformation

Figure B.10: Support and cross-beam deformation
(dashed line = non-converged (post-peak))

C

DETAILED RESULTS CMA ANALYSIS

C.1. CMA CALIBRATION 1:2 SCALE NO BENDING

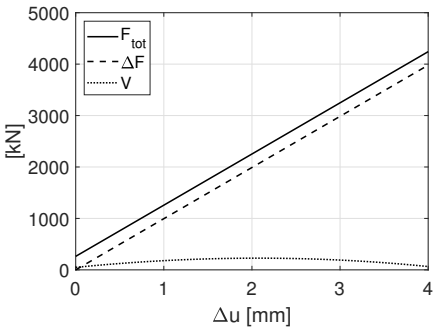

(a) Total force, membrane force and shear force

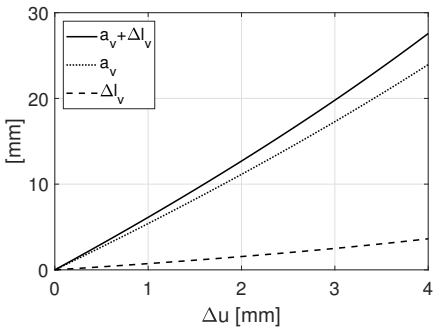

(b) Vertical deformations

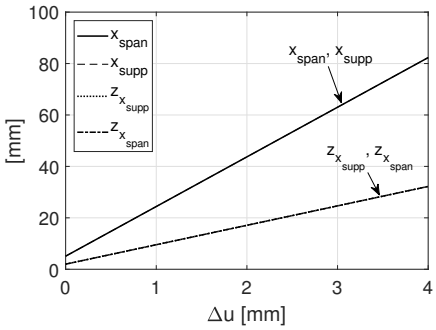

(c) Compression zones height and edge distance to stress resultant

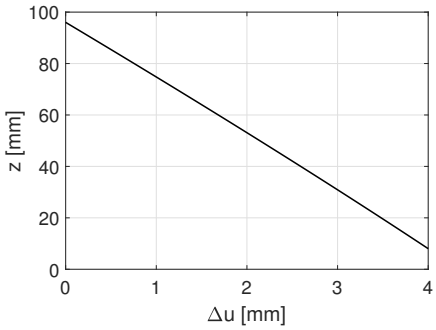

(d) Internal lever arm

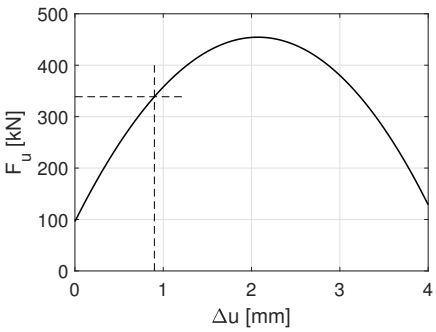

(e) Ultimate concentrated load ($F_{u,max}$ = 454.4 kN, Δu = 0.90 mm at F_u = 338.7 kN)

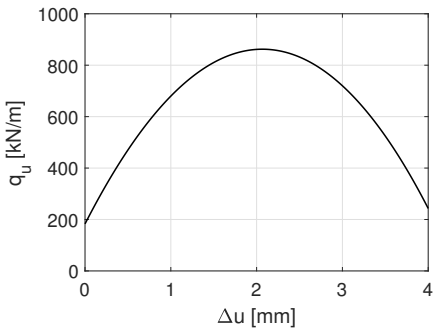

(f) Ultimate distributed load

Figure C.1: Detailed results of Chapter 8 Section 8.2.4.
$L = B$ = 1050 mm, h = 100 mm, f_{cm} = 65 N/mm^2, TPL = 2.5 N/mm^2, k_{hor} = 995000 N/mm, $\zeta_{span} = \zeta_{supp} = 0$

C.2. CMA CALIBRATION 1:2 SCALE FULL BENDING

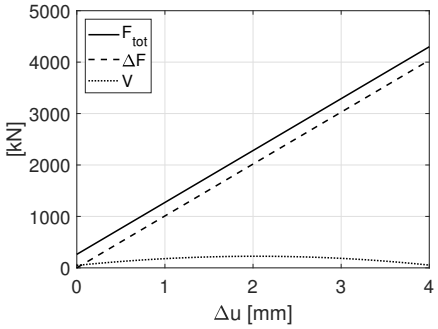

(a) Total force, membrane force and shear force

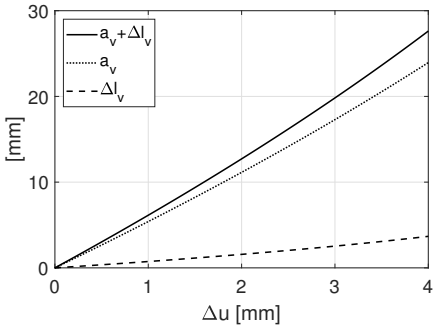

(b) Vertical deformations

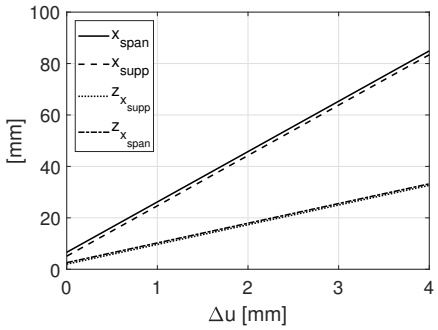

(c) Compression zones height and edge distance to stress resultant

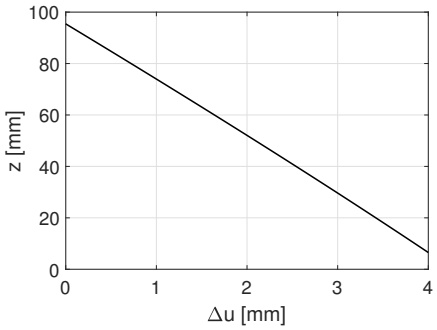

(d) Internal lever arm (z_u = 76 mm at F_u = 338.7 kN)

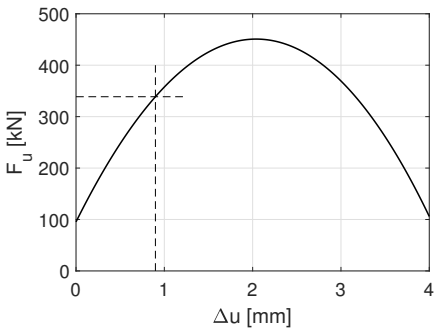

(e) Ultimate concentrated load ($F_{u,max}$ = 450.8 kN, Δu = 0.90 mm at F_u = 338.7 kN)

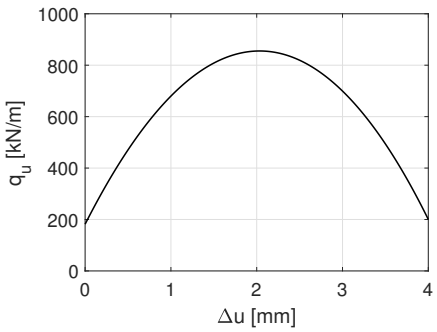

(f) Ultimate distributed load

Figure C.2: Detailed results of Chapter 8 Section 8.2.4.
$L = B$ = 1050 mm, h = 100 mm, f_{cm} = 65 N/mm^2, TPL = 2.5 N/mm^2,
k_{hor} = 1009000 N/mm, ζ_{span} = 0.067, ζ_{supp} = 0

C.3. CMA CALIBRATION 1:1 SCALE NO BENDING

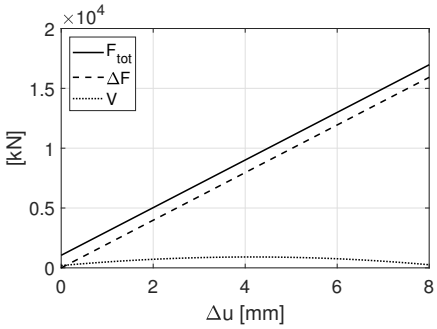

(a) Total force, membrane force and shear force

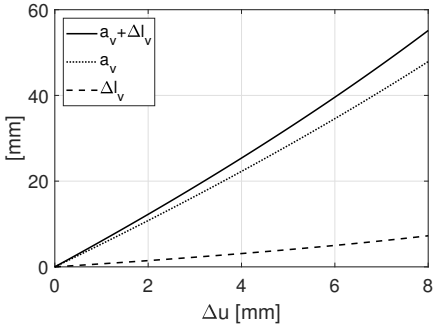

(b) Vertical deformations

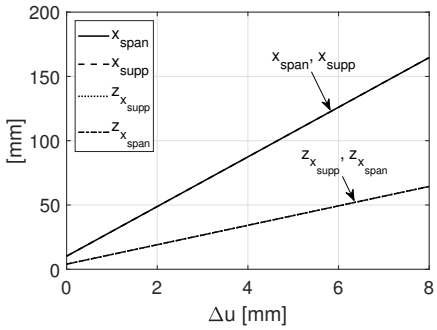

(c) Compression zones height and edge distance to stress resultant

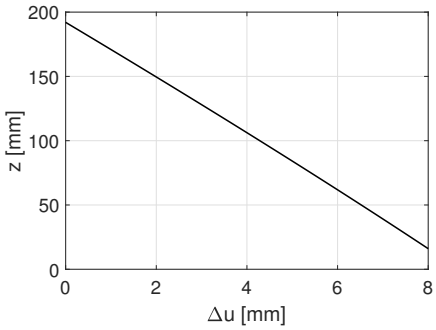

(d) Internal lever arm

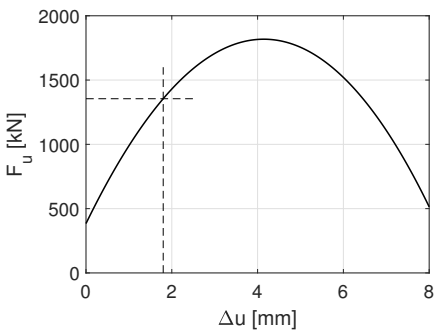

(e) Ultimate concentrated load ($F_{u,max}$ = 1818 kN, Δu = 1.80 mm at F_u = 1354.8 kN)

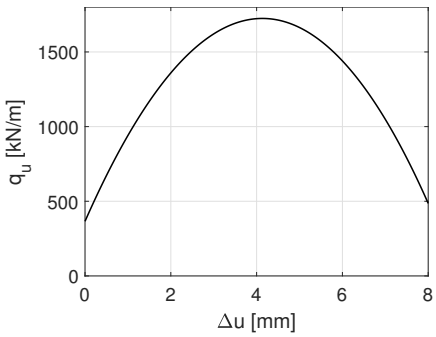

(f) Ultimate distributed load

Figure C.3: Detailed results of Chapter 8 Section 8.2.4.
$L = B = 2100$ mm, $h = 200$ mm, $f_{cm} = 65$ N/mm^2, TPL = 2.5 N/mm^2, $k_{hor} = 1990000$ N/mm, $\zeta_{span} = \zeta_{supp} = 0$

C.4. CMA CALIBRATION 1:1 SCALE FULL BENDING

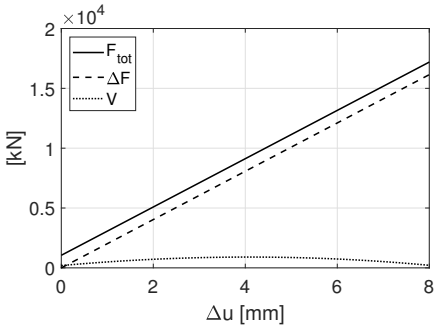

(a) Total force, membrane force and shear force

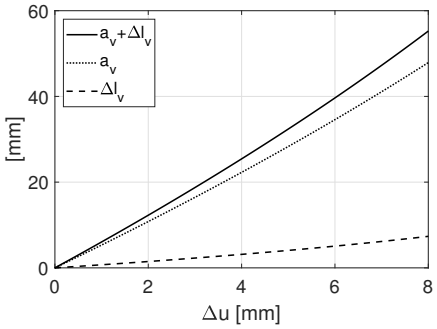

(b) Vertical deformations

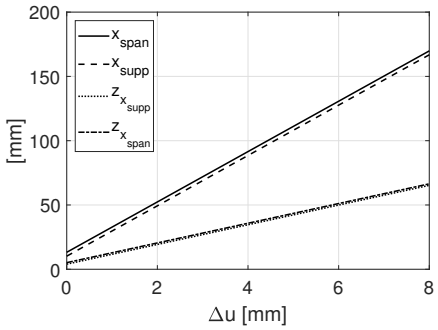

(c) Compression zones height and edge distance to stress resultant

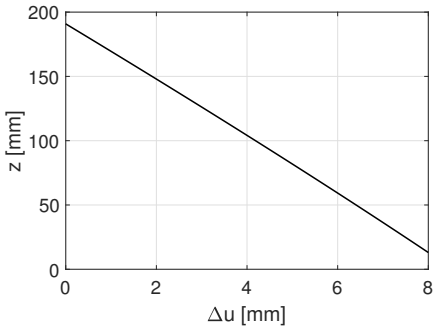

(d) Internal lever arm (z_u = 152 mm at F_u = 1354.8 kN)

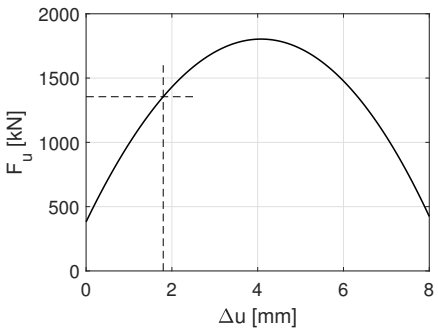

(e) Ultimate concentrated load ($F_{u,max}$ = 1803 kN, Δu = 1.80 mm at F_u = 1354.8 kN)

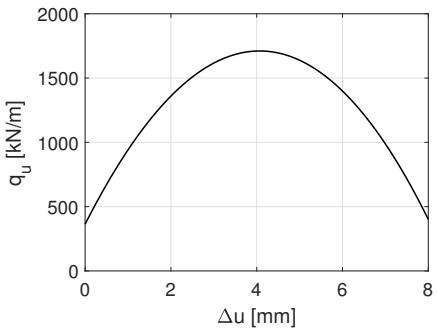

(f) Ultimate distributed load

Figure C.4: Detailed results of Chapter 8 Section 8.2.4.
$L = B$ = 2100 mm, h = 200 mm, f_{cm} = 65 N/mm^2, TPL = 2.5 N/mm^2, k_{hor} = 2018000 N/mm, ζ_{span} = 0.067, ζ_{supp} = 0

C.5. CMA TESTS 1–2 VECHT BRIDGE CALCULATION 1

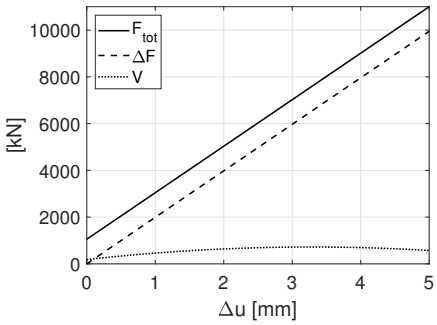

(a) Total force, membrane force and shear force

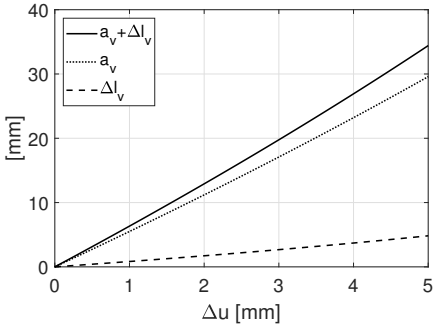

(b) Vertical deformations

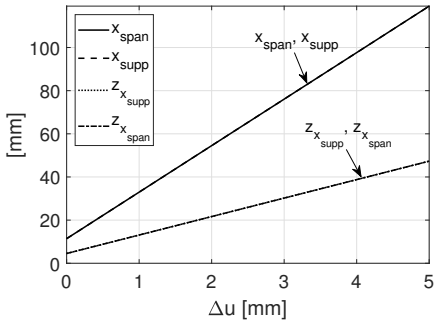

(c) Compression zones height and edge distance to stress resultant

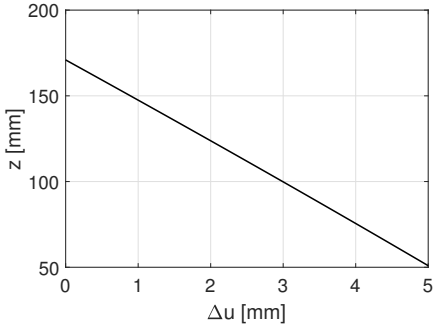

(d) Internal lever arm

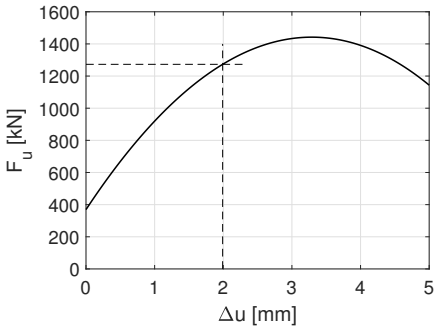

(e) Ultimate concentrated load
($F_{u,max}$ = 1442 kN, Δu = 1.99 mm at F_u = 1273 kN)

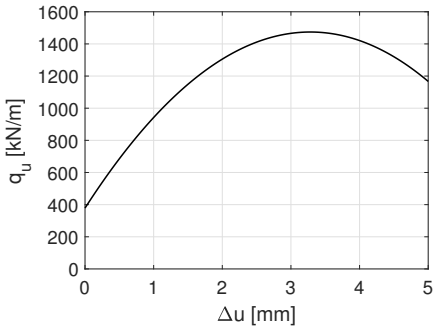

(f) Ultimate distributed load

Figure C.5: Detailed results of Chapter 8 Section 8.2.4.
$L = B$ = 1950 mm, h = 180 mm, f_{cm} = 60.3 N/mm^2, TPL = 3.0 N/mm^2,
k_{hor} = 1990000 N/mm, $\zeta_{span} = \zeta_{supp} = 0$

C.6. CMA TESTS 1–2 VECHT BRIDGE CALCULATION 2

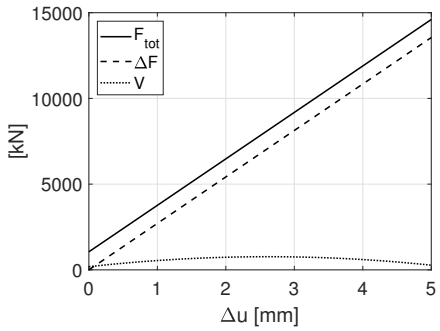

(a) Total force, membrane force and shear force

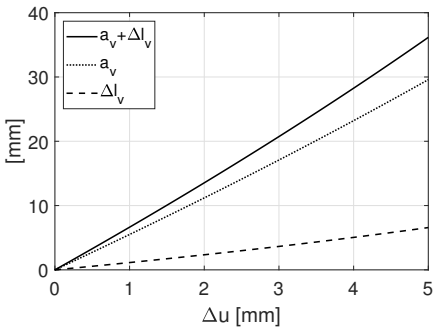

(b) Vertical deformations

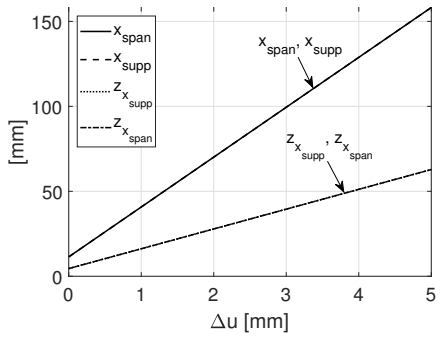

(c) Compression zones height and edge distance to stress resultant

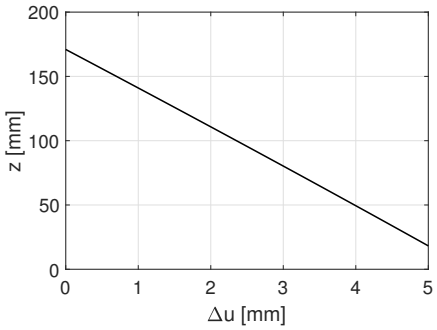

(d) Internal lever arm

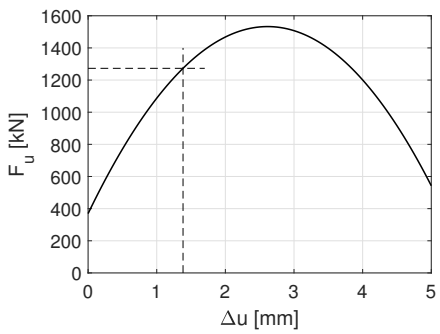

(e) Ultimate concentrated load
($F_{u,max}$ = 1533 kN, Δu = 1.38 mm at F_u = 1273 kN)

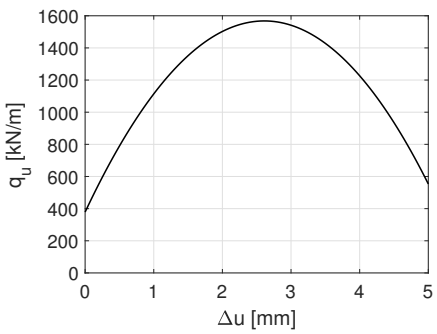

(f) Ultimate distributed load

Figure C.6: Detailed results of Chapter 8 Section 8.2.4.
$L = B$ = 1950 mm, h = 180 mm, f_{cm} = 60.3 N/mm^2, TPL = 3.0 N/mm^2,
k_{hor} = 2710000 N/mm, $\zeta_{span} = \zeta_{supp} = 0$

D

DETAILED RESULTS CAA ANALYSIS

D.1. CAA RESULTS T-BEAM WITH SLAB NO BENDING

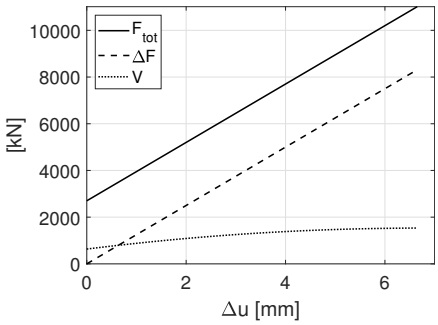

(a) Total force, membrane force and shear force

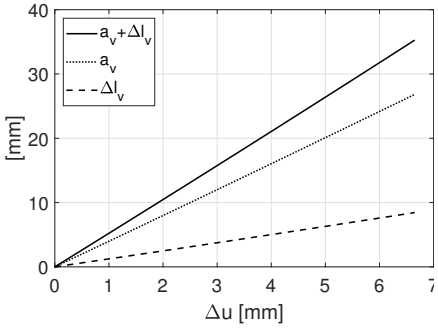

(b) Vertical deformations

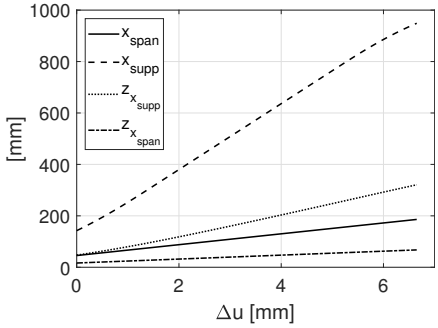

(c) Compression zones height and distance to center of gravity

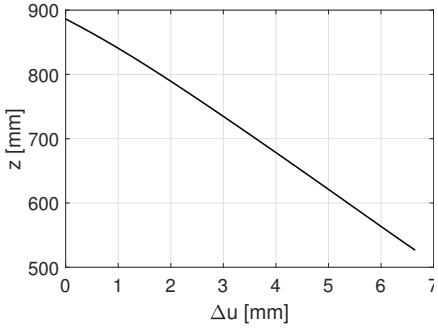

(d) Internal lever arm

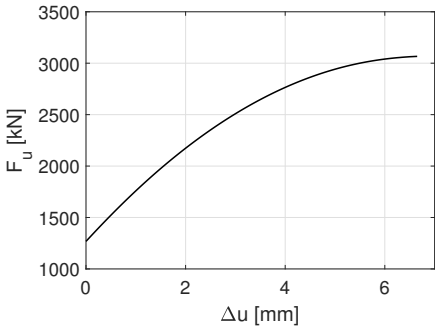

(e) Ultimate concentrated load

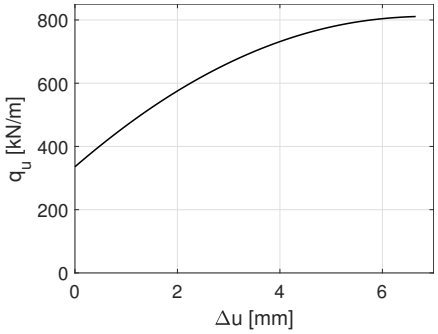

(f) Ultimate distributed load

Figure D.1: Detailed results of Chapter 8 Section 8.2.5 Table 8.6.
T-beam with integrated deck slab (Appendix E Figure E.3a), L = 7550 mm, h = 950 mm, k_{hor} = 1250000 N/mm, $\zeta_{span} = \zeta_{supp} = 0$ and prestressing = 100%

D.2. CAA RESULTS T-BEAM WITH SLAB AND BENDING

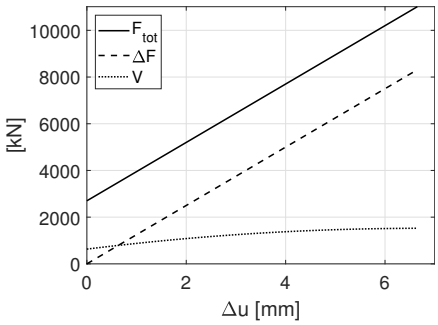

(a) Total force, membrane force and shear force

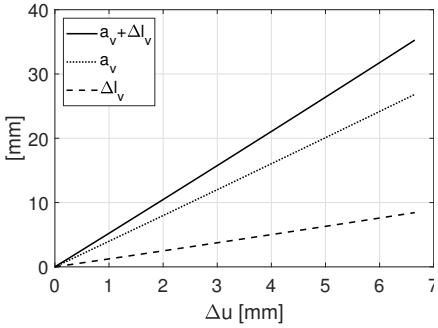

(b) Vertical deformations

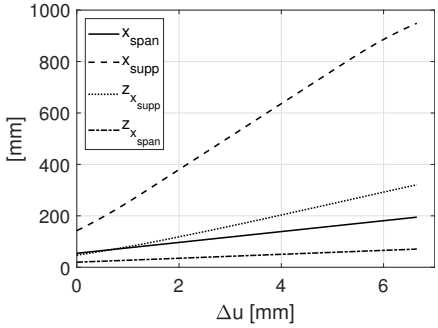

(c) Compression zones height and distance to center of gravity

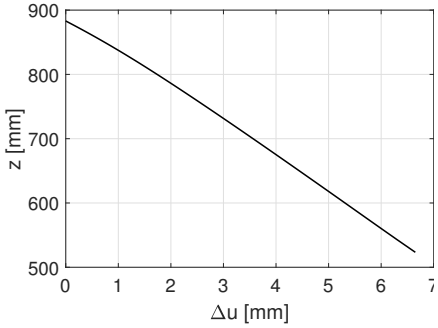

(d) Internal lever arm

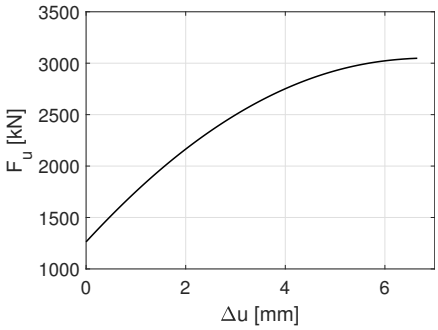

(e) Ultimate concentrated load

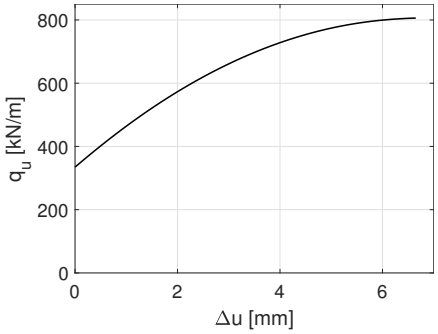

(f) Ultimate distributed load

Figure D.2: Detailed results of Chapter 8 Section 8.2.5 Table 8.7.
T-beam with integrated deck slab (Appendix E Figure E.3a), L = 7550 mm, h = 950 mm,
k_{hor} = 1250000 N/mm, ζ_{span} = 0.047, ζ_{supp} = 0 and prestressing = 100%

D.3. CAA RESULTS T-BEAM AFTER PUNCHING NO BENDING

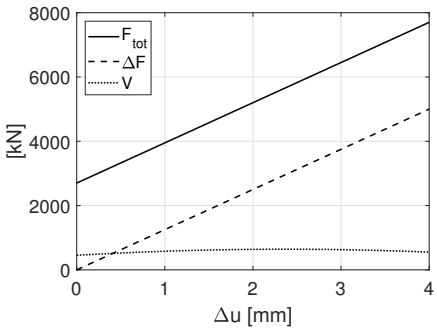

(a) Total force, membrane force and shear force

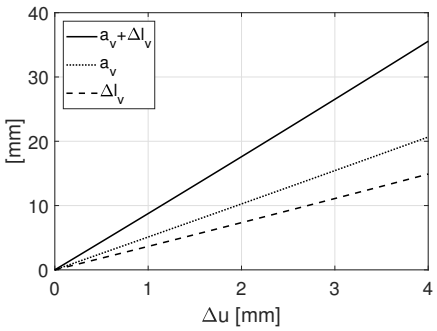

(b) Vertical deformations

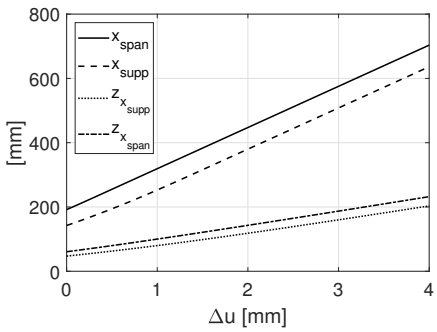

(c) Compression zones height and distance to center of gravity

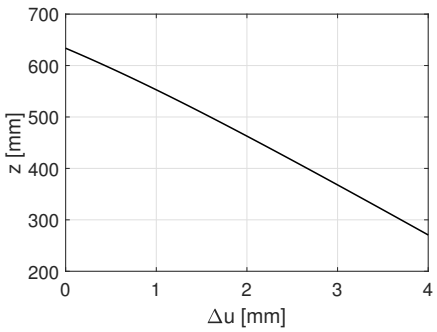

(d) Internal lever arm

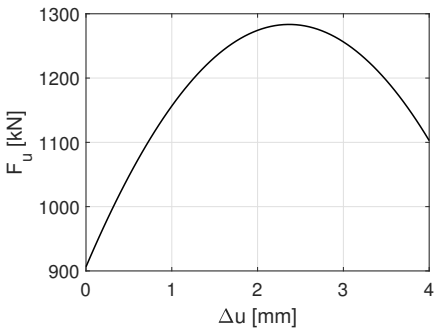

(e) Ultimate concentrated load

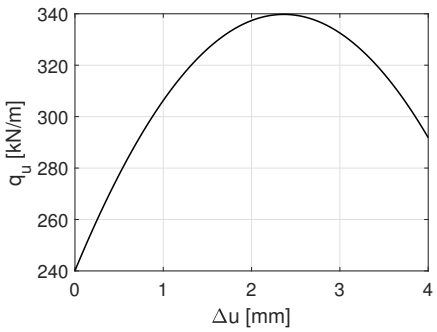

(f) Ultimate distributed load

Figure D.3: Detailed results of Chapter 8 Section 8.2.5 Table 8.8.
T-beam with reduced cross-section after punching (Appendix E Figure E.3b),
L = 7550 mm, h = 742 mm, k_{hor} = 1250000 N/mm, $\zeta_{\text{span}} = \zeta_{\text{supp}} = 0$ and prestressing = 100%

D.4. CAA RESULTS T-BEAM AFTER PUNCHING AND BENDING

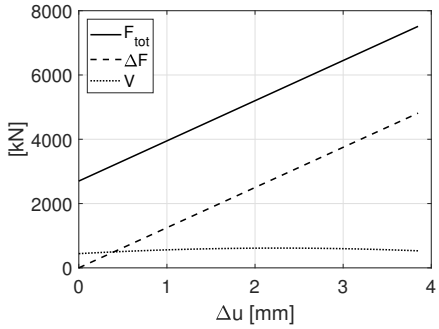

(a) Total force, membrane force and shear force

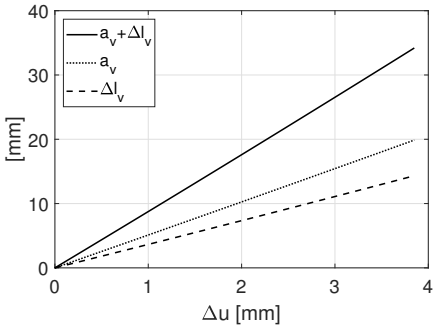

(b) Vertical deformations

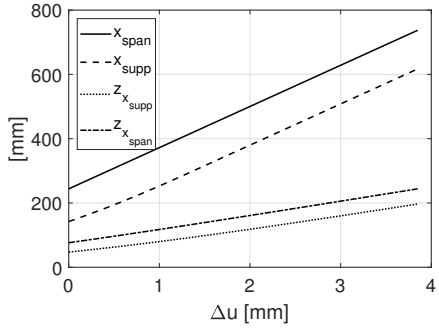

(c) Compression zones height and distance to center of gravity

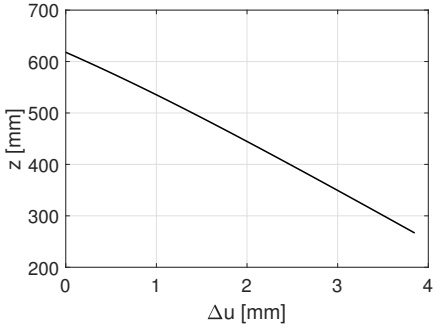

(d) Internal lever arm

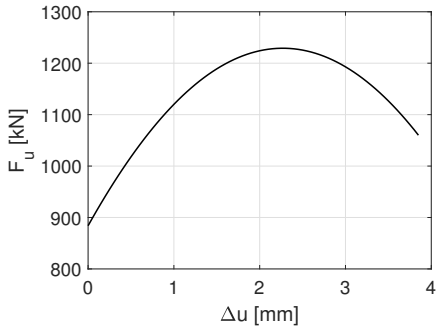

(e) Ultimate concentrated load

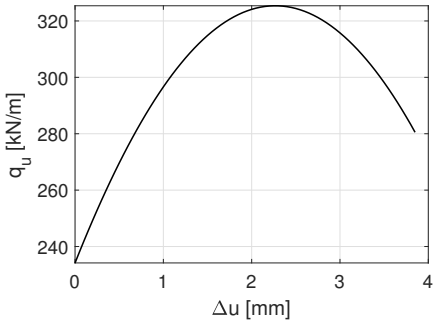

(f) Ultimate distributed load

Figure D.4: Detailed results of Chapter 8 Section 8.2.5 Table 8.9.
T-beam with reduced cross-section after punching (Appendix E Figure E.3b),
L = 7550 mm, h = 742 mm, k_{hor} = 1250000 N/mm, ζ_{span} = 0.094, ζ_{supp} = 0 and prestressing = 100%

D.5. CAA RESULTS TEST 1 VECHT BRIDGE

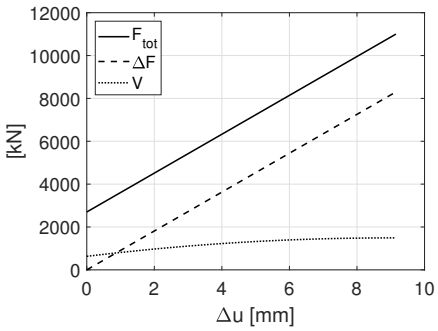

(a) Total force, membrane force and shear force

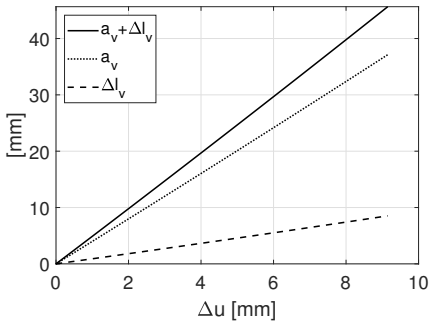

(b) Vertical deformations

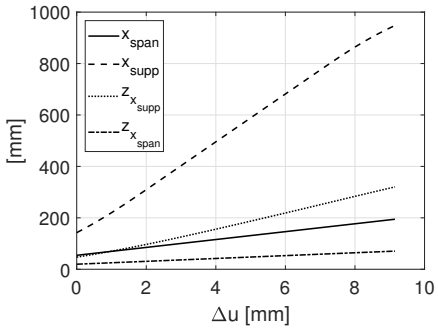

(c) Compression zones height and distance to center of gravity

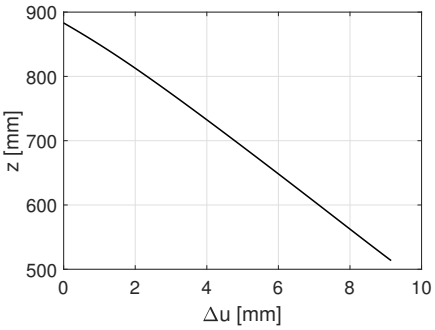

(d) Internal lever arm

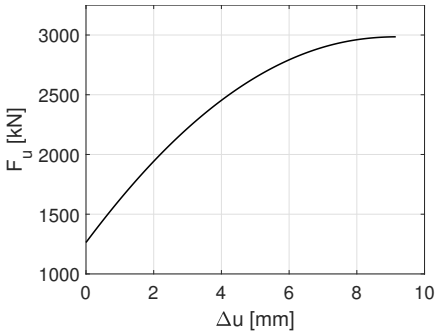

(e) Ultimate concentrated load

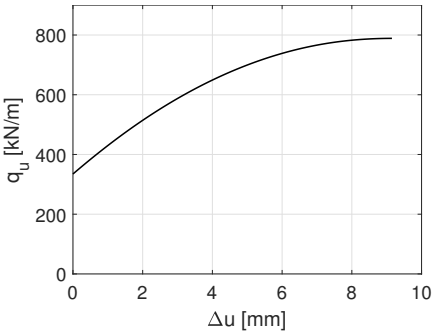

(f) Ultimate distributed load

Figure D.5: Detailed results of Chapter 8 Section 8.2.5.
T-beam with integrated deck slab (Appendix E Figure E.3a), L = 7550 mm, h = 950 mm, k_{hor} = 907000 N/mm, ζ_{span} = 0.044, ζ_{supp} = 0 and prestressing = 100%

E

SECTIONAL PROPERTIES T-BEAM VECHT BRIDGE

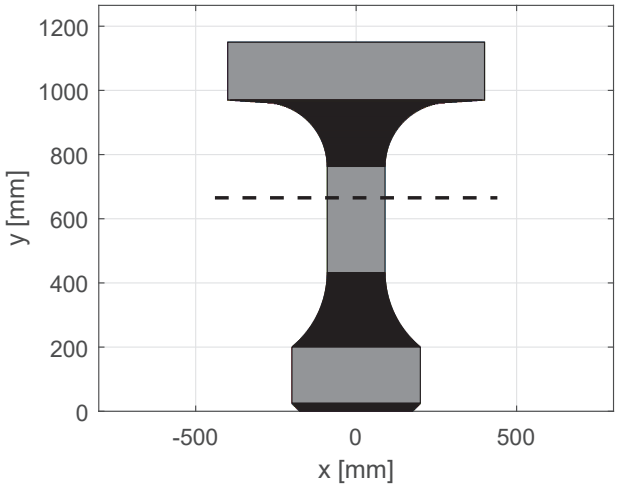

A_c = 398247 mm^2
z_{cb} = 665.22 mm
z_{ct} = 484.78 mm
I_c = 6.0208e+10 mm^4
W_{cb} = 9.0509e+07 mm^3
W_{ct} = 1.2420e+08 mm^3
S_y = 7.0637e+07 mm^3

(a) T-beam

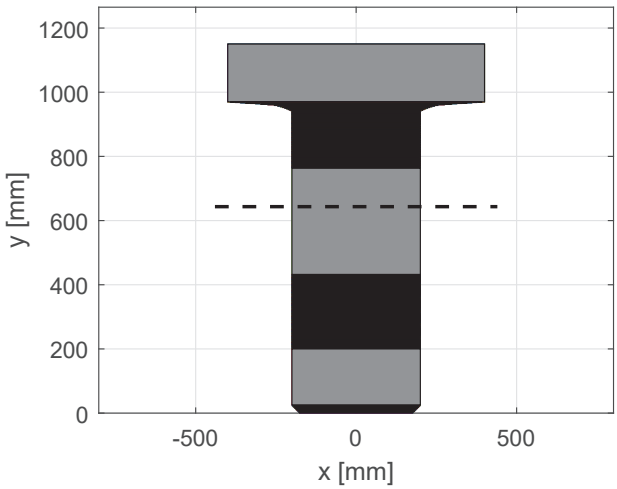

A_c = 534684 mm^2
z_{cb} = 643.37 mm
z_{ct} = 506.63 mm
I_c = 6.5624e+10 mm^4
W_{cb} = 1.0200e+08 mm^3
W_{ct} = 1.2953e+08 mm^3
S_y = 8.2389e+07 mm^3

(b) T-beam end block

Figure E.1: Sectional properties T-beam and T-beam end block

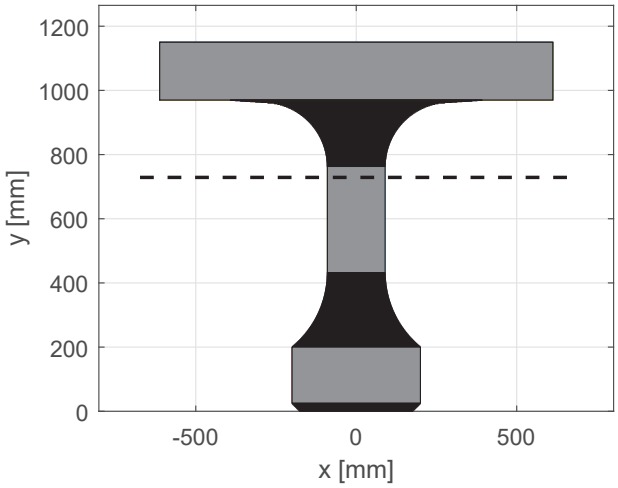

A_c = 474747 mm^2
z_{cb} = 728.84 mm
z_{ct} = 421.16 mm
I_c = 7.0416e+10 mm^4
W_{cb} = 9.6615e+07 mm^3
W_{ct} = 1.6719e+08 mm^3
S_y = 8.2364e+07 mm^3

(a) T-beam with integrated deck slab

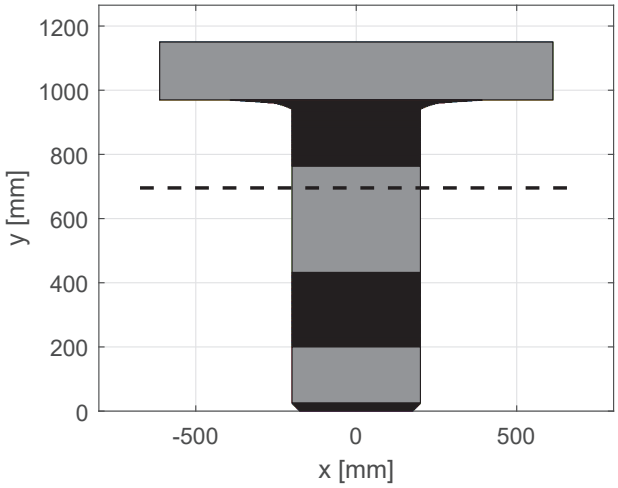

A_c = 611184 mm^2
z_{cb} = 695.52 mm
z_{ct} = 454.48 mm
I_c = 7.7448e+10 mm^4
W_{cb} = 1.1135e+08 mm^3
W_{ct} = 1.7041e+08 mm^3
S_y = 9.6320e+07 mm^3

(b) T-beam end block with integrated deck slab

Figure E.2: Sectional properties T-beam and T-beam end block including acting width integrated deck slab

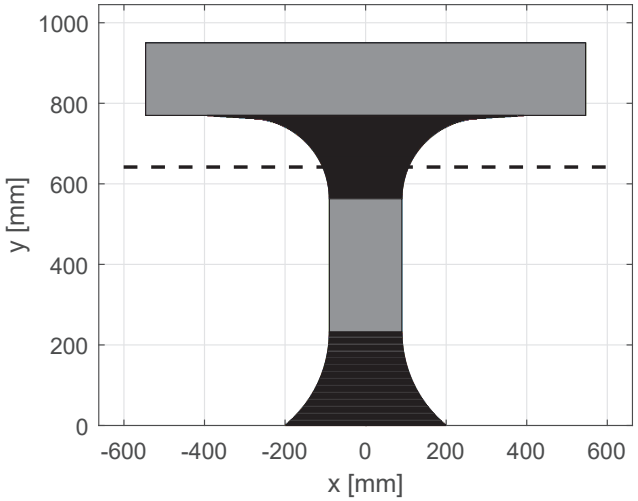

A_c = 371471 mm^2
z_{cb} = 641.74 mm
z_{ct} = 308.26 mm
I_c = 3.1418e+10 mm^4
W_{cb} = 4.8957e+07 mm^3
W_{ct} = 1.0192e+08 mm^3
S_y = 4.6170e+07 mm^3

(a) T-beam including fictitious acting width integrated deck slab

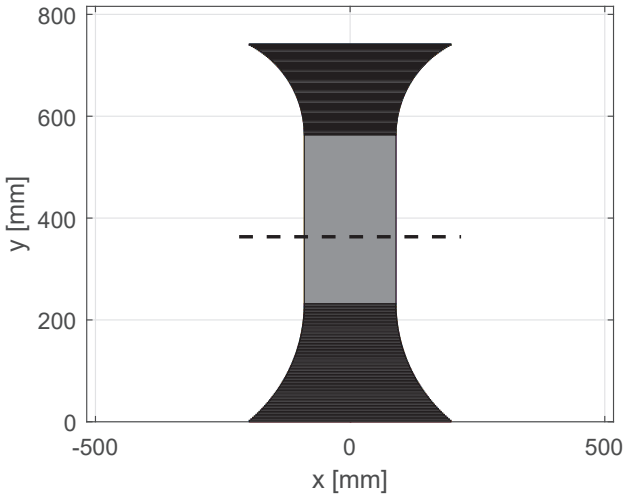

A_c = 160203 mm^2
z_{cb} = 363.31 mm
z_{ct} = 378.29 mm
I_c = 8.9047e+09 mm^4
W_{cb} = 2.4510e+07 mm^3
W_{ct} = 2.3539e+07 mm^3
S_y = 1.6650e+07 mm^3

(b) T-beam with reduced cross-section after punching

Figure E.3: Sectional properties T-beam used in CAA analysis

ACKNOWLEDGEMENTS

It has been a real privilege doing this research. First of all, I want to thank my former promotor Dick Hordijk who supported and inspired me greatly at the start of my research and helped me overcoming my initial struggles. I very much like to thank my former copromoter Cor van der Veen for supporting me during my whole PhD period even after retiring from the TU Delft. It has been a real privilege and pleasure working together and going to the various conferences and (DIANA) workshop meetings in different countries. Without your valuable knowledge and your guidance I would not have achieved the work I present here.

I wish to thank my promoter, Max Hendriks. It has been an unexpected and pleasant surprise that you have become my new promotor after you have also supervised my master's thesis at the TU Delft many years ago. I really enjoyed our talks and discussions together and you have steered me in the right direction and helped me tremendously in ultimately finishing my thesis. I wish to thank my new promotor Eva Lantsoght for her much appreciated guidance, seemingly unlimited support, and all of the reading and correcting of the various parts of the thesis. Of course I would also like to thank you for providing me with sufficient energy by means of all the nice chocolates from Ecuador!

The financial support of my employer Van Hattum en Blankevoort is gratefully acknowledged. I feel very privileged to have been given the opportunity of a part-time PhD. I especially wish to thank René Beurze (former director of Volker InfraDesign), Sipke Huitema (former manager of the Civil Engineering group at Volker InfraDesign) and Hans Galjaard (retired former colleague at Van Hattum en Blankevoort) in supporting me in this endeavour. I want to thank my many other colleagues at Van Hattum en Blankevoort for their support and flexibility at all the projects we worked on together during all the years in which I had to split my time between Van Hattum en Blankevoort and the TU Delft.

I wish to thank Rijkswaterstaat (RWS) for their financial support of this research. I especially wish to thank Ane de Boer, who not only helped me with his extensive knowledge of DIANA but also with his contribution involving the testing of the Vecht bridge. I also very much like to thank you for the many (international) DIANA meetings you helped organize.

Concerning the testing of the Vecht bridge, I wish to thank all the colleagues of the Concrete Structures group at the TU Delft who helped me tremendously during this huge undertaking: Yuguang Yang, Marco Roosen, Fred Schilperoort, Eva Lantsoght, Cor van der Veen, Albert Bosman and student Thomas Harrewijn. I very much like to thank Rutger Koekkoek, for his mammoth efforts in the preparation and testing of the Vecht bridge. Without your efforts this project would have never been possible. I like to thank Frank Linthorst and Danny den Boef of Witteveen+Bos, responsible for the logistics and safety during the tests, and Otto Illing and the late Chris Huissen of Mammoet, responsible for applying the load during the collapse tests.

I wish to thank all of the members of the 'Gebruikerscommissie' (user committee) who helped guide me during our yearly meetings together: Herbert van der Ham (former RWS), Arthur Slobbe (TNO) and Coen van der Vliet (Arcadis).

And last but not least, I wish to thank all my friends and family for supporting me over the years.

CURRICULUM VITÆ

Sebastiaan Willem Hendrik ENSINK

22-12-1972 Geboren in Nijmegen, Nederland.

OPLEIDINGEN

2014–2024 Promovendus aan de TU Delft
Technische Universiteit Delft, faculteit Civiele Techniek en Geowetenschappen
Afdeling: 'Engineering Structures', sectie: 'Concrete Structures'
Proefschrift:
System behaviour in prestressed concrete T-beam bridges

2007–2010 Master of Science in Civil Engineering
Technische Universiteit Delft, faculteit Civiele Techniek en Geowetenschappen
'Structural Engineering', specialisatie: 'Structural Mechanics'
Afstudeeronderzoek:
Simulation of steel-concrete bond-slip with sequentially linear analysis using interface elements

1993–1999 HTS Civiele Techniek
Hogeschool Arnhem-Nijmegen
Specialisatie: constructie

1990–1993 MTS Weg- en Waterbouwkunde
Technisch College Nijmegen

1985–1990 HAVO
Lindenholt College Nijmegen

CURSUSSEN

2013 Grondmechanica en funderingstechniek 1 (CGF1)

2007 Betonconstructeur BV

2005 HTI Betonconstructeur

COMMISSIES

2020– NEN-EN 1991-2 Werkgroep Brugbelastingen (lid normcommissie)

2020– NEN-EN 1992-2 Werkgroep Betonnen Bruggen (lid normcommissie)

WERKERVARING

2010–	Senior Specialist, Van Hattum en Blankevoort *Voormalige functies:* Specialist, Hoofdconstructeur, Senior Constructeur *Projecten:* Princes Magriettunnel A7, renovatie & herberekening toeritten Koopvaardersschutsluis, renovatie & herberekening sluiskolk Windpark Venlo, funderingsontwerp Windpark Landtong Rozenburg, funderingsontwerp Windpark De Rietvelden, funderingsontwerp A1/A28 Knooppunt Hoevelaken, ontwerp bruggen & viaducten OpenIJ, deelontwerp binnenhoofd zeesluis IJmuiden OV-Saal, renovatie & herberekening spoorviaduct Hoogwatergeul Veessen-Wapenveld, ontwerp bruggen Omlegging A9 Badhoevedorp, ontwerp tunnels & viaducten Ontpoldering Noordwaard, ontwerp bruggen
2001–2007	Tekenaar / constructeur, Royal Haskoning
2001–2003	Tekenaar, Tunnel Engineering Consultants (TEC)
1999–2001	Tekenaar, Bouwdienst Rijkswaterstaat (afdeling Tunnelbouw)

PUBLICATIES

2019	Ensink, S.W.H., Hendriks, M.A.N., and van der Veen, C. Non-linear analysis of prestressed concrete T-beams. In *Advances in Engineering Materials, Structures and Systems: Innovations, Mechanics and Applications - Proceedings of the 7th International Conference on Structural Engineering, Mechanics and Computation*, pages 1360–1365.
2018	Ensink, S.W.H., van der Veen, C., Hordijk, D.A., Lantsoght, E.O.L, van der Ham, H., and de Boer, A. Full-size field test of prestressed concrete T-beam bridge. In *Euro-bridge*, 2018. Edinburgh, Scotland.
2016	Ensink, S.W.H., van der Veen, C., and de Boer, A. Shear tests on large prestressed concrete T-beams. In *fib Symposium*, 2016. Cape Town, South Africa.
2015	Ensink, S.W.H., van der Veen, C., and de Boer, A. Shear or bending? Experimental results on large T-shaped prestressed concrete beams. In *Proceedings of the 16th European bridge conference*, 2015.
2012	Ensink, S. W. H., van de Graaf, A., Slobbe, A.T., Hendriks, M.A.N., den Uijl, J. and Rots, J.G. Modelling of bond behaviour by means of sequentially linear analysis and concrete-to-steel interface elements. In *Proceedings of the Fourth International Symposium "Bond in concrete 2012: Bond, Anchorage, Detailing": General aspects of bond*, volume 1, pages 161–167, 2012.

TU Delft